NEUTRON SCATTERING STUDIES OF THE ELECTRON-DOPED HIGH-TEMPERATURE SUPERCONDUCTOR NEODYMIUM CERIUM COPPER OXIDE

A DISSERTATION
SUBMITTED TO THE DEPARTMENT OF PHYSICS
AND THE COMMITTEE ON GRADUATE STUDIES
OF STANFORD UNIVERSITY
IN PARTIAL FULFILLMENT OF THE REQUIREMENTS
FOR THE DEGREE OF
DOCTOR OF PHILOSOPHY

Eugene Makalu Davenport Motoyama
December 2009

This dissertation is online at: http://purl.stanford.edu/gm903my1415

I certify that I have read this dissertation and that, in my opinion, it is fully adequate in scope and quality as a dissertation for the degree of Doctor of Philosophy.

Martin Greven, Primary Adviser

I certify that I have read this dissertation and that, in my opinion, it is fully adequate in scope and quality as a dissertation for the degree of Doctor of Philosophy.

Aharon Kapitulnik, Co-Adviser

I certify that I have read this dissertation and that, in my opinion, it is fully adequate in scope and quality as a dissertation for the degree of Doctor of Philosophy.

Steven Kivelson

Approved for the Stanford University Committee on Graduate Studies.

Patricia J. Gumport, Vice Provost Graduate Education

This signature page was generated electronically upon submission of this dissertation in electronic format. An original signed hard copy of the signature page is on file in University Archives.

Abstract

While the mechanism for the high transition temperatures (T_c) in the cuprate superconductors remains unsolved, antiferromagnetic fluctuations on the copper-oxygen sheets are thought to play an important role. Long-range antiferromagnetic order is present in the undoped insulating parent compounds, whereas superconductivity is observed when these materials are doped with a sufficient number of holes or electrons. Because these two phases are well separated on the hole-doped side of the phase diagram, the interplay between antiferromagnetism and superconductivity is perhaps better studied in the electron-doped compounds, where the two phases appear to overlap. In this Thesis work, single crystals of electron-doped $Nd_{2-x}Ce_xCuO_4$ (NCCO) were grown over a wide range of cerium concentration, and the following two neutron scattering studies were performed on these crystals.

In the first study, an energy-integrating neutron scattering method is used to measure the two-dimensional instantaneous magnetic correlation length as a function of temperature and doping. For $x < 0.12$, the correlation length diverges at the same temperature at which magnetic Bragg peaks appear, as expected. For $x > 0.12$, on the other hand, the correlation length remains finite down to the lowest measured temperatures. Since bulk superconductivity is only found above about $x = 0.13$, this shows that there is no genuine coexistence between superconductivity and long-range antiferromagnetic order, which was previously thought to extend to $x = 0.17$.

The second study is the first inelastic neutron scattering investigation of an electron-doped cuprate superconductor in an applied magnetic field. This experiment measures how the weakening of superconductivity due to a magnetic

field affects the antiferromagnetic response. An advantage of the electron-doped cuprates is that the critical field H_{c2} required to completely suppress superconductivity is relatively low ($\sim 10\,\mathrm{T}$). In zero field, the antiferromagnetic excitation spectrum of NCCO ($x = 0.166$) is gapped below 2.5 meV. The gap energy is found to decrease linearly with applied field and to extrapolate to zero near H_{c2}. The observed behavior indicates that the non-superconducting ground state is similar to the (zero-field) paramagnetic state at temperatures above T_c, and thus that superconductivity and antiferromagnetism are not competing orders in this part of the phase diagram.

Acknowledgements

The research and results described in this Thesis would not have been possible without the help of others, and I would like to thank everybody for their help and support over the years.

I have had the fortune to have an adviser that has been personally interested in my research and that has been involved in the details from the very beginning. I thank Martin for his strong sense of direction in this complex field of research.

The current and former members of our research group deserve a lot of my thanks. I'd like to thank Patrick Mang who mentored me during my first six months in the group, both in the laboratory and at the neutron beamlines. He is also the one who pioneered both of the projects described in this Thesis.

Over the years, other members of our group have taught and helped me with the various techniques used in my research. I want to particularly thank Inna Vishik, who taught me a lot of the laboratory techniques, despite being an undergraduate at the time. She was a great help to me while she was in the group. I also thank Guichuan Yu, who has been the group expert on all of the characterization techniques, such as SQUID magnetometry, preparations for ICP measurements, and machine shop work.

Guichuan, Yuan Li and Guillaume Chabot-Couture have been long-time group-mates, and I thank all of them for the long discussions we've had on the fourth floor that, despite the resulting decrease in productivity, have kept me interested in science over the years. I also thank Guichuan and Yuan for their company during our time at the neutron scattering facilities.

I also acknowledge the instrument scientists and collaborators that have helped

me with all of the beam-line measurements. Daniel Petitgrand at the LLB was my primary collaborator at that laboratory for the field-effect measurements described in Chapter 4. Owen Vajk, a former member of our research group, was for many years my primary collaborator at the NCNR for the correlation length measurements described in Chapter 3, and I especially thank him for the occasions in which he performed the measurements for me when I was unable to travel. I also thank Jeff Lynn and William Ratcliff at the NCNR for their help with the instruments. The more recent spin correlation measurements at HFIR were only possible with the help of Jerel Zarestky, Ovidiu Garlea and Wei Tian. And I would like to thank Tomo Uemura and Graeme Luke for letting us use some of their μSR beamtime at TRIUMF for our samples, and their students Jeremy Carlo, Travis Williams and Soo Kyung Kim for running the instrument.

My thanks go out to all of my friends for making life at Stanford fun. I firmly believe that their strong friendships have been key to surviving the ups and downs of the otherwise isolated research life of a graduate student.

I thank my mother and father for their support; I feel lucky to have them as parents. Finally, I thank my wife Jamie for her love and companionship, and especially for her patience and understanding during my long work hours and frequent travels.

Contents

List of Tables

List of Figures

Chapter 1

Introduction

This Chapter attempts to motivate the neutron-scattering studies of the electron-doped cuprates described in this Thesis. It contains general background material on the high-T_c cuprate superconductors and a basic discussion of their physical properties. The last Section contains an outline of the remainder of the Thesis.

1.1 Studying the cuprate superconductors

There exist many incentives for studying the cuprate superconductors. These include the development of practical applications, the drive towards a theoretical understanding of high-T_c superconductivity, and a basic scientific curiosity about the physics of complex low-dimensional systems in general.

Practical applications. Superconductivity is a phenomenon with two defining properties. The first is perfect conductivity: below a certain critical temperature T_c, a material's electrical resistivity falls to zero. The second is perfect diamagnetism (the Meissner effect): electrical current spontaneous forms to screen external magnetic fields. Superconductivity is not uncommon: many elemental metals, such as aluminum (T_c = 1.2 K) and lead (T_c = 7.2 K), are superconductors at low temperatures.

One could suppose that the lossless transmission of electrical current would

have many potential practical applications. Unfortunately, the T_c values of these materials are typically below 10 K. Applications are thus limited by the ability to cool to and maintain such low temperatures.

This situation suddenly changed with the discovery of high-T_c superconductivity in 1986 by Bednorz and Müller [1]. They found that the compound $La_{2-x}Ba_xCuO_4$ has an onset T_c of about 35 K. The years that followed were an exciting time in which there was discovery after discovery of copper-oxide compounds with higher and higher transition temperatures. Considering the rapid pace of discovery and increase in T_c, the ultimate discovery of room-temperature superconductivity was no longer inconceivable.

The discovery of new materials with higher T_c values stalled after only a handful of years. The prospect of room-temperature superconductivity is no longer mentioned explicitly in publications. However, the discovery of materials with T_c values above 77 K (the temperature of liquid nitrogen) has enabled the application of superconductivity in some particular niches, including short segments of high-current power lines [2].

Scientific curiosity. After the discovery of superconductivity in 1911 by H. Kamerlingh Onnes [3], it took many decades before a successful microscopic theory was formed. The BCS theory of superconductivity, established in 1957 by Bardeen, Cooper and Schrieffer [4], explained that superconductivity is the result of a net attractive interaction between electrons caused by interactions with phonons (lattice vibrations), and set a theoretical upper limit for T_c of about 30 K. The theory agreed with experimental data, and the phenomenon of superconductivity appeared to be solved.

The discovery of high-T_c superconductivity in the cuprates cannot be explained by BCS theory. The excitement that followed was partially motivated by the prospect of room-temperature superconductivity and the implied practical applications. Scientifically, the goal was the formation of a theory that would explain the apparent violation of the BCS limit.

Remarkably, more than twenty years after the discovery by Bednorz and Müller,

even some of the most basic questions about the mechanism are still actively debated. The reason why a theory has not yet been found is that the physics of the cuprates is complicated and varied. The near-term motivation in the field is the challenge of finding and studying the interesting behavior of these complex systems; understanding high-T_c superconductivity is a long-term goal. The ultimate legacy of high-T_c research may be the growth and increasing sophistication of the rich scientific field of complex materials.

1.2 Physical properties of the cuprates

1.2.1 Crystal structure

The high-T_c cuprates share some general characteristics. The fundamental building block of the crystal structure of these materials is the copper-oxygen (CuO_2) sheet. The two-dimensional square lattice of copper and oxygen atoms is widely believed to contain the essential physics of the system. The remaining part of the structure varies from material to material, and is called the charge reservoir layer. By adjusting the chemical composition of the charge reservoir layers, the density of charge carriers on the copper-oxygen sheet can be changed. Depending on the particular compound, these charge carriers may be holes or electrons; the cuprates are thus broadly classified as either hole- or electron-doped [5].

The cuprates can further be classified by the number of copper-oxygen sheets between neighboring charge reservoir layers. For example, the original high-T_c material $La_{2-x}Ba_xCuO_4$ is a single-layer hole-doped cuprate. The mercury-based compound $HgBa_2Ca_2Cu_3O_{8+\delta}$, the material with the highest measured T_c so far ($T_c = 135\,K$ at ambient pressure [6]), is a three-layer compound. On the other hand, the electron-doped cuprates such as $Nd_{2-x}Ce_xCuO_4$ (NCCO) share the same single-layer crystal structure (see Figure 1.1).

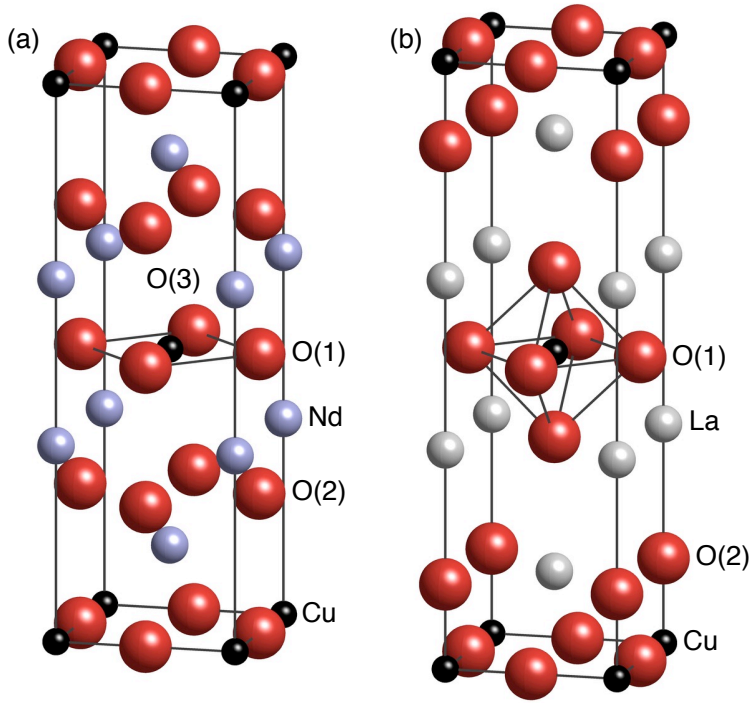

Figure 1.1: The crystal structures of (a) Nd_2CuO_4, the parent compound of $Nd_{2-x}Ce_xCuO_4$ (NCCO) and of (b) La_2CuO_4, the parent compound of hole-doped $La_{2-x}Ba_xCuO_4$ and $La_{2-x}Sr_xCuO_4$. The lattice constants are approximately $a = b = 3.9\,\text{Å}$ and $c = 12.1\,\text{Å}$ for Nd_2CuO_4 and $a = b = 3.8\,\text{Å}$ and $c = 13.2\,\text{Å}$ for La_2CuO_4. While the oxygen ions around the copper ions have an octahedral arrangement in the T-structure of La_2CuO_4, the T'-structure of stoichiometric Nd_2CuO_4 nominally lacks the apical oxygen below and above the copper. Nonetheless, a small fraction of apical oxygen sites O(3) is occupied [7]. The radii of the illustrated atoms are half of their respective ionic radii.

1.2.2 Electronic structure

The parent compounds of all high-T_c cuprates are insulators. In fact, one of the early surprises was that superconductivity could arise in such presumed insulating materials. For example, Nd_2CuO_4 is insulating and becomes metallic and superconducting only after a sufficient amount of electrons is added via chemical substitution of Ce for Nd.

The undoped compounds are not standard band-theory insulators, but so-called Mott insulators [8]. The Cu^{2+} ions contain nine $3d$-electrons out of a maximum of

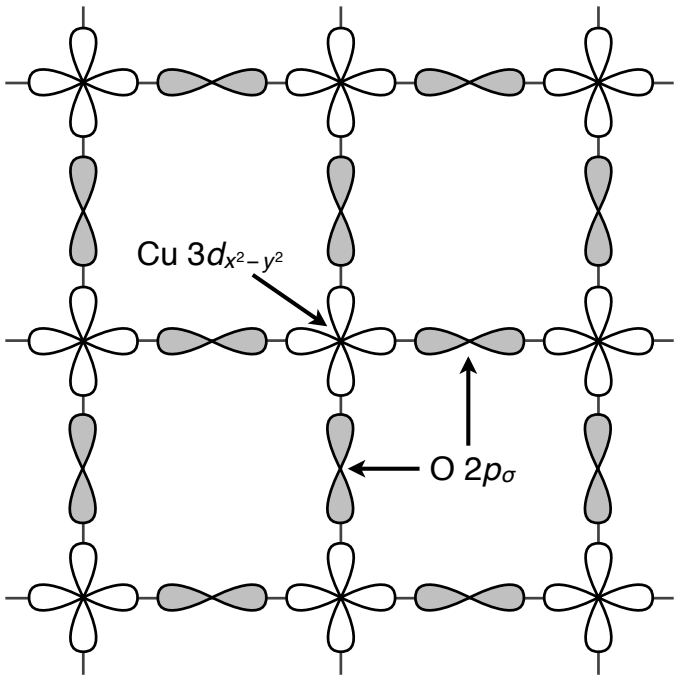

Figure 1.2: Schematic diagram of the CuO_2 plane. In the undoped cuprates, the O $2p_\sigma$ orbitals are filled and the Cu $3d_{x^2-y^2}$ orbitals are half-filled.

ten; this means that the orbital with the highest energy is half-filled. Due to the tetragonal crystal field this is the $3d_{x^2-y^2}$ orbital [9]. Naïvely, one would think that a half-filled electronic band at the Fermi level is the signature of a metal. In a Mott insulator, however, the carriers are highly localized, and there is an energy cost U for two carriers to be on one site due to the Coulomb repulsion between them. The carriers are thus immobile, and the system is insulating. In the band picture, the half-filled band is split into a filled lower Hubbard band and an empty upper Hubbard band, with a gap energy of U.

The situation in the cuprates is slightly more involved, due to the presence of the O^{2-} ions and their valence orbitals. The relevant O^{2-} orbitals are the $2p_\sigma$, i.e., the in-plane orbitals which lie along the Cu–O–Cu directions [9]. The O $2p_\sigma$ and Cu $3d_{x^2-y^2}$ orbitals are shown in Figure 1.2. The energy level of the oxygen $2p_\sigma$ band happens to be in between the upper and lower Hubbard bands of the copper $3d_{x^2-y^2}$

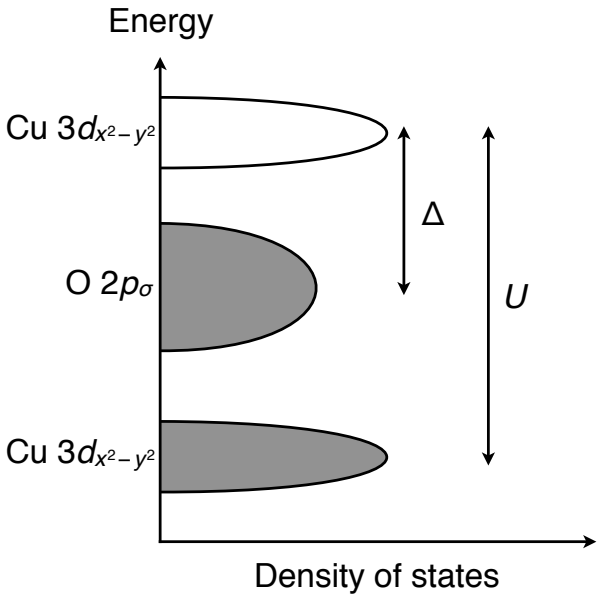

Figure 1.3: Schematic for the density of states in the three-band Hubbard model. The Cu $3d_{x^2-y^2}$ band is split into an upper Hubbard band and a lower Hubbard band by the on-site Coulomb repulsion U. The filled O $2p_\sigma$ band lies within the Mott gap, a distance Δ away from the upper Hubbard band.

orbital[1] (see Figure 1.3). In other words, it is easier to remove an electron from the filled oxygen orbitals than to remove one from the half-filled copper orbital. The Fermi energy lies between the oxygen $2p$ band and the upper Hubbard band, whose separation is the charge transfer gap Δ, i.e., the energy it takes to transfer an electron from the O^{2-} ion to the Cu^{2+} ion. The undoped cuprates are thus more properly called charge-transfer insulators.

The three-band Hubbard model (one copper orbital and two oxygen orbitals) is believed by many to contain all of the relevant low-energy electronic interactions in the CuO_2 sheet [10]. Because this model is still quite involved, many theorists use the simpler one-band Hubbard model, treating the charge transfer gap Δ as the

[1]More precisely, the hybridization of the Cu $3d_{x^2-y^2}$ and O $2p_\sigma$ bands result in a filled bonding band at large binding energy and a half-filled antibonding band near the Fermi energy [9]. It is this antibonding band which is split by Coulomb repulsion.

effective value for U. The one-band Hubbard model is written as

$$H = \sum_{ij\sigma} t_{ij} c^{\dagger}_{i\sigma} c_{j\sigma} + U \sum_{i} n_{i\uparrow} n_{i\downarrow} \,, \tag{1.1}$$

where $c^{\dagger}_{i\sigma}$, $c_{i\sigma}$, and $n_{i\sigma} = c^{\dagger}_{i\sigma} c_{i\sigma}$ are the creation, annihilation and number operators, respectively, for an electron with spin σ (up or down) at site i. The hopping integral t_{ij} is not limited to nearest-neighbor sites (written as t), and can be extended to next-nearest neighbors (t'), and so on.

1.2.3 Magnetic properties

The undoped parent compounds exhibit another important characteristic: their ground state is antiferromagnetically ordered. The Cu^{2+} ions each have a spin-$\frac{1}{2}$ magnetic moment, and at low enough temperatures, the system orders such that the moments at two neighboring copper sites are antiparallel. The antiferromagnetic superexchange interaction [11] is a process in which electrons with antiparallel spins on adjacent sites can take advantage of hybridization (which can be small due to U) and reduce their kinetic energy by hopping between neighboring sites. Electrons with parallel spins are restricted from this process by the Pauli exclusion principle. The result is an antiferromagnetic interaction energy J, which is equal to $4t^2/U$ in the $t/U \to 0$ limit. The antiferromagnetic Heisenberg Hamiltonian is written as

$$H = J \sum_{\langle ij \rangle} \mathbf{S}_i \cdot \mathbf{S}_j \,, \tag{1.2}$$

where $\mathbf{S}_i$ is the spin on site i, and $\langle ij \rangle$ denotes that the sum is over nearest neighbors. While the result $J = 4t^2/U$ is in the limit of strong coupling U, antiferromagnetic coupling can be postulated independently given the empirical evidence, even if U is not necessarily large. Many theoretical approaches for the doped cuprates use the Heisenberg Hamiltonian as a starting point, and with the addition of hopping terms, they are called t-J models.

The temperature below which a material orders antiferromagnetically is the

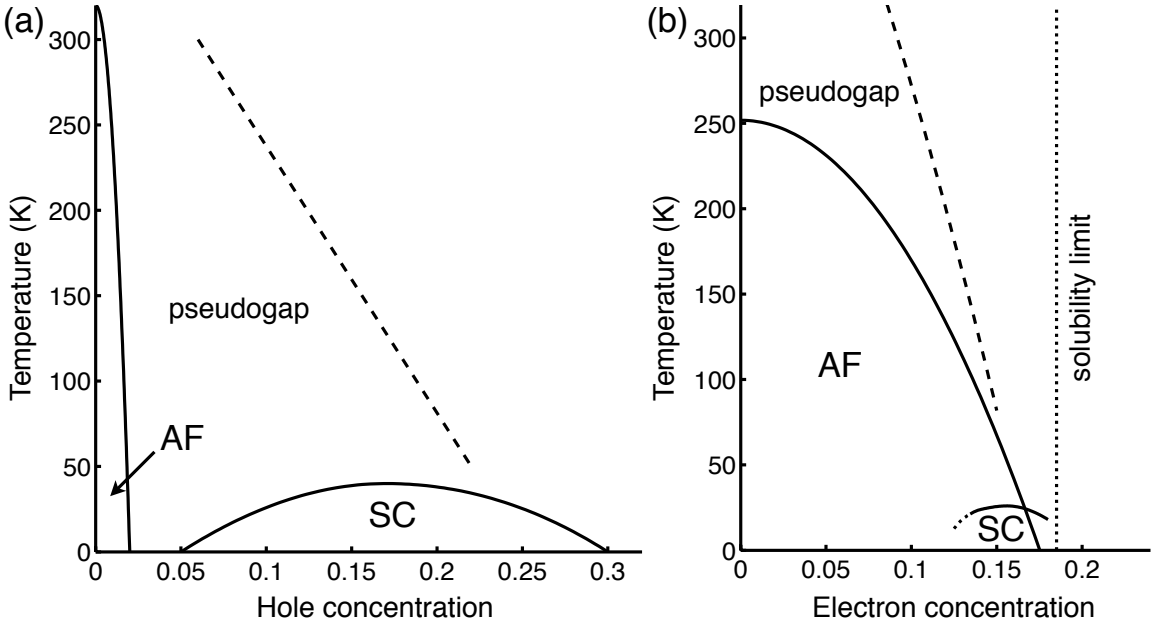

Figure 1.4: Schematic temperature-doping phase diagrams of (a) $La_{2-x}Sr_xCuO_4$ and (b) oxygen-reduced $Nd_{2-x}Ce_xCuO_4$. Indicated in both diagrams are the antiferromagnetic (AF) phase, the superconducting (SC) phase, and the "pseudogap" region (see Section A.2.3 for a discussion of the pseudogap).

Néel temperature T_N. As the insulating parent compounds are doped with holes or electrons, the antiferromagnetism becomes weaker (T_N decreases) and eventually disappears. Superconductivity occurs in a range of higher carrier concentrations: the concentration at which T_c is maximized is called optimal doping, superconducting compounds with fewer carriers are called underdoped, and those with more carriers are called overdoped. Beyond these general statements, however, the details of the phase diagram differ significantly between hole- and electron-doped cuprates.

As described in the previous Section, holes added to the system reside primarily on the valence orbitals of the oxygen ions. These holes carry their own spin and frustrate the magnetic interaction between neighboring copper moments, and the result is a rather large weakening of the antiferromagnetic state. In $La_{2-x}Sr_xCuO_4$, antiferromagnetism disappears around a hole concentration of $x = 0.02$ per copper atom. Superconductivity appears at around $x = 0.05$ and extends to about $x = 0.3$,

with an optimal doping around $x = 0.16$ [12]. The phase diagram is shown in Figure 1.4(a).

When electrons are doped into the CuO_2 sheets, they start to fill the copper $3d_{x^2-y^2}$ orbitals. The result is an effective dilution of the spin system (1.2), which only gradually weakens the antiferromagnetism. The antiferromagnetic phase thus extends much farther in doping [13, 14] and appears to overlap with the superconducting phase [15, 16]. In NCCO,[2] the superconducting phase begins around $x = 0.13$ and extends up to the solubility limit of about $x = 0.18$ [17]; see Figure 1.4(b) for the phase diagram of NCCO. The dotted portion of the T_c curve indicates the uncertainty in how far bulk superconductivity extends to lower doping: there have been reports of traces of superconductivity down to $x = 0.08$ [18], whereas bulk superconductivity seems to only appear around $x = 0.14$ [16].

The generally accepted view (before our publication [19]) has been that long-range antiferromagnetic order persists to about $x = 0.17$ [14, 20]. One of the results of this Thesis is that the nature of the antiferromagnetic phase changes around $x = 0.12$, and that genuine long-range order does not overlap with the superconducting phase.

While static magnetic order is absent outside of the antiferromagnetic region of the phase diagram, correlated fluctuations of the spin system still exist. The magnetic excitation spectrum changes its behavior in the superconducting state, an indication that there is an interaction between the spins and the superconducting carriers. Indeed, magnetism may be a key to understanding the mechanism of high-T_c superconductivity, and an important focus of the field is to study the relationship between magnetism and superconductivity in these systems. The work in this Thesis is part of this effort.

1.3 Outline

Chapter 2 describes the laboratory methods used during the research for this Thesis. Section 2.1 describes the crystal growth of NCCO using the traveling-solvent

[2] More precisely, oxygen-reduced NCCO. See Sections 2.2 and 3.1.3.

floating-zone method, and Section 2.2 is a discussion of the subsequent oxygen-reduction procedure. Section 2.3 contains descriptions of the relevant laboratory characterization techniques: SQUID magnetometry, ICP spectroscopy, and Laue diffraction. Neutron scattering, the main probe of magnetic properties used in this Thesis, is described in Section 2.4. This is followed in Section 2.5 by a brief description of μSR, a magnetic probe complementary to neutron scattering.

Chapter 3 describes a study of the instantaneous antiferromagnetic correlation length in NCCO. The site-diluted spin-$\frac{1}{2}$ square-lattice Heisenberg antiferromagnet is briefly discussed, and so is a previous study of as-grown, non-superconducting NCCO. Then I describe my measurements on oxygen-reduced NCCO, showing the remarkable change of behavior between non-superconducting and superconducting samples. The neutron scattering results are supplemented with some results from μSR measurements.

Chapter 4 describes inelastic neutron scattering measurements of the antiferromagnetic excitation spectrum in superconducting NCCO. My results primarily concern the energy gap in the spectrum that appears in the superconducting state. I describe the results of the effect of a magnetic field on this gap and discuss the possible implications for the non-superconducting ground state. I also discuss the possible relationship between the decrease in spectral weight due to the gap and the increase of spectral weight seen at higher energies.

This Thesis has three appendices. Appendix A contains a table of samples, information supplemental to the material in Chapter 3, and a discussion of two-axis neutron scattering simulations. Appendix B contains derivations of the neutron scattering cross section formulas, aggregated from a few textbooks and translated into modern notation. Appendix C is a detailed derivation of the Cooper-Nathans formula for the neutron scattering resolution function and its application to the two-axis energy-integrating technique.

Chapter 2

Methods

In this Chapter, I describe the laboratory and experimental methods used in my research. The laboratory work at Stanford has involved both growing crystals and characterizing them. Most of the actual experiments were performed at various external user facilities. The principal results contained in this Thesis are those from neutron scattering measurements, which would not have been possible without the preceding laboratory work.

The first Section describes the procedure I used for growing single crystals of NCCO. The traveling-solvent floating-zone (TSFZ) technique has been essential for growing the large single crystals of relatively high purity necessary for the inelastic neutron scattering studies described in Chapters 3 and 4. Section 2.2 describes the oxygen reduction process performed after the growth that is required for the crystals to become superconductors. Recent scenarios for the mechanism of the reduction process are discussed. In Section 2.3, I describe the following laboratory characterization techniques: SQUID magnetometry, used for measuring the superconducting transition (Section 2.3.1); ICP spectroscopy, used to characterize the chemical composition (Section 2.3.2); and Laue diffraction, used to check the crystal structure and orientation (Section 2.3.3). Section 2.4 contains an introduction to neutron scattering as well as a description of the triple-axis spectrometer. I also describe the two-axis energy-integration technique used to measure instantaneous magnetic correlations. Finally, in Section 2.5, I describe μSR, a local magnetic probe

complementary to neutron scattering.

2.1 Crystal growth

A successful experimental effort in condensed matter physics depends on a reliable supply of samples. In our research group, we tackle this issue by growing our own samples.

Most condensed matter physics experiments require single-crystal samples: the interest usually lies in the anisotropy of the physical properties displayed by these complex materials. The high-T_c superconductors, in particular, are layered materials, and most of the interesting physics is found to result from the two-dimensional CuO_2 plane. Single crystals are thus a prerequisite for studying the quasi-two-dimensional properties.

I first describe in theoretical terms how to obtain single crystals of NCCO. Naïvely, one would guess that melting NCCO in powder form and cooling it slowly would produce a single crystal, provided the cooling rate was slow enough. This is, for instance, how single crystals of silicon are grown in industry. However, unlike elemental silicon, NCCO melts incongruently: as the material is heated, there is a phase separation into a (Nd,Ce)-rich solid and Cu-rich liquid. The temperature at which this takes place is 1315 ± 5°C, as indicated in Figure 2.1 [21]. According to this phase diagram, NCCO dissolves into liquid CuO between 1050°C and 1315°C. As small amounts of NCCO are dissolved into pure CuO, the melting point decreases to a minimum at a composition of 90% CuO, after which it increases. If one starts with a molten system of between 80% and 90% CuO, slow cooling will allow the NCCO precipitate to form into single crystals. This approach is generally called flux- or solvent-growth.

Figure 2.2 shows the temperature at which NCCO decomposes as a function of Ce concentration x. Note that in the solid-liquid mixture phase at high temperature, the Ce content of the liquid phase is lower than that of the solid phase. A similar effect likely occurs at the phase boundary where the crystal growth takes place (at lower temperatures), and would affect the Ce concentration of the grown crystals;

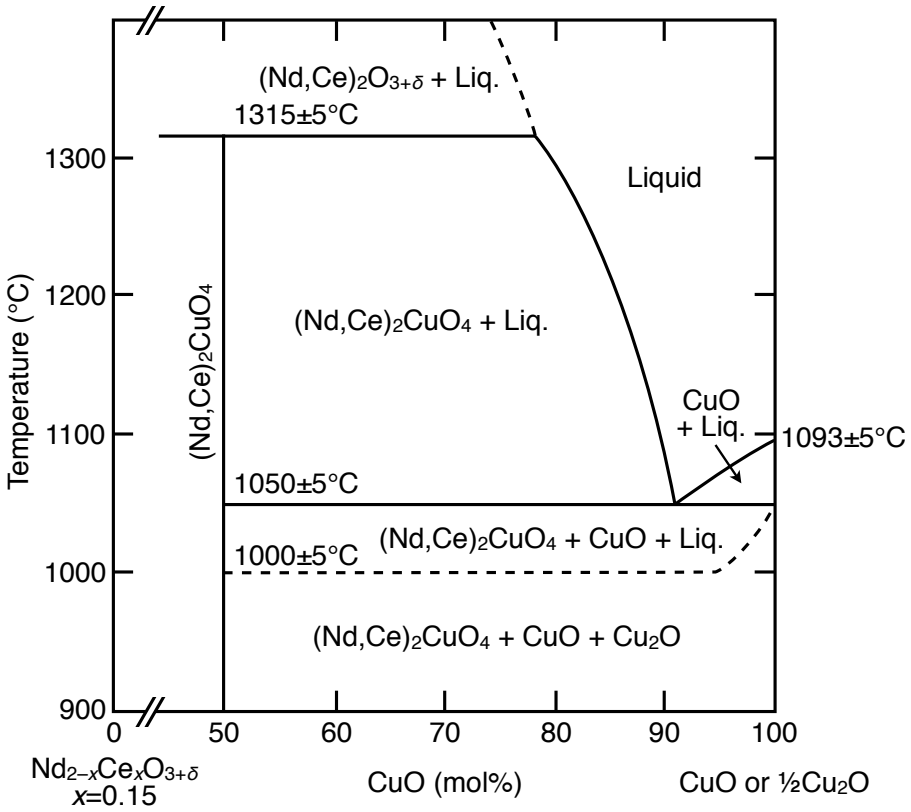

Figure 2.1: Temperature-composition phase diagram of the $Nd_{1.85}Ce_{0.15}O_{3+\delta}$ – CuO system, adapted from Ref. [21]. $(Nd,Ce)_2CuO_4$ (NCCO) is shown as the vertical line at 50% CuO composition. Above 1315 ± 5°C, NCCO decomposes into a mixture of solid $(Nd,Ce)_2O_3$ and a Cu-rich liquid. In order to form NCCO crystals, one must start with a composition between the peritectic point at ($\sim$ 80%, 1315°C) and the eutectic point at ($\sim$ 90%, 1050°C). Slowly cooling the liquid will then allow the NCCO precipitate to form into single crystals.

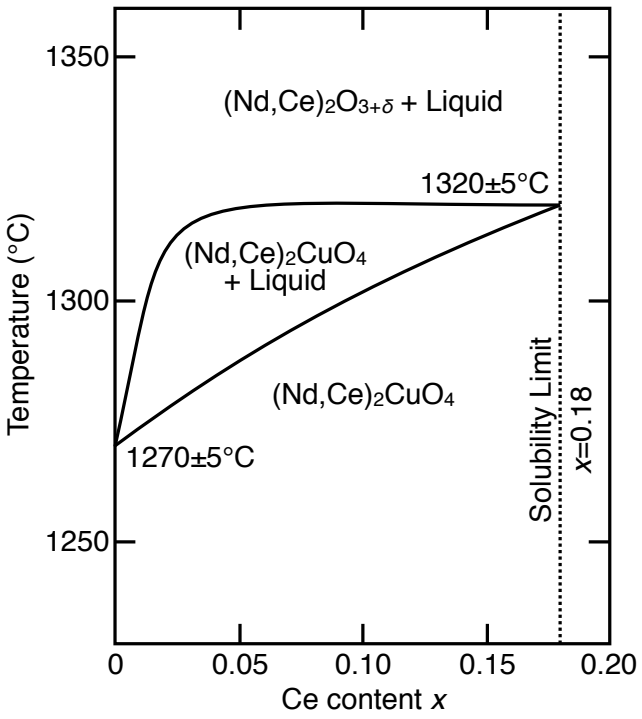

Figure 2.2: The decomposition temperature of $Nd_{2-x}Ce_xCuO_4$ as a function of Ce concentration x, adapted from Ref. [21]. This diagram also indicates the solubility limit for NCCO of $x = 0.18$.

this possibility is discussed further in Section 2.3.2.

I grew NCCO crystals using the TSFZ method. Instead of using a crucible inside a furnace to melt the solution, the technique uses focused light from halogen bulbs to create a single hot spot where the solvent is melted. The molten solvent is suspended between a "feed rod" of material, which dissolves into the solvent, and the crystal, which grows out of the solvent. Among other advantages, this method avoids the contamination issues associated with the use of crucibles. In the following paragraphs, I describe in detail the procedure I used in the laboratory to grow large single crystals of NCCO.

Mixing powders

The first step is to mix powders of Nd_2O_3 (light blue in color), CeO_2 (pale yellow), and CuO (dark gray) in stoichiometric amounts, and to heat the powders so that the following solid-state chemical reaction (calcination) takes place:

$$(1 - \tfrac{x}{2}) \cdot Nd_2O_3 + x \cdot CeO_2 + CuO \longrightarrow Nd_{2-x}Ce_xCuO_4 + \tfrac{x}{4} \cdot O_2 \qquad (2.1)$$

Because the powders are hydroscopic (to varying degrees), they are dried before they are weighed. The rare-earth oxides Nd_2O_3 and CeO_2 are dried at 1000°C, and CuO is dried at 600°C. After the powders have cooled down, the appropriate amounts[1] are weighed on an analytic balance to within 4 significant digits (typically to the nearest milligram). Because the powders continually absorb moisture from the air, the measurements may become inaccurate if a significant amount of time is spent during the weighing process.

The powders are mixed using a mortar and pestle. In order to significantly reduce the particle size and to effect an efficient rate of mixing, the powders are mixed as a slurry in ethanol. In principle, any solvent may be used, but ethanol has the advantages of drying quickly, as well as being less toxic than other quickly drying solvents. The mixing into a homogenous slurry takes 20 to 30 minutes.

Once the slurry has dried, the resulting blue-gray powder is collected into a ceramic (alumina) crucible and heated at 850°C for 12 hours. This first calcination results in a gray powder. The powder undergoes another two rounds of wet-mixing with mortar and pestle, with successive calcinations at 900°C and 950°C for 12 hours each. After the second and third calcinations, the resulting powder is black. X-ray powder diffraction measurements have shown that the final powder is single-phase NCCO.

[1]The drying process is not perfect. The effect on the growth of slight difference in feed rod composition is discussed later. I have found that, given these drying conditions, adding a slight excess of 1.3% Nd_2O_3 is optimal.

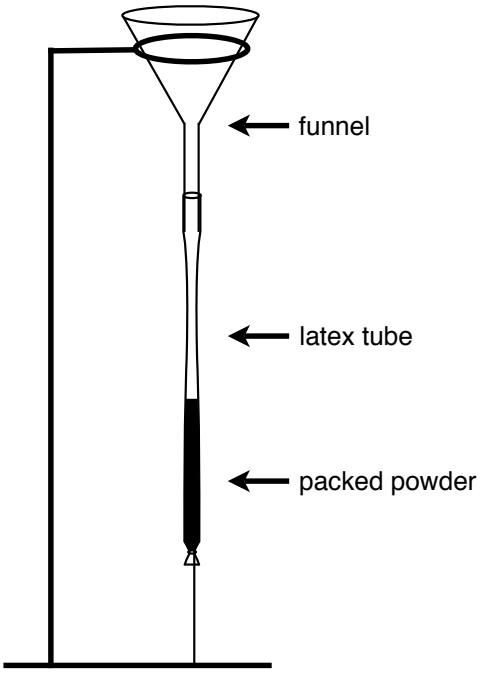

Figure 2.3: Illustration of the powder packing setup. NCCO powder is slowly poured into the latex tube through the funnel and tamped down using a thin steel rod.

Packing a feed rod

The second step is to transform the NCCO powder into a "feed rod" for use in the TSFZ furnace. The NCCO powder is packed into shape before being sintered in a furnace to form a dense polycrystalline solid.

The packing process is a technique that has evolved over the history of our research group, and it is the step in the crystal growth process that requires the most experience to master. The aim of the packing and sintering process is to form a cylinder of packed powder which has a uniform diameter (typically 5–6 mm), and is as long as possible (typically 9–10 cm). The necessity of a uniform diameter and long length will become clear from the discussion of the TSFZ process itself.

The powder packing setup is illustrated in Figure 2.3. Surgical latex tubes (purchased from a veterinary supply store) have an appropriately uniform diameter and elasticity. The tube is cut to a length of about 20 cm, turned inside-out, and the

white powder originally lining the tube is wiped off.[2] A knot is tied at one end, and this end of the tube is fixed to the base of a stand. The open end of the tube is placed on the end of a glass funnel. The NCCO powder is added through the funnel a small amount at a time and tamped down using a long steel rod with a flat tip. The powder is packed tightly enough so that it does not yield to a moderate amount of finger pressure. Care is taken so that the packed powder has a uniform diameter along its length. The packing continues until the length of the powder is 13 or 14 cm,[3] a process that can take 30 minutes to an hour.

The air in the tube is then pumped out as follows. A piece of cotton ball is inserted and tamped down at the top of the powder. The latex tube is removed from the packing setup, and the open end of the tube is placed on the nozzle of a vacuum pump. During the few minutes of pumping, the packed powder is rolled carefully between two flat plates to make the surface smooth. The rolling may also help evacuate the tube. The open end of the tube is then twisted and tied off without losing the vacuum inside. The tube is then loosely attached with rubber bands to one or two metal half-cylinder shells to keep it straight during the following compression process.

The latex tube containing the packed powder is placed into a water-filled pressure chamber of a hand-operated hydraulic press (see Figure 2.4). The press is pumped up to its maximum pressure of 70 MPa, which translates through the piston to an isostatic pressure of 190 MPa. The size of the powder rod is visibly smaller after this compression. The latex tube is then cut away from the powder rod. As the powder rod is very brittle, this step requires care and patience.

The powder rod is now sintered at 1220°C, just below the melting point, to form a solid polycrystalline rod. One method is to hand-drill a hole into one end of the rod (once again being very careful), pass some high-temperature-resistant Ni-Cr wire through this hole, and hang the rod vertically inside of a large cylindrical alumina crucible. The alumina container serves to keep the temperature at the rod uniform during the sintering process, and suspending the rod prevents the powder from

[2] I believe that the white powder is a form of starch; such organic material is not likely to be detrimental to the crystal growth, but it is best not to take that chance.

[3] This length is limited by the length of the pressure chamber.

Figure 2.4: The hand-operated hydraulic press used to compress the packed powder.

touching and reacting with anything. For NCCO, fortunately, placing the powder rod horizontally in a zirconia tube is sufficient. This sintered rod can then be used as the feed rod in a TSFZ growth.

The traveling-solvent floating-zone method

The TSFZ furnace uses four ellipsoidal mirrors and specially-made halogen bulbs (150 W in the case of NCCO growth) with the filaments arranged in a single plane. The positions of the bulbs are such that the images of the filaments coincide in the center of the furnace with a limited vertical extent of perhaps 3–4 mm. During a growth, the molten solvent is suspended between the feed rod connected to the

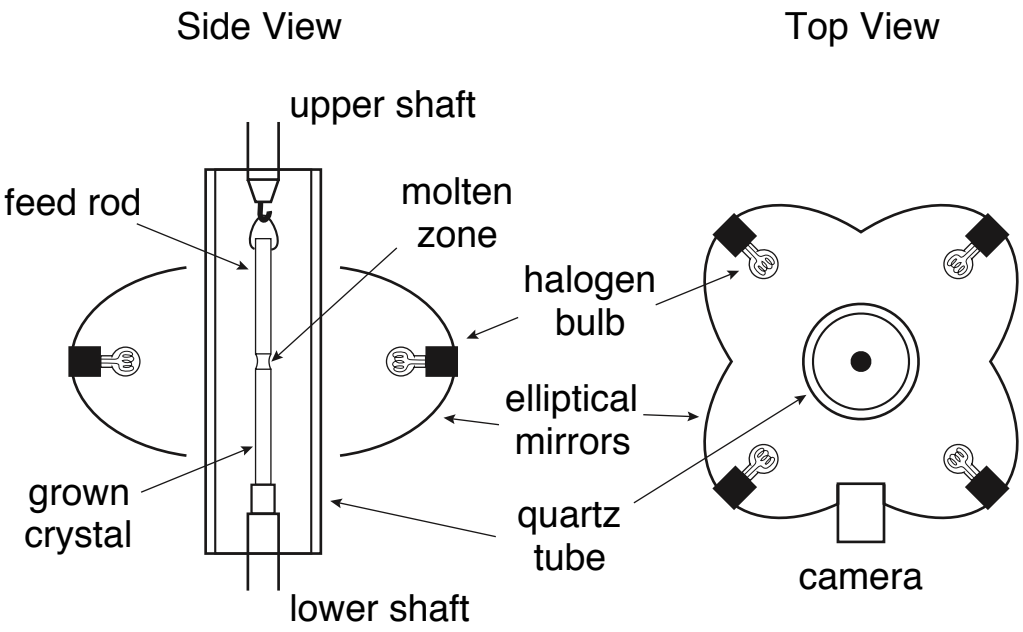

Figure 2.5: An illustration of the traveling-solvent floating-zone furnace. Reproduced from Ref. [22].

upper shaft and the crystal connected to the lower shaft. The upper and lower shafts are counter-rotated, typically at rates around 20 rpm,[4] so that the molten zone is constantly in a state of being mixed and that any thermal gradients are averaged. The entire mirror stage is moved slowly upwards at a rate of 0.5 mm/h, dissolving the feed rod at the same time as forming the crystal. See Figure 2.5.

In order to start a growth, one begins with a seed crystal. I typically use an NCCO crystal, approximately 10 mm long, from a previous growth. Since it serves only to seed the growth, the seed crystal need not be of the same composition as the feed rod. One end is tapered on a polisher to form a conical tip, similar to the tip of a pencil. The other flat end is glued to an alumina cylinder, which is in turn inserted into a holder. The holder, which screws into the lower shaft, has six screws used to adjust the position of the seed crystal so that its tip lies along the central

[4]The rotation rates of the upper and lower shafts should be kept slightly different to avoid forming a resonance condition in the liquid. For example, 21 rpm for the upper shaft and 19 rpm for the lower shaft.

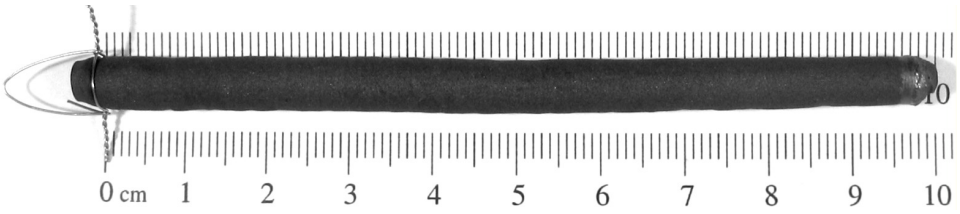

Figure 2.6: A typical NCCO feed rod. A 22-gauge Ni-Cr wire has been wrapped in the groove cut into the left end. The solvent CuO has been attached onto the right end.

axis of the furnace.

The last component of the crystal growth setup is the solvent. As described earlier in this Chapter, the growth requires a molten mixture of 80–90% CuO. I have found that attaching pure CuO to the end of the feed rod and letting some NCCO dissolve into the molten CuO at the beginning of the growth works to achieve the correct solvent composition. 175 mg of CuO powder[5] is first formed into a pellet using a pellet press with a bore diameter of 5 mm. The pellet is then sintered at 950°C for 12 hours, and subsequently melted onto one end of the feed rod using the TSFZ furnace itself. The feed rod is held using the six-screw holder "upside-down" on the lower shaft. The CuO pellet is balanced on the tip (which is first polished flat if necessary). The furnace's quartz tube is put into place, and the furnace power is then ramped up until the CuO melts onto the feed rod.

The feed rod (with CuO) is then placed on a hook attached to the upper shaft of the furnace. This is done by carving a groove along the circumference of the feed rod at the end opposite to the added CuO, and then wrapping the groove with some Ni-Cr wire and forming a loop (see Figure 2.6). The feed rod is hung vertically, adjusting the wires as necessary, such that its entire length lines up with the central axis of the furnace.

The atmosphere inside the quartz tube surrounding the growth can be controlled. The NCCO crystals were grown in 4 atm of oxygen. As-grown, NCCO contains an excess amount of oxygen [23], and it may be that the growth is stabilized in an environment in which an excess amount of oxygen is possible. I have

[5]The effect of differing amounts of initial CuO solvent is discussed later.

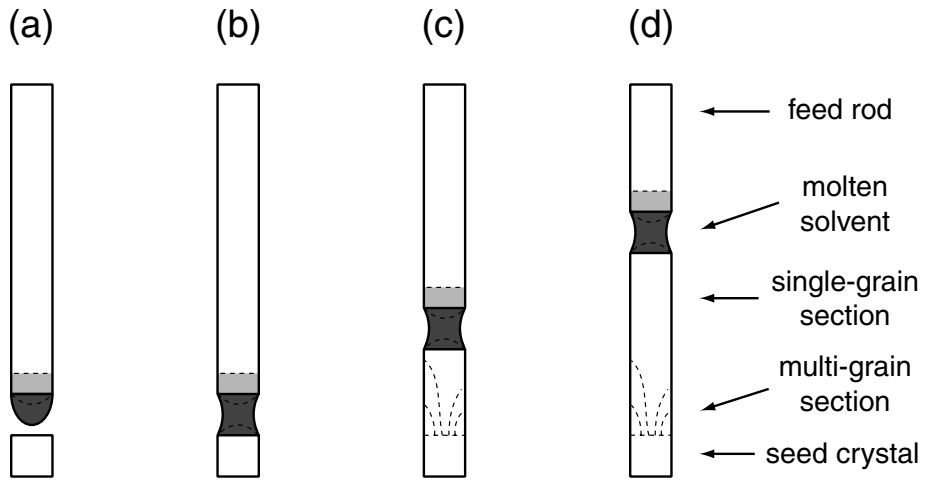

Figure 2.7: The typical progression of a TSFZ crystal growth. There usually are multiple grains at the beginning of a growth, but one grain eventually dominates, leading to a single crystal. Reproduced from Ref [22].

not experimented with changing the atmosphere of the growth. It has come to my attention recently that a low-oxygen atmosphere may actually be beneficial for the crystal growth of Ce-doped crystals [24].

In controlling the positions of the feed rod and seed crystal, there are two degrees of freedom: the position of the mirror stage, and the position of the upper shaft stage. The growth process begins by ramping up the furnace power and melting the CuO solvent on the tip of the feed rod, and then attaching it to the seed crystal by lowering the mirror stage and upper shaft stage together. All the while, the upper and lower shafts are being counter-rotated so that the temperature at any point remains relatively constant. The system is then left to mix for an hour or so in an attempt to form a clean interface between the seed crystal and the solvent, so that the new crystal will grow directly from the seed. The mirror stage is then moved upwards at the growth rate of 0.5 mm/h. Ideally, that is all that is needed to grow a large single-grain crystal.

However, it is often the case that the growth is not properly seeded. In this case, multiple grains form at once. Fortunately, grains with a certain orientation (*c*-axis

Figure 2.8: An image from the TSFZ furnace camera of an NCCO growth. The polycrystalline feed rod is above the molten zone, while a single-grain crystal is below the molten zone. Behind the molten zone are images of the filaments reflected by the mirrors.

perpendicular to growth direction) are favored over others. A particular grain will begin to dominate, and secondary grains eventually disappear. Figure 2.7 illustrates this process. The progression from multiple grains to a single grain is easily seen through the camera, as the grain boundaries are visible due to the small amount of solvent that remains inside them. In addition, the growth of a single grain is often apparent from visible facets on the surface of the growth. Figure 2.8 shows an image from the furnace camera during a growth of NCCO.

Operating a TSFZ furnace

Many adjustments have to be made, both before and during a growth, to increase the chances of obtaining a single-grain crystal.

The temperature of the molten zone cannot be controlled directly, and is not even measured. The temperature depends not only on the power supplied to the bulbs, but also on factors such as the size, reflectivity, and heat dissipation of the hot spot. The growth must be monitored often to make sure the right amount of

power is used. The power may be increased manually, but should not be decreased too quickly during a growth, because it may cause the seeding of secondary grains; in this case, a programmable controller is used to slowly ramp the power lower.

If the temperature at the molten zone is too high, gravity causes the solvent to droop, and the crystal widens. The rate of material taken out of the solvent becomes greater than the rate of material being dissolved into the solvent. This leads to a progressively narrower molten zone, and eventually the solvent will detach from the feed rod and fall to the side of the crystal. Because the solvent is lost, reattachment is usually not possible. To make things worse, the thermal shock to the top part of the crystal due to the molten solvent causes it to be structurally weak and unusable. On the other hand, if the temperature at the molten zone is too low, the solid (undissolved) portions of the feed rod and crystal knock against each other. If left unchecked, the knocking becomes violent enough to cause the solvent to detach. Thus the main challenge during a growth is to maintain the temperature in the narrow range available that avoids both potential problems.

During a growth, there may be a need to cause the crystal to become narrower. For example, secondary grains will disappear faster for a narrower crystal. This requires, in addition to lowering the power, the decrease in the rate of feed rod being added to the solvent. This is done by continually raising the upper shaft stage at a small rate. For example, if this upper shaft "pulling" speed is set to 0.1 mm/h, then for a growth rate of 0.5 mm/h the feed rod dissolves into the solvent at a 20% slower rate. In equilibrium, the width of the growing crystal narrows so that the amount of material being grown equals the amount of material being dissolved.

Another set of concerns comes from considering the composition of the molten solution. Sometimes the solution shifts away from the ideal composition. Consider the case when the solution becomes too CuO-rich. This can happen (usually late in a growth) if the feed rod composition is slightly off stoichiometry with too much CuO. If this happens, some CuO flows over the sides of the crystal, decreasing the CuO concentration of the solution and allowing the growth of the crystal to continue. However, this process causes the "crystal" to widen and the molten zone

to narrow, and care must be taken to avoid a detachment.

The solution may also be too CuO-rich at the beginning of the growth, if too much CuO was used to start the growth process. In this case, proper seeding from the seed crystal does not take place, and the composition of the solution changes unpredictably as random amounts of CuO and NCCO condense out of the system. This commonly leads to a sudden drop of the melting point and detachment of the growth. Even if detachment does not occur, the precipitation of excess CuO may prevent a single grain of NCCO from forming.

The other end of the composition spectrum is problematic as well. The composition of the solution may become CuO-poor. This can happen near the beginning of the growth if the amount of CuO used was too small. In this case, even if a single grain is seeded from the seed crystal, at some point the single grain disappears and the growth must start again from many multiple grains. It should be noted that after the growth, outside of the furnace, this portion of the crystal decomposes after a few days. It could be that a relatively large amount of $(Nd,Ce)_2O_3$ is deposited in between the multiple grains.[6]

The amount of CuO added to the feed rod before the growth and the fine-tuning of the feed rod composition are thus important aspects for a successful growth. Note that the composition issues are still coupled to the adjustments in power and pulling rate discussed above. For instance, decreasing the power decreases the volume of molten solvent, increasing the concentration of CuO, and may lead to the overflow of solvent onto the crystal. After years of adjustments, I have found that 175 mg of CuO solvent, a 1.3% increase to the nominal amount of Nd_2O_3 in the feed rod,[7] a feed rod diameter of 5 mm, and a constant pulling rate of 0.1 mm/h, as a good set of crystal growth parameters.

Because of these complications, a 10-cm feed rod does not necessarily yield a similarly-sized single crystal. A growth can be considered successful if it yields a single-grain crystal of at least 3 or 4 cm, such that it can be used for inelastic neutron

[6] $(Nd,Ce)_2O_3$ is also discussed later in the context of decomposition in the oxygen-reduction process.

[7] It may be that, even after drying the powders, Nd_2O_3 retains more water than the other ingredients.

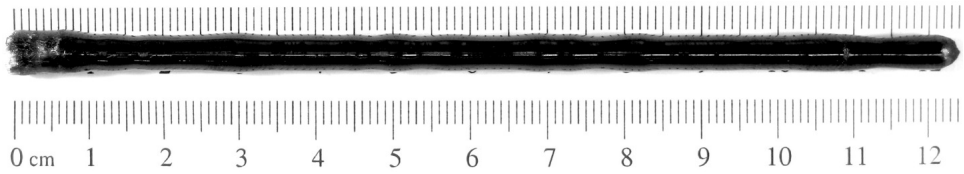

Figure 2.9: A photograph of an NCCO crystal after growth. In this particular growth the seeding of the crystal was successful, and the entire crystal is a single grain.

scattering.

Ideally, there is time after the growth to have the a crystal sit in air before any further preparations, as parts of it may be structurally weak. These parts typically break off and disintegrate over the course of a few days. I speculate that there are microscopic inclusions that absorb moisture and expand. After this happens, the remaining portions of the crystal can be considered stable and should be able to handle moisture and cleaning solvents, as well as the high and low temperatures during the heat treatment and characterization steps described below.

2.2 Reduction

As-grown, NCCO is not superconducting. Even if the Ce concentration is large enough, NCCO (and the other electron-doped cuprates) must be heat treated in an oxygen-reducing environment to become superconducting.

2.2.1 Microscopic mechanism

The microscopic mechanism of the oxygen reduction step is still under debate, but in the last few years there have been a number of more detailed studies on the effects of oxygen reduction on the electron-doped compounds. I give a brief history of this subject and then describe the latest studies.

Carrier concentration

Changing the oxygen concentration of a crystal is known to change the carrier concentration. Naïvely, the removal of one oxygen atom would add two electrons to (or, equivalently, remove two holes from) the system, since the oxygen becomes an O^{2-} ion inside the solid. Localization and other effects may lower the number of mobile carriers per oxygen that are added or removed, but the effect is still significant. In fact, the carrier concentration of many hole-doped cuprates is adjusted by adding or removing oxygen from the systems [25]. These include $La_2CuO_{4+\delta}$, which behaves similarly to $La_{2-x}Sr_xCuO_4$, and the commonly-studied double-layer system $YBa_2Cu_3O_{6+x}$.[8]

At the time of the discovery of superconductivity in NCCO [17], it was thought that the only effect of the oxygen reduction step is to increase the electron density high enough to initiate superconductivity. However, transport measurements performed a few years later showed that reduction causes a dramatic change in the resistivity at all temperatures while the Hall coefficient does not change appreciably above $T = 100\,\mathrm{K}$ [26]; it was concluded that the effect of reduction cannot be a simple change in carrier density.

Apical oxygen

Structural refinement analysis of neutron diffraction measurements performed on single-crystal Nd_2CuO_4 revealed that as-grown crystals contain approximately 10% of apical O(3) oxygens per formula unit (not part of the ideal T' structure; see Figure 1.1) [7]. Furthermore, the amount of excess oxygen significantly decreases to about 4% per formula unit after oxygen reduction. No change was found in the quantity of in-plane O(1) and out-of-plane O(2) oxygens. Further transport measurements showed that oxygen reduction decreases the residual resistivity $\rho(T \to 0)$, but otherwise does not affect the temperature dependence of resistivity [27]. These findings led to the consensus that oxygen reduction allows superconductivity to form through the decrease in disorder due to the removal of O(3) apical

[8] In both of these compounds, there is a tendency for the excess oxygen to order.

oxygens. This view came to be widely held, despite the lack of clear evidence of the removal of apical oxygens in $x = 0.15$ NCCO [28].

A more detailed series of transport measurements made use of ion irradiation [29]. The reasoning behind the study is that ion irradiation increases disorder while leaving the carrier concentration unchanged, and by comparing the effects of oxygen concentration to ion irradiation, one can hope to differentiate the effects of reduction on disorder and carrier concentration. It was found that, in superconducting $Pr_{2-x}Ce_xCuO_{4\pm\delta}$ ($x = 0.17$) thin films, both oxygenation and ion irradiation increase residual resistivity and decrease T_c. Furthermore, it was found that oxygenation decreases the Hall coefficient R_H, but that irradiation leaves it largely unchanged. Using an empirical model, it was determined that oxygenation effectively changes the electron density from $x = 0.17$ to $x = 0.16$, but that T_c decreases because of the introduction of disorder. This study was the first to quantify the change in carrier density due to oxygen reduction. The actual change is quite small, showing that disorder effects indeed dominate those of reduction.

This work did not determine the mechanism of disorder due to oxygenation. In fact, it supports the view that the decrease in disorder is due to the removal of O(3) apical oxygens [29]. However, Raman scattering and infrared transmission measurements on NCCO [30] and $Pr_{2-x}Ce_xCuO_{4\pm\delta}$ (PCCO) [31] indicate that reduction has no effect on the apical oxygens. In the Raman scattering data, the feature associated with O(3) is observed to increase with Ce concentration and to remain unaffected by reduction, and the conclusion is that O(3) is bound relatively strongly to the nearby Ce^{4+} ion. In both works, measurements of the rare-earth crystal-field excitations using infrared transmission spectroscopy revealed that the effect of reduction changes at a Ce concentration of about $x = 0.08$. With the help of Madelung potential calculations, it was determined that below this concentration, the out-of-plane oxygen O(2) is removed, while above this concentration, the in-plane oxygen O(1) is removed [30, 31]. The surprising conclusion is that, in order for superconductivity to form, oxygen must be removed from the very CuO_2 planes thought to be crucial for superconductivity.

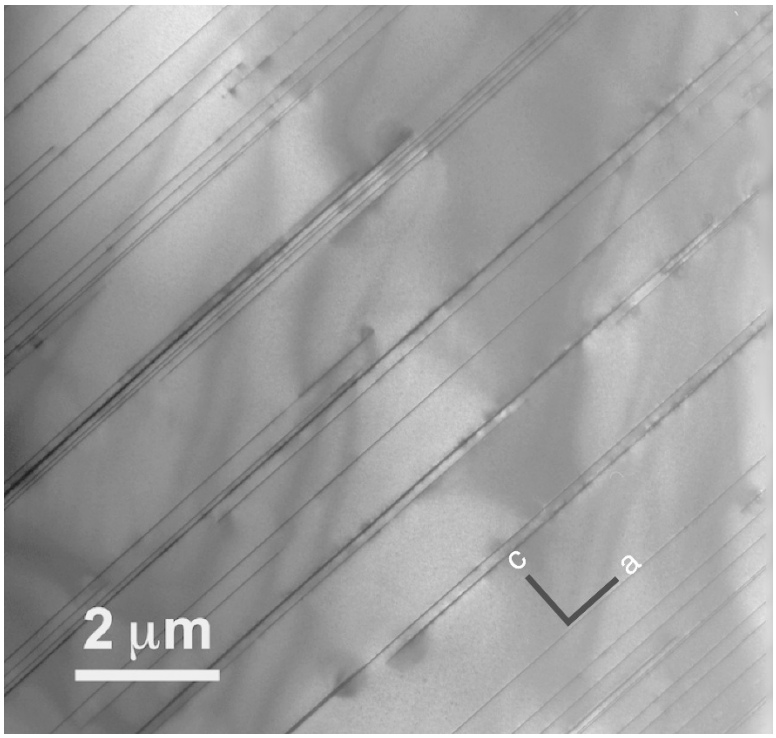

Figure 2.10: Transmission electron microscopy (TEM) image of oxygen-reduced NCCO ($x = 0.16$), reproduced from [23]. The thin lines are layers of the secondary phase $(Nd,Ce)_2O_3$.

Copper deficiency

A key ingredient to understanding this apparent contradiction lies in the partial decomposition of NCCO during oxygen reduction and the formation of an epitaxial secondary phase $(Nd,Ce)_2O_3$. This phase was discovered by our group in the context of explaining the appearance of magnetic diffraction peaks observed in reduced NCCO crystals [23], and is discussed in Chapter 4. Figure 2.10 is a transmission electron microscopy (TEM) image of oxygen-reduced NCCO. The secondary phase regions are typically 60 Å wide along the *c*-direction (perpendicular to the CuO_2 planes) and more than 1 μm parallel to the CuO_2 planes, making up a typical volume fraction of 1% [23].

Kang *et al.* [32] argue that, since this secondary phase contains no Cu ions, they must travel during the reduction process to the CuO_2 planes in the majority phase

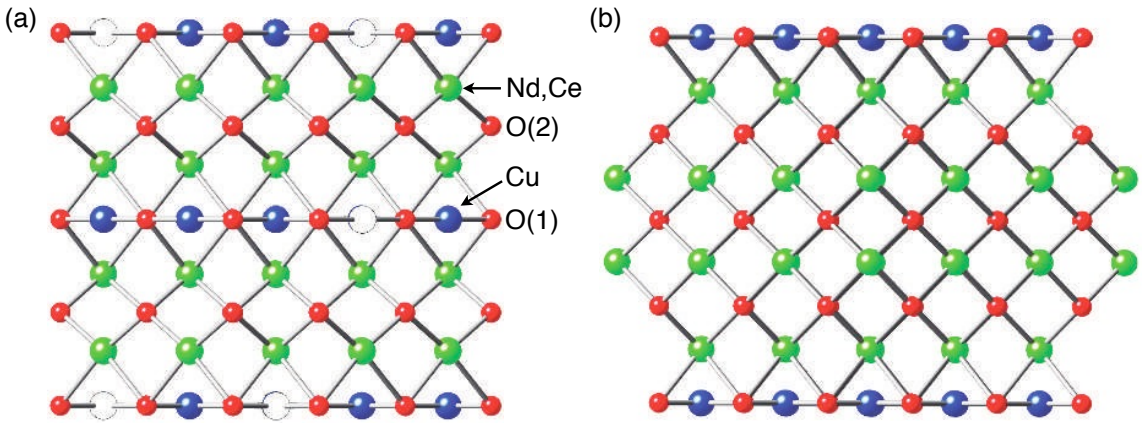

Figure 2.11: Illustration of the effect of oxygen reduction on the crystal structure of electron-doped cuprates. (a) Structure of Cu-deficient as-grown material. (b) Structure of oxygen-reduced material with a Cu-free secondary phase and CuO_2 planes with Cu vacancies repaired. Reproduced from [32].

(see Figure 2.11). This in turn implies that there probably are Cu vacancies in the CuO_2 planes in the as-grown crystals. The chemical equation reads

$$R_2Cu_{1-f}O_{4+\alpha} \longleftrightarrow (1-f)R_2CuO_{4+\beta} + f\,R_2O_3 + (\alpha - \beta + f(1+\beta))\,O\,, \qquad (2.2)$$

where R indicates the rare-earth element(s), f is the secondary phase volume fraction, and α and β are the amounts of excess oxygen in the oxygenated and reduced samples, respectively. As implied by the double arrow, measurements indicate the reduction process to be fully reversible. Kang *et al.* measured the Cu and O occupancies of $Pr_{1-x}LaCe_xCuO_{4\pm\delta}$ ($x = 0.12$) using neutron powder diffraction and refinement analysis [32]. It was found that the as-grown and re-oxygenated samples have a Cu deficiency of 1.2-2.3%, but that the reduced samples have full Cu occupancy. The amount of Cu deficiency is consistent with the secondary phase volume fraction of 1.6% measured by X-ray powder diffraction. The as-grown and re-oxygenated samples were found to contain an excess of oxygen ($\alpha \approx 0.02$–0.07), and the reduced samples a deficiency of oxygen ($\beta \approx -0.06$). The predicted amount of oxygen loss from Equation (2.2) is then about 0.04, which agrees with thermogravimetric measurements during the reduction process [32].

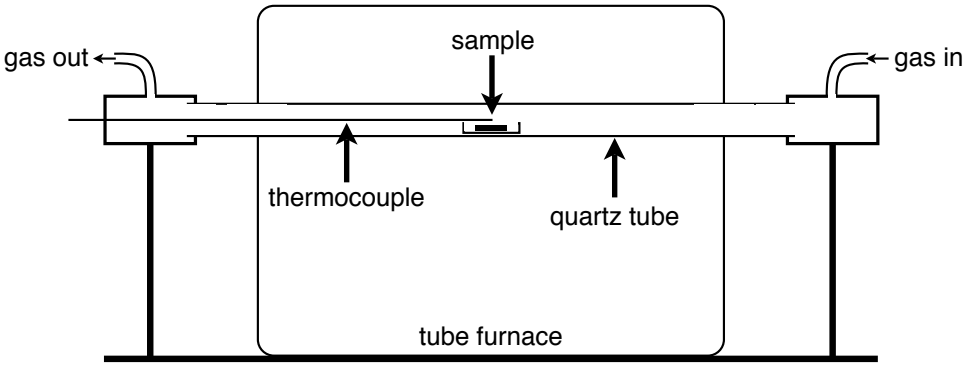

Figure 2.12: Illustration of the annealing furnace setup used for heat-treating NCCO crystals.

This study has shown that oxygen reduction drives the phase separation of the sample into a small volume fraction of the Cu-free secondary phase and a majority volume fraction with full Cu occupancy. Moreover, the prevalent disorder in the as-grown samples, previously attributed to excess apical oxygens, is due to Cu vacancies in the CuO_2 planes which would tend to localize electrons. This picture is consistent with a number of recent studies: in an X-ray photoemission spectroscopy study of NCCO, Xu *et al.* [33] find that a particular Cu core-hole state, in which the hole is screened by an itinerant electron, is weak or absent in the as-grown state. They conclude that oxygen reduction has delocalized the doped electrons.[9] In an angle-resolved photoemission measurement of as-grown PCCO, Richard *et al.* [34] find that there is a leading-edge gap at the Fermi surface that cannot be fully explained by the antiferromagnetic order; they mention the possibility that this gap is caused by the Cu vacancies. Finally, in a transport study on overdoped PCCO, Gauthier et al. [35] conclude that even the hole-like quasiparticles experience a delocalization upon oxygen reduction.

2.2.2 Laboratory procedure

An illustration of the annealing furnace setup is shown in Figure 2.12. The NCCO crystal is wrapped in steel mesh before being placed inside an alumina crucible, which minimizes direct contact between the crystal and the crucible. The crucible is then inserted into the quartz tube inside the tube furnace. On either end of the quartz tube are steel cylinders fixed to the baseboard. The ends of the steel cylinders are capped shut and the atmosphere inside the quartz tube can be controlled by flowing gas into the right cylinder and letting gas flow out of the left cylinder. The flow is controlled using a flow meter before the gas inlet. An oxygen sensor is used to measure the oxygen concentration of the gas leaving the furnace. A thermocouple is inserted to provide a more accurate temperature reading near the sample position than indicated by the tube furnace.

Figure 2.13 shows the phase stability diagram for NCCO ($x = 0.15$) as a function of temperature and oxygen partial pressure. Ideally, one would treat a sample at a certain temperature and a certain oxygen partial-pressure, and the sample would asymptotically approach an equilibrium oxygen concentration. In practice, a two-step procedure is used. The first step is 10 hours in flowing argon at a thermocouple temperature of 970°C (a furnace temperature of 941°C). The flow rate is 50–100 mL/min, and the laboratory-grade argon has an oxygen concentration of about 1 ppm, which translates to an oxygen partial pressure of 10^{-6} atm, or about 10^{-3} torr. The oxygen concentration in the sample does not come to equilibrium during this procedure: annealing for longer than 10 hours at this temperature eventually causes the crystal to decompose.[10]

The second step is a 20-hour anneal in flowing oxygen at a lower temperature of 500°C (a furnace temperature of 484°C). We have found that this step yields a slight further increase in T_c of up to 1 K. I believe that this second step serves to relax the strains in the crystal caused by the harsh high-temperature environment

[9] Although they attribute the electron localization to excess oxygens, their data are consistent with localization by the Cu vacancies.

[10] Note that in Figure 2.13, a point at 970°C and 10^{-6} atm would be in the decomposed phase.

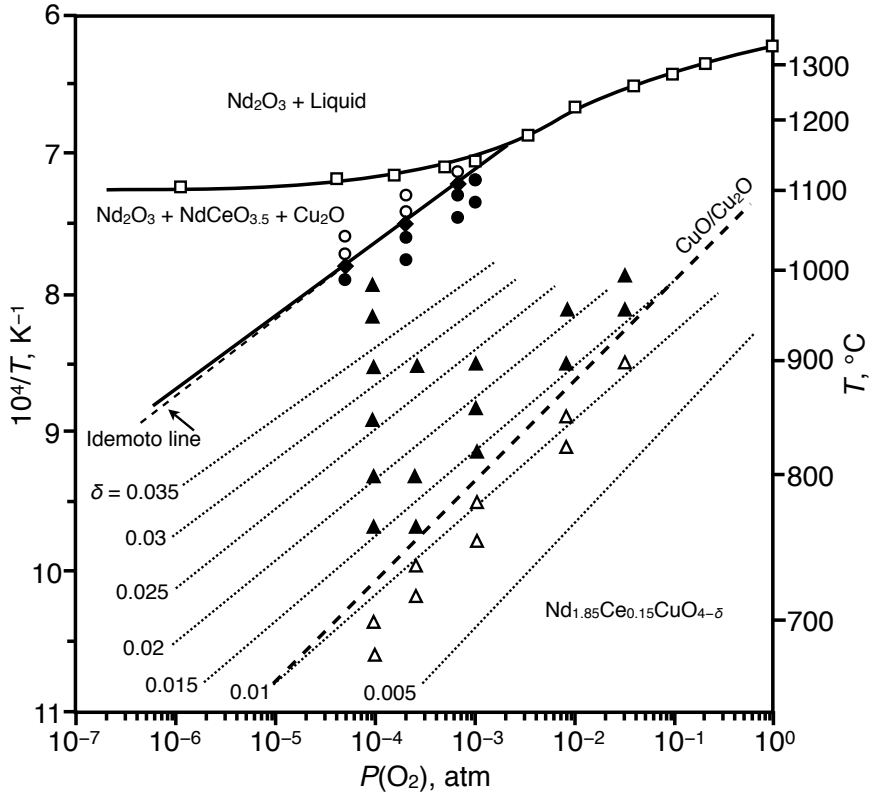

Figure 2.13: Phase stability diagram for $Nd_{1.85}Ce_{0.15}CuO_{4-\delta}$, adapted from [36]. The solid curve with the open squares indicates the solidus line (where partial melting occurs). The diagonal solid line below it indicates where NCCO decomposes. The solid triangles indicate samples for which superconductivity was observed, and the open triangles where superconductivity was not observed. The dotted lines are iso-composition lines.

of the first step.[11]

The procedure described above is the one that was found to maximize T_c in a study of $x = 0.14$ NCCO crystals [37]: given the 10-hour duration, a temperature which is too low does not cause enough oxygen reduction, whereas a temperature much higher than 970°C causes decomposition. Instead of optimizing the procedure for each doping level, which is in any case only possible for superconducting samples, this same procedure has been used across the entire doping range

[11] If this is the case, the atmosphere for this second step should not be important; this is something that I have not personally tested.

investigated in this Thesis.

2.3 Laboratory characterization

In this Section, I discuss various laboratory characterization techniques used to measure basic properties of the crystals prior to neutron scattering measurements. Section 2.3.1 describes the use of SQUID magnetometry to measure the T_c of superconducting samples. Section 2.3.2 describes the determination of the Ce concentration of crystals using ICP spectroscopy, and contains a discussion of Ce inhomogeneity issues. Section 2.3.3 is a description of the Laue diffractometer that serves as the first step in orienting the crystal axes of a sample.

2.3.1 SQUID magnetometry

The critical temperature T_c of a superconductor is one of its defining characteristics, and thus it is important to have a method of measuring this property. In principle, one could measure the resistivity of a sample to determine the T_c by observing at what temperature the resistivity drops to zero. However, the process of preparing a sample for such a measurement is quite tedious. The preferred basic method of measuring T_c is magnetometry. One measures the temperature at which the Meissner effect is seen, i.e., when the sample turns into a perfect diamagnet and expels all magnetic fields.

Our laboratory uses a magnetometer commercially manufactured by Quantum Design, the MPMS XP.[12] In general, a magnetometer is a device that measures the magnetic moment of a sample. This is done by measuring the magnetic field produced by this magnetic moment or, more precisely, by measuring the magnetic flux that passes through a conducting loop near the sample. The MPMS makes use of a superconducting quantum interference device (SQUID) to measure magnetic flux. Commercial SQUIDs are small devices, typically 30 microns across [38], and include a superconducting coil which wraps around the loop of the SQUID many

[12]Magnetic property measurement system.

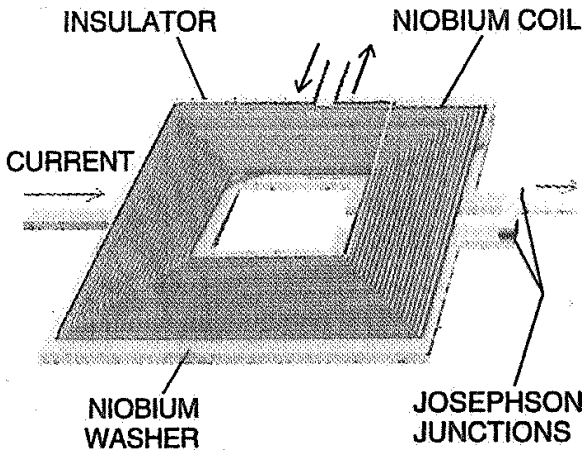

Figure 2.14: Diagram of a commercial SQUID, reproduced from [38]. A coil wraps around the SQUID many times to enhance the signal, and is connected to a pickup loop at the site of measurement.

times to enhance the signal (see Figure 2.14). The coil is, in turn, connected to a pickup loop located near the sample.

A magnetometer measures the magnetic moment not only as a function of temperature, but also as a function of applied magnetic field. One can imagine a pickup coil that forms two loops, oppositely oriented above and below the sample, which would cancel the magnetic flux due to the applied field. The SQUID would then read the difference in magnetic flux through the two loops. By measuring the signal as a function of the sample position with respect to the two loops, one could calculate the magnetic field due to the sample itself. The MPMS takes this one step further by using a second-derivative setup: four loops precisely positioned and oriented so that any gradient in the applied field is canceled out [39]. See Figure 2.15 for a schematic of the SQUID system of the MPMS.

During a measurement, at each temperature and applied field, a scan is done as a function of sample position. As long as the sample is small compared to the distance between the loops, the signal as a function of sample position has the same line shape as produced by an ideal dipole moment. The measurement program fits the scan to the predetermined shape, and the fitted amplitude is a measure of the

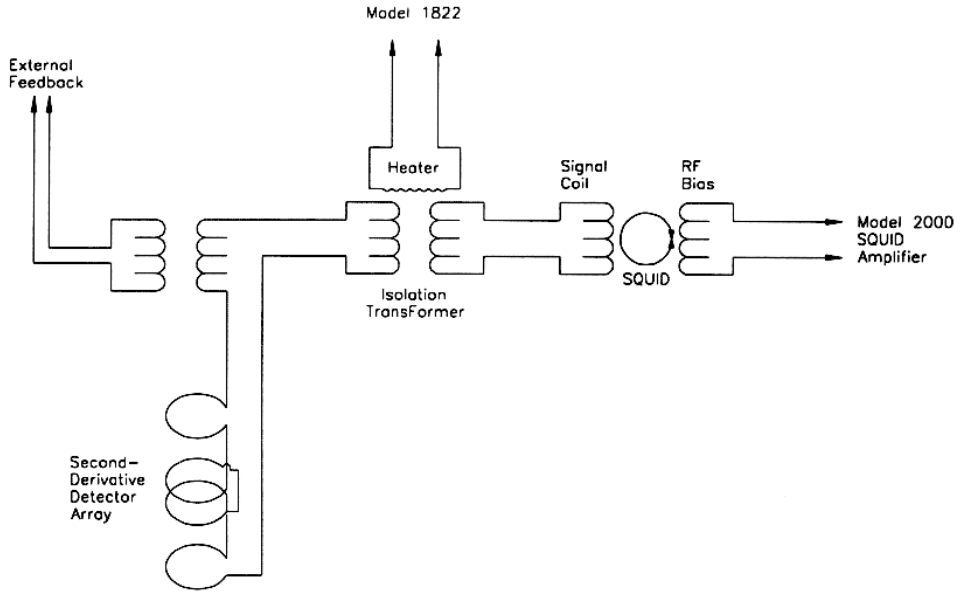

Figure 2.15: Schematic for the SQUID system in the MPMS, reproduced from [39].

sample's magnetic moment.[13]

Unfortunately, the NCCO crystals used for neutron scattering are typically large enough so that the position scans do not have the correct shape. In principle, one could use the raw data from the scan to determine the proper value for the magnetic moment (by integration, for instance), but only a qualitative determination of the magnetic moment is necessary for measuring the T_c of a sample. I have simply decreased the scan range so that the fitting converges to a reasonable value.

In the case of superconductors, the samples are diamagnetic below T_c, so that a positive applied magnetic field (typically around 5 Oe)[14] results in a negative magnetic moment. Above T_c, the paramagnetic samples show a comparatively weak positive magnetic moment. However, the amount of diamagnetism in the superconducting state depends on whether the field is applied before or after cooling the sample through T_c. Typically, the zero-field-cooled (ZFC) signal is stronger than the field-cooled (FC) signal. This well-known effect is due to flux

[13]The instrument has been calibrated using a sample with a known magnetic moment

[14]The oersted (Oe) is the cgs unit of the magnetizing field **H**. In vacuum, it is equal to the gauss (G), the cgs unit of the magnetic field **B**. Both are equal to 10^{-4} tesla (T).

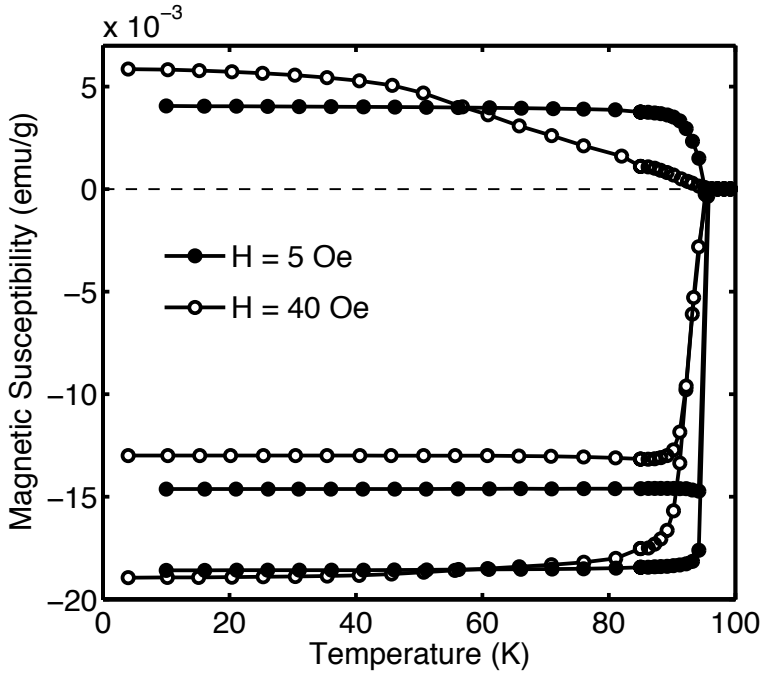

Figure 2.16: SQUID data from a superconducting sample of $HgBa_2CuO_{4+\delta}$, reproduced from [41]. The measurements were performed in applied magnetic fields of 5 Oe (black circles) and 40 Oe (open circles). The three sets of data at each field are zero-field-cooled (most negative), field-cooled (less negative), and the remnant moment (positive).

pinning [40].

The ZFC signal is from the full Meissner state of the sample. As the magnetic field is increased, surface currents form to cancel the magnetic field inside the sample. In fact, in this case, it is only necessary for the surface of the sample to be superconducting.[15] On the other hand, in the FC case, magnetic flux already penetrates the sample as the sample is cooled below T_c. Some of the flux is pinned, due to chemical impurities or physical defects, and so a full Meissner state does not form. The ratio of the FC signal to the ZFC signal can thus be a measure of the amount of defects in a sample. A third possible measurement is that of the remnant moment [42]: the sample is cooled below T_c in a field, and then the field

[15]This can be a problem, for example, when a heat-treatment process causes only the surface of the sample to have a higher T_c.

is turned off. In this situation, the pinned flux provides a net positive moment, approximately the difference between the FC and ZFC values. As the temperature is increased, the flux becomes de-pinned and the remnant moment drops to zero at T_c. The remnant-moment effect provides proof that the pinning originates from the bulk of the sample. The three types of measurements are illustrated in Figure 2.16. Note that for the simple case of measuring T_c in NCCO, it has been sufficient to measure the ZFC signal as a function of temperature.

2.3.2 ICP spectroscopy

The chemical composition of a crystal is largely determined by the composition of the powder used to produce it. However, it is important to measure the chemical composition of a crystal after it has been grown. Inductively-coupled plasma (ICP) atomic-emission spectroscopy has revealed a systematic difference between nominal and actual compositions in my crystals, as well as concentration gradients within the crystals.

Atomic-emission spectroscopy is one of the oldest analytical instrumental techniques. Atoms are thermally excited into higher electronic states and, when returning to their ground state, emit photons at certain frequencies. These frequencies, of course, depend on the element. At each frequency, the number of photons is proportional to the number of atoms of that element.

In the case of ICP spectroscopy, the source of thermal energy is a plasma flame. Argon gas is seeded with additional electrons and injected into a region of strong high-frequency magnetic fields. The resulting plasma has temperatures between 6000 and 10,000 K and enough thermal energy to electronically excite an aerosolized solution injected into the flame [43]. One of the main advantages of the ICP setup is the high ionization efficiency, and thus the ability to measure low concentrations [44].

Our group utilizes the ICP measurement service at the School of Earth Sciences at Stanford. Although the newer technique of ICP mass spectroscopy is now considered the forefront of chemical analysis techniques [44], I have found that ICP

atomic emission spectroscopy already exceeds the measurement precision needed for the NCCO samples that I have grown.

Procedure for preparing samples

The nature of ICP spectroscopy dictates that the sample must be in some sort of liquid form. To meet this requirement, small pieces of NCCO crystals are dissolved in a 5% nitric acid solution. The following paragraphs detail the procedure for the preparation used by our research group.

The glassware I have used is the 150 mL Erlenmeyer flask, using one flask per sample. Since they are reused, the first step is to thoroughly clean the required number of these flasks. The inside of a flask is cleaned using a brush and detergent. It is rinsed three or more times with tap water before being rinsed an additional three or more times with the building deionized water. The outside of the flask is then wiped dry to prevent contamination in the next step: a further triple-rinsing with ultra-pure water (henceforth "ICP water") available from the laboratories at the School of Earth Sciences. ICP water has been purified to a parts-per-billion level of solute, and has a resistivity greater than 18 MΩ cm. Plastic wrap is placed over the clean flasks whenever they are not being used.

In the next step, concentrated nitric acid is the placed into each flask. The final goal is 50 mL of 5% nitric acid, and concentrated nitric acid has a listed concentration of 65–70%. Using 67% as an approximate value, this translates to 3.7 mL of nitric acid per flask. The concentrated nitric acid is first poured into a small beaker that has been cleaned using the same method as with the flasks. A disposable plastic pipette is then used to measure out the 3.7 mL to each flask.

Because concentrated nitric acid slowly releases noxious fumes (of nitrogen dioxide, a poison), the acid in each flask is diluted slightly to about 30% by adding ICP water. It is not, however, diluted down to 5% at this point, because the acid needs to remain concentrated enough to dissolve the crystals. The same beaker can be used for the water (after rinsing), as well as the same pipette. I add 3.7 mL of ICP water, but the amount is not that important. Afterwards, plastic wrap is again placed over the flasks.

The next step is to put the NCCO samples into the flasks. Here there are several issues to consider. The first is that the ICP measurements are not sensitive to concentrations which are too high. The upper limit is 100 parts per million (ppm), by mass. In NCCO, the Nd atoms constitute the heaviest portion of the compound, and setting Nd to 100 ppm translates to 7.8 mg of NCCO for every 50 mL of solution. There is also a practical lower limit to the mass of NCCO used. The analytical balance used for mass measurements cannot reliably measure masses below 0.5 mg or so, and I have observed that ICP measurements of samples much less than 1 mg have noticeably worse precision. The mass of NCCO put into solution is recorded, but only as a qualitative check of the data. Because only the ratio of the concentrations is important, the volumes of liquid used for the samples can be approximate.

Even samples as small as a few milligrams can take many days to dissolve. When time is limited (the usual case), the sample can be crushed into powder as follows. The piece of crystal is placed in a folded tube of weighing paper, such that there are many layers of paper between it and the outside. The sample is then crushed by hitting it in a clean mortar with a clean pestle. The tube of weighing paper is then unfolded slowly over another piece of weighing paper, which catches the powder. The powder is then weighed and carefully tapped into a flask. In the case where the initial piece of crystal is too large, the crystal is crushed into powder, as above, but only a portion of the powder is placed into the flask.

Once a flask contains a sample, its mouth is sealed with Parafilm,[16] taking care that the side with paper backing ends up facing the interior of the flask. The flask is then labeled using a marker on the glass surface (so that the label can be easily removed before the next measurement).

The dissolving process can be accelerated by heating the flasks. The flasks are placed on a hot plate and set well below the boiling point of water. Plastic wrap is again placed over the flasks, because the Parafilm may break upon expanding due to the heating of the air inside the flasks. When heated, the NCCO samples usually

[16]Parafilm is a flexible, moldable, self-adhering plastic film manufactured by Pechiney Plastic Packaging, Inc.

dissolve in less than a day.

Once the NCCO is dissolved into the acid, ICP water is added to each flask to dilute the solution to 50 mL (and thus 5% nitric acid). The solution is then dispensed into test tubes. The test tubes are standard glass test tubes, 13 mm diameter by 100 mm in length. Being quite inexpensive, they are disposed of after each use. Each new test tube is, however, rinsed with a small amount of the solution it will be filled with. A small square of Parafilm is used to cover the mouth of the tube while it is shaken. The tube is then emptied and the Parafilm discarded. A small KimWipe[17] is used to wipe the mouth of the tube and immediately discarded. The test tube is then filled nearly to the top with the solution, sealed with a new square of Parafilm, and labeled.

Typically, three test tubes are filled for each flask of solution (and thus for each NCCO sample). This is used as a final check for contamination and also to see the fluctuations in the readings from the ICP instrument. The test tubes are placed in a test tube rack and covered with plastic film for transport to the ICP facility.

Procedure for preparing standards

Solutions must also be prepared with known concentrations of the same ions to be measured, and these serve as standards used for calibration purposes during the ICP measurement. While precise amounts of liquids were not used for samples, they are quite necessary for the standards. There are actually three solutions that are required. The first is the "high standard," whose ion concentrations should be higher than in all of the samples. The high standard is also subject to the 100 ppm upper limit mentioned above. The second is the "quality control," in which the ion concentrations are exactly half of those in the high standard. The quality control standard is measured periodically during the measurement of the samples. The third is the "matrix," which is simply the solvent. In our case, this is 5% nitric acid.

Solutions of "plasma standards" are sold by chemical companies (e.g., Alfa Aesar); 1000 ppm solutions of Nd, Ce, and Cu in 5% nitric acid are used for NCCO.

[17] KimWipes are a type of lint-free cleaning tissue manufactured by Kimberly-Clark Corporation.

The glassware used in standards preparation is volumetric (the volumes must be precisely measured). Because volumetric pipettes come only in certain sizes, the concentrations chosen for the high standard and quality control are limited. Typically, one pipette is chosen per element and used twice for the high standard and once for the quality control. The set of concentrations that I have used for NCCO is 100 ppm Nd, 20 ppm Ce, and 40 ppm Cu for the high standard, which means concentrations of 50 ppm Nd, 10 ppm Ce, and 20 ppm Cu for the quality control. In 100 mL volumetric flasks, this translates to a 5 mL pipette for Nd, a 1 mL pipette for Ce, and a 2 mL pipette for Cu.

The first step is again the cleaning of glassware. A brush should not be used to clean a volumetric flask. Instead, concentrated nitric acid is first used to clean the inner surface. This is followed by several rinses with deionized water and three rinses with ICP water. The volumetric pipettes must also be dried; a heat gun may be used (with care) to blow out the water droplets. The final containers for the three liquids, usually plastic bottles, must also be cleaned and dried.

The 5% nitric acid solution is made first. Because the concentration of nitric acid is not important, a disposable graduated pipette is used to measure the amount of concentrated nitric acid into a large flask and diluted with ICP water. The high standard and quality control solutions are made in 100 mL volumetric flasks. The appropriate amount of 1000 ppm standards is measured into the flasks using the volumetric pipettes. The nitric acid from the large flask is then transferred using any clean pipette to fill the volumetric flasks up to their fill line, taking care to mix the solution periodically (by closing them with their cleaned glass stoppers). The high standard, quality control, and remaining matrix are then dispensed into the clean (and dry) plastic bottles. The bottles are labeled with the ion concentrations, as well as the date. If there is enough solution left after the measurements, the standards may be reused.

Ce inhomogeneity in NCCO

The data available from an ICP measurement are the concentrations of the Nd, Ce, and Cu ions for each test tube. For every sample, the Ce concentrations for the

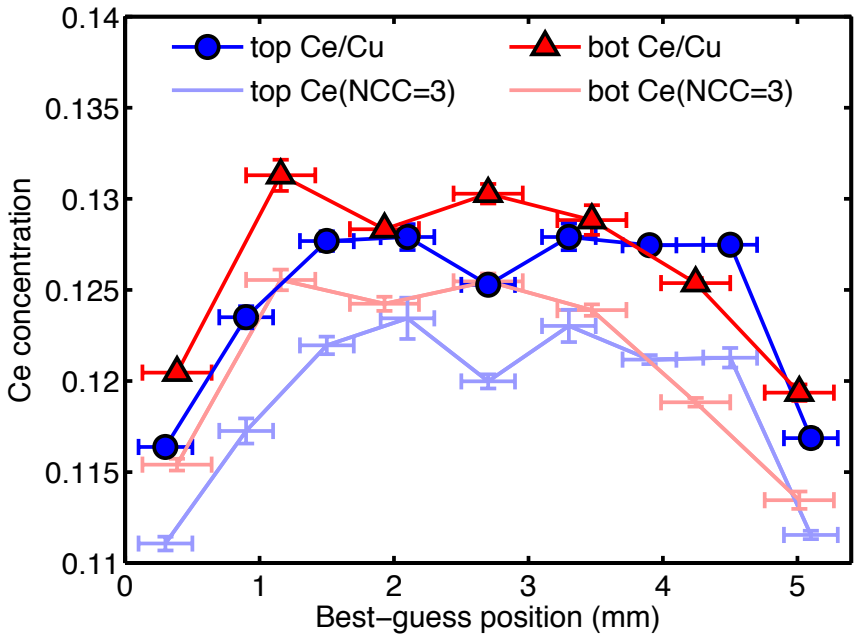

Figure 2.17: Ce concentration as a function of position along the diameter at the top and bottom of crystal Eugene24, nominally $x = 0.121$.

three test tubes are averaged. There are actually a few different ways of calculating the Ce concentration. The simplest is to assume that the Cu concentration is 1 per formula unit and report the ratio of Ce and Cu values. This is what is used in this Thesis when quoting "actual" Ce concentrations. Another method is to assume the Nd and Ce concentrations together add to 2. And the final is to assume that the Nd, Ce, and Cu concentrations together add to 3. The first and last of these three methods are compared in Figure 2.17. The systematic difference indicates a slight deficiency of Cu and a slight excess of Nd.

Figure 2.17 also shows how the measured Ce concentration can change depending on the position in the crystal. The figure shows the Ce concentration as a function of position across the diameter of the crystal, where the two extreme positions indicate the surface of the crystal cylinder. The circles and triangles indicate measurements from the top (just above the neutron piece) and bottom (just below the neutron piece), respectively, and are separated by about 4 cm. Because it is desirable to have samples with homogenous Ce concentration, the more recent

crystals have had their surface portions removed with a polisher to a depth of approximately 1 mm. The ICP data from the surface regions are discarded, and the remaining data from the top and bottom pieces are used to estimate the average Ce concentration (and the spread in Ce concentration) of the sample measured with neutron scattering.

It has recently come to my attention that a low-oxygen atmosphere for the growth may affect the Ce inhomogeneity of NCCO crystals [24, 45]. Experimenting with the growth atmosphere may be an avenue for future study.

2.3.3 Laue diffraction

Although visible grain boundaries on the surface of a grown crystal indicate multiple grains, a crystal with a smooth surface may or may not be a single grain. While neutron scattering can be used in principle to check whether a crystal contains multiple grains, and is commonly used for a final "crystal check" before actual measurements begin (see Section 2.4 below), time at the neutron spectrometer is precious. Our research group uses a Laue diffractometer at Stanford to check the integrity of the crystal structure of a sample, and to find a rough orientation of its crystal axes before neutron scattering measurements are performed.

Laue diffraction was in fact the method used in 1912 by Max von Laue in the first X-ray diffraction studies that elucidated the crystalline structure of solids [46]. It is a diffraction technique that uses a range of X-ray energies, rather than the more typical monochromatic beam employed in most modern scattering techniques. Scattering with a monochromatic (neutron) beam is described in Section 2.4 and discussed in detail in Appendix B. However, I provide here a brief real-space description of diffraction to illustrate the advantages of the Laue technique for crystal checks and alignment.

In the textbook description of Bragg diffraction, a beam with wavelength λ is incident on a set of planes at an angle θ from normal incidence and reflected at the same angle θ. The reflected wave constructively interferes (and thus scattering occurs) only when the path length difference equals an integral number of

wavelengths. The formula is

$$2d \sin\theta = n\lambda \,, \tag{2.3}$$

where d is the spacing between planes and n is an integer. This means that, given a monochromatic beam pointed at a sample, the crystal axes must be oriented precisely so that the angle between the vector normal to the planes and the beam is θ. Moreover, for different sets of planes, and thus different values of d, the crystal axes must be oriented differently for scattering to occur. Given a random unknown orientation of the crystal axes, the chance is quite low that any Bragg diffraction occurs.

In Laue diffraction, the beam is composed of a continuum of wavelengths, typically resulting from Bremsstrahlung: a beam of electrons with suitable energies is shot at a target (tungsten),[18] and X-rays are produced when the electrons decelerate in the material. Given this Laue beam incident on a sample, every set of planes with spacing d at any angle θ to the beam can produce scattering, provided the corresponding wavelength λ lies in the range of wavelengths. Consequently, a pattern of scattered X-rays will form with any random orientation of the crystal axes. Laue diffraction thus has the advantage of immediate detection, whereas the single-wavelength techniques used for more precise measurements require precise alignment for scattering to occur.

Because X-rays do not penetrate very far into a solid,[19] a backscattering setup is used in which an area detector is positioned on the same side of the sample as the incident beam. The sample is mounted on a goniometer which can be used to change the orientation of the crystal relative to the incident beam while looking at the Laue pattern from the detector on a computer screen. A Laue pattern with high symmetry indicates orientation along a high-symmetry axes of the crystal structure. The pattern may be compared with previous measurements to confirm the axis orientation. Figure 2.18 shows the Laue pattern along the c-axis for an

[18] Tungsten is a heavy enough element so that its core-level excitations are too large to be excited. In a target composed of a lighter element, these core-level excitations would be excited and produce a spectrum of X-rays with sharp characteristic frequencies.

[19] The penetration depth for the hard X-rays used in Laue instruments is on the order of a few μm.

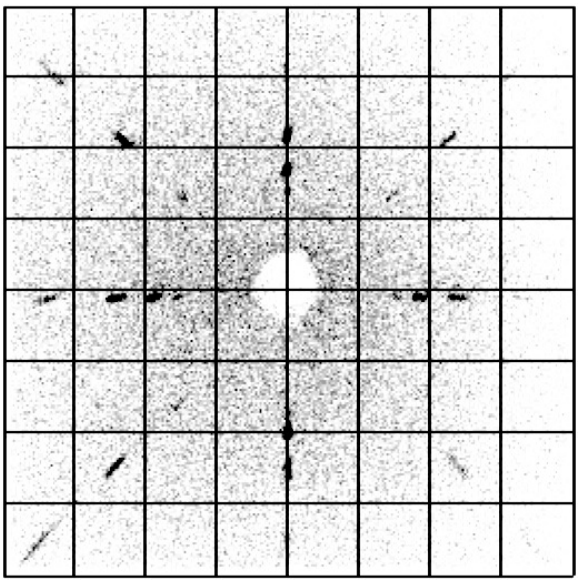

Figure 2.18: Laue backscattering pattern along the *c*-axis in NCCO crystal Eugene19, nominally $x = 0.125$. The *a*-axis ([100]-direction) is horizontal and vertical, and the [110]-direction is along the diagonals. The open circle in the middle indicates the opening in the detector through which the X-rays are emitted.

NCCO crystal.

For NCCO, the *c*-axis is usually perpendicular to the growth direction. The implies that growth perpendicular to the *c*-axis is faster than growth along the *c*-axis, so that grains that form with the *c* axis perpendicular to the growth direction eventually dominate other grains.

In addition to alignment, the Laue instrument is used to check the macroscopic integrity of the crystal structure of a sample. Using motors attached to the sample stage, the sample is moved horizontally and vertically to check whether the Laue pattern changes. Because the X-rays do not penetrate very far into the sample, it is also necessary to turn the sample around to check whether the Laue pattern is reversed. Only samples which appear to be single-grain from Laue measurements are chosen for neutron scattering measurements.

2.4 Neutron scattering

This Section describes the neutron scattering techniques used in the measurements of NCCO detailed in the following two Chapters of this Thesis. Neutron scattering is the principal tool for measuring the magnetic structure and dynamics of a solid. Its advantages can be illustrated by considering the basic properties of the neutron. The first is that the neutron has no electric charge; this allows it to penetrate deeply into solids, and provides a true bulk measurement of physical properties. Neutrons interact with matter in two distinct ways: via the nuclear force and via the electromagnetic force through the neutron's magnetic moment. With respect to the scattering of solids, these interactions allow neutrons to probe the arrangement of the nuclei (i.e., crystal structure) as well as magnetic fields due to orbital moments and/or the arrangement of unpaired electron spins (i.e., magnetic order).

Neutron scattering is particularly effective because of a fortunate coincidence: neutrons thermalized by the heavy-water moderator surrounding a reactor core (kept at approximately room temperature) have wavelengths on the order of angstroms, which is ideal for probing atomic distances, while the energies of "thermal" neutrons (on the order of tens of meV) are ideal for probing the many excitation processes of interest in solids [47]. In comparison, photons with suitable wavelengths (i.e., X-rays) have energies that are six orders of magnitude larger, and therefore require an energy resolution correspondingly more precise to probe the same energy scales. Note that although magnetic scattering is possible with X-rays, the cross section is many orders of magnitude smaller than for neutrons.

Consider a beam of neutrons with momentum[20] $\mathbf{k}_i$ incident on a sample. In a scattering experiment one measures the number of neutrons as a function of their scattered momenta $\mathbf{k}_f$. The energy and momentum of a neutron are related by

$$E = \frac{\hbar^2 k^2}{2m_n}, \tag{2.4}$$

[20] $\mathbf{k}$ is technically the wavevector, and the momentum is $\mathbf{p} = \hbar\mathbf{k}$

and the physically important parameters turn out to be

$$\hbar\omega = E_i - E_f \tag{2.5}$$

$$\mathbf{Q} = \mathbf{k}_f - \mathbf{k}_i\,, \tag{2.6}$$

where $\hbar\omega$ is the energy transfer[21] and $\mathbf{Q}$ is the momentum transfer.[22] The scattering is said to be elastic or inelastic when the energy transfer is zero or non-zero, respectively. Elastic scattering measures the static structure (nuclear or magnetic) of the system, whereas inelastic scattering probes excitations, i.e., deviations from the time-averaged structure.

2.4.1 Neutron scattering cross section

The following formulas for the neutron scattering cross section are derived in detail in Appendix B.

Elastic nuclear scattering. The cross section for elastic nuclear scattering from a crystal lattice is given by (B.81):

$$\left.\frac{d\sigma}{d\Omega}\right|_{\text{nuc,el}} = N\frac{(2\pi)^3}{v_0}|F_{\text{N}}(\mathbf{Q})|^2\sum_i \delta(\mathbf{Q}-\mathbf{G}_i)\,, \tag{2.7}$$

where N is the number of unit cells, v_0 is the volume of the unit cell, the $\mathbf{G}_i$ are the reciprocal lattice vectors, and

$$F_{\text{N}}(\mathbf{Q}) = \sum_j \overline{b}_j e^{i\mathbf{Q}\cdot\mathbf{d}_j} e^{-W_j} \tag{2.8}$$

is the static nuclear structure factor. The vectors $\mathbf{d}_j$ describe the positions of the nuclei in the unit cell, and $\overline{b}_j$ is the average scattering length of the j-th atom. The W_j contribute to the Debye-Waller factor (the decrease in coherent scattering due

[21] Although the energy transfer is $\hbar\omega$, the $\hbar$ is frequently omitted, as in "$\omega = 3$ meV."

[22] Note that I use the convention from [47], in which the momentum and energy transfers have different signs. See Footnote 2 on page 146.

to thermal motion), usually written as e^{-2W}. The formula shows that nuclear elastic scattering occurs only when the momentum transfer $\mathbf{Q}$ coincides with a reciprocal lattice vector $\mathbf{G}$, and this statement is the momentum-space equivalent of the Bragg condition (2.3). The relative intensity of Bragg peaks is determined by the structure factor.

In practice, the lattice structure of the crystals is already well known, and the nuclear Bragg peaks are used to align the samples in the spectrometer at the beginning of an experiment.

Inelastic nuclear scattering. The cross section for inelastic nuclear scattering is primarily due to one-phonon scattering, which is given by (B.94):

$$\left.\frac{d^2\sigma}{d\Omega dE_f}\right|_{1\text{ph}} = \frac{k_f}{k_i} N \sum_m \frac{n(\omega_m)+1}{2\omega_m} |\mathcal{F}_\text{N}(\mathbf{Q})|^2 \delta(\omega - \omega_m(\mathbf{Q}))\,, \tag{2.9}$$

where $\omega_m(\mathbf{Q})$ is the dispersion of the m-th phonon branch, $n+1$ is the Bose population factor given by

$$n(\omega)+1 = \frac{1}{1-e^{-\hbar\omega/k_\text{B}T}}\,, \tag{2.10}$$

and the dynamic nuclear structure factor is

$$\mathcal{F}_\text{N}(\mathbf{Q}) = \sum_j \frac{\bar{b}_j}{\sqrt{M_j}} (\mathbf{Q}\cdot\mathbf{e}_{mj}) e^{i\mathbf{Q}\cdot\mathbf{d}_j} e^{-W_j}\,, \tag{2.11}$$

where M_j is the mass of the j-th atom and $\mathbf{e}_{mj}$ is the polarization of the j-th atom in the m-th phonon branch.

While the measurement of phonon spectra in the high-T_c cuprates is an important subject [48], this Thesis is concerned with the magnetic spectrum. Phonon measurements are, however, used as part of a normalization procedure to determine the absolute units of the magnetic susceptibility.[23] In principle, all of the quantities in (2.9) and (2.11) are calculable, but the formula simplifies further when

[23] Absolute units may also be calculated by measuring several nuclear Bragg peak intensities, but this method is complicated by extinction due to multiple scattering.

considering acoustic phonons in the limit $\omega \to 0$. In this case, the polarization $\mathbf{e}_j$ of all of the atoms in the unit cell is the same. The factor $\mathbf{Q} \cdot \mathbf{e}$ can then be taken out of the sum, and the formula for the cross section becomes

$$\left.\frac{d^2\sigma}{d\Omega dE_f}\right|_{\text{acoustic}} = A\frac{k_f}{k_i}\hbar^2 N \frac{n(\omega)+1}{2E}\left|\sum_j \frac{\bar{b}_j}{\sqrt{M_j}} e^{i\mathbf{Q}\cdot\mathbf{d}_j}\right|^2 (\mathbf{Q}\cdot\mathbf{e}_m)^2 \delta(E - E_m(\mathbf{Q}))\,, \qquad (2.12)$$

where the $\hbar^2$ is due to changing from ω to $E = \hbar\omega$ and the Debye-Waller factor e^{-2W} has been ignored, because it only becomes significant at relatively high temperatures. N is the number of unit cells,[24] most easily given in units of moles. If the $\bar{b}_j$ are given in fm, the M_j in atomic mass units (amu), $\mathbf{Q}$ in Å^{-1}, and E in meV, then $\hbar^2$ is best given as $\hbar^2 = 4.18\,\text{amu}\,\text{meV}\,\text{Å}^2$, and the cross section has the units of $\text{fm}^2\,\text{mol/meV}$. A is the prefactor that must be determined for the particular spectrometer and neutron flux used; it can be thought of as the conversion factor between $\text{fm}^2\,\text{mol/meV}$ and detector counts per monitor rate.

Because the formula for the phonon cross section was derived assuming a perfectly harmonic system, one must take into account the finite phonon lifetime by replacing the delta function with a Lorentzian of the form

$$\delta(\omega - \omega_m(\mathbf{Q})) \to \frac{1}{\pi}\frac{\Gamma_m(\mathbf{Q})}{\Gamma_m^2(\mathbf{Q}) + (\omega - \omega_m(\mathbf{Q}))^2}\,, \qquad (2.13)$$

where Γ is the Lorentzian half-width at half-maximum.[25] Taking this model into account, the measured signal is then deconvolved with the instrument resolution to find A,[26] and A is used to calculate the absolute units of magnetic susceptibility (see the Section on inelastic magnetic scattering below).

[24] The number of unit cells may be different from the number of formula units, the definition for N used in (2.18) for inelastic magnetic scattering.

[25] The ResLib package [49] provides a "single-mode" convolution routine that has built-in functionality for the Lorentzian broadening.

[26] Care needs to be taken with the contribution of harmonics to the monitor rate and the $1/k_i$ monitor efficiency (see Section 2.4.2). Note that the ResLib package [49] takes care of the k_f/k_i factor, and that it can be set up to take the monitor efficiency into account as well.

Elastic magnetic scattering. In this Thesis, elastic magnetic scattering is used to determine whether the system is magnetically ordered. It is, in fact, a direct measure of the order parameter. For antiferromagnetically-ordered systems like the undoped cuprates, the magnetic unit cell is double the size of the structural unit cell, and the cross section is given by (B.154):

$$\left.\frac{d\sigma}{d\Omega}\right|_{\text{mag,el}} = N_{\text{M}} \frac{(2\pi)^3}{v_{0\text{M}}} \sum_i \delta(\mathbf{Q} - \mathbf{G}_{\text{M}i}) |\mathbf{F}_{\text{M}}(\mathbf{Q})|^2 \,, \tag{2.14}$$

where N_{M} is the number of magnetic unit cells, $v_{0\text{M}}$ is the volume of the magnetic unit cell, and the $\mathbf{G}_{\text{M}i}$ are the magnetic reciprocal lattice vectors. The magnetic structure factor is given by

$$\mathbf{F}_{\text{M}}(\mathbf{Q}) = \sum_j \gamma r_0 f_j(\mathbf{Q}) \langle \mathbf{S}_{\perp j} \rangle e^{\mathbf{Q}\cdot\mathbf{d}_j} e^{-W} \,, \tag{2.15}$$

where j labels the spins in the magnetic unit cell, γr_0 is the interaction length of neutrons with electron spins,[27] $f(\mathbf{Q})$ is the magnetic form factor, and $\langle \mathbf{S}_\perp \rangle$ is the spin[28] projected onto the plane perpendicular to $\mathbf{Q}$. Antiferromagnetic Bragg peaks occur at reciprocal lattice positions that are distinct from nuclear Bragg reflections, making it easy to distinguish the two.

Note that according to (2.14), the intensity of magnetic Bragg peaks is linearly proportional to N_{M}, but proportional to the square of S. By performing measurements of different samples under identical conditions, one can calculate the ratio of the ordered moment strength (assuming the same magnetic volume fraction N_{M})

$$\frac{S_1}{S_2} = \sqrt{\frac{I_1}{I_2}} \,. \tag{2.16}$$

For NCCO, there is a complication due to the Nd^{3+} moments, which order around

[27] In another fortunate coincidence, the magnetic interaction length γr_0 and the nuclear scattering lengths b are all around the same magnitude of a few fm (10^{-15} m), which means that the typical nuclear and magnetic intensities are similar.

[28] In general, $\mathbf{S}$ can represent the total angular momentum $\mathbf{J} = \mathbf{L} + \mathbf{S}$. In the case of the magnetic moment of Cu^{2+}, the orbital moment is quenched, and L is effectively zero.

3 K,[29] but whose effects can be observed up to a few tens of K [15]. The measurement of the low-temperature Cu^{2+} ordered moment must take the effects of the Nd^{3+} moments into account. For Nd_2CuO_4, the intensities of two commonly studied magnetic Bragg peaks are given by [50][30]

$$\begin{aligned} I(\tfrac{1}{2},\tfrac{1}{2},1) &\propto (S_{\mathrm{Cu}} f_{\mathrm{Cu}} - 1.2\, S_{\mathrm{Nd}} f_{\mathrm{Nd}})^2 \,, \\ I(\tfrac{1}{2},\tfrac{1}{2},3) &\propto (S_{\mathrm{Cu}} f_{\mathrm{Cu}} + 1.9\, S_{\mathrm{Nd}} f_{\mathrm{Nd}})^2 \,. \end{aligned} \tag{2.17}$$

Thus one can calculate the strengths of the moments of both ion species by measuring both Bragg peaks. In practice, the $(\frac{1}{2},\frac{1}{2},1)$ Bragg peak intensity has a minimum in its temperature dependence around 6 K, and the intensity of the $(\frac{1}{2},\frac{1}{2},3)$ peak is recorded at this "compensation" temperature; it is this value that is compared among different NCCO samples.

Inelastic magnetic scattering. The inelastic magnetic scattering cross section is given by (B.181)[31]

$$\left.\frac{d^2\sigma}{d\Omega dE_f}\right|_{\mathrm{mag,inel}} = (\gamma r_0)^2 \frac{k_f}{k_i} N |f(\mathbf{Q})|^2 e^{-2W} \frac{n(\omega)+1}{2\pi\mu_{\mathrm{B}}^2} \chi''(\mathbf{Q},\omega) \,, \tag{2.18}$$

where μ_{B} is the Bohr magneton and $\chi''(\mathbf{Q},\omega)$ is the imaginary part of the dynamic magnetic susceptibility.

The dynamic susceptibility is the quantity of physical interest in most neutron scattering experiments of magnetic materials. It is usually plotted in "arbitrary units." However, it is desirable to calculate the absolute units of χ'' to be able to compare the strength of the magnetism with other systems and with theoretical calculations, or even to compare measurements of the same system on different

[29] The Cu^{2+} moments order spontaneously at higher temperatures, and the ordering of the Nd^{3+} moments is aided by polarization due to the ordered Cu^{2+} moments. When the Nd^{3+} moments order, they have an effect, in turn, on the Cu^{2+} moments.

[30] Here (and throughout this Thesis) I use tetragonal notation, whereas [50] uses orthorhombic notation. Also note that, while the spin structure proposed for Nd_2CuO_4 in [50] differs from that shown later in [51] (and shown in Figure 3.5), these equations still hold.

[31] The Landé factor has been set to $g = 2$.

spectrometers. The dynamic susceptibility is the generalization of the usual (static, $\omega = 0$) magnetic susceptibility, and thus has the same units. Both quantities describe how a magnetic system responds to a magnetic field. The units are thus (energy/field)/field. On the atomic scale, the appropriate unit for the magnetic moment is the Bohr magneton $\mu_B = 5.788 \times 10^{-5}$eV/T. The typical units for the magnetic susceptibility are μ_B^2/eV/f.u., where the formula unit (f.u.) refers to the atoms as listed in the chemical formula.

Rewriting the inelastic magnetic cross section given by (2.18) gives

$$\left.\frac{d^2\sigma}{d\Omega dE_f}\right|_{\text{mag,inel}} = A\frac{k_f}{k_i}N(n(\omega)+1)(\gamma r_0)^2\frac{1}{2\pi}|f(\mathbf{Q})|^2\frac{1}{\mu_B^2}\chi''(\mathbf{Q},\omega)\,, \tag{2.19}$$

where the Debye-Waller factor has again been ignored. Here N is the number of formula units, and the magnetic interaction length is $\gamma r_0 = 5.39$ fm. An empirical formula for the Cu^{2+} magnetic form factor $f(\mathbf{Q})$ in the cuprates is found in the literature [52, 53]. The magnetic scattering data are deconvolved using the same technique as for the phonon measurement, and the value of A found with phonons (see the previous Section on inelastic nuclear scattering) is used to convert from the number of counts to $\chi''(\mathbf{Q},\omega)$ in units of μ_B^2/meV/f.u.

One more step is usually required to obtain a reliable value of the magnetic susceptibility in absolute units. Because the susceptibility can be sharp in $\mathbf{Q}$, the signal is often resolution-limited in momentum. In those case, the integrated area is a much more reliably extracted value than the intrinsic amplitude or width. Consequently, the $\mathbf{Q}$-averaged susceptibility $\chi''(\omega)$ is often the value that is plotted:

$$\chi''(\omega) \equiv \frac{\int \chi''(\mathbf{Q},\omega)\,d\mathbf{Q}}{\int d\mathbf{Q}}\,, \tag{2.20}$$

where the integrals are defined to be taken over one Brillouin zone. Note that $\chi''(\omega)$ has the same units as $\chi''(\mathbf{Q},\omega)$. In the cuprates, when the magnetism is two-dimensional, there is no ℓ-dependence (other than through the form factor), and thus the integrals over ℓ cancel. In addition, the integral in the denominator

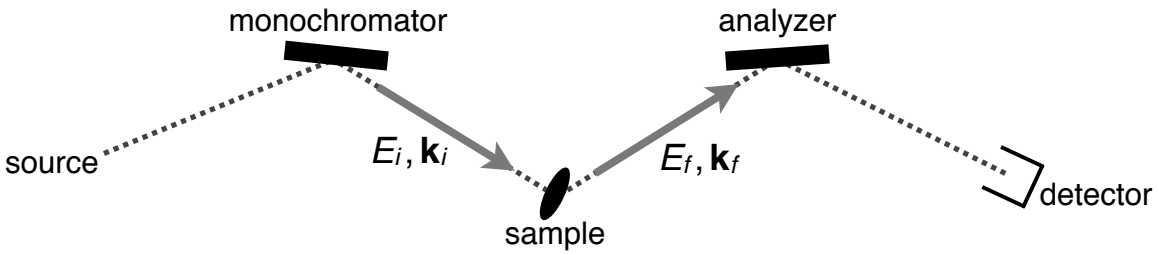

Figure 2.19: Illustration of the basic components of a triple-axis spectrometer. The monochromator determines the energy and momentum of neutrons incident on the sample, and the analyzer selects the energy and momentum of neutrons scattered from the sample.

is equal to 1 when working in reciprocal lattice units. Assuming an isotropic two-dimensional Gaussian form for the intrinsic signal gives

$$\chi''(\mathbf{Q},\omega) = \chi''(\omega)\frac{1}{2\pi\sigma^2}\exp\left(-\frac{(h-h_0)^2+(k-k_0)^2}{2\sigma^2}\right), \tag{2.21}$$

where σ is the Gaussian width in reciprocal lattice units. This model is used in the deconvolution of the data. Typically, each constant-energy scan in momentum space is deconvolved independently using a model with constant $\chi''(\omega)$ and σ.[32] Finally, the deconvolved values of $\chi''(\omega)$ can be plotted as a function of ω in the absolute units μ_B^2/eV/f.u.

2.4.2 Triple-axis spectrometer

Figure 2.19 shows the main components of a triple-axis neutron-scattering spectrometer. The type of neutron source used in this Thesis work is the nuclear reactor.[33] The high-energy neutrons that are liberated in nuclear fission are thermally moderated inside a tank of heavy water ($T \sim 300$ K) surrounding the reactor

[32] If the data are of high enough quality, one could allow for an energy-dependent value of σ in the model.

[33] The other type is a spallation neutron source, in which pulses of high-energy protons impact a heavy-element target to produce pulses of high-energy neutrons (which can then be moderated). Such a source is typically useful in time-resolved measurements of neutron energies, but the time-averaged flux of neutrons can be low compared to nuclear reactor sources.

core. Neutrons may also be moderated by liquid hydrogen ($T = 20\,\mathrm{K}$) or heated graphite ($T \sim 1400\,\mathrm{K}$) to obtain 'cold' or 'hot' energy distributions, respectively. Beam tubes which avoid a direct line-of-sight with the core allow these moderated neutrons to enter the experimental hall.

In the spectrometer there are three changes in the direction of the neutron path: at the monochromator crystal, at the sample, and at the analyzer crystal. The monochromator and analyzer are specially manufactured crystals (typically of pyrolytic graphite[34]) which are used to select neutrons of specific energies via Bragg reflection: the monochromator selects the energy E_i of the neutrons incident on the sample, and the analyzer selects the energy E_f of the neutrons scattered from the sample that are allowed to enter the detector.[35] The monochromator and analyzer, together with the geometry, determine the momenta $\mathbf{k}_i$ and $\mathbf{k}_f$ of incident and scattered neutrons, respectively. A computer is used to control the six motors that move the angular position (θ) and angular deflection (2θ for reflection) at the three axes; once the sample is aligned, one only needs to input the desired $\mathbf{Q}$ and ω to move the motors to the proper positions.

For most spectrometers, the scattering is limited to the horizontal plane. Thus the momentum transfer $\mathbf{Q}$ is limited to a corresponding plane in $\mathbf{Q}$-space, and this scattering plane is chosen based on the requirements of the experiment. For the quasi-two-dimensional cuprates, a common choice is the ($hk0$) plane, with the (001) direction (the c-axis) perpendicular to the scattering plane. Another common choice is ($hh\ell$), which is the plane defined by the (110) and (001) directions.

Alignment of a crystal involves a total of five degrees of freedom at two (usually) orthogonal Bragg positions. One degree of freedom is the angular position (θ) of the sample table. Two more are the tilt of the sample table (motor-controlled goniometers) along the two axes which bring the desired crystal plane to the horizontal. There is a limit to how much the sample table can tilt, and thus coarse

[34]Pyrolytic graphite is a form of carbon in which sheets of graphene are stacked as in graphite, but whose relative planar orientations are random. Bragg scattering thus only occurs for $\mathbf{Q}$ perpendicular to the planes.

[35]A neutron detector utilizes pressurized ^{3}He gas. ^{3}He nuclei are very efficient at absorbing neutrons, and the nuclear reaction releases energetic charged particles that can be detected by, e.g., a Geiger counter.

adjustments to the sample orientation are sometimes made to the sample holder itself. Finally there are the (potentially different) lattice constants along the two directions; a 'θ-2θ' scan is performed in which one changes the magnitude of $\mathbf{Q}$ without changing its direction.

There is a great deal of freedom in choosing the sample environment. In the experiments detailed in this Thesis, temperatures as low as 1.4 K and as high as 450 K were accessed, as well as magnetic fields as high as 6.5 T. All sample enclosures, as well as the sample mounts, are constructed of aluminum, an element that is practically transparent to neutrons.[36]

While the formulae in Section 2.4.1 assume definite values of $\mathbf{k}_i$ and $\mathbf{k}_f$, in a real spectrometer the detector counts neutrons with ranges of initial and final momenta. The rate of detection for a momentum transfer of $\mathbf{Q}_0 + \Delta\mathbf{Q}$ and an energy transfer of $\omega + \Delta\omega$ when the spectrometer is set to $(\mathbf{Q}_0, \omega_0)$ is called the resolution function, which has a somewhat complicated dependence on the spectrometer configuration. One method of controlling the resolution is to use collimators: these are parallel blades of cadmium (an element with a high neutron absorption cross section) that limit the horizontal angular spread along the straight sections of the neutron path. Tighter collimations improve the planar resolution at the expense of neutron flux. The calculation of the resolution function for a spectrometer using collimators is detailed in Appendix C. A point of note is that, for two-axis energy-integrating scans (see Section 2.4.3), calculations show that the momentum resolution is predominantly determined by the collimator after the sample.

Another aspect of modern spectrometers that affects the resolution function is the use of focusing monochromators and analyzers. A horizontally-focusing monochromator, for example, consists of several vertical strips of crystal which move and/or rotate (typically to a curved arrangement) so that the Bragg condition is better satisfied across the entire monochromator area, and also so that more of the original neutron flux is incident on the sample. Useful neutrons no longer have parallel trajectories, and thus collimators are undesirable in such focusing experiments. Because of the better satisfied Bragg condition across the curved monochromator,

[36] Aluminum powder reflections can still give rise to spurious elastic scattering.

the energy of the incident neutrons is better defined. Consequently, in a setup using focusing monochromators and analyzers, the energy resolution is typically improved. However, because the neutron trajectories are more poorly defined, this comes at the expense of a poorer momentum resolution.

In principle, given a particular point in $(\mathbf{Q}, \omega)$-space, there is still a degree of freedom in choosing E_i (or E_f). In practice, however, this choice is limited to a set of discrete values. These are the neutron energies at which particular filters are most effective at removing higher-order neutrons. Bragg reflection at the monochromator or analyzer crystal allows the reflection of neutrons at the fundamental wavelength λ, but also at $\lambda/2$, $\lambda/3$, etc. (corresponding to energies of $4E$, $9E$, etc.) Filters are used to remove this higher-order contamination, and they are effective only in certain ranges of energy. The most common energies are 5 meV (with a beryllium filter), 13.7 meV, 14.7 meV, 30.5 meV, and 41.0 meV (with a pyrolytic graphite filter). In an inelastic experiment, there is still a choice of placing the filter before or after the sample (i.e., fixing E_i or E_f to one of these values).

A neutron monitor is a device placed at the opening of the beam tube (between the monochromator and the sample) that measures the flux of neutrons. The count rate at the detector is normalized to the monitor rate so that a change in the flux of incident neutrons does not introduce any systematic errors. The flux of neutrons from a reactor is dependably constant; rather, the changes in flux occur when changing the incident energy. The contribution from higher-order neutrons changes as well, and thus when changing E_i, one must apply a correction factor that has been previously determined for the spectrometer.

The efficiency of the monitor is proportional to $1/k_i$.[37] This actually cancels the factor of $1/k_i$ in the scattering cross section. Therefore, in an experiment with k_f (and E_f) fixed, the factor k_f/k_i can be ignored, and the measurement is directly proportional to the scattering function $S(\mathbf{Q}, \omega)$ (see Appendix B). In an inelastic magnetic neutron scattering measurement, dividing by the Bose factor $(n+1)$ yields a value that can be plotted as the dynamic susceptibility $\chi''(\mathbf{Q}, \omega)$ in "arbitrary units," albeit still convolved with the spectrometer resolution function.

[37] This is stated, but never attributed, in [47].

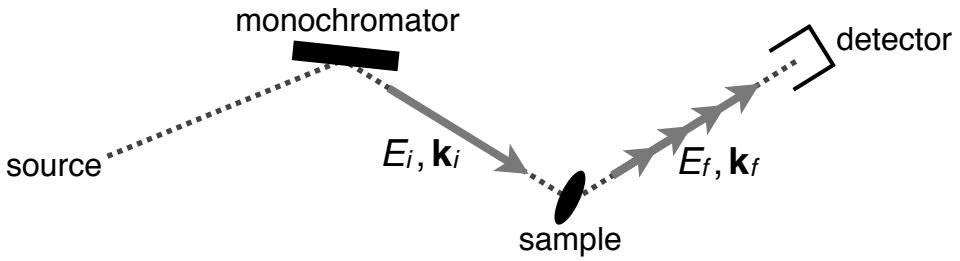

Figure 2.20: Illustration of the basic components of a two-axis instrument. Unlike a triple-axis spectrometer, the detector collects neutrons of all final energies.

2.4.3 Two-axis energy integration

A simpler instrument and a predecessor of the triple-axis spectrometer is the two-axis instrument, illustrated in Figure 2.20, in which the detector counts neutrons with all final energies. Two-axis instruments measure the energy-integrated cross section $\frac{d\sigma}{d\Omega}$, and are still used in modern times in the form of neutron diffractometers (usually with an array of detectors) to determine crystal structures from the pattern of Bragg reflections. A rarer use of a two-axis setup is the energy integration method described here. With a two-axis instrument, energy integration takes place automatically, of course, but usually along with a meaningless integration over $\mathbf{Q}$. This can be avoided in the special case of low-dimensional magnetism [54].

Although the magnetically ordered state of the cuprates extends in three dimensions, the magnetic coupling between planes is much weaker than the coupling within the planes. Thus in the disordered state (at high temperatures or at high carrier doping), the magnetism is two-dimensional. In $\mathbf{Q}$-space, this means that the magnetic signal is largely independent of ℓ.[38] In the two-axis energy integration method, the scattering plane is $(hh\ell)$ and $\mathbf{k}_f$ is aligned parallel to the c-axis, so that all of the detected neutrons have the same in-plane momentum transfer. This is illustrated in Figure 2.21.

In practice, two-axis measurements are performed on a triple-axis instrument. The instrument is put into "two-axis mode" by removing the analyzer,[39] fixing the

[38] Excepting the relatively slowly-varying magnetic form factor $f(\mathbf{Q})$.

[39] Equivalently, the analyzer can be rotated to be perpendicular to the beam; the analyzer crystal is usually thin enough to be effectively transparent.

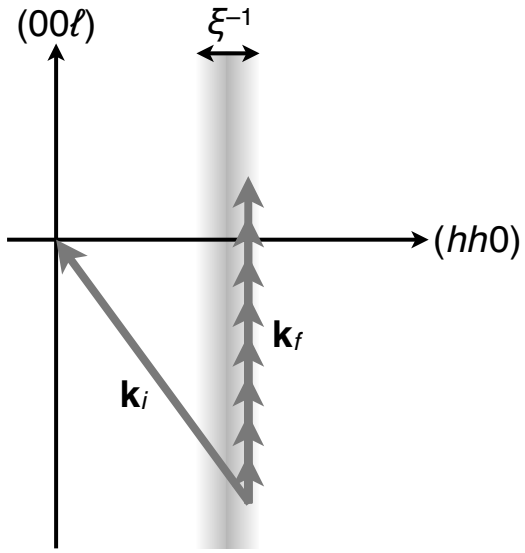

Figure 2.21: **Q**-space diagram illustrating the two-axis energy integration method for a two-dimensional magnetic system.

detector arm parallel to the analyzer arm, and removing the collimator between the analyzer and detector. Because all final energies are desired, there must be no filter after the sample. The two-axis scans are performed by instructing the instrument to perform a certain "elastic" scan in **Q**-space. Given the desired in-plane momentum, the ℓ value of **Q** is calculated so that $\mathbf{k}_f$ is properly parallel to the c-axis for the whole scan.[40]

The energy-integration aims to measure the instantaneous (equal-time) scattering function:

$$S_{\text{inst}}(\mathbf{Q}_{2D}) = \int S(\mathbf{Q}_{2D}, \omega)\, d\omega\,. \tag{2.22}$$

In practice, the integration ranges from $\omega = 0$ to $\omega = E_i$, so E_i must be large

[40]The formula is

$$\ell = \tfrac{1}{c^*}(k_i - \sqrt{k_i^2 - a^{*2}h^2})\,,$$

where $a^* = 2\pi/(a\sqrt{2})$ and $c^* = 2\pi/c$ are the reciprocal lattice vectors along $(hh0)$ and (00ℓ). Because this trajectory in **Q**-space is curved, and because the computer software controlling the instrument is typically limited to straight scans in **Q**-space, the trajectory is usually divided into multiple segments.

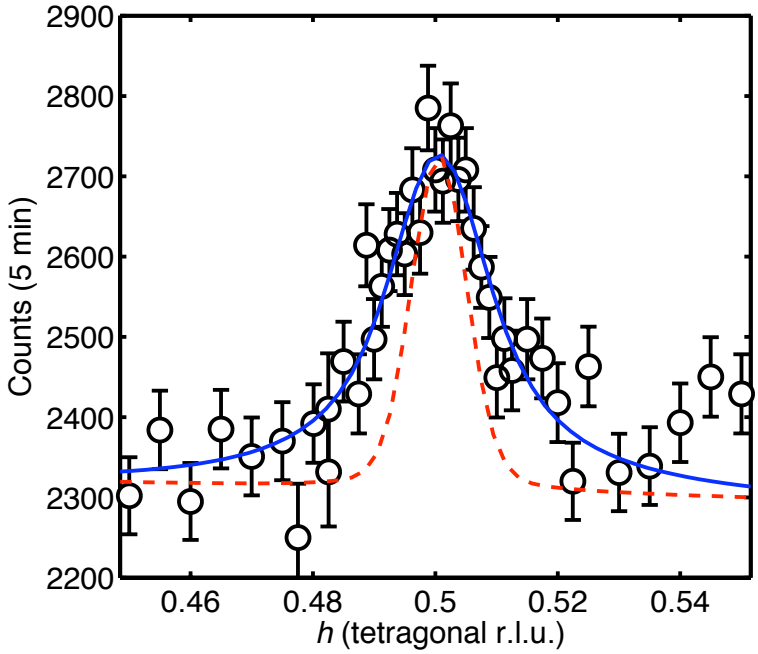

Figure 2.22: Example of two-axis data, from a measurement of NCCO with $x = 0.118$ at a temperature of $T = 220\,\mathrm{K}$. The data are fit (solid curve) to a two-dimensional Lorentzian (2.23) convolved with the instrument resolution (dashed curve). The fit yields a correlation length value of $\xi/a = 23 \pm 6$.

enough to cover the relevant dynamic range.[41] This range is smallest (and thus the measurements most accurate) near a continuous phase transition to long-range magnetic order. The measurements described in Chapter 3 were made using $E_i = 14.7\,\mathrm{meV}$. One can check whether this E_i is sufficiently high by repeating some measurements at higher E_i. This test has been performed on La_2CuO_4 [55] and the system $La_2Cu_{1-z}(Zn,Mg)_zO_4$ [56] (described in Section 3.1.2), but was not repeated for NCCO.[42]

Quantitative measurements must, of course, include the effects of the instrument

[41] At finite temperatures, scattering from negative ω is included. The integral can be considered to be over $\omega = 0$ to $\omega = E_i$ with the (combined) population factor $2n + 1$ in the integrand. The effects of temperature and instrument resolution on the integration are discussed in Section A.3.

[42] For $x < x_c$ (see Chapter 3), there is good reason to believe that $E_i = 14.7\,\mathrm{meV}$ yields a good estimate of the instantaneous correlation length. Similar to La_2CuO_4 [55] and $La_2Cu_{1-z}(Zn,Mg)_zO_4$ [56], the system approaches a second-order transition to antiferromagnetic order. For $x > x_c$, further measurements with larger E_i are, in principle, desirable for a more quantitative result.

resolution. The resolution function calculations are different from the triple-axis case and are discussed in Appendix C. The focus of Chapter 3 will be the measurement of the instantaneous antiferromagnetic correlation length ξ. The two-axis data are fit to the instrument resolution convolved with a two-dimensional Lorentzian

$$S_{\text{inst}}(\mathbf{q}_{\text{2D}}) = \frac{S(0)}{1 + q_{\text{2D}}^2 \xi^2} = \frac{A}{q_{\text{2D}}^2 + 1/\xi^2}\,, \tag{2.23}$$

where $q_{\text{2D}} = |\mathbf{q}_{\text{2D}}|$ is the planar distance in reciprocal space from the center of the signal at the antiferromagnetic wavevector $(\frac{1}{2}, \frac{1}{2})$. Example data from a two-axis measurement are shown in Fig. 2.22.

While energy-dependence information is lost, a major advantage of the two-axis measurement is the significantly improved counting rate. Meaningful data can be collected even on older instruments with lower flux at which inelastic measurements are not feasible. By using tight collimations, the **Q**-space resolution is significantly better than for triple-axis scans. The technique has been used on two-dimensional magnetic systems as far back as 1971 [54].

2.5 μSR

Muon spin relaxation/rotation/resonance[43] (μSR) is a technique that probes the internal magnetic field of a sample using the magnetic moment of muons. At a μSR facility, a beam of spin-polarized muons is incident on a sample. A muon that comes to rest inside the sample will precess in response to the local magnetic field before decaying with a lifetime of 2.2 μs. Because the decay products of the muon are directed preferentially with respect to its spin, the final spin direction can be inferred statistically from the detection of the decay.

Polarization of the muons occurs during their production. A beam of high-energy ($\sim$ 500 MeV) protons hits low-Z nuclei such as those of carbon or beryllium;

[43]The mnemonic acronym μSR was coined in 1974, and was intended to evoke an association with nuclear magnetic resonance (NMR) and electron spin resonance (ESR); the term is used in any situation where the muon magnetic moment is used to probe matter [57].

one of the possible results is the production of a positive pion (π^+) that is nearly at rest.[44] This decays after 26 ns into a positive muon (μ^+) and a neutrino. These muons are emitted isotropically with a relatively low kinetic energy of 4.1 MeV,[45] and because of maximal parity violation, they all have their spins polarized opposite to their momentum [57].

When a positive muon decays at rest (e.g., inside the sample), it decays into a positron (e^+) and two neutrinos. Again because of parity violation, the positron preferentially decays in the direction of muon spin polarization with an angular distribution of

$$W(E, \theta) = 1 + a(E)\cos(\theta)\,, \tag{2.24}$$

where θ is the angle of the positron direction with respect to the muon spin direction, and a is an asymmetry parameter that depends on the positron energy E. When all positron energies are sampled, the effective value is $a = \frac{1}{3}$.

In a typical setup, the muon polarization is along the beam direction, and two positron detectors are placed forward (F) and backward (B) of the sample to statistically determine the final muon spin direction projected along the initial spin direction. The raw asymmetry is calculated as $(B - F)/(B + F)$ and is plotted versus time of decay. Because the muon starts out polarized towards the backward detector, the asymmetry signal is a maximum at $t = 0$ and decays in different ways at later times depending on the magnetic field environment at the muon site(s).[46] Generally speaking, if there is a static magnetic field of the same strength and direction at each muon site (e.g., in a magnetically ordered system), the muons precess, and the asymmetry signal oscillates like

$$A(t) \propto e^{-\lambda t}\cos(\omega t + \phi)\,, \tag{2.25}$$

where ω is the oscillation frequency (proportional to the internal magnetic field)

[44] Among the other possibilities are the production of negative pions, which are immediately captured by the nuclei, or pions that are not at rest, which do not decay into 100% polarized mono-energetic muons.

[45] Whereas the rest mass of the muon is 106 MeV.

[46] Calculations can estimate the location of the muon site in the crystal lattice. Interpretation of data can become more complicated when there is more than one muon site.

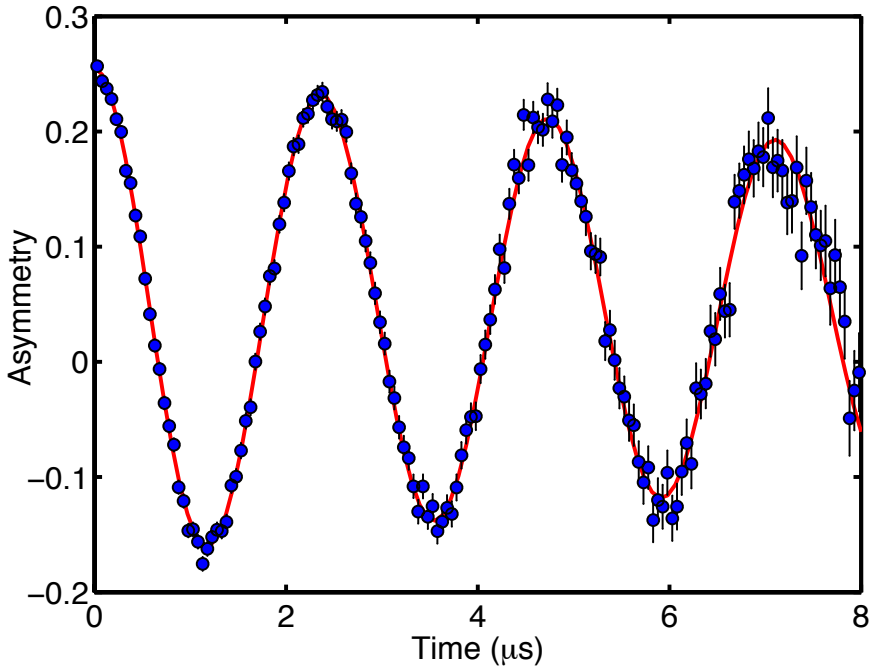

Figure 2.23: Example μSR data for a sample of NCCO with $x = 0.123$ in a weak transverse field of 40 G at $T = 175$ K. In such a setup the muon spins precess with maximal amplitude.

and λ is the decay rate of the envelope. If the magnetic field at the muon sites is randomly fluctuating, such as in a paramagnetic state, the signal relaxes like

$$A(t) \propto e^{-\lambda t}\,, \tag{2.26}$$

where λ is the relaxation rate.[47] The muon signal decays faster (with a larger relaxation rate) in a more slowly fluctuating internal magnetic field. If there are multiple behaviors, the signals simply add.

The total muon asymmetry can be calibrated by applying a weak transverse field at high temperatures (in the paramagnetic state of the sample). Such a field causes maximal precession of the muons, and in the paramagnetic state the envelope of the oscillation decays very slowly. An example of such a measurement is shown in

[47] There is, of course, room for much more sophisticated analysis. I am not familiar enough with μSR to provide any more details, but nothing further is needed for our current limited data.

Figure 2.23. Fitting the data to (2.25) plus a constant yields values for the maximal asymmetry and for the baseline (i.e., the asymmetry value for unpolarized muons).

For the measurements of NCCO samples described in Section 3.2.3, the Néel temperature was determined using both zero-field and longitudinal-field measurements. In the zero-field case, the data above the ordering temperature behave like (2.26) and the data below the ordering temperature behave like (2.25). In general, the data are fit to a sum of the two behaviors. A plot of the rotation frequency in (2.25) as function of temperature is then similar to the order parameter measurement using elastic neutron scattering (see Section 3.2.1).

In longitudinal-field measurements, a magnetic field is applied along the original direction of muon polarization. Such a field does not cause precession of the muon spins and overwhelms any smaller static field caused by magnetic order that would otherwise cause precession. A longitudinal field does not, however, affect the relaxation due to internal magnetic field fluctuations. Plotting the relaxation rate λ as a function of temperature then yields a peak at the transition temperature: at low temperatures the relaxation rate is low because the magnetic system is ordered, whereas at high temperatures the relaxation rate is low because the magnetic system fluctuates very quickly. This measurement of λ is similar to $1/T_1$, where T_1 is the spin-lattice relaxation time in nuclear magnetic resonance (NMR) terminology.

While μSR lacks the momentum information of neutron scattering, it is sensitive to much longer timescales. As a rough illustration, consider that, while a typical elastic neutron scattering measurement has an energy resolution on the order of 1 meV ($\sim$ 0.1 THz), the μSR timescale is set by the muon decay rate of 2.2 μs ($\sim$ MHz), which is five orders of magnitude longer. Consequently, something that appears to be static in a neutron scattering measurement may be revealed as fluctuating using μSR. In particular, the magnetic ordering temperature according to μSR can be lower than that measured by "elastic" neutron scattering (see Section 3.2.3).

Another difference between the techniques is that μSR is a probe sensitive to a different set of behaviors in the same sample, whereas neutron scattering can only measure the average behavior. For instance, the magnitude of an oscillating signal

(calibrated using the weak transverse field data) can measure the magnetically ordered volume fraction of a sample.

Chapter 3

Magnetic correlations in NCCO

In this Chapter, the two-axis neutron scattering technique is used to map out the magnetic correlations in NCCO as a function of temperature and Ce concentration. I find that there is no genuine overlap between long-range magnetic order and superconductivity in NCCO.[1] Theoretical background and previous two-axis neutron scattering results are discussed in Section 3.1. Section 3.2 contains the results of my experiments, and is followed by a discussion of the results in Section 3.3.

3.1 Background

3.1.1 Quantum nonlinear sigma model

In this Chapter, I use a theoretical result for the temperature dependence of the antiferromagnetic correlation length (3.2). Although this equation is not derived here, it is instructive to discuss the context in which the theory was developed.

Soon after the high-T_c cuprates were discovered, there was intense interest to understand the magnetism of these complex materials, starting from the Mott-insulator parent compounds. In particular, the theoretical effort centered around the Heisenberg model (Equation 1.2), with spin $S = \frac{1}{2}$, on a two-dimensional square

[1] While this Chapter is largely based on [19], I show newer data collected on higher-quality samples (see Section 2.3.2).

lattice. Although the parent compounds are known to have antiferromagnetically ordered ground states (Section 1.2.3), there is no obvious reason that the ground state of the two-dimensional model should be ordered.[2]

The quantum nonlinear sigma model (QNLσM) was developed to derive the static and dynamic properties of the spin-$\frac{1}{2}$ Heisenberg antiferromagnet based on the assumption of long-range order at $T = 0$ [58]. The derived properties were found to agree well with neutron scattering results on La_2CuO_4 [59], lending confidence to the initial assumption of a long-range ordered ground state. The consensus now is that the spin-1/2 Heisenberg model on a square lattice does indeed have robust magnetic order at $T = 0$, although there is yet to be a rigorous proof [60].

The QNLσM is the simplest effective continuum model describing the long-wavelength dynamics of a lattice Heisenberg model [58]. A microscopic derivation exists in the semiclassical limit $S \to \infty$ [61], but the parameters of the model are difficult to determine for smaller S. The two parameters of the theory are the spin stiffness[3] ρ_s and the spin-wave velocity c_s, and these are treated as phenomenological input parameters determined from fits to experiments and simulations.[4]

Renormalization-group analysis leads directly to an exponentially diverging

[2]The ground state of any Heisenberg antiferromagnet is non-trivial (unlike, e.g., for the Ising model, which has a discrete order parameter). In particular, the state with full staggered magnetization cannot be the ground state, since it is not an eigenstate of the Hamiltonian. Generally, one says that the staggered moment is affected by quantum fluctuations [58], and a spin-$\frac{1}{2}$ system exhibits the strongest fluctuations.

[3]The spin stiffness is the energy cost (per spin) of introducing a twist of θ between neighboring rows in the ground state. It is defined as [62]

$$\rho_s = \frac{1}{N} \left. \frac{d^2 E_0(\theta)}{d\theta^2} \right|_{\theta=0},$$

where E_0 is the energy of the ground state and N is the number of spins. In the limit of large S, $\rho_s = JS^2$ [58]. The spin stiffness is positive for a long-range ordered system and zero in the absence of long-range order.

[4]Note that since there are two independent parameters J and S in the lattice model, there are two independent parameters ρ_s and c_s in the corresponding low-temperature continuum model. These two values have been calculated in terms of J and a from numerical simulations in the special case of the spin-$\frac{1}{2}$ nearest-neighbor Heisenberg antiferromagnet (see, e.g., [63]).

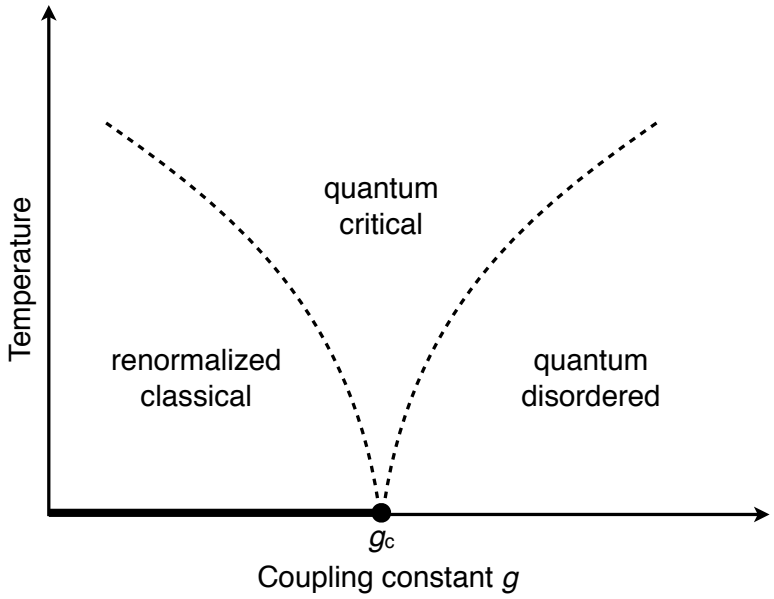

Figure 3.1: Phase diagram of the quantum nonlinear sigma model as a function of temperature and coupling parameter g. The correlation length ξ behaves differently in the three regimes, as discussed in the text. The thick line indicates antiferromagnetic order at $T = 0$.

correlation length as a function of temperature in the $T \to 0$ limit [58]:[5]

$$\xi(T) = C_\xi a e^{2\pi\rho_s/k_B T}\,, \tag{3.1}$$

where a is the lattice spacing and C_ξ is a dimensionless constant that depends on the choice of the system. This relation is for the case in which there is assumed to be long-range order at $T = 0$ (the "renormalized classical" regime). At large enough values of the dimensionless coupling constant $g \sim \hbar c_s/a\rho_s$, there is a "quantum disordered" regime in which quantum fluctuations prevent order even at $T = 0$. In this case the result is that the correlation length ξ approaches a finite value as $T \to 0$ [58]. At $T = 0$, these two regimes are separated by a quantum critical point; at the critical coupling g_c, the correlation length is expected to have a power-law dependence of $\xi \propto T^{-1}$ [58]. Close to g_c the correlation length crosses over between

[5]This equation is the result of two-loop renormalization-group equations, whereas earlier one-loop results [64] led to an incorrect $1/T$ prefactor.

the different behaviors as a function of temperature. Figure 3.1 illustrates these three regimes of the phase diagram.

The relation (3.1) has been extended [65] to

$$\xi(T) = \frac{e}{8}\frac{\hbar c_s}{2\pi\rho_s}\left[1 - \frac{T}{4\pi\rho_s} + O(T^2)\right] e^{2\pi\rho_s/k_B T}, \tag{3.2}$$

where the constant C_ξ from (3.1) has been calculated, and an $O(T)$ correction has been added. Further calculations [66] include such effects as the discreteness of the lattice, but the data quality on NCCO presented in this Thesis does not justify the use of these more sophisticated equations.

Before beginning the discussion of experimental results, note that the above theory deals with a completely two-dimensional system. According to the Mermin-Wagner theorem [67], it is impossible for a two-dimensional system with a continuous order parameter to have a symmetry-breaking transition (such as for antiferromagnetic order) at a non-zero temperature. The undoped cuprates, on the other hand, show three-dimensional magnetic order around $T_N \sim 300\,\mathrm{K}$. In most cases,[6] the tetragonal symmetry and body-centered arrangement of the system causes a frustration of the interplanar coupling; in Nd_2CuO_4 the exchange interaction between adjacent CuO_2 planes is as low as $J' \sim 10^{-8}J$ [50]. This is too small to explain the observed transition to three-dimensional order; the mechanism instead starts with the XY anisotropy[7] of about 10^{-4} that exists in the systems due to spin-orbit coupling. As the temperature is lowered, this anisotropy leads to a cross-over from two-dimensional Heisenberg to two-dimensional XY correlations. This allows for a Kosterlitz-Thouless transition [68] (a non-symmetry-breaking order), in which

[6] In La_2CuO_4, an orthorhombic distortion of the lattice breaks the tetragonal symmetry, partially lifting the interplanar frustration. This allows an effective exchange interaction of $J' \sim 10^{-5}J$ between adjacent CuO_2 planes.

[7] The Hamiltonian for the Heisenberg system (1.2) can be written as

$$H = \sum_{\langle i,j\rangle}\left(J_x S_i^x S_j^x + J_y S_i^y S_j^y + J_z S_i^z S_j^z\right),$$

where $J_x = J_y = J_z = J$. In the case of XY anisotropy, $J_x = J_y = J_{XY} > J_z$. As the temperature is lowered in such a system, the correlations become more and more like those of a pure XY system, in which the spins directions are restricted to the xy-plane.

the planar correlation length begins to diverge [50, 69]; when this length becomes large enough, the (otherwise weak) interplanar coupling causes three-dimensional order to take over. Despite this mechanism for three-dimensional order, the results of the two-dimensional QNLσM are robust outside the narrow regime of XY criticality, as evidenced by the good agreement with experimental data on La_2CuO_4 [64] and $Sr_2CuO_2Cl_2$ [70].[8]

3.1.2 Site-diluted antiferromagnet

The comparison of the QNLσM with experimental data was extended to the case of the site dilution of the spins [56, 72]. The site-diluted nearest-neighbor Heisenberg model is given by

$$H = J \sum_{\langle i,j \rangle} p_i p_j \, \mathbf{S}_i \cdot \mathbf{S}_j \,, \tag{3.3}$$

where $p = 1$ on magnetic sites and $p = 0$ on nonmagnetic sites (with concentration z). In the absence of quantum fluctuations, random dilution causes long-ranger order to disappear above the percolation threshold $z_p \approx 41\%$: there is a "geometric" transition from an infinite cluster of nearest-neighbor interactions to unconnected finite clusters. Until the publication of [72], it was unclear if the strong effects of quantum fluctuations in the case of $S = \frac{1}{2}$ might shift the phase transition to a dilution concentration smaller than z_p.

The experimental realization of the spin-$\frac{1}{2}$ site-diluted Heisenberg antiferromagnet was $La_2Cu_{1-z}(Zn,Mg)_zO_4$ (LCZMO), i.e., the parent compound La_2CuO_4 with spin-$\frac{1}{2}$ Cu^{2+} ions replaced by non-magnetic Zn^{2+} and Mg^{2+} ions. Because Zn^{2+} and Mg^{2+} have ionic radii that are larger and smaller than Cu^{2+}, respectively, it was possible to grow crystals with large values of z, in particular to values above z_p. Measurements of the Néel temperature revealed that long-range order persists all the way to a $z = 39\%$ sample, indicating that the quantum fluctuations in the

[8] Note that (3.1) and (3.2) only hold in the limit $T \to 0$. At experimentally accessible temperatures (i.e., above T_N) the equations do not agree with experimental data for $S > \frac{1}{2}$ (e.g., $S = \frac{5}{2}$ [71]). Calculations have shown that quantitative agreement truly occurs only at much lower temperatures, and that the good agreement for $S = \frac{1}{2}$ at the measured temperatures is somewhat coincidental [63].

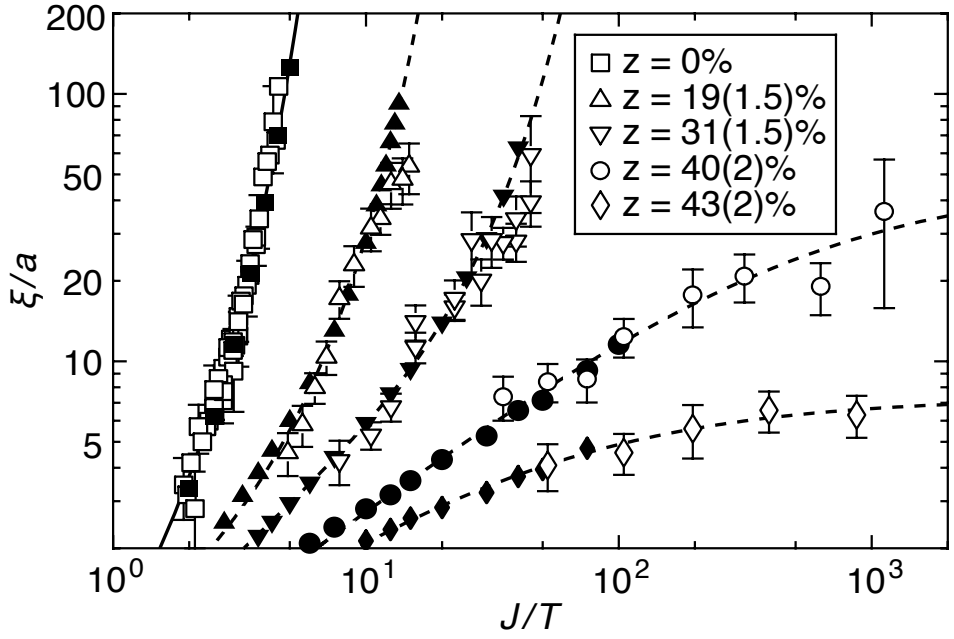

Figure 3.2: Log-log plot of correlation length ξ (in units of the planar lattice constant a) versus inverse temperature J/T for LCZMO, where $J = 135\,\text{meV} \approx 1570\,\text{K}$ is the value for undoped La_2CuO_4. The open symbols are data from neutron scattering, and filled symbols are from Monte Carlo simulations of (3.3). The curves are fits to (3.4) for $z < z_p$ and (3.5) for $z > z_p$. Adapted from [56].

system do not noticeably shift the location of the percolation transition.

Above the Néel temperature of each sample, the two-axis energy-integrating technique was used to measure the correlation length $\xi(z, T)$ (see Section 2.4.3). At lower dilution concentration z, $\xi(T)$ effectively follows the form (3.2) of the renormalized classical regime, despite the fact that the random dilution breaks the translational symmetry that exists in the QNLσM.[9] At higher z, near the percolation threshold, the correlation length shows power-law behavior, indicating a critical regime. The data for $z > 30\%$ were best fit to the heuristic cross-over form [56]

$$\xi(T) = \frac{e}{8}\frac{c_s}{2\pi\rho_s}\frac{e^{2\pi\rho_s/T}}{1 + (4\pi\rho_s/T)^{-\nu_T}}\,, \tag{3.4}$$

[9]The parameters c_s and ρ_s were estimated from fits of $\xi(T)$ to (3.2).

where ν_T is the power-law exponent. Finally, for $z > z_p$, the correlation length was found to be finite at low temperatures, as expected, since the magnetic system is broken up into finite-sized clusters. The data for $z > z_p$ were fit to the heuristic form

$$\frac{1}{\xi(z,T)} = \frac{1}{\xi_0(z)} + \frac{1}{\xi_T(T)}, \tag{3.5}$$

where ξ_0 is the $T = 0$ value and $\xi_T \propto T^{-\nu_T}$ is the high-temperature power-law behavior. The model nature of LCZMO is apparent from the good agreement between the experiment and quantum Monte Carlo simulations of (3.3) (see Figure 3.2).

3.1.3 As-grown NCCO

While the randomly site-diluted Heisenberg antiferromagnet can be studied experimentally by measuring LCZMO, it does not have any direct relevance to the magnetism of hole-doped cuprates: as discussed in Chapter 1, doped holes reside on the O $2p$ orbitals, introducing frustration and changing the magnetic nature of the system. On the other hand, doped electrons tend to reside on the Cu ions; this changes them to a full $3d^{10}$ configuration and renders them non-magnetic (to a first approximation). Thus the electron-doped cuprates are somewhat similar to the site-diluted antiferromagnet, with a rough correspondence between the dilution concentration and the electron concentration. The main difference is that the electrons (and thus the non-magnetic sites) are not static, but itinerant.

A comparison between neutron scattering results of as-grown NCCO and Monte Carlo simulations of the site-diluted Heisenberg model was made by Mang *et al.* [14]. Unlike the oxygen-reduced NCCO discussed throughout most of this Thesis, as-grown NCCO does not superconduct at any attainable Ce concentration, and the antiferromagnetic phase extends across the entire doping range ($0 \leq x \leq 0.18$).

Two-axis measurements (Section 2.4.3) of the correlation length were performed above the Néel temperature of each sample. The temperature dependence $\xi(T)$ was found to be well described by the exponential form (3.1). Moreover, it was found that there is good agreement between the experiment and Monte Carlo simulations of the site-diluted model (3.3) [14]. In the simulations, quantitative

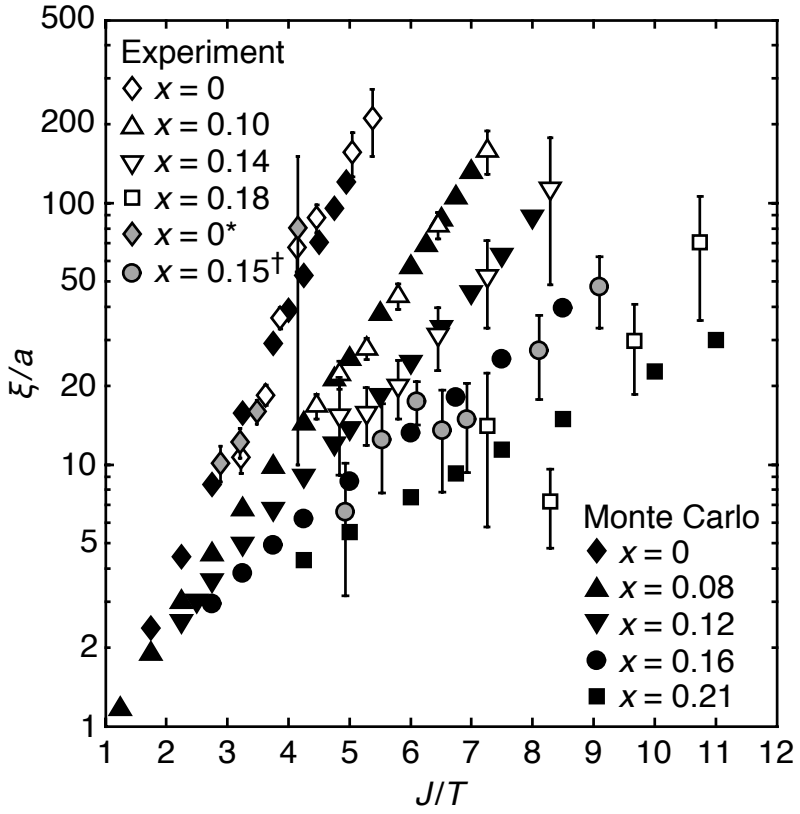

Figure 3.3: Antiferromagnetic correlation length ξ (in units of the planar lattice constant a) as a function of inverse temperature J/T for as-grown NCCO (open symbols) and from Monte Carlo simulations of the randomly site-diluted Heisenberg model (3.3) (filled symbols), where $J = 125\,\text{meV} = 1450\,\text{K}$. Adapted from [14] (* data from [73]; † data from [15]).

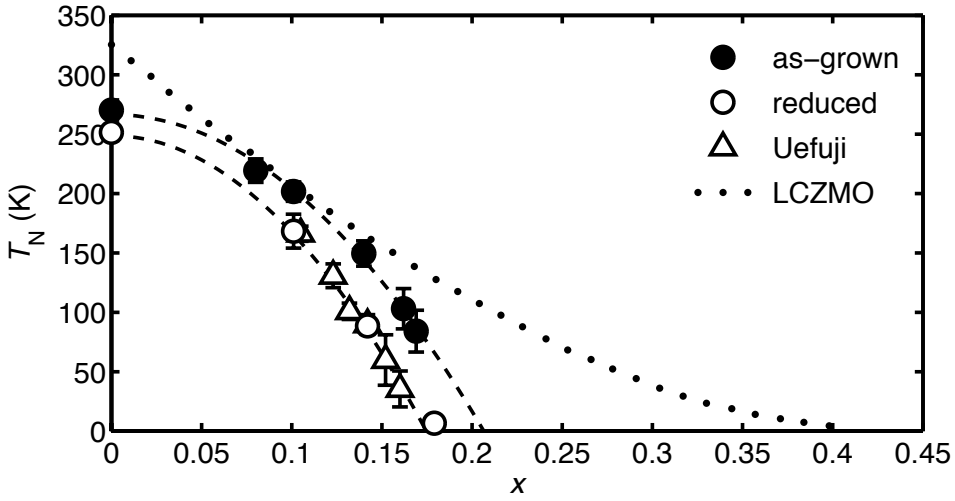

Figure 3.4: Néel temperature T_N of NCCO as a function of (nominal) electron concentration x. Filled and open circles show T_N of as-grown and reduced NCCO, respectively [14]. Open triangles show T_N measured by neutron scattering by Uefuji *et al.* [20]. The dotted curve indicates the Néel temperature in the site-diluted antiferromagnet LCZMO [72]. Adapted from [14].

agreement was found when the dilution concentration differed slightly from the electron concentration x, and the antiferromagnetic superexchange constant was set to the value $J = 125\,\text{meV}$ of the undoped system [14] (see Figure 3.3). The correlation length ξ measured by the energy-integrating method is, of course, an instantaneous (equal-time) property. As described above, when viewed at any instant, the magnetism should resemble a system with static site dilution. Thus, for this observable, there are no significant effects due to the itinerancy of the electrons within the accessible doping range.

The itinerancy of the electrons has more pronounced effects on the Néel temperature and the ordered moment, which are both static ($t \to \infty$) properties. The Néel temperature $T_N(x)$ of as-grown NCCO approximately follows a parabolic form, extrapolating to zero around $x \approx 0.21$ [14] (see Figure 3.4). The concave doping dependence contrasts the convex dependence in LCZMO, where T_N only reaches zero at the percolation threshold $z \approx 0.41$ [72].

The ordered moment also decreases rapidly with doping and, consistent with

the behavior of $T_N(x)$, approaches zero much more rapidly than the case of random dilution [14]. Because the ordered moment is a measure of the strength of the magnetic order at long times, it is clearly more sensitive to the difference between quenched dilution and itinerant electrons.

Having measured these magnetic properties of as-grown NCCO, performing similar measurements in oxygen-reduced NCCO (where superconductivity appears) is the natural next step.

3.2 Results

In Section 3.2.1, I present the measurements performed on the static ($t \to \infty$) properties of the oxygen-reduced samples using elastic neutron scattering. Section 3.2.2 contains the results for the instantaneous ($t = 0$) magnetic correlations using the two-axis energy-integrating technique. Then, in Section 3.2.3, I show some results using the μSR technique.

The neutron-scattering measurements were performed at the NIST Center for Neutron Research (NCNR) at the Gaithersburg, Maryland, location of the National Institute of Standards and Technology (NIST), as well as at the High Flux Isotope Reactor (HFIR) at Oak Ridge National Laboratory in Oak Ridge, Tennessee. At NIST, I used the triple-axis spectrometer BT9,[10] where the typical configuration was a fixed initial energy of $E_i = 14.7\,\text{meV}$, collimations of 40′–47′–sample–20′–open, and two PG filters "on k_i" (i.e., between monochromator and sample). At HFIR, the spectrometer I used was HB-1A, which is a fixed-initial-energy spectrometer with $E_i = 14.66\,\text{meV}$. The configuration used was 48′–48′–sample–20′–open for the collimations and a PG filter on k_i. At both facilities, the scattering plane was $(hh\ell)$.

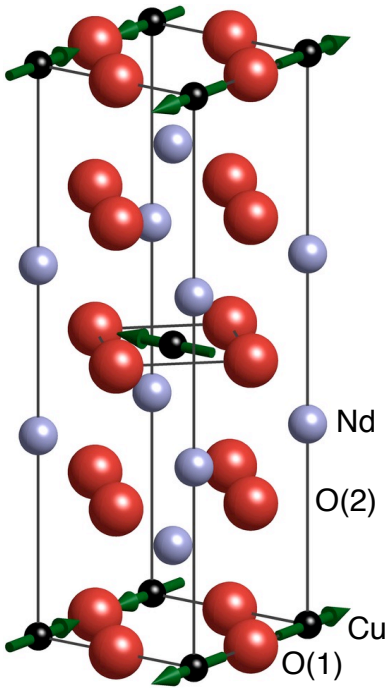

Figure 3.5: Illustration of the non-collinear Cu^{2+} spin structure found in the magnetically ordered state of NCCO. In the undoped system Nd_2CuO_4 there are two spin reorientation transitions within the ordered state. The illustrated Cu^{2+} structure is found in phase-I (75 K $< T <$ 275 K) and phase-III ($T <$ 30 K). In the phase-II structure (30 K $< T <$ 75 K) the spins are rotated by 90 degrees about the c-axis [51]. These spin reorientations are absent in the Ce-doped systems [15]. Below the Néel temperature of the Nd^{3+} subsystem ($T_N \approx 3$ K), the direction of every Nd^{3+} moment matches that of the Cu^{2+} moment directly above or below it.

3.2.1 Elastic neutron scattering

As mentioned before, the magnetic order of the Cu^{2+} moments is antiferromagnetic. This defines the preferred relative orientation of the spins with respect to each other within a single CuO_2 plane, but it does not define the actual spin orientations and, in particular, their relationship between different planes. Measurements of magnetic Bragg peak intensities (and thus of the static magnetic structure factor; see (2.15) in Section 2.4.1) have allowed the determination of the spin structure of Nd_2CuO_4

[10] A few of the oldest data sets were taken at the former triple-axis spectrometer BT2 which had very similar capabilities.

[50, 51]. The Cu^{2+} moments lie along the Cu–O–Cu bond directions, and spins in next-nearest-neighbor planes are aligned in the same pattern. The spins in the plane between these are pointed 90 degrees away in a non-collinear configuration. See Figure 3.5 for an illustration.

The magnetic structure factor is such that there is no intensity at the $(\frac{1}{2}, \frac{1}{2}, 0)$ position. The magnetic Bragg reflections typically used in the study of static magnetic properties are $(\frac{1}{2}, \frac{1}{2}, 1)$ and $(\frac{1}{2}, \frac{1}{2}, 3)$.

Néel temperature

The magnetic Bragg peak intensity is measured as a function of temperature; the intensity is zero above the Néel temperature and non-zero below the Néel temperature. Generally, physical quantities near a continuous (second-order) phase transition have power-law dependences. In this case, the relevant quantity is

$$M \propto (T_N - T)^{\beta}\,, \tag{3.6}$$

where the order parameter here is the staggered magnetization M, and β is its critical exponent. In practice, the transition can be quite rounded (e.g., due to Ce inhomogeneity), and the temperature-dependence of the Bragg peak intensity is fit to a power-law convolved with a Gaussian distribution of Néel temperatures.[11] See Figure 3.6 for some examples.

Careful measurement of the order parameter in Nd_2CuO_4 has yielded a value of $\beta = 0.27(1)$ for the exponent [37]. The values of β found in the Ce-doped samples are consistent with this result for the undoped system, and the Néel temperature values discussed in this Thesis are based on fits where β is fixed to 0.27. This is important for the larger Ce concentrations, where the transitions are very broad and β is difficult to determine independently.

The value $\beta = 0.27$ is close to the effective value $\beta_{\text{eff}} = 0.23$ shown by Bramwell and Holdsworth to be universal to physical two-dimensional XY systems [74]. The magnetic moment of an XY system decreases extremely slowly as a function of the

[11] The power-law exponent for the intensity is, of course, 2β.

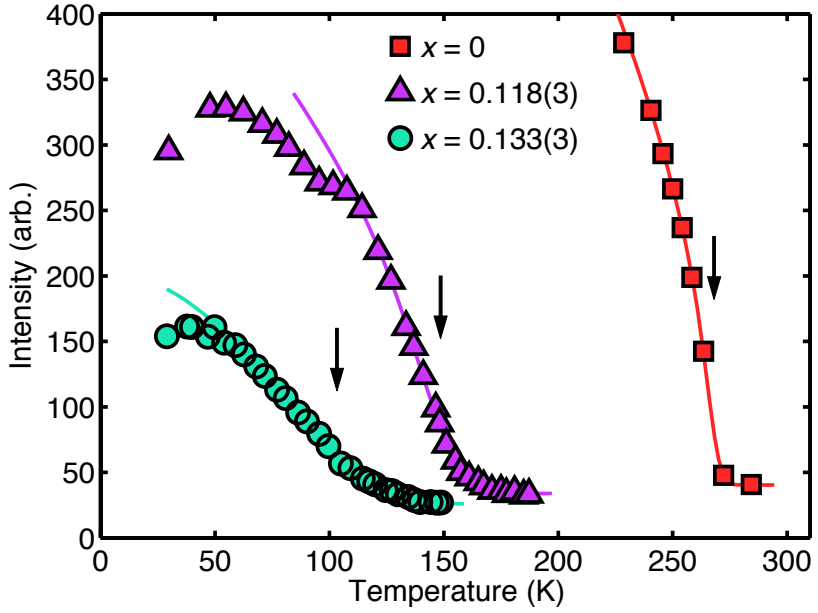

Figure 3.6: Intensity of the magnetic Bragg peak $(\frac{1}{2}, \frac{1}{2}, 1)$ as a function of temperature for representative NCCO samples. The Nd_2CuO_4 sample (labeled $x = 0$) is as-grown, whereas the two Ce-doped samples are oxygen-reduced. The $x = 0.133(3)$ sample is superconducting. The data are fit to a power-law convolved with a Gaussian to extract values for T_N (arrows) and the spread in T_N. The downturn at low temperatures is due to the effects of the Nd^{3+} moment (see Section 2.4.1). The kink seen in the $x = 0.118$ data may be from a minority volume fraction with a separate ordering temperature.

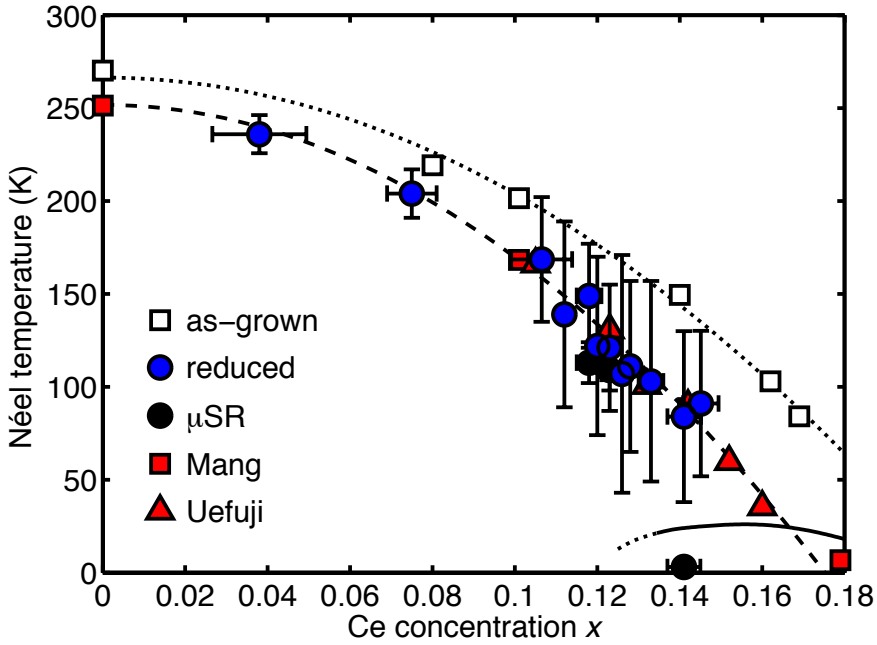

Figure 3.7: Néel temperature T_N as a function of Ce concentration for oxygen-reduced NCCO (filled circles). Horizontal error bars indicate estimated Ce inhomogeneity (see Section 2.3.2). Vertical error bars represent the 1σ spread in T_N from fits described in the text. Open and filled squares are as-grown and oxygen-reduced NCCO data, respectively, from Mang *et al.* [14]. Triangles are oxygen-reduced NCCO data from Uefuji *et al.* [20]. All data are from elastic neutron scattering measurements except the black circles, which are from μSR measurements described in Section 3.2.3. The solid curve indicates superconducting T_c in the oxygen-reduced samples.

system size, and while the magnetic moment is zero in the limit of infinite extent, it was shown that reasonably sized systems fall well within the finite realm. The calculations show that, close to the transition, the magnetization curve resembles a power-law with $\beta = 0.23$ [75]. The slightly larger experimental value of $\beta = 0.27$ lies in between this result and the value $\beta \approx 1/3$ for a three-dimensional XY system [75].

The results of fitting the order parameter in the samples I have grown are shown in Figure 3.7, along with values from the literature [14, 20]. The Néel temperature decreases steadily with x and extrapolates to zero around $x \approx 0.17$. The apparent

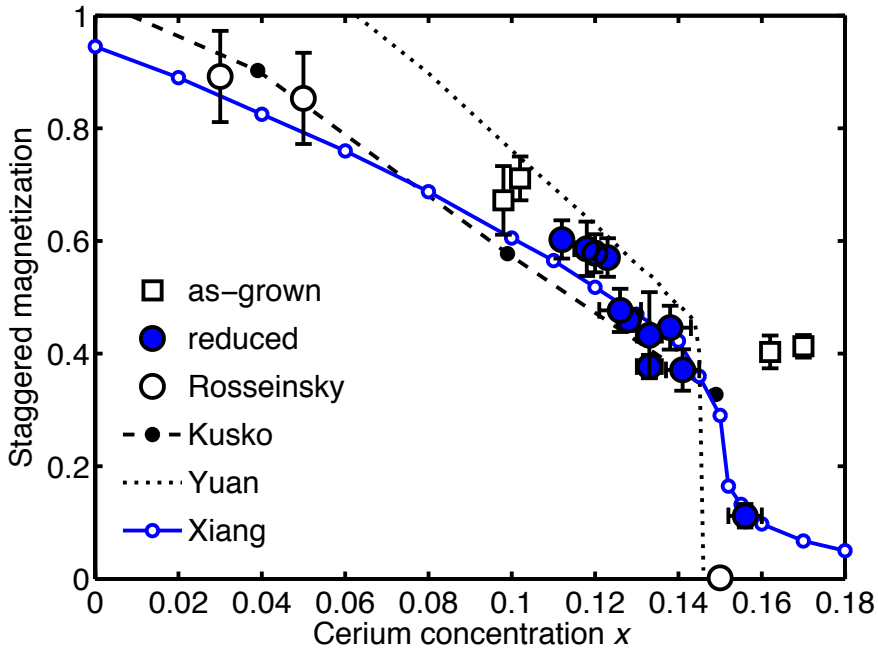

Figure 3.8: The staggered magnetization (or ordered moment strength) as a function of Ce concentration for as-grown (squares) [14] and oxygen-reduced (circles) NCCO, normalized to the $x = 0$ value. Data from Rosseinsky *et al.* [76] (open circles) are included to indicate low-x behavior. The curves indicate theoretical calculations by Kusko *et al.* [77], Yuan *et al.* [78], and Xiang *et al.* [79].

width of the Néel transition becomes larger as the Ce concentration increases, and compared with the as-grown system, the oxygen-reduced samples have values of T_N that are lower. Mang *et al.* [14] observed that the doping dependence in the reduced system resembles a rigid shift of $\Delta x \approx -0.03$ compared to the trend in the as-grown system. More recent studies [29] have shown that oxygen reduction only changes the carrier concentration by about $\Delta x \approx -0.01$, and that other effects of oxygen reduction dominate (see Section 2.2.1).

Ordered moment

Another measure of the static magnetic order is the low-temperature ordered moment.[12] As discussed above in Section 3.1.3, its doping dependence in as-grown NCCO is much steeper than in the site-diluted system. In oxygen-reduced NCCO, the ordered moment has a value similar to as-grown NCCO at lower x, but it falls to much smaller values at higher x (see Figure 3.8). Mang *et al.* [14] suggested that the approximately rigid shift $\Delta x \approx -0.03$ seen in the Néel temperatures $T_N(x)$ between as-grown and reduced samples might also apply to the ordered moment values, but the newer data presented here indicate otherwise.

Figure 3.8 also includes curves from theoretical calculations.[13] After the results of a doping dependence study in oxygen-reduced NCCO by angle-resolved photoemission spectroscopy (ARPES) were published [80], there were efforts by theorists to explain the non-trivial behavior of the Fermi surface. Kusko *et al.* [77] were able to reproduce the observed behavior using a one-band Hubbard model (t-U model) in which U changes with x. Calculation of the magnetization using their model is shown in Figure 3.8 and matches the data reasonably well. However, the low values and unphysical doping dependence of U were unexplained. The second theoretical curve in Figure 3.8 is a result by Yuan *et al.* [78], who used a t-J model to explain the ARPES data. One problem with their theory is that the antiferromagnetic superexchange J is too small to account for the large energy gap at low x. The most recent of the theories, by Xiang *et al.* [79], seems to resolve the inconsistencies of the prior calculations. They begin with a two-band model and arrive at a t-U-J model in which there is a doping-dependent effective U, and J is the true superexchange energy. The calculation of the magnetization using this model is shown in Figure 3.8. Their calculation is a mean-field one (quantum fluctuations are not taken into account), which would exaggerate the magnetization, especially at higher doping [79]. The agreement with the data point at $x = 0.156$

[12] I use the terms "ordered moment" (magnetic moment per site) and "staggered magnetization" (magnetic moment per unit volume) interchangeably.

[13] The theoretical curves are matched to the data by setting the experimental value at $x = 0$ to $M(0) = 0.4t$, following [79].

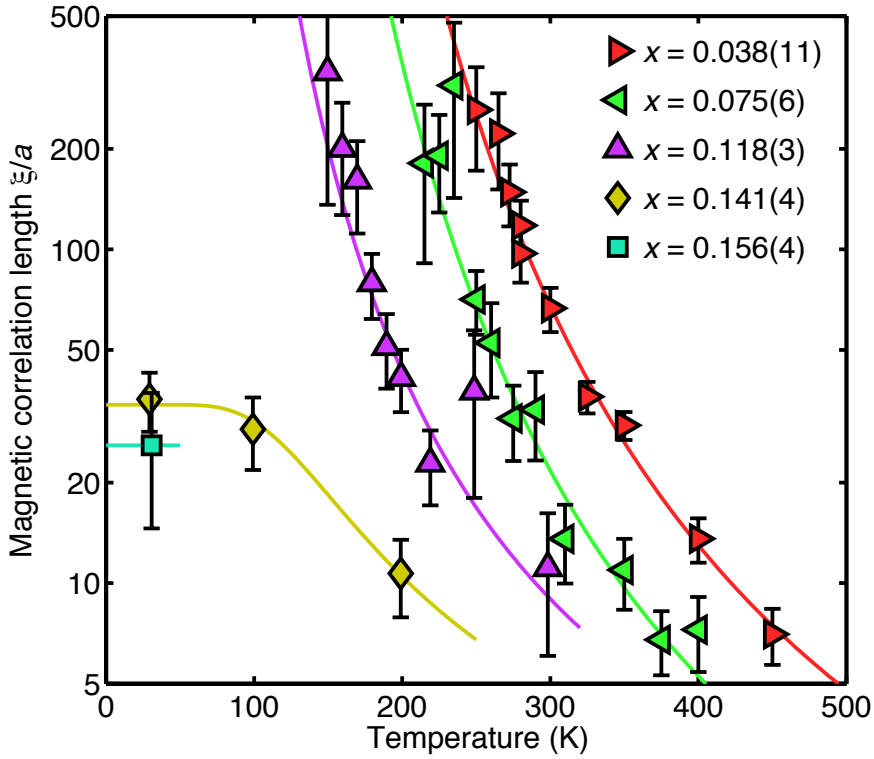

Figure 3.9: Instantaneous antiferromagnetic correlation length on a logarithmic scale as a function of temperature for representative oxygen-reduced NCCO samples across a wide range in Ce concentration x. The curves for $x \leq 0.118$ are fits to (3.2). The curves for $x \geq 0.141$ are guides to the eye.

is a coincidence, especially in light of the fact that static order disappears around $x = 0.14$, as shown in Section 3.2.3.

3.2.2 Two-axis neutron scattering

Here I discuss the measurements of the instantaneous antiferromagnetic correlation length in oxygen-reduced NCCO using the two-axis energy-integrating technique (described in Section 2.4.3). Results of these measurements were first reported in [19] and are summarized in Section A.2.1. Here I present the results from newer measurements performed on samples with better-defined Ce concentrations (see Section 2.3.2).

Figure 3.9 shows the antiferromagnetic correlation length as a function of temperature for a set of representative samples. It is clear that there are two types of behavior. The temperature dependences for $x = 0.038$, 0.075, and 0.118 are described well by the QNLσM form (3.2), and they are similar to the results for as-grown NCCO. The correlation length is very large ($\xi/a \approx 400$) at the Néel temperature obtained from elastic neutron scattering (Figure 3.7), indicating a good correspondence between the two types of measurements. However, the behavior at the two higher doping levels $x = 0.141$ and 0.156 is qualitatively different: the correlation length does not diverge and remains finite down to the lowest temperatures that were measured.[14] This is the case despite the fact that elastic neutron scattering measurements indicate magnetic order in these samples below 70–90 K. This apparent contradiction is discussed in Section 3.3.

Figure 3.10 shows the correlation length data for a representative set of samples in the region where there is a change in the temperature dependence behavior (see Section A.2.1 for data for more samples). The figure contains the data for $x = 0.118$ and $x = 0.141$ from Figure 3.9 as well as data from three samples with intermediate Ce concentration values. Of these, the data for $x = 0.126$ and $x = 0.133$ were obtained first. These two results seem to indicate that, upon cooling, the correlation length increases until the temperature reaches 100–150 K or so, and then at even lower temperatures it decreases again to match the low-temperature value for $x = 0.141$. The data for $x = 0.123$ are the most recent: the sample was selected for its well-defined Ce concentration (with a greater confidence because of its relatively small size[15]), and instead of displaying behavior between those of the $x = 0.118$ and $x = 0.126$ samples, the temperature dependence of the correlation length is, within the errors, identical to that for $x = 0.141$. This suggests that the peculiar non-monotonic behavior of the $x = 0.126$ and $x = 0.133$ samples is due

[14]The figure does not show the lowest measured temperature. In particular, it does not include measurements in the superconducting state (below $T_c \approx 25$ K), where a gap opens in the excitation spectrum (see Chapter 4). Because the momentum width at lower energies is smaller than at higher energies [81], the two-axis momentum width increases, and the length decreases. See Figure A.3 for complete data sets. See Section A.3 for simulations of two-axis measurements based on triple-axis data that show a decrease of the correlation length in the superconducting state.

[15]This is one of the reasons for the larger errors on the correlation length values.

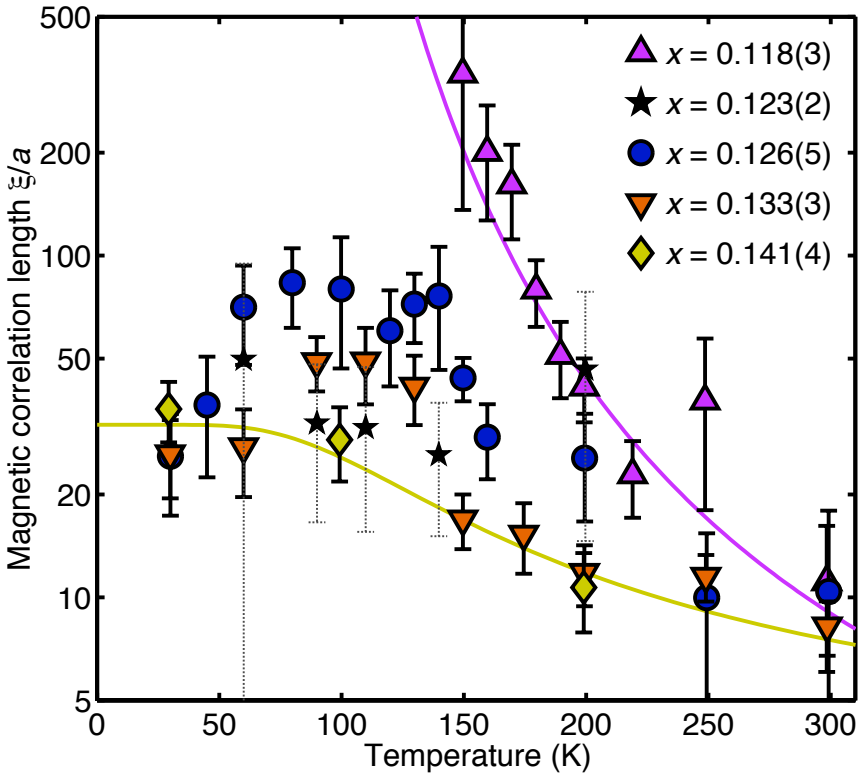

Figure 3.10: Instantaneous antiferromagnetic correlation length on a logarithmic scale as a function of temperature for representative samples in the range $0.118 \leq x \leq 0.141$. The curve for $x = 0.118$ is a fit to (3.2). The curve for $x = 0.141$ is a guide to the eye.

to their Ce inhomogeneity. Their underlying behavior is probably close to that for $x = 0.141$; note how the curve drawn for $x = 0.141$ neatly passes through most of the data for $x = 0.133$ and the high- and low-temperature data for $x = 0.126$. The departure from this $x = 0.141$ behavior may be due to minority volume fractions that have lower Ce concentrations and behave qualitatively like the $x = 0.118$ sample. The anomalous increase in the correlation length occurs at intermediate temperatures because the signal from these minority fractions is strongest at these temperatures (see Section A.2.2 for a discussion). All of this suggests that the change of behavior from long-range to short-range correlations occurs in a very narrow Ce concentration range of $x_c = 0.119(2)$.

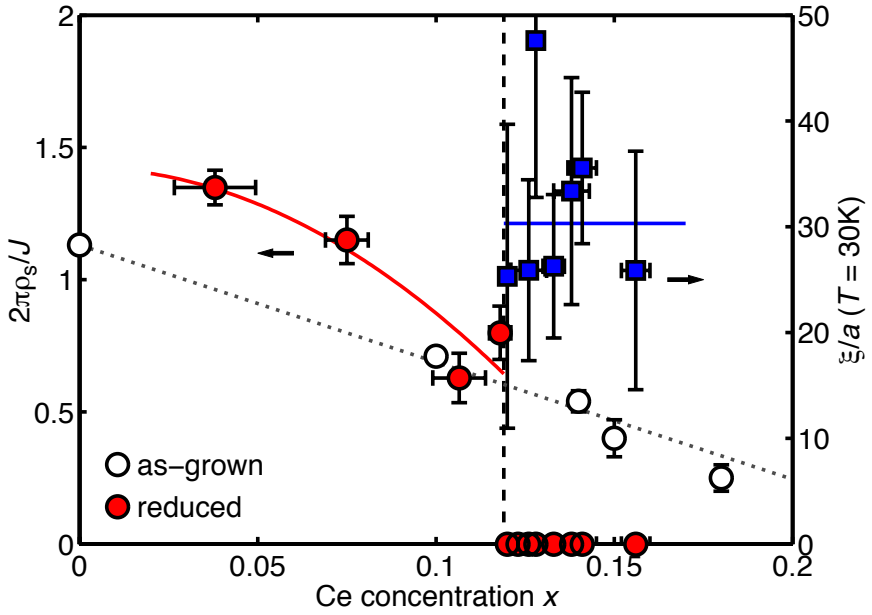

Figure 3.11: The spin stiffness, plotted as the quantity $2\pi\rho_s/J$ (where $J = 125\,\text{meV}$ is the antiferromagnetic superexchange energy estimated for Nd_2CuO_4), for as-grown [14] and oxygen-reduced NCCO (open and filled circles, left scale). Also plotted is the correlation length at $T = 30\,\text{K}$ (squares, right scale). The dotted line is a fit to the as-grown data for $2\pi\rho_s/J$, while the solid curves are guides to the eye for the oxygen-reduced data. The vertical dashed line indicates $x_c = 0.119$, the location of a discontinuity in both data sets for the oxygen-reduced samples.

Figure 3.11 shows the discontinuous nature of the behavior at x_c. The spin stiffness, estimated from a fit of the correlation length data to (3.2), is a property of the long-range ordered ground state.[16] For $x < x_c$, this quantity decreases gradually with increasing Ce concentration, and is still a large fraction of J just below x_c.[17] For $x > x_c$, where there is no genuine long-range order, the spin stiffness is zero. The result is a discontinuity at $x = x_c$. This behavior is in stark contrast to that of as-grown NCCO, where the spin stiffness continuously decreases with x. Figure 3.11 also shows the discontinuity seen in the correlation length at a temperature $T = 30\,\text{K}$

[16] See definition in Footnote 3 on page 66.

[17] It is unknown why, for the oxygen-reduced system, the spin stiffness at lower Ce concentrations seems to be larger than the (as-grown) undoped value. An enhancement around $x = 0.04$ is found in calculations by Markiewicz, but the theory also incorrectly predicts larger correlation lengths at that doping (see Figure 18 in [82]).

for samples with $x > x_c$. The data are consistent with a constant value of $\xi/a \approx 30$ even very near x_c. For $x < x_c$, of course, the correlation length has diverged and is effectively infinite.

3.2.3 μSR

In order to further investigate the behavior near x_c, some of the crystals were measured using μSR. These measurements were performed at the M20 beamline of the TRIUMF laboratory in Vancouver, British Columbia. The c-axes of the samples were mounted parallel to the initial muon polarization. The samples[18] with $x = 0.118$ and $x = 0.123$ were measured in zero magnetic field and in a longitudinal field of 100 G over a wide range of temperatures. A third sample[19] with $x = 0.141$ was measured mostly in the zero-field condition.

The zero-field and longitudinal-field time series for $x = 0.118$ are shown in Figure 3.12. In zero-field, as the sample is cooled, the magnetic moments of the system fluctuate more slowly and the relaxation rate of the muon spin increases. Below $T = 100$ K there is clear oscillation of the muon spin, indicating that the system is magnetically ordered. The zero-field data are fit to the sum of an oscillating component (2.25) and an exponentially relaxing component (2.26). In the longitudinal-field data, the muon signal exhibits the relaxation behavior at all temperatures; the curves are fits to (2.26). The relaxation rate is slow at high temperatures, becomes faster at $T = 120$ K and 100 K, and slows down again at lower temperatures. This is consistent with a phase transition in the 100–200 K temperature range.

The temperature dependences of the zero-field rotation frequency and the longitudinal-field relaxation rate are shown in Figure 3.13. The rotation frequency is proportional to the internal magnetic field at the muon site, and is thus proportional to the strength of the staggered moment in the magnetically ordered phase.

[18] These are the same samples that have been measured with neutrons; it is fortunate that μSR measurements allow for such large sample sizes.

[19] This is not the sample measured with neutron scattering. It was measured earlier, and the μSR data are not as complete as for the other two samples.

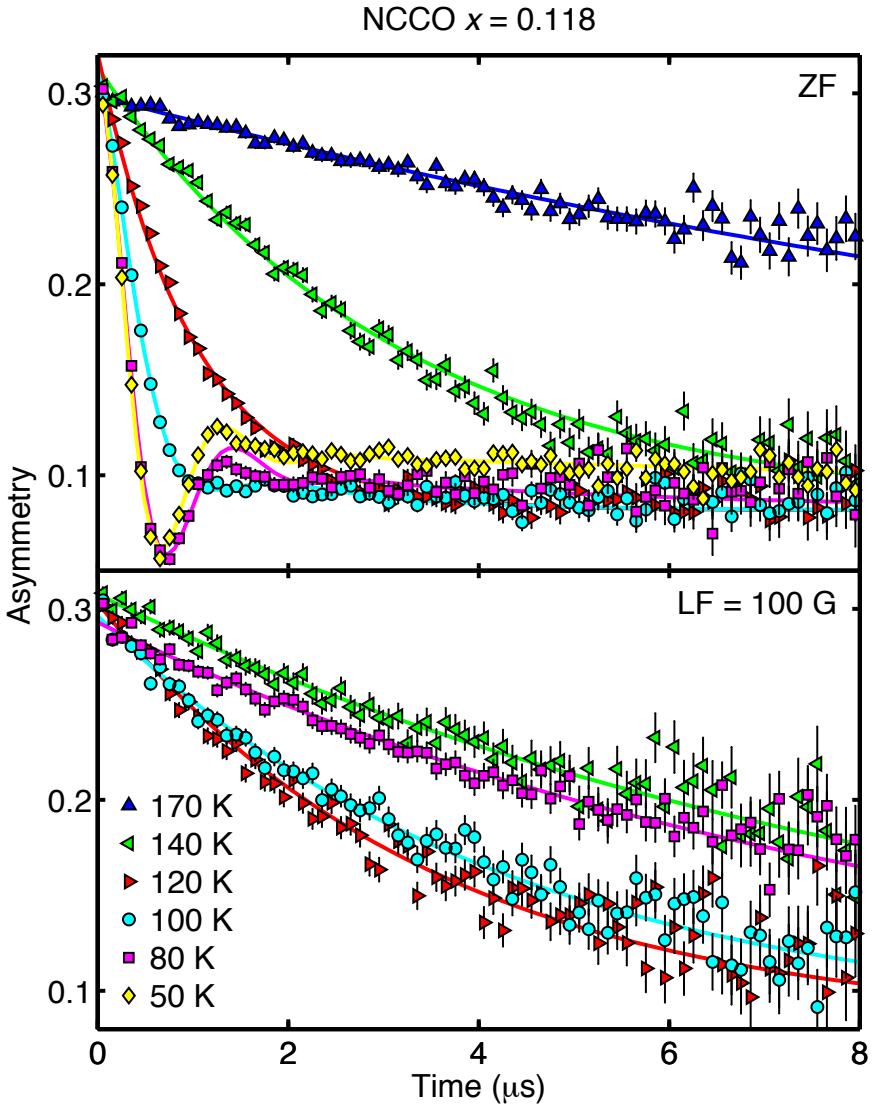

Figure 3.12: μSR time series for oxygen-reduced NCCO with $x = 0.118$ in zero applied field (top panel) and in a longitudinal field of 100 G (bottom panel) at representative temperatures. The curves are fits to the data, as described in the text.

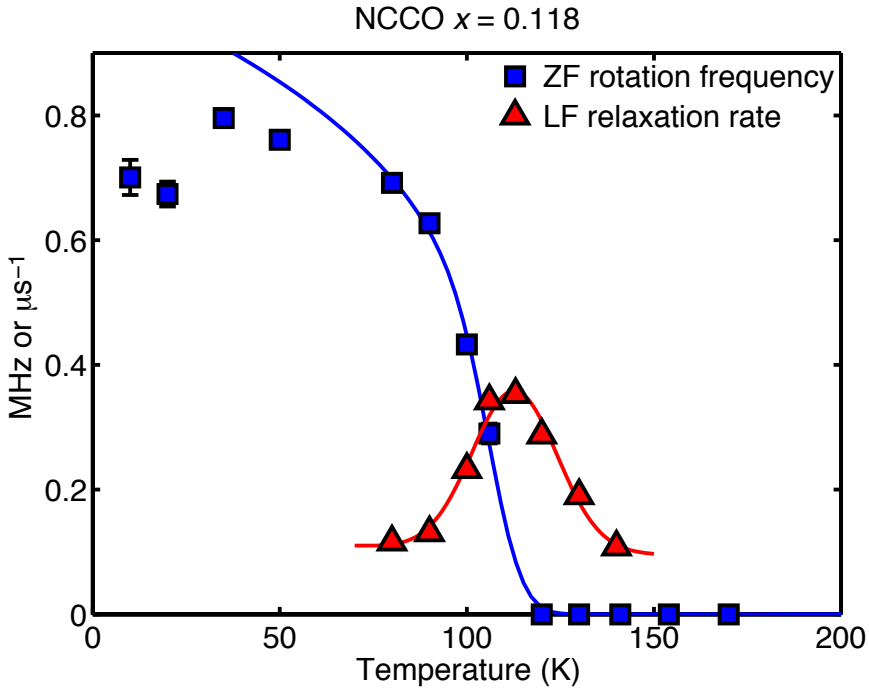

Figure 3.13: The zero-field rotation frequency (squares) and longitudinal-field relaxation rate (triangles) as a function of temperature for oxygen-reduced NCCO with $x = 0.118$, from fits to the time series in Figure 3.12. The curve for the rotation frequency is a fit to a rounded power-law function, and the curve for the relaxation rate is a fit to a Gaussian, as described in the text.

Note that the decrease in frequency at the lowest temperatures is likely due to the effects of Nd^{3+} spins, analogous to the behavior of the (101) magnetic Bragg peak (Figure 3.6). The temperature dependence near the transition is fit to the same function used to analyze the magnetic Bragg peak intensity, namely a power-law function convolved with a Gaussian. The power-law exponent is fixed to $\beta = 0.27$, and the fit yields $T_N = 108\,\mathrm{K}$ with a Gaussian width of $\pm 15\,\mathrm{K}$. The longitudinal-field relaxation rate peaks at the transition temperature with a fit to a Gaussian that yields $T_N = 113\,\mathrm{K}$ with a Gaussian width of $\pm 11\,\mathrm{K}$. The transition temperature for the two methods are thus consistent with each other. This result is plotted in Figure 3.7, along with the following results from the other two samples.

Figure 3.14 shows the results of the same analysis performed on the $x = 0.123$

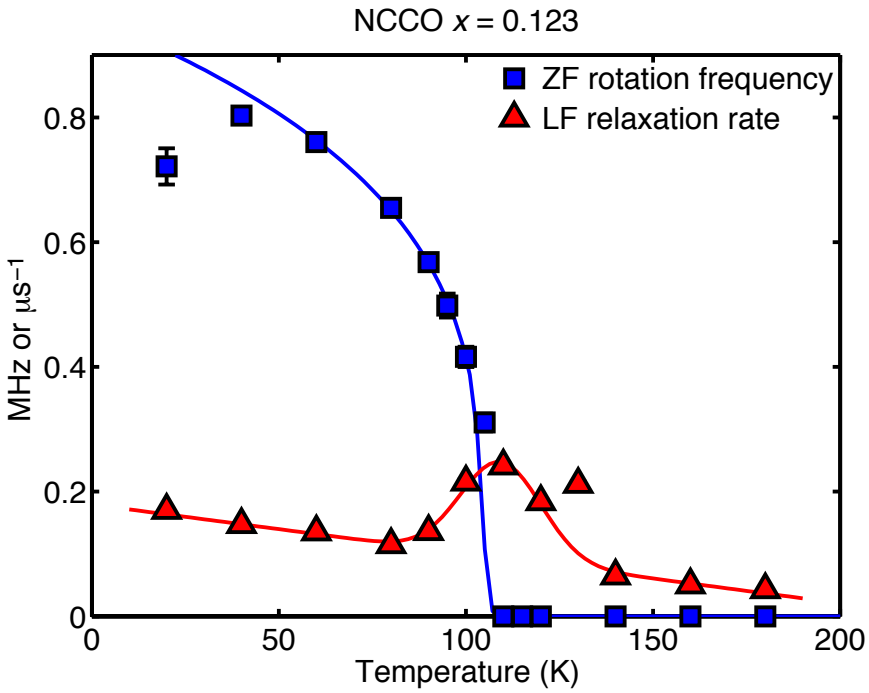

Figure 3.14: The zero-field rotation frequency (squares) and longitudinal-field relaxation rate (triangles) as a function of temperature for oxygen-reduced NCCO with $x = 0.123$, from fits to time series data (not shown). The curve for the rotation frequency is a fit to a rounded power-law function, and the curve for the relaxation rate is a fit to a Gaussian, as described in the text.

sample. Surprisingly, despite the differences in the two-axis neutron scattering results, this sample is almost indistinguishable from $x = 0.118$ in the μSR measurements. The sample shows static magnetic order below a transition temperature of $T_N = 105 \pm 3$ K according to zero-field measurements and $T_N = 109 \pm 11$ K according to longitudinal-field measurements.

There is a significant difference between the T_N values measured by μSR and those obtained from elastic neutron scattering ($T_N = 149 \pm 28$ K and $T_N = 121 \pm 33$ K for $x = 0.118$ and $x = 0.123$, respectively). However, as mentioned in Section 2.5, there is a difference of five orders of magnitude in the timescales probed by these two techniques. It is reasonable to suppose that the magnetic system evolves gradually from fast fluctuations at higher temperature to true static order near

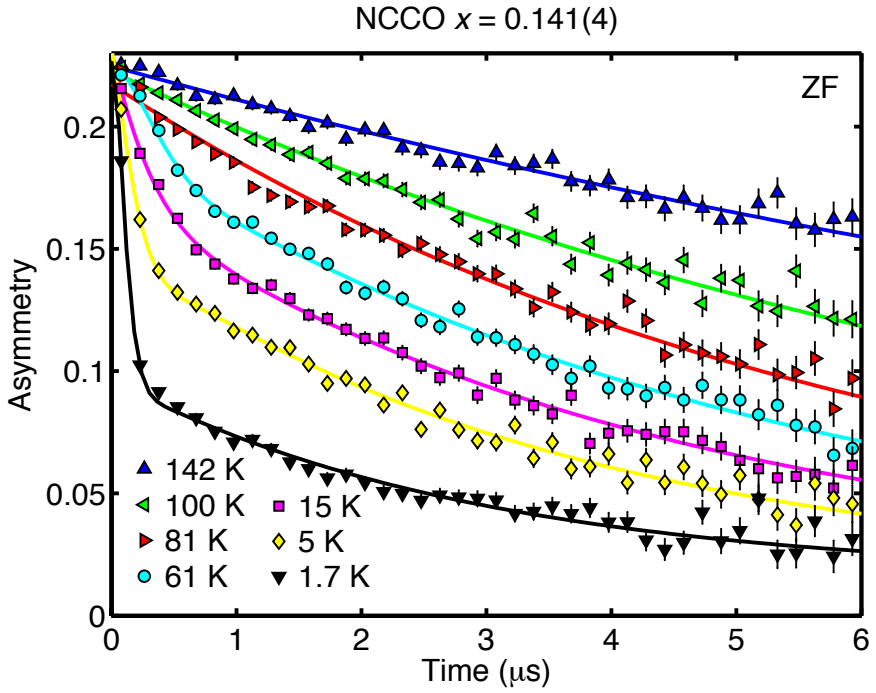

Figure 3.15: Zero-field μSR time series for oxygen-reduced NCCO with $x = 0.141$. This sample does not show static order above $T = 5\,\mathrm{K}$. The curves are fits to the sum of an exponentially relaxing component and an oscillating component, as discussed in the text.

100 K. The observation of rather broad transitions in elastic neutron scattering (Figure 3.6) when compared to μSR is consistent with this explanation.

Note that there are reports by one group of two characteristic transition temperatures ("T_{N1}" and "T_{N2}") revealed by μSR [16, 83, 84]. Based on measurements of NCCO and $Pr_{1-x}LaCe_xCuO_4$ (PLCCO), it is claimed that the higher of these temperatures is consistent with T_N from neutron scattering. From the above analysis, there is clearly only one characteristic temperature, and this temperature marks the onset of true static magnetic order; it is consistent with the lower temperature T_{N2}. The higher temperature T_{N1} is probably an effective temperature at which the slowing down of magnetic fluctuations first enters the μSR time window; the agreement between T_{N1} and the neutron-scattering T_N claimed in [16, 83] could be a coincidence.

For both samples, the zero-field data[20] were used to calculate the volume fraction of the oscillating component, which is a lower bound to the volume fraction of the magnetically ordered phase.[21] The $x = 0.118$ and $x = 0.123$ data yield volume fractions of 91% and 87%, respectively. Thus the magnetically ordered volume fraction is consistent with 100% and does not change noticeably across x_c.

Finally, Figure 3.15 shows time series for a $x = 0.141$ sample[22] in which there is no evidence of an oscillatory component above $T = 5\,\mathrm{K}$. Unfortunately, this older experiment did not include a systematic series of longitudinal-field measurements. It is difficult to determine a characteristic temperature with the limited data and thus to discern whether there is robust static order in this sample. Nevertheless, it is clear that, as measured by μSR, true static order disappears around $x = 0.14$, well before the value $x = 0.17$ indicated by elastic neutron scattering measurements.

3.3 Discussion

The antiferromagnetic correlation length results are summarized as a color plot in the phase diagram shown in Figure 3.16. The plotted length has been smoothed and interpolated to cover all regions of the phase diagram. The behavior at lower temperatures is shown as a discontinuity (vertical dashed line) at x_c that separates long-range order (white region) from short-range correlations. The data reflect the assumption that, as discussed previously, the strange behavior seen in some samples (e.g., $x = 0.126$) is due to Ce inhomogeneity and not genuine. The discontinuous nature is borne out in the raw data for $\xi(30\,\mathrm{K})$ shown in Figure 3.11. The behavior above T_N has been smoothed between $x = 0.117$ and $x = 0.121$, reflecting an intuition that the discontinuity cannot extend to higher temperatures.

One caveat regarding the color plot is that detailed measurements have not been

[20] Calibrated using weak-transverse-field data; see Section 2.5.

[21] The measurement is a lower bound because muons that do not happen to stop at the most common muon stopping site experience a different local magnetic field and do not contribute to the primary oscillating component. A method using a weak transverse field more accurately measures the magnetically fluctuating volume fraction; this measurement was unfortunately not performed for these samples.

[22] See Footnote 19 on page 85.

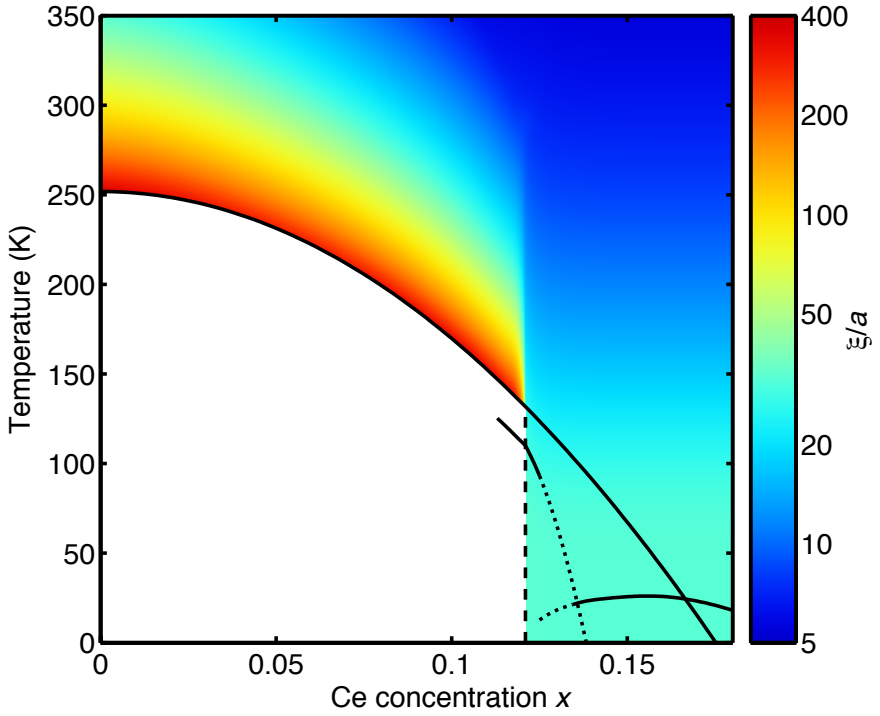

Figure 3.16: Temperature-doping phase diagram of oxygen-reduced NCCO with the antiferromagnetic correlation length plotted in color (see text for caveats). The vertical dashed line indicates the sudden transition at x_c from long-range order (white area) to short-range correlations. The long solid curve indicates the apparent T_N from neutron measurements (Figure 3.7), while the partially dotted curve near x_c represents T_N from μSR measurements. The dome in the lower right represents the superconducting phase, and the dotted portion of this dome indicates some uncertainty in whether the samples below $x \approx 0.14$ exhibit bulk superconductivity.

performed above $x = 0.141$;[23] I make the assumption that the correlation length at higher temperatures becomes doping-independent for $x > x_c$, as is the case at low temperatures (Figure 3.11). In addition, the correlation length becomes smaller in the superconducting state,[24] but this is not reflected in Figure 3.16.

Overlaid on the correlation length information are the Néel temperature T_N measured from elastic neutron scattering (solid curve) and μSR (partial curve), as well as the superconducting transition temperature T_c (dome at lower right). To the left of x_c, $T_N(x)$ from neutron-scattering matches the contour of constant correlation length $\xi/a \approx 400$; this behavior is consistent with the case of as-grown NCCO and the notion that there is a rapid crossover to XY behavior near T_N [14]. To the right of x_c, however, T_N no longer corresponds to a region of large correlation lengths. This apparent discrepancy is seen neither in as-grown NCCO, where static Néel order exists throughout the accessible doping range, nor in the LCZMO system, where magnetic order does disappear at high enough dilution.

Clarifications

In [19] we suggested that the magnetic Bragg signal for $x > x_c$, when the magnetic correlations remain finite at low temperature, could arise from volume fractions in the sample that have not undergone complete oxygen reduction, and that the bulk of the sample may be magnetically disordered at low temperatures. However, there is no anomaly seen in the staggered magnetization (Figure 3.8) around x_c that would indicate that the magnetic Bragg peaks in the samples with $x > x_c$ come from small volume fractions. Moreover, the μSR measurements discussed in Section 3.2.3 indicate that genuine static order is seen with high volume fraction, at least for the $x = 0.123$ sample.

The QNLσM contains a quantum critical point [58] (see Section 3.1.1), and the

[23] The superconducting sample $x = 0.145$ studied in [19] (data reproduced in Figure A.2) was very large, and its Ce concentration was not measured as systematically as the more recent samples shown here. While the temperature dependence of its correlation length is qualitatively similar to that of $x = 0.141$, including these data in Figure 3.16 was not satisfactory.

[24] see Footnote 14 on page 82.

correlation length behaviors for $x < x_c$ and $x > x_c$ seem like they might correspond to the model's renormalized classical and quantum disordered regimes, respectively. However, there is no longer any evidence of power-law behavior in the temperature-dependence of the correlation length that would be expected at a quantum critical point. The doping dependence of the spin stiffness would also be expected to decrease continuously with a power-law behavior; instead, from studying the newer, more homogeneous crystals, this quantity appears to be discontinuous (Figure 3.11). The doping dependence of the low-temperature correlation length also does not indicate power-law behavior as x_c is approached from above. There remains a possibility of a quantum critical regime in a very narrow range of x. However, after many years of study, the likely scenario for the NCCO phase diagram is that it exhibits a first-order transition at x_c

Two components of magnetic correlations

In a magnetic system with XY anisotropy, like NCCO, the spin fluctuations within the plane can behave differently from fluctuations out of the plane. In principle, since the two-axis experiments measure a combination of in-plane and out-of-plane correlation lengths, there exists a possibility that samples with $x > x_c$ actually exhibit long-range order, while the short-range correlations measured are due to the finite out-of-plane component. Here I argue that this is unlikely.

According to calculations [69], the in-plane length diverges at the Néel temperature T_N,[25] whereas the out-of-plane length effectively continues to follow the exponential temperature dependence (3.1) of a Heisenberg system below T_N. However, the out-of-plane length would be finite if the out-of-plane fluctuations below T_N (i.e., spin waves) were gapped. Assuming a spin-wave velocity equal to that found in Nd_2CuO_4, an out-of-plane correlation length of $30a$ would require a spin-wave gap of about 6 meV. Similar values of the out-of-plane spin-wave gap are indeed found in La_2CuO_4 [85], Nd_2CuO_4 [86], and $Sr_2CuO_2Cl_2$ [87]. However, there is no obvious explanation why this behavior should change suddenly at $x_c = 0.119$.

[25] Technically, at the Kosterlitz-Thouless transition; see Section 3.1.1.

The main reason why this scenario is unlikely is that the two-axis neutron scattering measurement is quite sensitive to the in-plane correlations that do diverge at T_N. Neutron scattering measures magnetic excitations with polarizations perpendicular to $\mathbf{Q}$ (B.180). Using the geometry of the spectrometer, and integrating over all of the $\mathbf{Q}$ in a two-axis measurement, a simple calculation shows that the measurement should be approximately six times more sensitive to the in-plane (diverging) component than the out-of-plane (possibly non-diverging) component. Consequently, if a sample does transition to genuine long-ranged order upon cooling, the measured correlation length would increase much more strongly at T_N than the modest increase seen in some of the samples with $x > x_c$.

Magnetic order and superconductivity

This study of the antiferromagnetic correlation length in NCCO has significant implications for the relationship between the antiferromagnetic and superconducting phases. None of the samples with $x < x_c$ that exhibit long-range order are superconducting, and none of the superconducting samples exhibit long-range antiferromagnetic order. We can say with confidence that there is no coexistence of genuine long-range antiferromagnetic order with superconductivity in NCCO, a conclusion we have previously suggested as a possibility in [19].

The μSR results near x_c are consistent with the elastic neutron scattering results: despite the significant qualitative change in the magnetic correlations, there only seems to be a smooth evolution of T_N with Ce concentration. There is one issue that remains unresolved: whether static magnetic order, as measured by μSR, coexists with superconductivity. This issue was addressed in [16], where it was claimed that there is indeed evidence for coexistence. It was reported that the volume fraction of the magnetic order does drop off suddenly above $x = 0.14$, but that superconductivity appears before the drop. The set of samples was relatively sparse in x, and only one of the samples ($x = 0.14$) exhibited this supposed coexistence. However, the magnetic order in this sample is only seen at a very low temperature

($T = 5\,\mathrm{K}$) and was probably caused by the Nd^{3+} moments.[26] Measurements of my own sample with $x = 0.141$ show no evidence of an oscillatory component above $T = 5\,\mathrm{K}$ (see Figure 3.15). As mentioned in Section 1.2.3, it is uncertain at which value of x bulk superconductivity first appears. Traces of superconductivity have been reported down to $x = 0.08$ [18], and have been seen down below $x = 0.13$ in my samples. However, bulk superconductivity has not been measured below $x = 0.14$ [16]. Consequently, there is as yet no conclusive evidence that static magnetic order of the CuO_2 planes coexists with bulk superconductivity. Further careful measurements by μSR and magnetometry should be performed in this region of the phase diagram to determine whether there is indeed microscopic coexistence of magnetic and superconducting orders.

In any case, the μSR measurements indicate that static magnetic order has disappeared at a Ce concentration $x \approx 0.14$, well before $x \approx 0.17$, as suggested by elastic neutron scattering. This is analogous to the difference at lower doping in the T_N values measured by μSR and elastic neutron scattering. The two techniques provide very different energy/time scales, and the "elastic" neutron scattering measurement are better thought of as quasi-elastic in the present case. Note that anomalies seen at $x \approx 0.17$ in transport measurements [88] have been attributed to the disappearance of magnetic order [89]. This interpretation is no longer plausible; the anomalies are more likely due to pseudogap physics and a change of the Fermi-surface topology near $x = 0.17$ (see Section A.2.3 for a discussion of the pseudogap).

Short-range magnetic order

It remains a surprise that the disappearance of genuine static order does not seem to correspond in any obvious way with the sudden change from long-range to short-range correlations at $x_c = 0.119(2)$. In particular, the combined neutron and μSR measurements imply that there is a region of the phase diagram between x_c and $x \approx 0.14$ that exhibits short-range ($\xi/a \approx 30$) static magnetic order.

[26] The same group's studies of PLCCO also contain only one sample that shows coexistence of static order with superconductivity, although in that case, there are no substantial rare-earth moments [84].

Because the ordering temperature does not show any anomaly across x_c, it is unlikely that the mechanism for magnetic order (i.e., the crossover from two-dimensional Heisenberg to two-dimensional XY physics) has suddenly changed. Instead, it could be that the magnetic system has been broken up into clusters, and that the correlation length cannot grow larger than the cluster size. The neutron-scattering data show that the correlation length for these samples has indeed reached its maximum value at T_N. One of the possible reasons for the clustering of the magnetic system is the qualitative change in the electronic state known to occur somewhere between $x = 0.10$ and $x = 0.15$: the introduction of hole-like carriers into the system [79, 80]. These holes could rapidly frustrate the magnetic system: in $La_{2-x}Sr_xCuO_4$ (LSCO), a hole concentration of only $x = 0.02$ destroys long-range magnetic order.[27] The short-range magnetic order in NCCO might correspond to the spin-glass regime that is found in LSCO between $x = 0.02$ and $x = 0.05$.

There is a clear qualitative difference between the situation in the two systems: in LSCO the spin-glass temperature is much smaller than the Néel temperature at slightly lower doping, while in NCCO, the ordering temperature is practically unchanged between long-range and short-range magnetic order. However, there are otherwise many similarities in the data. Correlation length measurements of LSCO in the spin-glass doping regime show a behavior similar to $x > x_c$ in NCCO: the correlation length attains a maximum finite value at a temperature near T_N of the undoped compound and remains constant at lower temperatures (see Figure 10 in [12]). Furthermore, μSR measurements of the spin-glass phase show that the muon rotation rate, and thus the strength of the internal magnetic field, decreases only slightly from that of the long-range ordered state at somewhat lower doping [90]. In this respect, the μSR data for NCCO are similar (compare Figures 3.13 and 3.14).

In principle, the existence of clusters can be tested by measuring the momentum-space extent of the elastic scattering at $(\frac{1}{2}, \frac{1}{2})$. Spin clusters have been found, for

[27] The disappearance of long-range order in NCCO happens faster than over the range $\Delta x = 0.02$; perhaps the effects of holes are even more sudden in a magnetic system already doped with electrons.

instance, in the spin-glass phase of LSCO at $x = 0.02$ [91]. The profiles of the magnetic Bragg peaks in NCCO were measured in this Thesis work as part of the order parameter measurements. However, a comparison of the Bragg peak widths of the $x = 0.118$ and $x = 0.133$ samples does not show any obvious signature of short-ranged order. Careful characterization of the magnetic Bragg peaks should be performed in the future to resolve this issue.

Another test, specifically for spin-glass behavior, can be performed using magnetometry measurements [92]. Cooling through the spin-glass transition temperature in both zero field and non-zero field conditions causes the spin system to freeze in different configurations, and this yields different values of the bulk magnetization. This type of measurement led to the discovery of "spin-glass-like" behavior in partially oxygen-reduced PLCCO [93]. In that study, the feature in the bulk susceptibility was seen at temperatures as high as 200 K. At any particular Ce concentration x, the spin-glass-like behavior appears and strengthens with oxygen-reduction, but then weakens and disappears as superconductivity appears in the system under even stronger oxygen reduction. It is possible that a similar signature could be seen in a sample of NCCO that exhibits static short-range magnetic order. Measurement of a piece from the $x = 0.133$ crystal yielded no such signature. At the time of writing, there is a plan to test a piece from the $x = 0.123$ crystal.

Comparison with other systems

Now that I have mapped out the phase diagram of the NCCO system, it is instructive to compare it to the various phase diagrams of other unconventional superconductors. Figure 3.17 shows phase diagrams for the iron arsenide compounds La(O,F)FeAs, Sm(O,F)FeAs, Ce(O,F)FeAs, and (Ba,K)Fe_2As_2 (in which superconductivity was recently discovered); the organic superconductor κ-(BEDT-TTF)$_2$X;[28] and the heavy fermion compound $CeRhIn_5$. Each of the phase diagrams contains antiferromagnetic order and superconductivity, but the relationship between the two phases varies. A possible commonality proposed in [100] is the existence

[28]BEDT-TTF is bis(ethylenedithio)tetrathiafulvalene, and X stands for the various anions indicated in Figure 3.17.

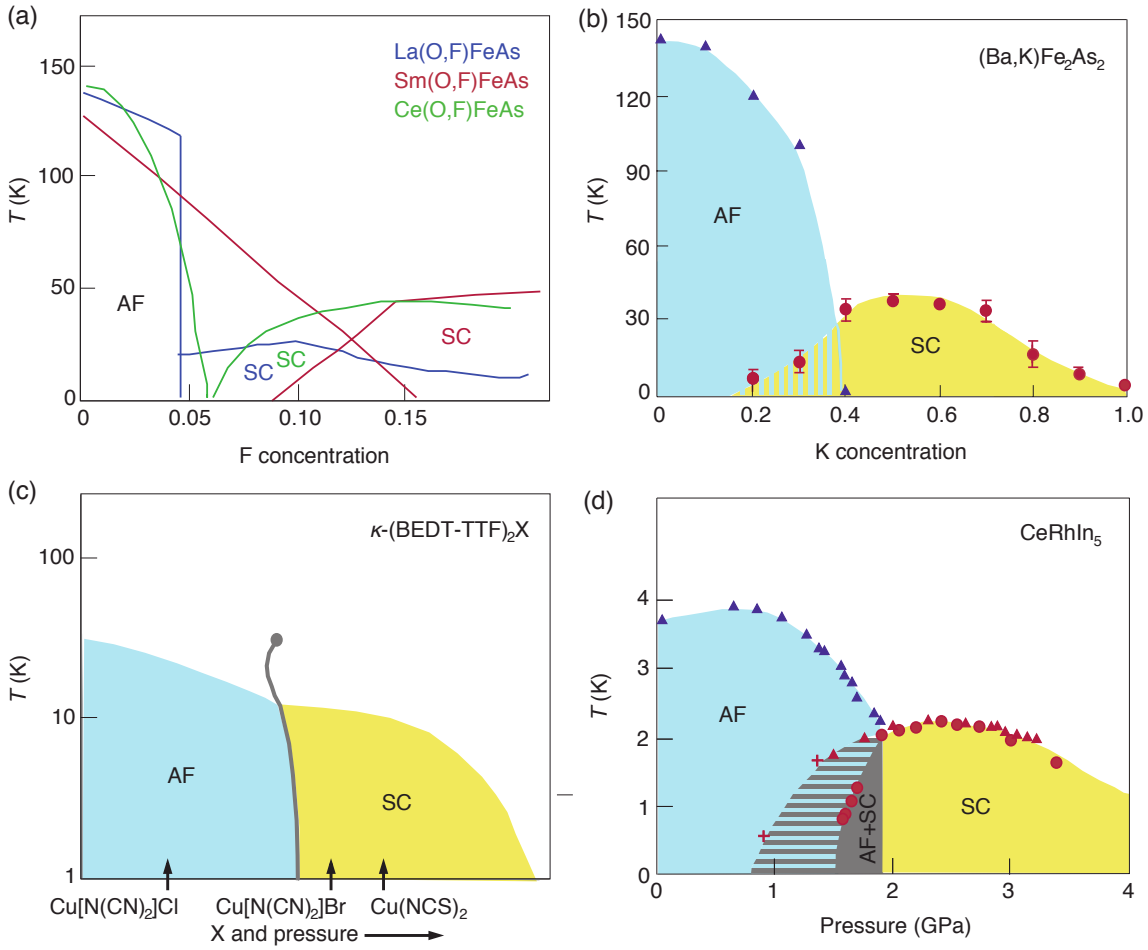

Figure 3.17: Phase diagrams of other unconventional superconductors: (a) the iron arsenide compounds La(O,F)FeAs [94], Sm(O,F)FeAs [95], and Ce(O,F)FeAs [96]; (b) the iron arsenide compound (Ba,K)Fe_2As_2 [97]; (c) the organic superconductor κ-(BEDT-TTF)$_2$X [98]; and (d) the heavy fermion compound $CeRhIn_5$ [99]. Adapted from [100].

of a first-order transition between the two phases. The sudden disappearance of magnetic order in La(O,F)FeAs is one manifestation of a first-order transition. In Sm(O,F)FeAs and (Ba,K)Fe_2As_2, where the magnetism and superconductivity seem to coexist, there may be microscopic phase separation, a possible signature of a first-order transition in the presence of disorder.

The improved phase diagram of NCCO is consistent with such a first-order transition from antiferromagnetic order to superconductivity. The sudden disappearance of long-range magnetic order at x_c is a compelling sign. And perhaps, due to disorder, the phase transition is not complete, resulting in the short-range magnetic order and trace superconductivity seen in the region $0.12 < x < 0.14$. As with the new iron arsenide compounds, further careful quantitative measurements are desirable.

Conclusions

To conclude, I have obtained a map of the doping and temperature dependence of the two-dimensional magnetic correlation length in the archetypical electron-doped cuprate superconductor $Nd_{2-x}Ce_xCuO_4$. Genuine long-range antiferromagnetic order ends suddenly at $x_c = 0.119(2)$, but short-range static order exists somewhat beyond x_c. I have found that the bulk superconducting phase is well-separated from the long-range ordered phase at $x < x_c$, which may be a fundamental property or due to disorder effects that cause a suppression of T_c. Furthermore, genuine static (short-range) order terminates around $x = 0.14$, near the first appearance of bulk superconductivity. The magnetism seen in elastic neutron scattering up to $x \approx 0.17$ is thus neither truly static nor genuinely long-range in nature.

Chapter 4

Magnetic field effect in NCCO

One strategy for studying the mechanism of superconductivity in the high-T_c cuprates is to suppress the superconductivity to see, in effect, the physical state of the system had superconductivity not occurred. For instance, if there is an ordered state that competes with superconductivity, this competing order might strengthen when superconductivity is suppressed.

A common method of suppressing superconductivity is to apply a strong magnetic field. In Section 4.1, I discuss previous magnetic-field-effect studies of the hole-doped compounds and of NCCO. I describe the results of my own measurements of NCCO in Section 4.2. Section 4.3 first follows the discussion of the results at the time of publication [101], and then continues with a discussion in light of more recent developments.

4.1 Background

4.1.1 Suppression of superconductivity with magnetic field

Just as the temperature at which superconductivity forms or disappears is referred to as the critical temperature T_c, the magnetic field at which superconductivity is suppressed is called the critical field. In type-II superconductors, such as the cuprates, a magnetic field above a certain lower critical field H_{c1} penetrates

into the sample bulk in the form of discrete vortices, the cores of which are non-superconducting, with each vortex containing one magnetic flux quantum.[1] On the other hand, the upper critical field H_{c2} is the magnetic field required for the complete suppression of bulk superconductivity, and is the more relevant quantity for this study.

Quite generally, there are two microscopic mechanisms for the suppression of superconductivity by a magnetic field. The first is orbital pair-breaking: paired electrons in a superconductor are in a certain orbital state (such as d-wave in the cuprates), and a magnetic field breaks the orbital symmetry and thus acts to break the electron pairs. The orbital pair-breaking field $H_{\rm orb}$ can be estimated by measuring the rate at which $H_{c2}(T)$ increases upon lowering the temperature from T_c. Extrapolating linearly to $T \to 0$ gives $H_{\rm orb}$ [104].

The second mechanism occurs as a result of the spins of the electrons. In cases in which the spins in each Cooper pair are oppositely aligned (such as in the cuprate superconductors), a magnetic field lowers the free energy of the non-superconducting Pauli-paramagnetic state, in which both spins are polarized along the applied field, relative to the free energy of the superconducting state. This mechanism is an upper limit to H_{c2} and is called the Chandrasekhar-Clogston or Pauli-paramagnetic limit [105, 106]. It is given by $H_{\rm P} = \Delta_0/\sqrt{2}\mu_{\rm B}$, where Δ_0 is the electronic superconducting gap.

While the upper critical field H_{c2} is conceptually easy to understand, for the cuprates it has been a difficult quantity to measure in practice. One practical reason is that, in the hole-doped cuprates, H_{c2} is exceedingly large at low temperatures. Even if that were not the case, resistivity measurements can be problematic because the presence of mobile vortices will lead to a non-zero resistance at fields below H_{c2}. One method claimed by proponents to provide an accurate measurement of H_{c2} is the Nernst effect [107], which is the thermoelectric analog of the Hall effect: if a thermal gradient $-\partial T/\partial x$ is applied along the x-direction while a magnetic field $\mathbf{H} = H\hat{\mathbf{z}}$ is applied along the z-direction, then the measured quantity is the voltage

[1] $\Phi_0 = h/2e$, where h is the Planck constant and $2e$ is the charge of a Cooper pair [102]. The formation of vortices in type-II superconductors is a result of the superconducting coherence length being smaller than the London penetration depth (by definition) [103].

(electric field E_y) along the y-direction. The Nernst signal is defined as the ratio $E_y/(-\partial T/\partial x)$. In the "vortex-liquid" state of a type-II superconductor, vortices form along z due to the magnetic field, move along x due to the thermal gradient, and cause a voltage along the y direction; the resulting Nernst signal is positive. A Nernst signal can also arise from mobile charge carriers due to the combination of the thermoelectric and Hall effects; this signal can be either positive or negative, and can usually be treated as a featureless background.[2]

Figure 4.1 shows the Nernst signal for optimally-doped NCCO ($x = 0.15$) [107]. At any particular temperature there are three characteristic fields. At low field strength, the Nernst signal is zero, because the vortices are pinned and do not move in response to the temperature gradient. At the vortex "melting" field $H_{\rm m}$, the Nernst signal increases strongly from zero, peaks at a certain field H^*, and then decreases again. The field at which the Nernst signal appears to reach zero again is interpreted to be the upper critical field $H_{\rm c2}$. These three fields are plotted in the inset of Figure 4.1. Note that Figure 4.1 also shows (for $T = 14\,{\rm K}$) that the resistivity becomes nonzero at $H_{\rm m}$ and saturates around H^*, but shows no feature at $H_{\rm c2}$ [107]: because mobile vortices cause non-zero resistivity even in the superconducting state, resistivity measurements cannot reliably determine $H_{\rm c2}$ in these type-II superconductors.

Figure 4.1 shows that $H_{\rm c2}$ is approximately 10–12 T, upon extrapolating to $T = 0$. Note the linear dependence of $H_{\rm c2}(T)$ with temperature, which is consistent with the expected behavior for the orbital mechanism for the suppression of superconductivity. The Pauli-paramagnetic limit is much higher, at $H_{\rm P} \approx 30$–$45\,{\rm T}$, estimated from measurements of the electronic gap Δ_0 using angle-resolved photoemission ($\Delta_0 \approx 2\,{\rm meV}$) [109] and Raman spectroscopy ($\Delta_0 \approx 3\,{\rm meV}$) [110]. Orbital effects also explain the strong anisotropy of $H_{\rm c2}$ with respect to the magnetic field direction; recent studies on $Pr_{2-x}Ce_xCuO_4$ thin films suggest that the large value of $H_{\rm c2}$ for a magnetic field parallel to the CuO_2 planes is determined by the Pauli paramagnetic limit [111].

[2]Recent measurements of Nd- and Eu-doped LSCO have shown that this quasiparticle signal can have a large temperature dependence at a density-wave-order transition [108]. However, this does not affect the interpretation of the NCCO data.

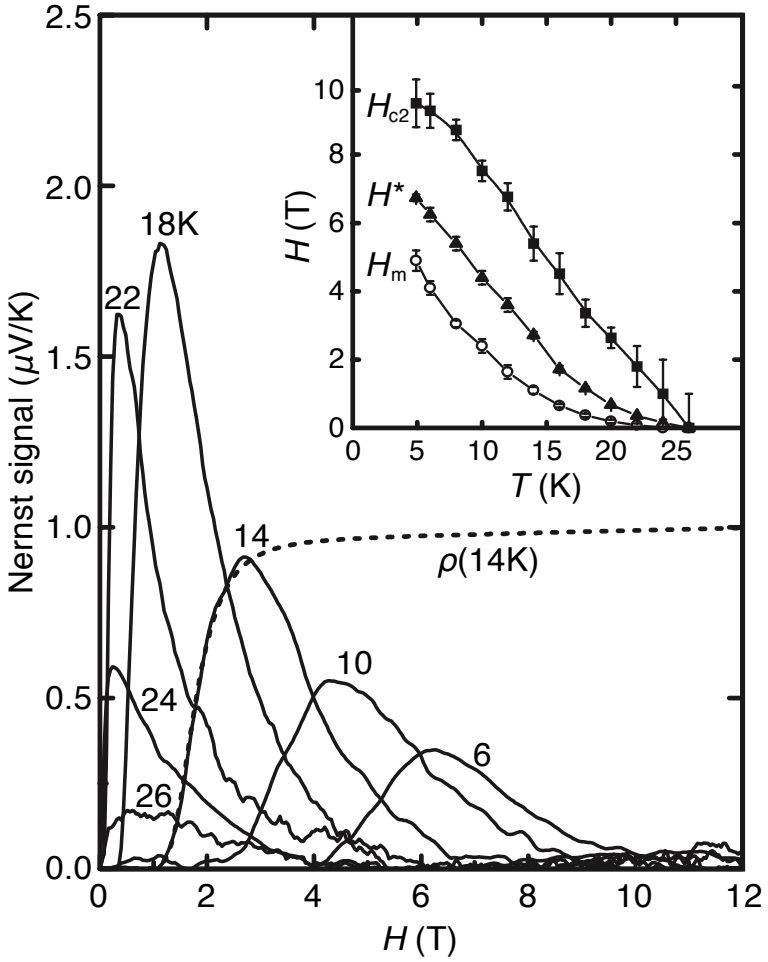

Figure 4.1: Nernst signal for NCCO ($x = 0.15$) as a function of magnetic field at several temperatures (main panel). Also shown are representative resistivity data at 14 K. The inset shows the upper critical field H_{c2}, estimated from the Nernst signal data, as a function of temperature. Also plotted in the inset are two other characteristic fields: the field H^* with maximum Nernst signal and the vortex-melting field H_m. Reproduced from [107].

For the hole-doped cuprates (and fields perpendicular to the CuO_2 planes), the upper critical field from Nernst measurements (using extrapolation to $T = 0$) is 50 T or greater [107]. Because the upper critical field in NCCO is significantly lower, this means that a much larger portion of the phase diagram can be explored in the electron-doped cuprates.[3]

4.1.2 Magnetic-field-effect studies of hole-doped cuprates

Magnetic-field-effect studies were performed first in the hole-doped cuprates. In these compounds, at hole concentrations that exhibit superconductivity, the low-energy magnetic response is incommensurate and manifests itself in neutron scattering as four peaks situated symmetrically around the two-dimensional antiferromagnetic wavevector at positions $(\frac{1}{2} \pm \delta, \frac{1}{2})$ and $(\frac{1}{2}, \frac{1}{2} \pm \delta)$ [112, 113, 114].

Superconducting $La_{2-x}Sr_xCuO_4$ (LSCO) in the underdoped regime ($0.06 \leq x < 0.14$) exhibits peaks at these incommensurate wavevectors in the elastic channel [115, 116]. Thus static[4] spin-density-wave (SDW) order coexists with superconductivity in these materials; this is one signature of the "stripe" order that seems to have some connection to superconductivity [117]. In optimally-doped and overdoped LSCO ($x > 0.15$), there is no static order, and the antiferromagnetic response is gapped [118]. While the attainable magnetic fields are small relative to H_{c2}, magnetic-field-effect studies show remarkable changes in samples both with and without static SDW order.

Figure 4.2 shows the result by Lake *et al.* [115] of a magnetic-field-effect on the SDW peaks seen in the superconducting state of underdoped LSCO ($x = 0.10$). The inset indicates the geometry of the system: the data were taken in a scan across one of the incommensurate SDW wavevectors, and the magnetic field was applied along the *c*-axis direction. The data show a clear increase of the elastic peak intensity. Thus, even a weak suppression of the superconductivity in underdoped LSCO strengthens the static SDW order already present in the system. A study of La_2CuO_{4+y} with an estimated hole concentration of $p = 0.14$ showed a similar

[3] The highest magnetic field attainable at neutron scattering facilities at present is about 15 T.
[4] Static on the time scale of elastic neutron scattering

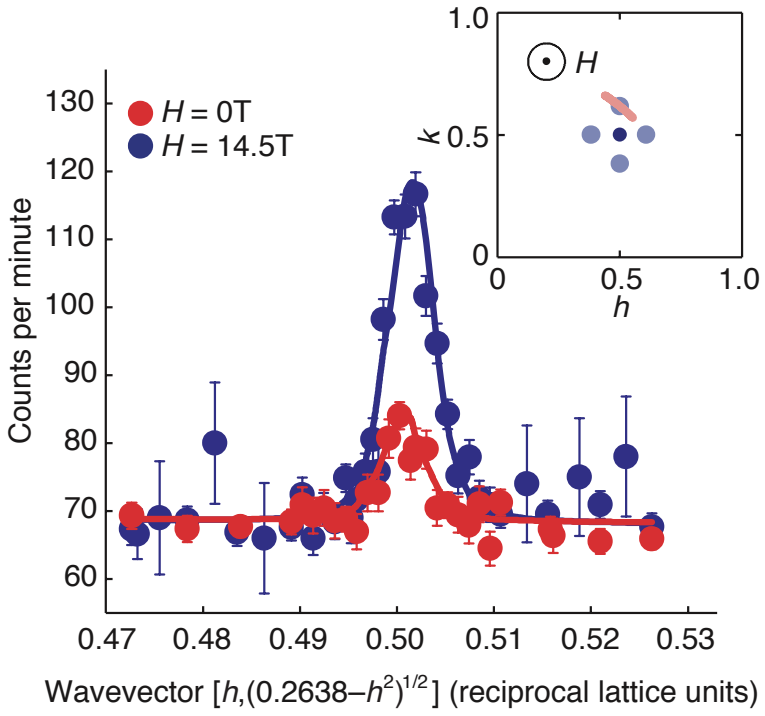

Figure 4.2: Elastic neutron scattering in zero magnetic field and in a magnetic field of $H = 14.5\,\mathrm{T}$ along the c-axis. The data are transverse scans centered at one of the incommensurate SDW wavevectors (indicated in the inset) and at a temperature of $T = 2\,\mathrm{K}$, deep in the superconducting state of the system. Adapted from [115].

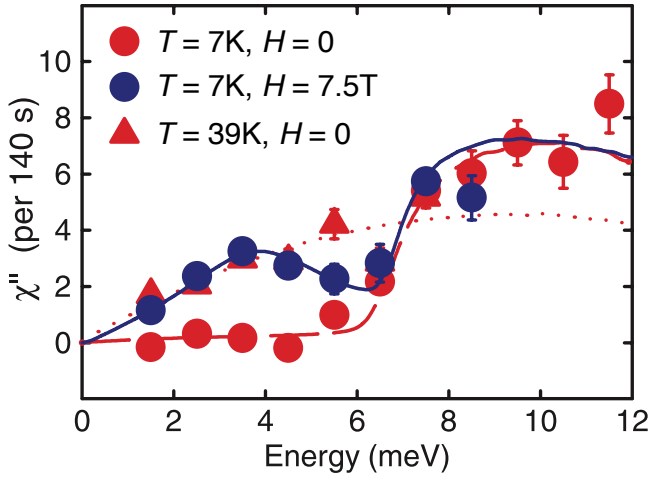

Figure 4.3: Incommensurate magnetic response as a function of energy in different temperature and magnetic field conditions for optimally-doped LSCO ($x = 0.16$). The zero-field ground state (red circles) has a gap in the magnetic spectrum which disappears in the normal state (red triangles and dotted curve). A magnetic field induces in-gap intensity (blue circles). Adapted from [119].

strengthening of the SDW order [116]. The two results suggest that the ground state of these systems in the absence of superconductivity is probably magnetically ordered.

The case of optimally-doped LSCO is also interesting. Figure 4.3 shows the result by Lake *et al.* [119] for LSCO ($x = 0.16$). Plotted is the magnetic susceptibility χ'' (i.e., the intensity divided by the Bose population factor $n + 1$) as a function of energy. The magnetic spectrum in the zero-field ground state ($T = 7\,\mathrm{K}$) is gapped with an energy of about $\omega = 7\,\mathrm{meV}$, and the disappearance of this gap in the normal state ($T = 39\,\mathrm{K}$) implies that the magnetic gap is tied to superconductivity. The main result is that a magnetic field of $H = 7.5\,\mathrm{T}$, which is small compared to H_{c2}, induces a signal below the gap that is comparable in strength to the normal state response. Similar results have been reported in overdoped LSCO samples with $x = 0.17$ [120] and $x = 0.18$ [121].

The strong in-gap intensity has been interpreted by Demler *et al.* [122, 123] to be a signature of the proximity to the static spin-density-wave order. As shown in Figure 4.4, their proposed phase diagram contains a pure superconducting (SC)

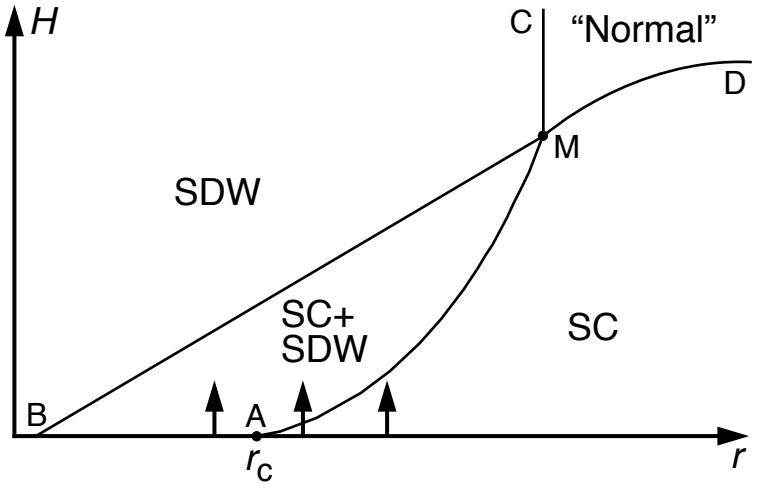

Figure 4.4: Generic phase diagram as a function of magnetic field H and a parameter r related to doping [122, 123]. The short arrows indicate experiments performed on LSCO (from left to right: [115], [124], [119]).

phase and a phase with coexisting superconducting and spin-density-wave orders (SC+SDW). The studies of underdoped LSCO are represented by the leftmost arrow in the SC+SDW phase, whereas the studies in optimally-doped and overdoped LSCO are represented by the rightmost arrow contained completely in the SC phase. Interestingly, an elastic neutron scattering study performed more recently by Khaykovich *et al.* [124] at an intermediate doping $x = 0.144$ shows that a relatively low magnetic field of $H = 3\,\mathrm{T}$ pushes the system from the SC phase into the SC+SDW phase (see Figure 4.5), as indicated by the middle arrow in Figure 4.4.

All of these experiments were performed on the widely-studied LSCO compound. A recent study of underdoped $YBa_2Cu_3O_{6.45}$ shows the strengthening of static SDW order in the system as a magnetic field is applied up to $H = 15\,\mathrm{T}$ [125], indicating that the behavior seen in LSCO may be universal to the hole-doped cuprates.

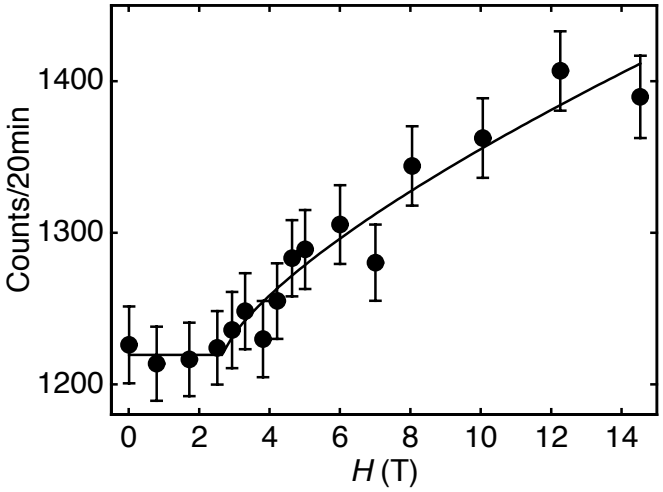

Figure 4.5: Intensity of the magnetic elastic peak at the SDW wavevector as a function of magnetic field in LSCO ($x = 0.144$). Reproduced from [124].

4.1.3 Elastic scattering studies of NCCO

Unlike the spin-density-wave order seen in the hole-doped cuprates, the magnetic response of the electron-doped cuprates remains commensurate at the antiferromagnetic wavevector $(\frac{1}{2}, \frac{1}{2}, \ell)$ [126]. Thus one might expect the phase diagram to be similar to the hole-doped case, with superconductivity coexisting with commensurate antiferromagnetic order instead of incommensurate spin-density-wave order. Experiments by Kang *et al.* [127] on NCCO ($x = 0.15$) seemed to agree with this naïve picture: a magnetic field perpendicular to the CuO_2 sheets was found to induce an elastic signal at $(\frac{1}{2}, \frac{1}{2}, 0)$. At $T = 5\,\mathrm{K}$, the response was found to increase immediately from zero[5] upon turning on the magnetic field, and to peak around $H = 7\,\mathrm{T}$, which was interpreted to be H_{c2}.

However, Mang *et al.* [23, 128] showed that this signal is spurious: it is due to the paramagnetic response of an epitaxial impurity phase $(Nd,Ce)_2O_3$ that forms during the oxygen-reduction procedure. Figure 4.6 shows the magnetic-field-dependence of the elastic signal in an NCCO sample with $x = 0.18$. The data were fit

[5]Even in superconducting NCCO samples that show static antiferromagnetic order at finite ℓ (e.g., $(\frac{1}{2}, \frac{1}{2}, 1)$), the reflection $(\frac{1}{2}, \frac{1}{2}, 0)$ is forbidden by the magnetic structure factor.

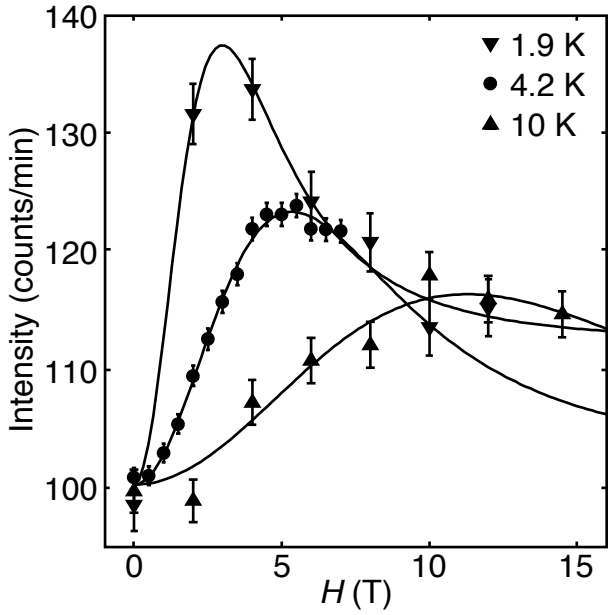

Figure 4.6: Intensity of the elastic magnetic peak at $(\frac{1}{2}, \frac{1}{2}, 0)$ as a function of applied magnetic field (perpendicular to the CuO_2 sheets) at several temperatures for NCCO ($x = 0.18$). This magnetic signal is due to a paramagnetic response from the impurity phase $(Nd,Ce)_2O_3$ formed during the oxygen-reduction process [23]. The curves are fits to a two-moment model. Adapted from [23].

to a two-moment model[6] for the Nd^{3+} moments that explains the dependence both on magnetic field and on temperature. Note in particular that the magnetic field at which the signal peaks increases with increasing temperature, and the proximity to H_{c2} in [127] was only coincidence. Key arguments by Mang *et al.* are that the same signal is present in a non-superconducting, but oxygen-reduced, $x = 0.10$ sample, and that field-induced peaks are also found at wavevectors commensurate with the lattice of the impurity phase, but incommensurate with the primary lattice.

Disagreement continued over whether there is a genuine magnetic-field effect on the elastic magnetic signal in the electron-doped cuprates. Many of the subsequent studies were of the related electron-doped compound $Pr_{1-x}LaCe_xCuO_4$ (PLCCO): unlike Nd^{3+}, neither Pr^{3+} nor La^{3+} have magnetic moments in their ground state, and thus the impurity phase $(Pr,La,Ce)_2O_3$ should not interfere with any genuine

[6]The epitaxial impurity phase has a non-trivial structure with two distinct rare-earth sites.

magnetic signal. Fujita *et al.* [129] studied the magnetic field effect on the intensity of the $(\frac{1}{2}, \frac{3}{2}, 0)$ magnetic Bragg peak[7] and found an enhancement of the existing antiferromagnetic order in underdoped PLCCO ($x = 0.11$), whereas they saw no peak with or without a magnetic field in an overdoped sample with $x = 0.15$.[8] Kang *et al.* [131] studied PLCCO samples with $x = 0.12$ at different degrees of oxygen reduction, and confirmed that there is no magnetic-field enhancement at the incommensurate peak $(\frac{1}{2}, \frac{1}{2}, 2.2)$ associated with the impurity phase. In an apparent contradiction to Fujita *et al.*, they found a small enhancement in a magnetic field at $(\frac{1}{2}, \frac{1}{2}, 0)$, but not at $(\frac{1}{2}, \frac{3}{2}, 0)$, in partially reduced superconducting samples. In addition, they reported that there is no magnetic-field effect at either wavevector in a fully reduced sample [131]. Thus, there seems to be some sort of enhancement of magnetic signal in some PLCCO samples, but there are as yet no definitive conclusions. Also, the differences between NCCO and PLCCO are large enough that nothing definite can be concluded about NCCO from these studies.

4.1.4 Magnetic excitation spectrum of NCCO

While the chemical and magnetic properties of NCCO complicate a search for a genuine field-induced elastic signal, they do not prevent useful measurements of the inelastic response. Just as in the hole-doped cuprates, inelastic neutron scattering measurements of optimally-doped NCCO revealed a gap in the magnetic excitation spectrum associated with superconductivity [126, 132]. In fact, this expected gap is absent in PLCCO [133]; this is another example of the differences between NCCO and PLCCO and may be a result of additional disorder in the chemically more complicated PLCCO system.

Figure 4.7 shows the results by Yamada *et al.* [126]. The two different samples of NCCO (both $x = 0.15$, but with different oxygen reduction conditions) exhibit gaps of 3–4 meV in the low-temperature spectra. Note the behavior of the spectra

[7] Unlike $(\frac{1}{2}, \frac{1}{2}, 0)$, this wavevector is an allowed magnetic Bragg peak for the antiferromagnetic order.

[8] The PLCCO phase diagram differs from that of NCCO; one difference is that the maximal T_c is attained at $x = 0.12$ [130].

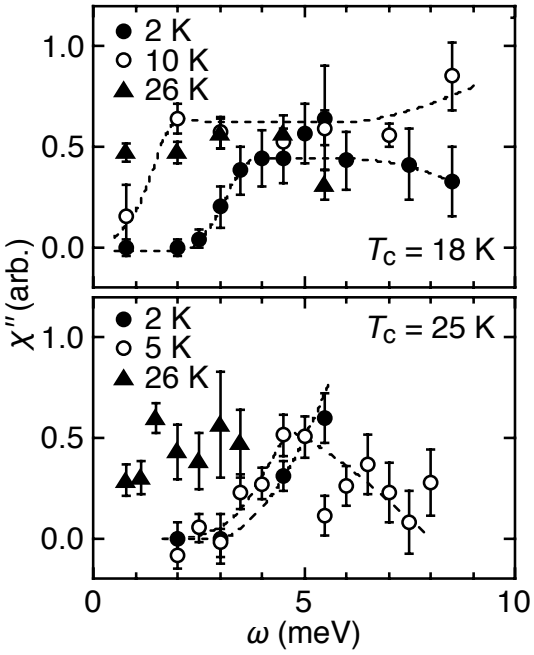

Figure 4.7: The magnetic susceptibility at $(\frac{1}{2}, \frac{1}{2}, 0)$ as a function of energy in two samples of NCCO (both $x = 0.15$) at several temperatures. The two samples have different values of T_c due to different oxygen reduction procedures. The spectra in the superconducting state are gapped, while the spectra above T_c are not. Adapted from [126].

as the temperature is increased: to a first approximation, the entire spectra shift to lower energies and retain a distinctly gapped shape. The magnetic excitations are no longer gapped above T_c: this indicates that the gap seen at lower temperatures is tied to the formation of superconductivity.

4.2 Results

Here I report the magnetic field effect on this gapped magnetic excitation spectrum of one sample of superconducting NCCO: similar to the effect of raising the temperature, the gap profile was found to shift rigidly to lower energies as the magnetic field strength was increased [101]. The publication reported the nominal Ce concentration $x = 0.15$ of the sample that was measured; the actual concentration as

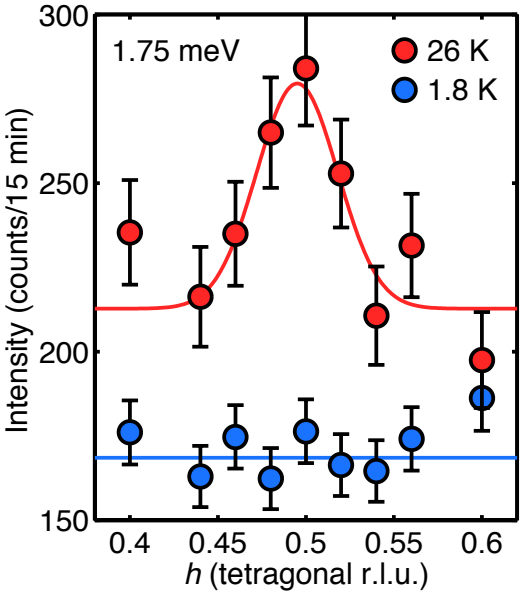

Figure 4.8: Intensity from transverse $(h, 1-h, 0)$ inelastic scans for NCCO ($x = 0.166$, $T_c = 22\,\mathrm{K}$) at an energy of $\omega = 1.75\,\mathrm{meV}$. The $T = 26\,\mathrm{K}$ data show a clear peak, whereas the signal is suppressed at $T = 1.8\,\mathrm{K}$ in the superconducting state.

measured by ICP atomic emission spectroscopy is $x = 0.166(10)$, and the sample has an onset T_c of 22 K.

The inelastic neutron scattering measurement was performed at Laboratoire Léon Brillouin at CEA/Saclay, in Saclay, France. We used the triple-axis spectrometer at the cold neutron beamline 4F2, which has a vertically-focusing double monochromator and a horizontally-focusing analyzer. The final energy was fixed to $E_f = 14.7\,\mathrm{meV}$ and the collimations were 60′–open–sample–open–open, which gives effective collimations of 243′–17.2′–sample–60′–60′.[9] The sample was mounted in the $(hk0)$ orientation inside a 7-Tesla vertical-field cryomagnet; in this configuration, the applied magnetic field is perpendicular to the CuO_2 plane.

Figure 4.8 establishes that the magnetic excitations at $(\frac{1}{2}, \frac{1}{2}, 0)$ are indeed gapped below T_c (in zero applied field). Shown are transverse $(h, 1-h, 0)$ scans at an energy transfer of $\omega = 1.75\,\mathrm{meV}$. As expected, there is a clear peak above T_c at $T = 26\,\mathrm{K}$,

[9]The effective collimations are used to calculate the instrument resolution function using the ResLib package [49], which does not explicitly include the possibility of two monochromators.

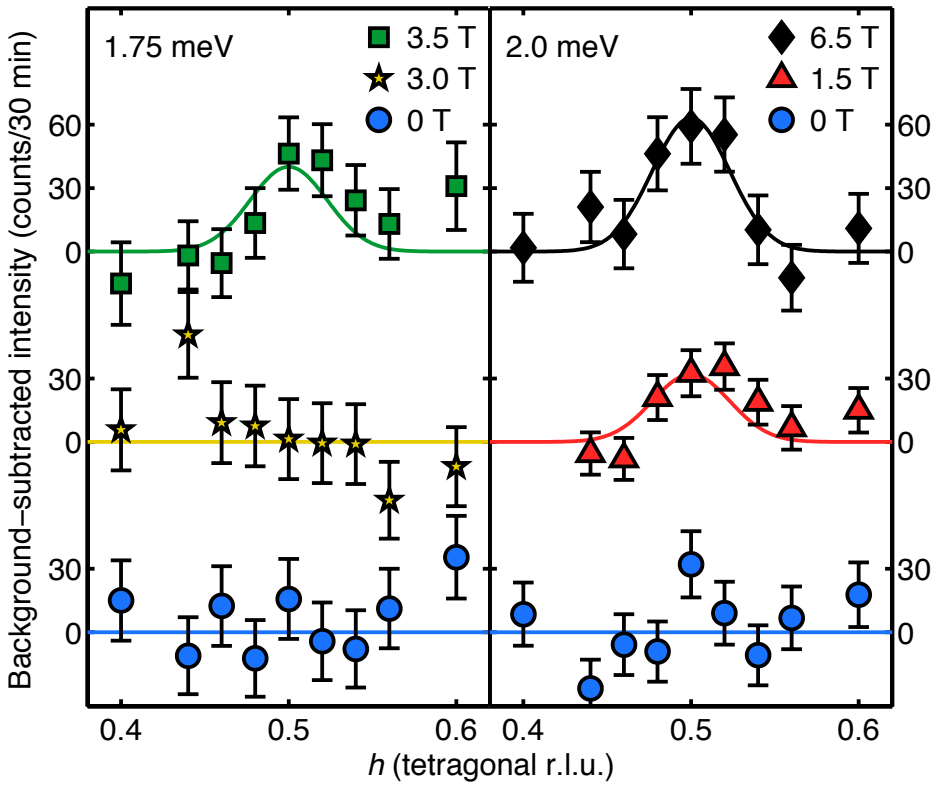

Figure 4.9: Representative transverse $(h, 1-h, 0)$ inelastic scans for NCCO ($x = 0.166$, $T_c = 22\,\mathrm{K}$) at a temperature of $T = 1.8\,\mathrm{K}$ and at energy transfers of $\omega = 1.75\,\mathrm{meV}$ (left panel) and $2\,\mathrm{meV}$ (right panel). Each data set has had a constant background level subtracted and is offset for clarity. The curves are fits to Gaussians centered at $h = 0.5$.

while the signal is suppressed below T_c at $T = 1.8\,\mathrm{K}$.

Figure 4.9 shows that an applied magnetic field can cause this suppressed signal to reappear. To ensure a macroscopically uniform internal field upon changing the field value,[10] the sample was heated above T_c and then cooled back down to $T = 1.8\,\mathrm{K}$ in the new field. At an energy transfer of $\omega = 1.75\,\mathrm{meV}$ (left panel), the magnetic excitations are completely suppressed up to $H = 3\,\mathrm{T}$, and they reemerge at $H = 3.5\,\mathrm{T}$. A similar behavior is seen at the slightly higher energy transfer of

[10]Turning on the magnetic field in the superconducting state would introduce vortices that enter the surface of the sample, but vortex pinning would lead to an inhomogeneous internal magnetic field.

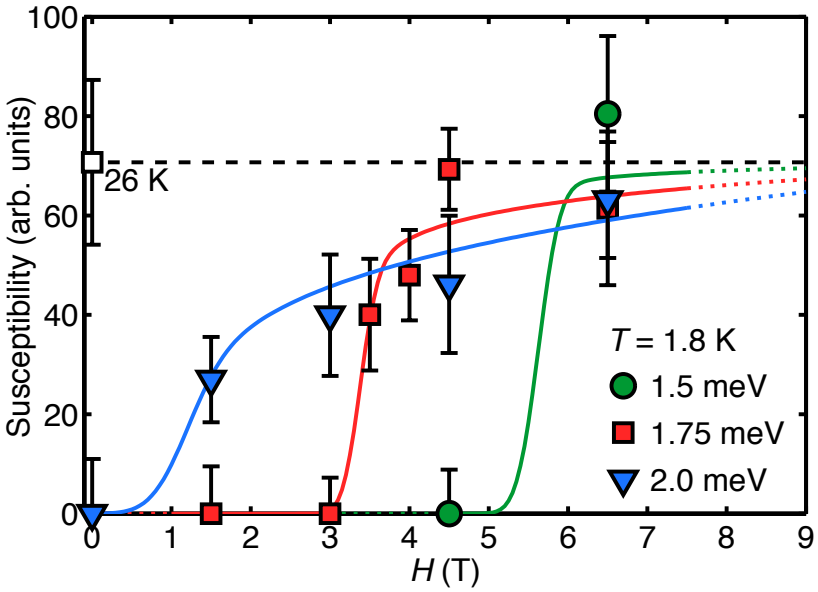

Figure 4.10: Magnetic susceptibility of NCCO ($x = 0.166$, $T_c = 22\,\mathrm{K}$) at $T = 1.8\,\mathrm{K}$ as a function of magnetic field for three representative energy transfers. The normal-state ($T = 26\,\mathrm{K}$) value is shown by the open square and horizontal dashed line. The curves are guides to the eye.

$\omega = 2.0\,\mathrm{meV}$ (right panel). In this case, the peak reappears at a lower field of $H = 1.5\,\mathrm{T}$.

The data are fit to Gaussians, and the values of the Gaussian amplitude from these fits are plotted as a function of magnetic field in Figure 4.10. Included are the two energy transfers from Figure 4.9 as well as $\omega = 1.5\,\mathrm{meV}$. At this lowest measured energy, the intensity remains suppressed until 5 or 6 T, whereas the intensity at $\omega = 1.75\,\mathrm{meV}$ emerges around 3 T. At $\omega = 2\,\mathrm{meV}$, the signal becomes non-zero as soon as a magnetic field is applied. Note that this intensity is plotted as the susceptibility, because the Bose population factor $n + 1$ at $T = 1.8\,\mathrm{K}$ is indistinguishable from 1 at these energies. The signal strength above T_c at $T = 26\,\mathrm{K}$ for $\omega = 1.75\,\mathrm{meV}$ is corrected by the Bose factor and shown as a horizontal dashed line. As the field is increased, the susceptibility at all three energies approaches this normal-state value.

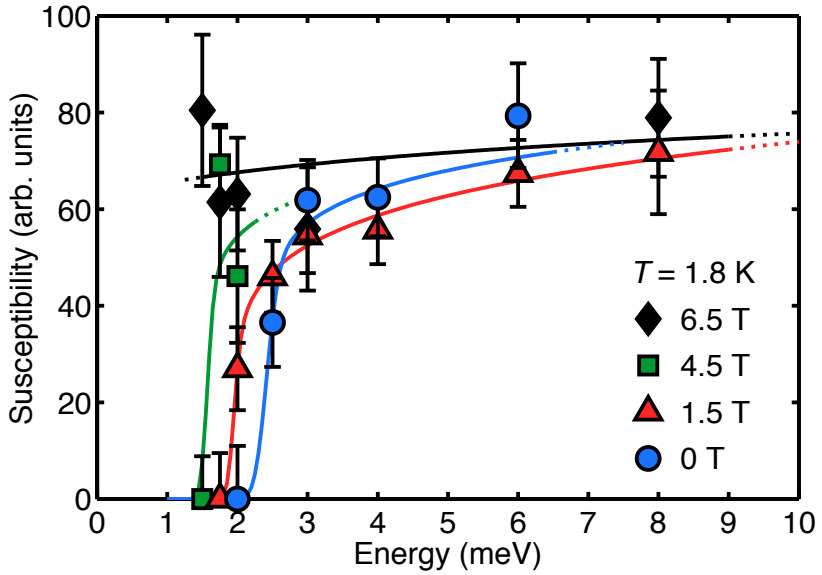

Figure 4.11: The magnetic excitation spectrum of NCCO ($x = 0.166$, $T_c = 22\,\mathrm{K}$) at several values of applied magnetic field. All data are for $T = 1.8\,\mathrm{K}$. Curves are guides to the eye.

The magnetic excitation spectrum (susceptibility versus energy) at low temperature ($T = 1.8\,\mathrm{K}$) is plotted at several magnetic field values in Figure 4.11. The zero-field data show that the energy of the magnetic gap in this sample is 2.5 meV, smaller than in previous work [132], but in accordance with the somewhat lower T_c and higher Ce concentration [110]. The figure shows that the profile of the excitation spectrum shifts rigidly to lower energies as the magnetic field is increased. In particular, note that the signal at lower energies remains zero, even for $H = 4.5\,\mathrm{T}$, while the signal is restored by the magnetic field at higher energies. At the largest field of $H = 6.5\,\mathrm{T}$, the gap can no longer be discerned. Due to a strong increase of the background level at lower energies and the non-zero energy resolution (1.3 meV, FWHM), measurements were not possible below $\omega = 1.5\,\mathrm{meV}$. The strong field-induced background probably results from an overlap of the resolution ellipsoid with the spurious $(Nd,Ce)_2O_3$ magnetic elastic signal [23].

At each magnetic field, I define the gap energy as the energy at which the signal reaches 50% of the maximum. This gap energy is plotted as a function of field in

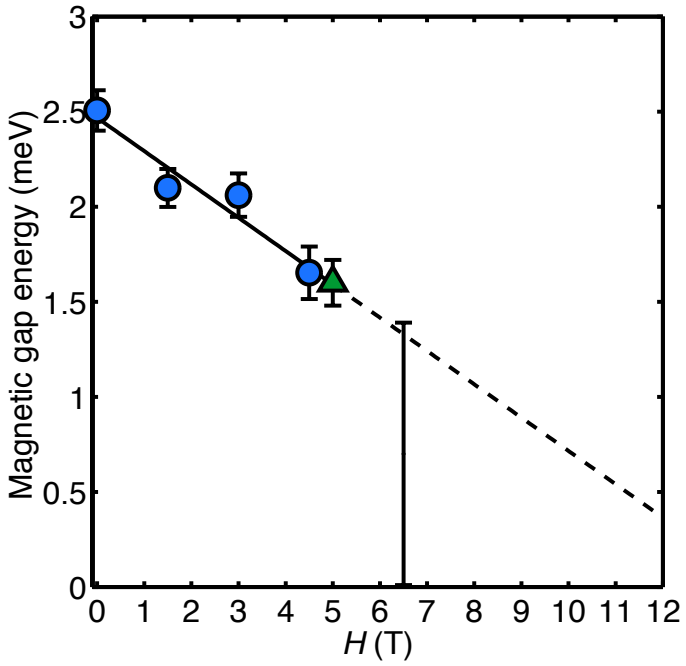

Figure 4.12: Magnetic-field dependence of the gap energy in the magnetic spectrum of NCCO ($x = 0.166$, $T_c = 22\,\mathrm{K}$) at $T = 1.8\,\mathrm{K}$. The relation is linear and extrapolates to a gap-closing field of $H_{gap} = 14 \pm 2\,\mathrm{T}$. The triangle represents data taken at $H = 5\,\mathrm{T}$ in a previous measurement of the same sample (see text). The vertical bar at $H = 6.5\,\mathrm{T}$ reflects the limited knowledge that the gap energy is less than 1.5 meV.

Figure 4.12. The magnetic gap decreases linearly with field, and extrapolating the linear behavior to zero yields $H_{gap} = 14 \pm 2\,\mathrm{T}$ for the estimated gap-closing field. The triangle in the figure represents data taken on a separate occasion on the same sample at $H = 5\,\mathrm{T}$ upon zero-field cooling. Although field cooling is preferred,[11] the result is independent of the cooling method, as might be expected at such high magnetic fields.

4.3 Discussion

Since the publication of the field-effect data, there have been some new developments in the field. Namely, there have been higher-quality zero-field data on

[11] See Footnote 10 on page 113.

PLCCO and NCCO that may have implications for how the above data should be interpreted.

In the first Section below, I discuss the above results in a self-contained context, not yet considering the results of the newer publications. Then, in Section 4.3.2, I describe the discovery of the "resonance" in the magnetic spectrum of PLCCO and NCCO and discuss the possible implications to this field-effect study.

4.3.1 Antiferromagnetism and superconductivity

The main results of this study are the rigid shift of the gapped magnetic spectrum to lower energies and the simple linear dependence of the magnetic gap energy with applied magnetic field. This field dependence is what one would obtain in a naïve picture of a spatially uniform response. In such a picture, the magnetic gap is proportional to the superconducting electronic gap, which in turn is proportional to T_c. According to the vortex Nernst effect measurements, T_c decreases linearly as a function of field (at least at lower fields) [107]. This implies a linear decrease of the SC electronic gap, as indeed measured by Raman spectroscopy [110]. What the data indicate is that the SC magnetic gap also decreases linearly as a function of field.

Note that while the data suggest a uniform magnetic response to a magnetic field, the vortex state is clearly not *electronically* uniform: in these strong magnetic fields, the superconducting bulk is penetrated by vortices with non-superconducting cores. Using the value of H_{c2} from the vortex Nernst measurement, the size of the vortex cores (i.e., the superconducting coherence length) is estimated to be 58 Å at optimal doping [107]. Interestingly, measurements of the antiferromagnetic correlation length (Chapter 3) on superconducting samples show that the relevant magnetic length scale is comparable to this value (10–20$a \approx$ 40–80 Å; see Figure A.3).

The field effect in NCCO is quite different from the case of optimally-doped LSCO. In both cases, the zero-field spectra exhibit a gap associated with superconductivity. However, while a magnetic field induces in-gap states in LSCO [119],

the gapped spectrum of NCCO undergoes a rigid shift towards lower energies. Because measurements below 1.5 meV have not been possible, it is natural to ask whether the formation of some in-gap states in NCCO could be hidden below this energy. Note, however, that the signal strength at 1.5 meV remains zero up until 4.5 T (Figure 4.10). Since the energy resolution here is 1.3 meV (FWHM), the experiment is sensitive to any in-gap intensity down to very low energies. In the context of the theory by Demler *et al.* [122, 123], NCCO probably corresponds to the region of the phase diagram (Figure 4.4) at large r, far from the transition line to magnetic (or spin-wave-density) order.

In contrast to LSCO, and in refutation of the initial elastic neutron scattering measurements on NCCO [127], these data suggest that the ground state in the absence of superconductivity does not contain long-range magnetic order. One indication is the similarity of applying a magnetic field and raising the temperature. In both cases, the profile of the magnetic spectrum shifts rigidly to lower energies. In the case of raising the temperature, the gap does not appear to close until superconductivity completely disappears at T_c [126]. And in the case of applying a magnetic field, the extrapolated gap-closing field (Figure 4.12) is consistent with upper critical field of $H_{c2} \approx 10$–12 T [107]. Consequently, the shrinking to zero of the magnetic gap coincides with the complete suppression of superconductivity. Moreover, the signal strength seen at high magnetic fields equals that in the normal state just above T_c (Figure 4.10). These similarities in behaviors suggests that the non-superconducting ground state at fields beyond H_{c2} resembles the paramagnetic "normal" state above T_c.

A second piece of evidence comes from our complementary study of Ni-doped NCCO.[12] Ni-doping is an alternative method of suppressing superconductivity: upon substituting only about 1% of Cu with Ni, superconductivity in NCCO is completely suppressed [134, 135, 136]. The antiferromagnetic correlation length was measured for an oxygen-reduced non-superconducting sample

[12]Note that a two-axis measurement requires the $(hh\ell)$ scattering geometry, and thus a magnetic field perpendicular to the CuO_2 plane would be a horizontal one and require different equipment. The horizontal-field magnets currently available at neutron scattering facilities do not exceed field strengths of 5 T.

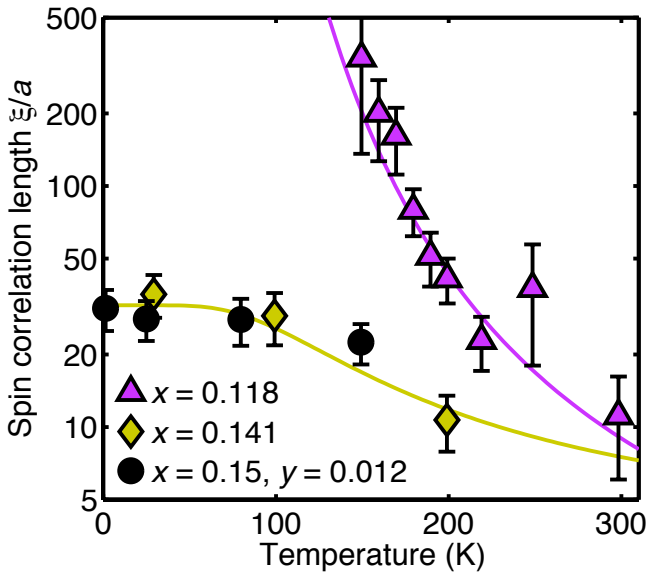

Figure 4.13: Antiferromagnetic correlation length of $Nd_{2-x}Ce_xCu_{1-y}Ni_yO_4$ ($x = 0.15$ and $y = 0.012$) on a logarithmic scale as a function of temperature. The amount of Ni is sufficient to completely suppress superconductivity, but the correlation length remains characteristic of a superconducting sample with short-range correlations (e.g., $x = 0.141$) and not of a non-superconducting sample with long-range antiferromagnetic order (e.g., $x = 0.118$).

of $Nd_{2-x}Ce_xCu_{1-y}Ni_yO_4$ (with $x = 0.15$ and $y = 0.012$) using the two-axis energy integrating technique (see Section 2.4.3). Figure 4.13 shows that this system at low temperatures has a finite correlation length. The temperature-dependence of the correlation length is identical to a similarly-doped superconducting sample with $x = 0.141$. In particular, note that removing superconductivity does not change the behavior to that of a non-superconducting sample with long-range antiferromagnetic order (the $x = 0.118$ data are shown for comparison in Figure 4.13). Clearly, the non-superconducting ground state induced by Ni-doping does not have long-range magnetic order. This lends credence to the implication of the field-effect study, namely that the non-superconducting state induced by a magnetic field also does not have long-range order.

4.3.2 Magnetic resonance

Since the publication [101] of the results in Section 4.2, there have been advances in the measurement of the zero-field magnetic excitation spectra in the electron-doped cuprates. In particular, recent studies have claimed to identify the magnetic resonance, a topic of strong interest in the hole-doped cuprates. The resonance is a magnetic excitation at the antiferromagnetic zone center $\mathbf{Q}_{\mathrm{AF}} = (\frac{1}{2}, \frac{1}{2})$, and is well-defined in momentum and energy. At optimal doping, the resonance appears upon cooling below T_c, and its intensity approximately follows a power-law behavior. It has been observed in many of the hole-doped cuprates, including $YBa_2Cu_3O_{6+\delta}$ [137, 138, 139, 140], $Bi_2Sr_2CaCu_2O_{8+\delta}$ [141, 142], $Tl_2Ba_2CuO_{6+\delta}$ [143], and most recently in $HgBa_2CuO_{4+\delta}$ [144]. Interestingly, similar magnetic resonances have been discovered in other unconventional superconductors,[13] namely the heavy fermion compounds UPd_2Al_3 [145] and $CeCoIn_5$ [146] and the newly discovered iron arsenide superconductors, such as $(Ba,K)Fe_2As_2$ [147]. Furthermore, our group has discovered a universal ratio $E_{\mathrm{r}}/2\Delta_0 = 0.64(2)$ between the magnetic resonance energy E_{r} and the superconducting electronic gap Δ_0 for all of these compounds [148]. How the magnetic resonance relates to the mechanism of superconductivity in these systems is the matter of an ongoing debate.

The case for universality of the magnetic resonance in the high-T_{c} cuprates was strengthened with the report by Wilson *et al.* [133] of a resonance in electron-doped PLCCO. Their data in Figure 4.14 show an enhancement around $\omega = 11$ meV upon cooling into the superconducting state (right panel). As with the hole-doped cuprates, the intensity of the peak increases below T_{c} (left panel). The energy of this feature in this electron-doped cuprate is much smaller than the typical magnetic resonance energy of 40–50 meV in the hole-doped cuprates, and it appears to follow the universal scaling with the electronic gap Δ_0 [148]. One difference with the hole-doped case is the lack of correspondence with a special point in the magnetic excitation spectrum (i.e., the saddle point of the "hourglass" dispersion). This is perhaps simply because, unlike the hole-doped case, the response at all energies

[13] Compounds whose superconductivity has not been explained by the BCS theory.

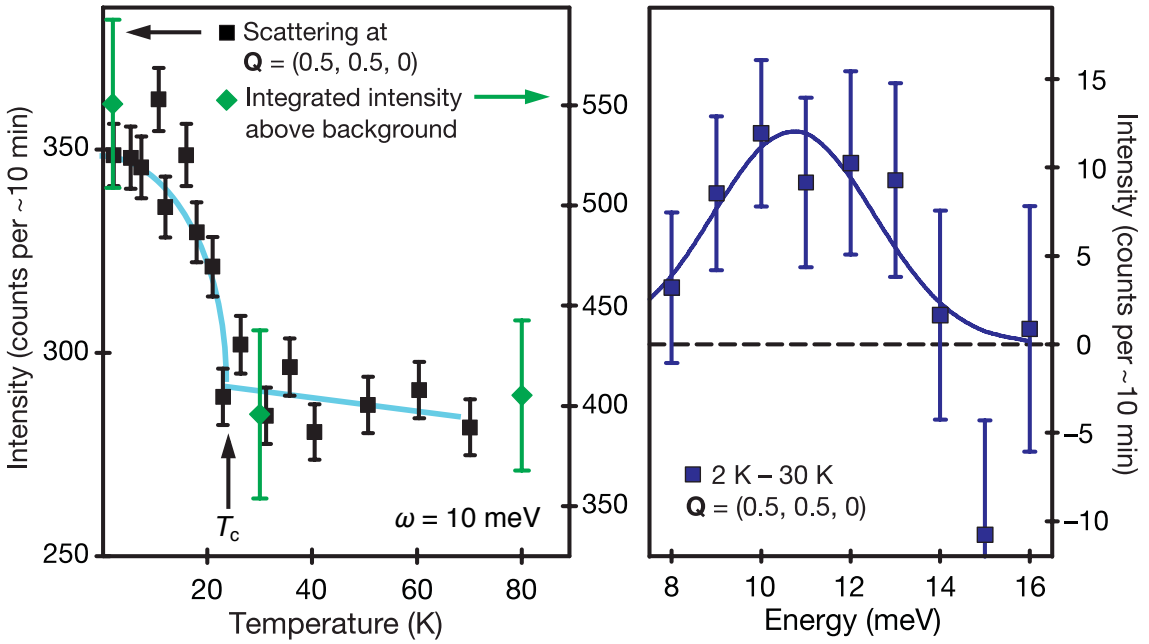

Figure 4.14: Evidence for a magnetic resonance in superconducting PLCCO ($x = 0.12$). Left panel shows the intensity at $\mathbf{Q} = (\frac{1}{2}, \frac{1}{2}, 0)$ and $\omega = 10\,\text{meV}$ as a function of temperature. Also included is the result for the integrated intensity of the peak found from full $\mathbf{Q}$-space scans at three temperatures. Right panel shows the intensity difference between 2 K and 30 K at $(\frac{1}{2}, \frac{1}{2}, 0)$ as a function of energy. Adapted from [133].

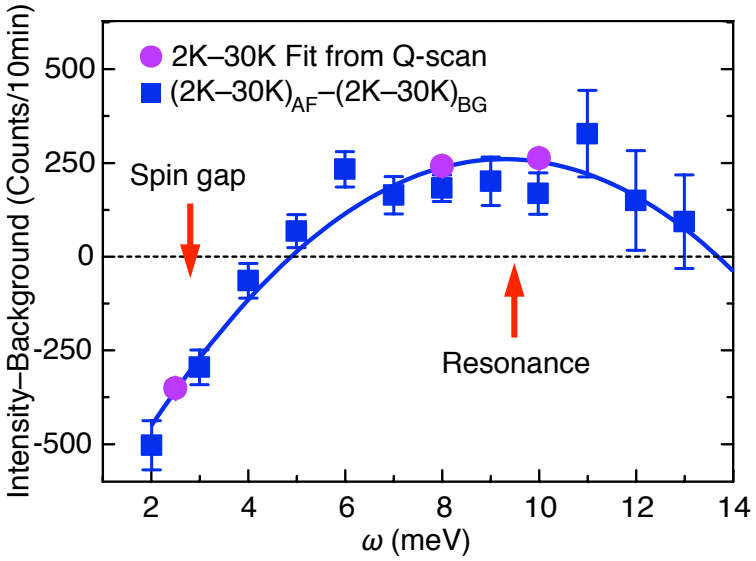

Figure 4.15: Intensity change due to superconductivity in NCCO $x = 0.15$. The circles are the difference in intensities found in **Q**-space scans between 2 K and 30 K. The squares are the difference between the intensity change at the antiferromagnetic wavevector $(0.5, 0.5, 0)$ and the intensity change at a background point $(0.66, 0.34, 0)$. Reproduced from [149].

in the electron-doped cuprates appears to be located at $(\frac{1}{2}, \frac{1}{2})$. Another minor point is that the intensity enhancement due to superconductivity is only about 30% of the total intensity (see the integrated intensity data in the left panel); this relatively weak intensity enhancement is likely the reason why the feature was not discovered any sooner.

The same group made similar measurements on a sample of optimally-doped NCCO [149]. Figure 4.15 shows the change in the magnetic excitation spectrum due to superconductivity. The data include only three points for which full momentum scans were performed across the antiferromagnetic wavevector, above and below T_c. At all of the other energies, only two points in **Q**-space were measured, and thus the uncertainties are higher. The data show a decrease in intensity at lower energies (due to the formation of the superconducting magnetic gap[14]) and an increase in intensity at higher energies. The authors concluded that NCCO, like

[14] As mentioned in Section 4.1.4, the superconducting magnetic gap has not been seen in PLCCO.

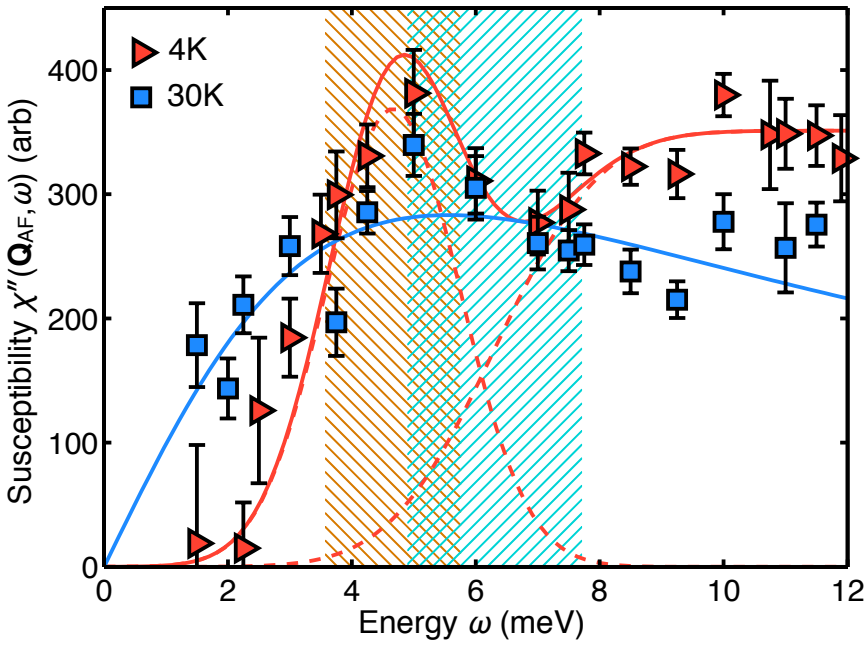

Figure 4.16: Susceptibility as a function of energy in NCCO ($x = 0.157(7)$) for $T = 4\,\mathrm{K}$ and $30\,\mathrm{K}$. The data are the fitted Gaussian amplitudes for transverse scans in **Q**-space at each energy and temperature. The shaded regions represent the spread in energies of the A_{1g} mode (left region) and B_{1g} mode (right region) expected from a sample with $x = 0.157(7)$ [110]. The curves are fits as described in the text.

PLCCO, exhibits a resonance around $\omega = 10\,\mathrm{meV}$. Note, however, that the intensity enhancement interpreted as the resonance is very broad, ranging from about 6 meV all the way up to 12 meV. Coupled with unavoidable systematic errors in the experiment and with a simple subtraction of intensities, it is difficult to accept the claim of a well-defined energy. Moreover, a resonance energy of around 10 meV would not follow the universal scaling relation with Δ_0 [148].

To investigate this further, our group performed careful measurements of the magnetic excitation spectrum of an NCCO sample with $x = 0.157(7)$ [81]. Figure 4.16 shows the susceptibility (intensity divided by the Bose factor) as a function of energy in the superconducting state at $T = 4\,\mathrm{K}$ and in the normal state at $T = 30\,\mathrm{K}$. Unlike the work by Zhao *et al.* [149], all of the data result from Gaussian fits to full scans in **Q**-space. The normal-state data are fit to a simple Lorentzian response

function

$$\chi''(\mathbf{Q}_{\mathrm{AF}}, \omega) \propto \frac{\Gamma\omega}{\Gamma^2 + \omega^2}\,, \tag{4.1}$$

where the fitted value for the characteristic energy is $\Gamma = 5.7 \pm 0.5\,\mathrm{meV}$. The 4 K data, on the other hand, are fit to the sum of two components (indicated as dashed curves). The first is a Gaussian, whose position and width are determined by the expected spread of the A_{1g} mode given the Raman scattering work by Qazilbash *et al.* [110] and the particular composition range of our sample. The second component is a step function convolved with a Gaussian whose position and width are determined by the expected spread of the B_{1g} mode given the same assumptions. The B_{1g} mode has been interpreted as $2\Delta_0$, the pair-breaking energy [110], and thus in this interpretation the step function in the magnetic spectrum is the true magnetic gap. The A_{1g} mode is more difficult to interpret, but has been associated with the magnetic resonance in some hole-doped cuprates [150]. Thus in this two-component interpretation of the data, there is an in-gap peak around $\omega = 5\,\mathrm{meV}$ that might be the magnetic resonance in NCCO: the magnetic susceptibility in this energy range increases monotonically below T_c [81], as would be expected for the magnetic resonance.

There are several strengths to this interpretation. Note that the fit to the 4 K data (as well as a similarly good fit to the difference of the two data sets [81]) has only two adjustable parameters, namely the amplitudes of the two components. The picture of two energy scales explains why the apparent gap in the magnetic spectrum around 3 meV is so small compared to the pair-breaking energy $2\Delta_0$. Moreover, unlike the interpretation by Zhao *et al.* [149], the ratio of the lower magnetic energy to $2\Delta_0$ is consistent with the universal value found for the hole-doped cuprates, heavy-fermion compounds, and iron-arsenides [148].

However, I have my doubts that the data conclusively show the existence of two energy scales.[15] First, the 4 K data (and the difference data not shown) have been fit to a rather complicated form, but are also consistent with a single step function around 3 meV and a constant value at higher energies. Second, these measurements

[15] This paragraph contains my personal opinions, and not necessarily those of the other authors of [81].

were performed on a sample with a relatively large Ce concentration range, and if the two-component interpretation is correct, one would expect sharp features in a sample with a better-defined Ce concentration. We have attempted further measurements on such samples, but have not seen such a sharpening of features so far. Third, at the low signal rates of these measurements, spurious peaks become more of a problem. If the enhanced intensity at 5 meV is real, then it should be present at different spectrometer conditions. However, an initial attempt at using a final energy of $E_f = 13.7$ meV (instead of the usual 14.7 meV) did not show any enhancement of intensity at 5 meV.

In any case, it is necessary to revisit the magnetic-field-effect study in light of the magnetic-resonance scenario. If there is indeed a magnetic resonance around 5 meV (in zero field), then what was interpreted as a magnetic gap of 2.5 meV in the $x = 0.166$ sample could be the leading edge of the magnetic resonance. It follows that it is this leading edge which decreases linearly with an applied magnetic field. Figure 4.10 shows that the leading edge remains well-defined up to the highest field at which it is still discernible; this implies that the magnetic resonance mode itself remains well-defined as the magnetic field is applied. Moreover, the intensity of the magnetic resonance seems to remain constant. Regarding the $2\Delta_0$ feature, it too must decrease linearly in energy along with the magnetic resonance (consistent with the Raman scattering results [110]), since the data show a rigid shift of the entire spectrum and no evidence of a separation between two energy scales. If the magnetic resonance energy remains proportional to 2Δ, then the observation that the gap decreases to zero at or near H_{c2} still holds. The correlation length measurement of the Ni-doped sample remains as strong evidence for the lack of long-range order in the non-superconducting ground state. The main conclusion of the magnetic-field-effect study still holds, namely, that superconductivity does not compete with antiferromagnetic order (at least in the sample that was measured).

Appendix A

Supplementary information

A.1 NCCO samples

Table A.1 lists all of the NCCO samples relevant to the studies described in this Thesis. Listed are the nominal Ce concentration, the actual measured Ce concentration, the mass (at the time of the principal measurement) and superconducting T_c. Most of the samples are oxygen reduced; the exceptions are noted in the Table. The Table also indicates the samples for which results are shown and/or discussed in this Thesis. All of the samples below the horizontal line have been prepared and characterized as described in Section 2.3.2, i.e., with multiple ICP measurements taken along the diameter of disks at either end and with surfaces polished to improve the Ce homogeneity. The Ce concentrations for the samples above the horizontal line were not measured as carefully. Dashes indicate measurements that were not performed before the sample was altered or lost (e.g., to disintegration).

While the measured actual Ce concentration differs from the nominal Ce concentration, the difference between the two is systematic. Figure A.1 shows the relationship between the actual and nominal Ce concentrations in recent samples. All of the samples represented in Figure A.1 have had their surfaces polished. The plotted values and error bars are the average and standard deviation of the ICP measurements from the inner portions of the disks from either end of each sample;

Name	Nominal x	Actual x	Mass (g)	T_c (K)
Mang19[†]	0.10	0.106(7)	1.64	0
Mang40[†§]	0.15	0.166(10)	4.96	22
Eugene1[†]	0.04	0.038(11)	4.40	0
Eugene2	0.15	—	2.36	22
Eugene3	0.04[*]	0.042(6)[*]	2.60	0
Yu-12:15:04[†]	0.125	0.129(6)	—	—
Eugene5[†]	0.075	—	—	0
Eugene6[†]	0.15	0.154(7)	—	24
Eugene8[†]	0.1325	0.134(6)	2.30	—
Eugene9[†]	0.1375	0.145(4)	4.11	19
Inna-8:25:05	0.135	0.142(6)	2.79	25
Eugene10B	0.1425	0.150(4)	1.55	26
Eugene11	0.13	0.134(4)	1.69	21
Eugene13[†]	0.17	0.181(4)	2.75	15
Eugene14	0.17	0.180(7)	7.67	19
Eugene15[♯]	0.134	0.141(4)	—	—
Eugene16[‖]	0.14	0.157(7)	6.17	25
Eugene19A[‡]	0.125	0.133(3)	4.17	24
Eugene19C	0.125	0.136(6)	3.12	24
Eugene20[‡]	0.131	0.138(5)	2.40	19
Eugene21[‡]	0.135	0.141(4)	3.22	24
Eugene22	0[*]	0[*]	2.78	0
Eugene23[‡]	0.146	0.156(4)	4.99	25
Eugene24[‡]	0.121	0.128(2)	3.58	20
Eugene26[‡♯]	0.105	0.118(3)	2.96	0
Eugene28B[‡]	0.115	0.126(5)	4.11	16
Eugene30	0.11	0.112(2)	1.25	15
Eugene32B[‡]	0.11	0.120(1)	1.98	12
Eugene34A[‡♯]	0.114	0.123(2)	2.03	0

[*] as-grown
[†] two-axis neutron scattering ([19], Figure A.2)
[‡] two-axis neutron scattering (Chapter 3, Figure A.3)
[§] inelastic neutron scattering ([101], Chapter 4)
[‖] inelastic neutron scattering ([81])
[♯] μSR (Chapter 3)

Table A.1: NCCO samples.

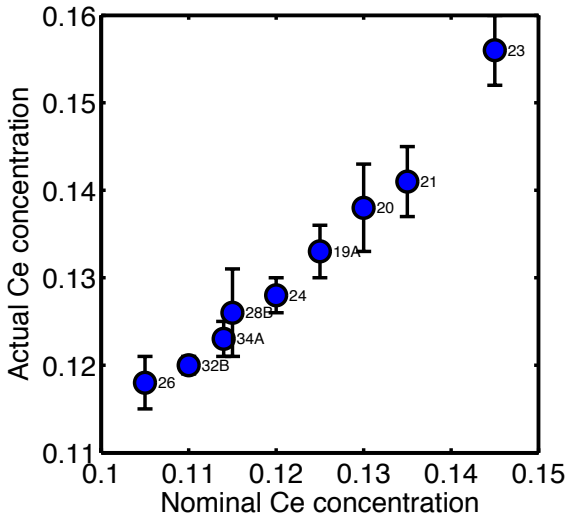

Figure A.1: Actual Ce concentration measured by ICP versus nominal Ce concentration in recent NCCO samples. The labels by the data points are sample numbers.

usually, a large portion of the spread is due to the difference of Ce concentration between the two ends of a sample. Perhaps because polishing removes a portion with lower Ce concentration (see Figure 2.17), the actual Ce concentration is consistently larger than the nominal Ce concentration; the difference is about $\Delta x = 0.01$.

A.2 Two-axis measurements

This Section contains material supplementary to Chapter 3.

A.2.1 Magnetic correlation length

Here I show the antiferromagnetic correlation length data that were left out of Figure 3.9 and Figure 3.10 for clarity. Figure A.2 shows data from older samples which were not grown using all of the refinements described in Section 2.1, and which did not receive the polishing treatment and systematic ICP measurements described in Section 2.3.2. Thus these samples have a larger Ce inhomogeneity and

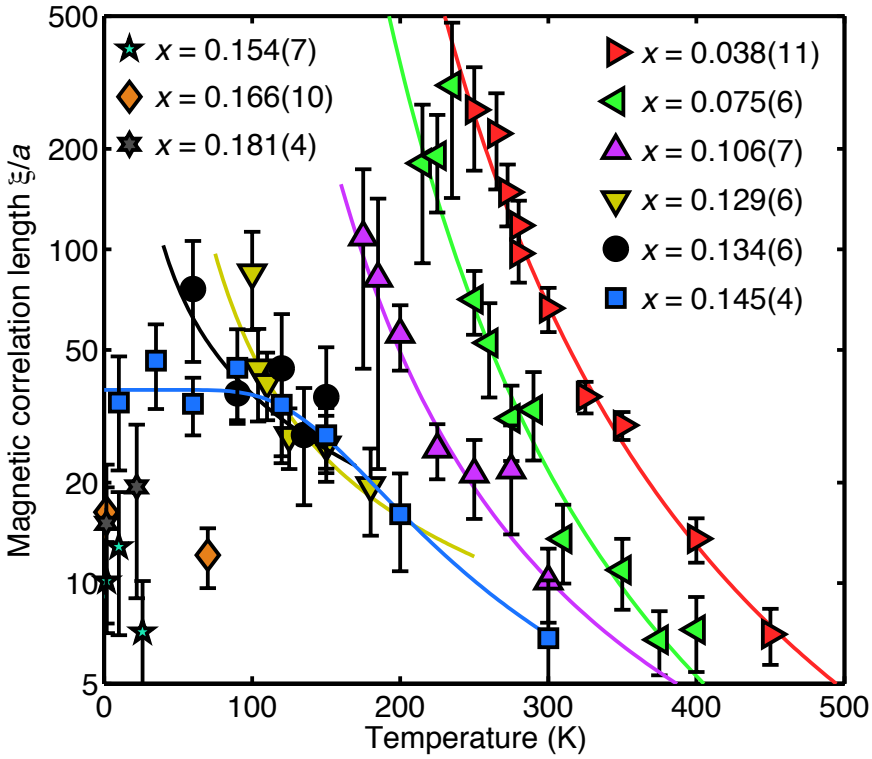

Figure A.2: Correlation length as a function of temperature in older samples. Most of these data are included in Figure 3 of [19].

some of the values and errors on x may be somewhat inaccurate. Most of these data are shown in Figure 3 of [19]. The behavior of the $x = 0.129$ and $x = 0.134$ samples led us to believe that the transition in behaviors occurs around $x = 0.134$, and that this doping level might constitute a quantum critical point. Newer measurements on samples with similar Ce concentrations ($x = 0.128$ and $x = 0.133$) have shown that the correlation length remains finite at lower temperatures. One limitation was the custom at the time of not performing measurements below the apparent Néel temperature (e.g., in the $x = 0.129$ sample).

Note also the correlation length values for $x > 0.15$. While the measured values are lower than the behavior seen in the newer $x = 0.141$ sample, they are not significantly lower considering the relatively large changes in x. While the correlation length may decrease intrinsically with increasing doping, part of the

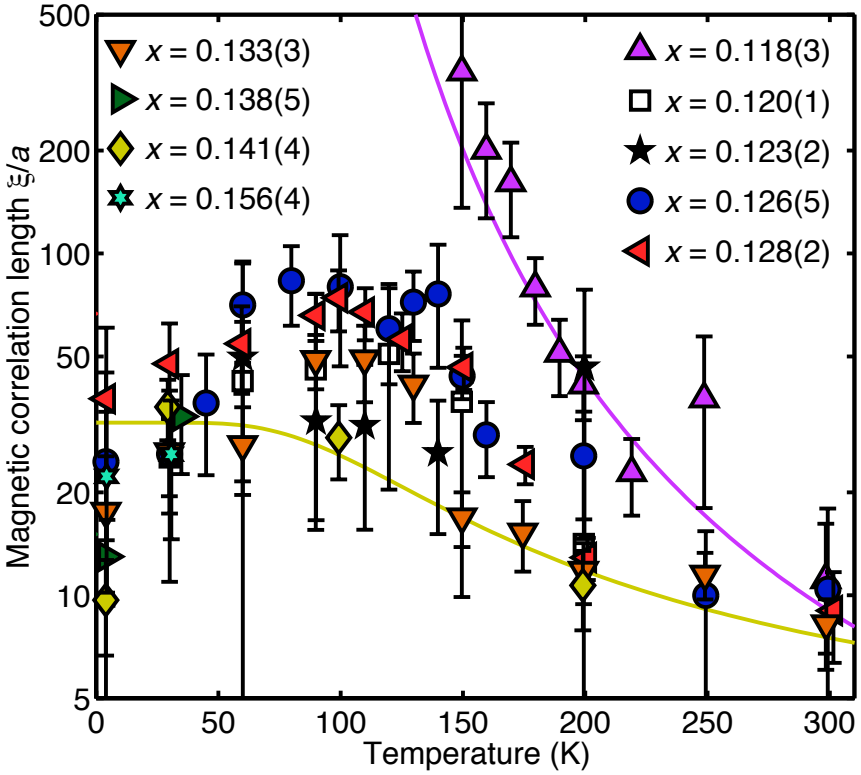

Figure A.3: Correlation length as a function of temperature in newer samples. Most of these data are included in Figure 3.10.

reason for the lower values could also be that many of these measurements were performed in the superconducting state (see below).

Figure A.3 shows all of the data from newer samples. It is the same as Figure 3.10, but contains data from additional samples[1] as well as correlation length results for $T \approx 4\,\mathrm{K}$ in the superconducting state. The correlation lengths at these lowest temperatures are lower than the values at $T \approx 30\,\mathrm{K}$ (in some cases significantly so). This is likely due to the opening of a gap in the magnetic excitation spectrum in the superconducting state (see Chapter 4).[2] Because the momentum width at

[1] While the Ce concentration range $\Delta x = 0.002$ for $x = 0.128$ is rather small according to the ICP measurements from the end pieces, this crystal is a relatively long sample and thus its true inhomogeneity may be larger.

[2] All correlation lengths shown here were obtained with $E_i = 14.7\,\mathrm{meV}$, which is 3–4 times larger than the superconducting magnetic gap.

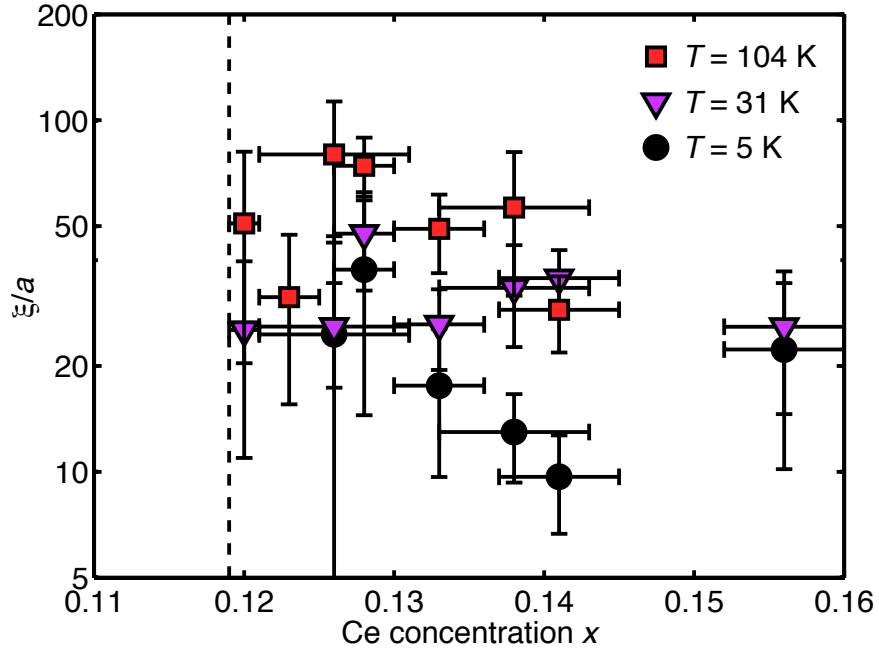

Figure A.4: Correlation length as a function of Ce concentration x in newer samples at three representative temperatures. The vertical dashed line indicates $x_c = 0.119$. The data labeled $T = 31$ K are included in Figure 3.11.

lower energies is smaller than at higher energies [81], the two-axis momentum width increases, and the measured correlation length decreases. See Section A.3 for simulations of two-axis measurements based on triple-axis data that show a decrease of the correlation length in the superconducting state.

The correlation lengths for the newer samples are shown in Figure A.4 as a function of Ce concentration. The data labeled $T = 31$ K are included in Figure 3.11 and show that the low-temperature correlation length (in the non-superconducting state) is essentially constant above $x_c = 0.119$ (vertical dashed line). The data at the higher temperature $T \approx 100$ K show a larger correlation length for some of the samples, but this may be due to a small volume fraction that behaves like $x < x_c$ (see Section A.2.2). Ignoring the two lowest-doped samples in the figure, the $T \approx 100$ K correlation length seems to increase as x_c is approached from above; with the addition of the newest data at $x = 0.120$ and $x = 0.123$ this is shown not

to be a significant effect. The data at $T = 5\,\mathrm{K}$ show that, as mentioned above, the correlation length tends to decrease in the superconducting state.

A.2.2 Two-axis amplitude

During the analysis of the two-axis scans the data are also fit to simple Gaussians (in addition to the usual fitting routine described in Section 2.4.3). The resulting values for the amplitude have been normalized by the sample mass and across the two spectrometers where these samples were measured,[3] and are plotted in Figure A.5. While this is not a true physical quantity because of the effects of the spectrometer resolution, the observed characteristics of the temperature dependence can provide some insight into the strange behavior of the correlation length in some samples.

The $x = 0.118$ sample is the only one shown in the figure that exhibits genuine long-range order according the measured correlation length. It is the only such sample that has been measured extensively below its Néel temperature.[4] As the temperature is lowered, the amplitude of the two-axis signal increases to a peak at its Néel temperature and then decreases.[5] Note, in particular, that the measured amplitude reaches zero above $T = 0$.

The behavior in the other samples (which do not show long-range order) is qualitatively different: the strength of the signal at the lowest temperatures remains non-zero. Note that the samples in which the peak in two-axis amplitude is the least pronounced (e.g., $x = 0.123$ and $x = 0.141$) show monotonic behavior of the correlation length. Conversely, the samples in which the peak is most pronounced (e.g., $x = 0.126$, $x = 0.128$, and $x = 0.133$) show an increase in the measured correlation length at the (same) intermediate temperatures (see Figure A.3). These samples (which tend to have larger measured Ce inhomogeneity) may contain small volume fractions that behave similar to the $x = 0.118$ sample, for which the correlation length is large and the temperature dependence of the intensity is

[3] Conditions at each spectrometer were largely kept the same for the measurement of different samples.

[4] In fact, I have not found any examples in the literature.

[5] The width of the signal remains resolution limited ($\xi > 200a$) below T_N (not shown).

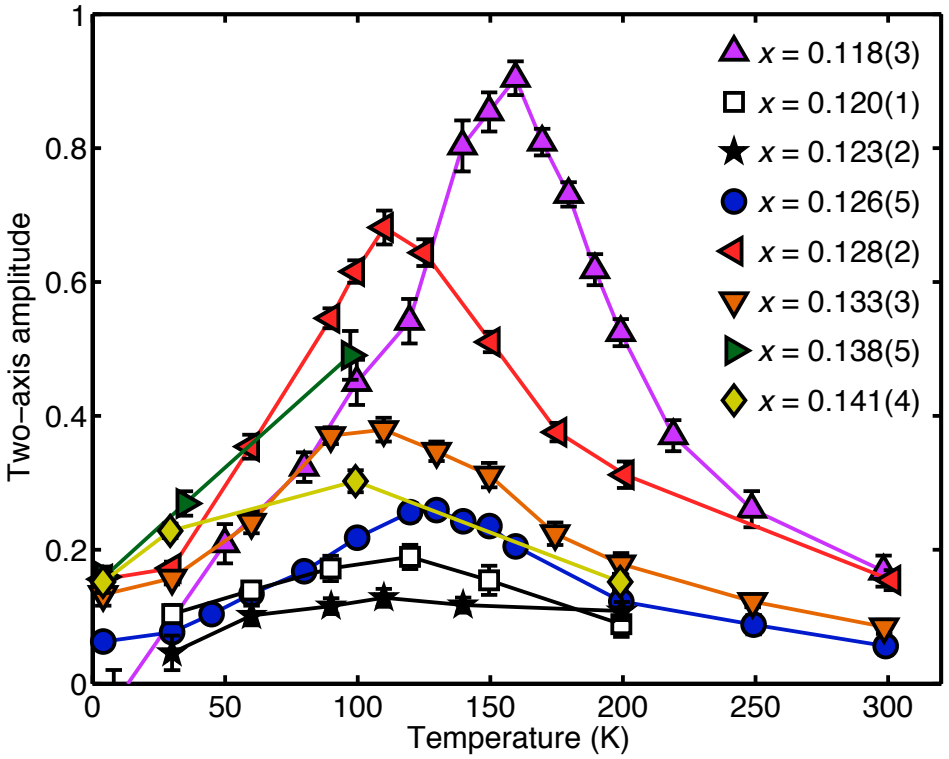

Figure A.5: The two-axis amplitude, normalized by mass and among spectrometers, plotted as a function of temperature for samples in the range $0.118 \leq x \leq 0.141$.

strongly peaked. Thus the increase in measured correlation length in these samples at intermediate temperatures may be an effect of inhomogeneity, and the genuine behavior for $x > x_c$ is exhibited by the samples with $x = 0.123$ and $x = 0.141$.

Figure A.6 shows that the two-axis amplitude at $T \approx 100\,\mathrm{K}$ does not exhibit an obvious dependence on Ce concentration x: these data vary quite widely (up to a factor of 5) even in a rather narrow Ce concentration range. This is due to the variation in Ce inhomogeneity, and is a further indication that not all of the samples exhibit genuine behavior around $T = 100\,\mathrm{K}$. On the other hand, the amplitude of the $T \approx 30\,\mathrm{K}$ signal has a smooth non-monotonic doping dependence, with a maximum near $x = 0.14$. From these data, it appears that samples just above $x_c = 0.119$ have intrinsically weaker signal (in the energy range, $E_i = 14.7\,\mathrm{meV}$, of the experiment).

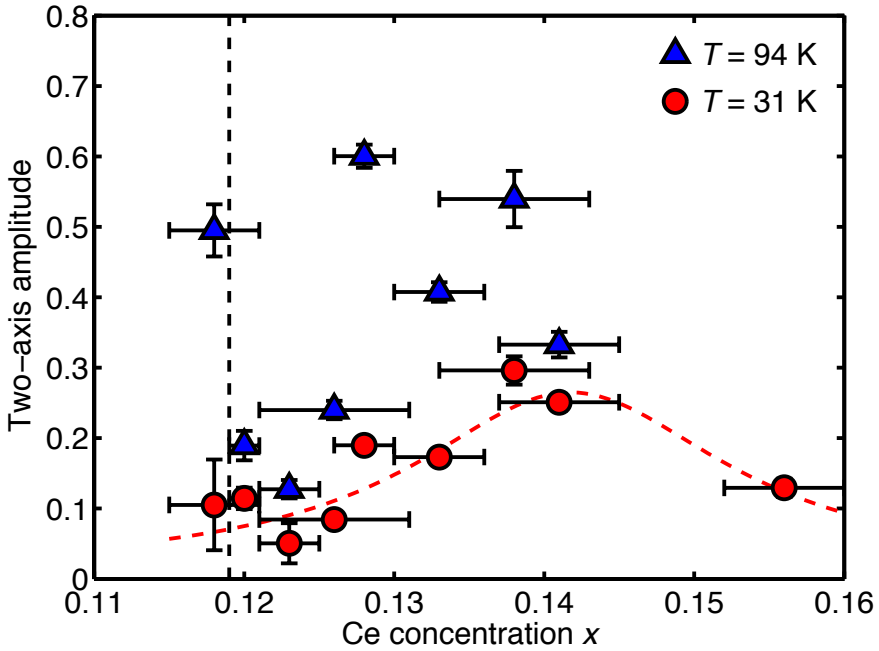

Figure A.6: The two-axis amplitude, normalized by mass and among spectrometers, as a function of Ce concentration x at $T \approx 100\,\mathrm{K}$ and $T \approx 30\,\mathrm{K}$. The dashed curve through the $T \approx 30\,\mathrm{K}$ data is a guide to the eye.

A.2.3 Pseudogap

The "pseudogap" phenomenon is a set of anomalies associated with the decrease in low-energy states (the opening of a partial gap) along parts of the Fermi surface. While a pseudogap exists in both hole-doped and electron-doped materials, the physical signatures are different enough that the phenomena may be fundamentally different in the two classes of materials [82, 151]. In the electron-doped cuprates, the pseudogap is observed in angle-resolved photoemission as a gap on the order of 100 meV located between the nodal (π, π) and antinodal $(0, 0)$ directions [80, 152], while in the hole-doped cuprates, the pseudogap is found along the antinodal directions and is similar in size to the superconducting gap [153].

In the electron-doped cuprates, the pseudogap is readily seen in optical conductivity spectra and found to develop below a temperature T^* that decreases monotonically with increasing Ce concentration. The results for NCCO crystals

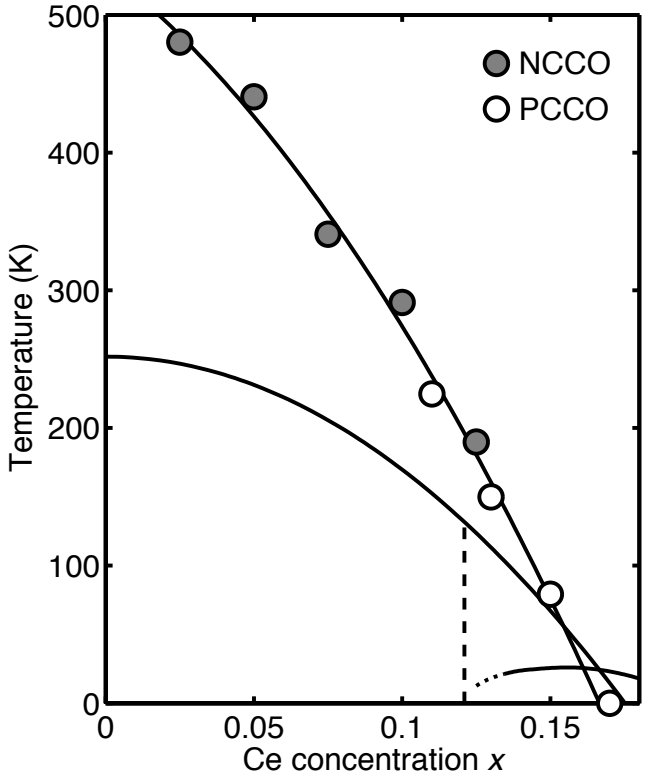

Figure A.7: The pseudogap temperature T^* as a function of Ce concentration as measured by optical spectroscopy on NCCO crystals [154] and $Pr_{2-x}Ce_xCuO_4$ (PCCO) films [155]. The curve through the points is a fit to a parabola and is used in the analysis of the magnetic correlation length along $T^*(x)$. Curves for T_N and T_c are provided for reference.

[154] and $Pr_{2-x}Ce_xCuO_4$ (PCCO) thin films [155] are shown in Figure A.7. Because the T^* curve separates regions in the phase diagram where the Fermi surface is disconnected (below and to the left of $T^*(x)$) and fully connected (above and to the right of $T^*(x)$), the Ce concentration x^* at which T^* drops to zero marks a possible topological transition of the Fermi surface [154]. Note that x^* is near the disappearance of apparent antiferromagnetic order around $x = 0.17$. Anomalies in transport measurements that have been reported in this region [88] may be associated with the pseudogap phenomenon and not with the magnetic transition, as has been claimed [89].

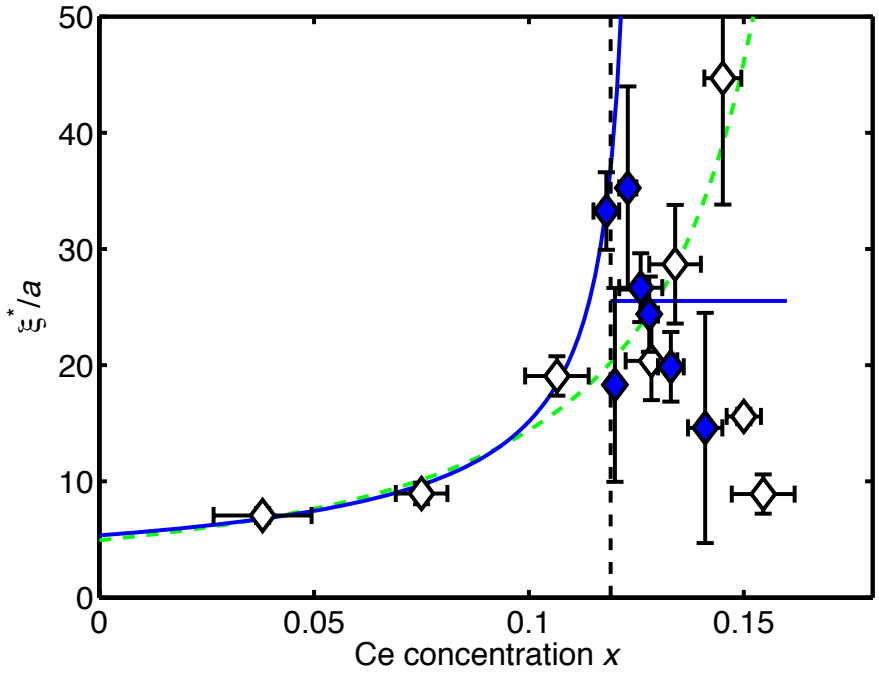

Figure A.8: Correlation length $\xi^* \equiv \xi(T^*)$ at the pseudogap temperature as a function of Ce concentration. Open and filled symbols represent data from older and newer samples, respectively. The vertical dashed line indicates $x_c = 0.119$. The solid curve is a power-law fit to the data with $x < x_c$, and the solid horizontal line indicates the average value for $x > x_c$. The dashed curve is the power-law relationship $\xi^*/a = (x^* - x)^{-1}$ reported in [19].

In [19], we reported a signature of the pseudogap in the correlation length data. The correlation length $\xi^* \equiv \xi(T^*)$ at the pseudogap temperature was found to have a power-law dependence on x. While ξ^* was found to decrease above $x \approx 0.15$, the behavior at lower doping followed the particularly simple form $\xi^*/a = (x^* - x)^{-1}$. The addition of the newer, more precise data shows that this form no longer describes the data well (see Figure A.8).[6] Below $x_c = 0.119$, a fit to the power-law form $\xi^*/a = A(x_0 - x)^{-\nu}$ yields the parameters $A = 1.4 \pm 1.1$, $x_0 = 0.125 \pm 0.01$,

[6]The older data are only inconsistent with the newer data in two respects. The value at $x = 0.145$ is rather high; this was a particularly large sample, that I believe must have had a larger Ce inhomogeneity than was apparent at the time. It probably contained a portion with the behavior of $x < x_c$ samples and thus had a larger correlation length than the newer $x = 0.141$ sample (compare Figures A.2 and A.3). The values at $x = 0.150$ and $x = 0.154$ are rather low; this is probably because of the effects of superconductivity in the measurements of these samples.

and $\nu = 0.6 \pm 0.3$. For $x > x_c$, ξ^* is relatively constant. It has been predicted theoretically that T^* is the temperature below which magnetic correlations become longer than a characteristic thermal length ξ_{th} [151]. This needs to be further tested with measurements on additional samples with $x < x_c$.

There have been recent reports that T^* corresponds to the onset of a novel magnetic order. Polarized neutron diffraction measurements of the hole-doped compounds $YBa_2Cu_3O_{6+x}$ [156, 157] and $HgBa_2CuO_{4+\delta}$ [158] indicate that this magnetic order preserves the translational symmetry of the lattice and is thus quite different in nature from the antiferromagnetic fluctuations usually studied with neutron scattering (including those studied in this Thesis). It remains an open question whether T^* in the electron-doped cuprates is associated with a similar sort of novel magnetic order.

A.3 Two-axis simulations

The two-axis measurements discussed in Chapter 3 and the inelastic triple-axis measurements described in Chapter 4 and in [81] are probes of the same antiferromagnetic excitation spectrum in NCCO. Here I attempt to tie the two types of measurements together by taking the measured excitation spectrum from triple-axis measurements and simulating two-axis scans. The simulations can then be compared to actual two-axis data.

While I have stated that the two-axis method measures the instantaneous scattering function (2.22)

$$S_{inst}(\mathbf{Q}_{2D}) = \int S(\mathbf{Q}_{2D}, \omega)\, d\omega\,, \tag{A.1}$$

this is not strictly true, even taking into account that the energy integration is over a finite range (up to $E_i = 14.7$ meV in this Thesis). There are two factors that change with the energy transfer ω. The first is the Bose population factor. Because the energy integration includes both positive and negative ω, the magnetic excitation at any particular ω is weighted by $2n(\omega) + 1$. The second factor is due to the resolution function. As described in Section C.2, the two-axis resolution function

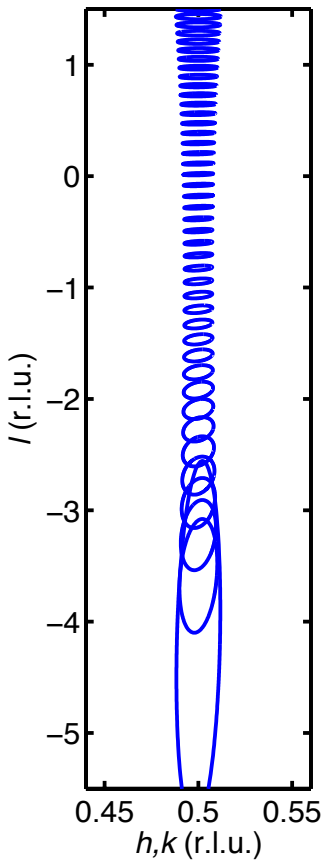

Figure A.9: Resolution function calculated for two-axis neutron scattering at several values of ℓ corresponding to several values of energy transfer ω. The ellipses represent 1σ loci of the Gaussian resolution function. The calculation uses $E_i = 14.7\,\text{meV}$. Note that the (h,k) and ℓ axes are not to scale.

depends on k_f, and thus on ω. Figure A.9 shows the resolution function at various values of ℓ (and thus energy). The positive ℓ values correspond to small ω, and the most negative ℓ value corresponds to an ω close to $E_i = 14.7\,\text{meV}$ (refer to Figure 2.21). Note that all of the fits to the two-axis measurements in Chapter 3 (and also in [14] and [56]) use a single resolution function, namely that for $\omega = 0$. Fortunately this is not a serious problem: as seen Figure A.9, the extent of the resolution ellipsoids along the (h,k) direction does not vary by very much.[7]

[7]The measurements aim to extract the in-plane correlation length; recall that the intrinsic signal is largely independent of ℓ since the magnetic system under investigation is two-dimensional.

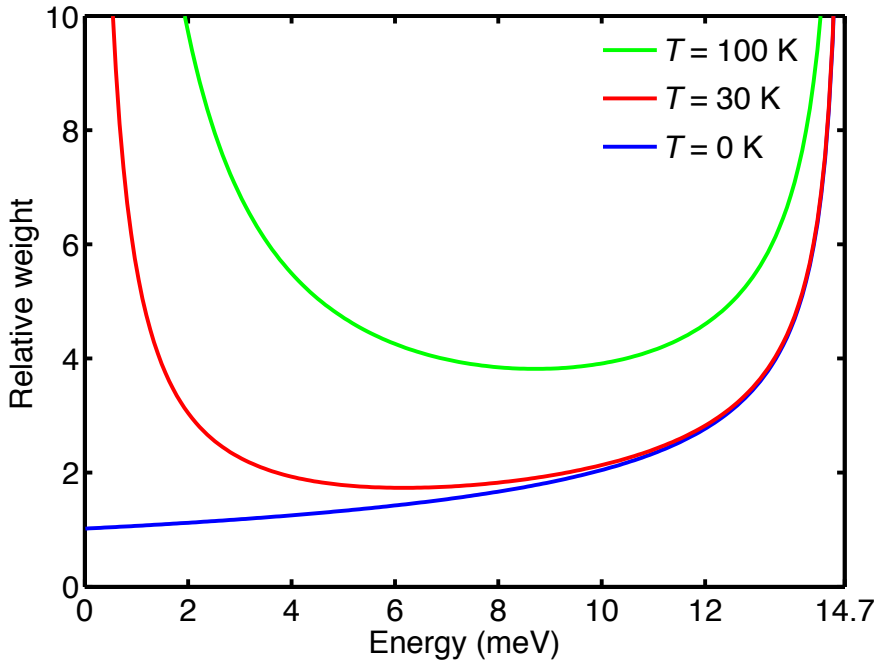

Figure A.10: Relative weight of the two-axis energy integration as a function of energy for the case of $E_i = 14.7\,\text{meV}$, including the effects of resolution and (temperature-dependent) Bose population factor.

The combined effect of the Bose factor and the resolution function is shown in Figure A.10. At zero temperature, where the Bose factor is 1, the resolution function causes the higher-energy excitations to be weighted strongly.[8] The Bose factor causes the lower-energy excitations to become weighted more strongly as the temperature is increased.

Thus there are two approximations made in the analysis of two-axis data; the first is that the resolution function for $\omega = 0$ approximates the effects of the full set of resolution functions. And the second is that the weighted distribution of energies (due both to resolution effects and the Bose factor) approximates the energy integration (A.1) for the instantaneous scattering function. While these may cause the absolute value of the fitted correlation length to differ slightly from the true value, the conclusions can still be quantitative. Note, for example, the

[8]Note that while the weight function diverges, the integral does not.

agreement between numerical results for the Heisenberg model and experimental data for LCZMO [56].

Comparison of simulations with experiment

Two-axis scans are simulated using the magnetic excitation spectrum of NCCO $x = 0.157$ (Figure 4.16) [81]. The signal is deconvolved from the calculated resolution function of the PUMA triple-axis spectrometer at the FRM-II in Garching, Germany. The intrinsic momentum width is modeled as increasing linearly with energy [81], and a smooth function is used for the energy-dependent (intrinsic) susceptibility. The simulated conditions are those at the BT9 and SPINS spectrometers at the NCNR in Gaithersburg, Maryland.

Figure A.11 compares the simulations with the data. The left panels compare simulations with an experiment on BT9 with $E_i = 14.7\,\text{meV}$, and the right panels compare simulations with an experiment on SPINS with $E_i = 5.0\,\text{meV}$.[9] The correspondence is far from perfect. There are broadly qualitative similarities, such as how the $T = 30\,\text{K}$ data have stronger intensity than the $T = 4\,\text{K}$ data and how the intensity difference becomes larger with $E_i = 5.0\,\text{meV}$. This is presumably because in that case a larger relative portion of the signal is gapped due to superconductivity. Another similarity is that, for the $E_i = 5.0\,\text{meV}$ case, the simulation correctly shows that the $T = 30\,\text{K}$ peak is sharper than the $T = 4\,\text{K}$ peak.

However, the major discrepancy is the clear difference between the simulations and experiments of the actual width of the peaks. For example, the calculation for $E_i = 5.0\,\text{meV}$ and $T = 30\,\text{K}$ yields a peak that is 60% wider than that of the corresponding experiment. This is probably due to the large uncertainty in determining the intrinsic (energy-dependent) width of the magnetic excitation spectrum. Triple-axis measurements generally use focusing monochromators and/or analyzers with open collimations, sacrificing momentum resolution for higher count rates. Thus the signal is usually very close to being resolution-limited, and a small error in calculating the resolution function will lead to large errors in the deconvolved

[9] With $E_i = 5.0\,\text{meV}$ the energy integration is over a much smaller range, and what is measured is different from the instantaneous correlations.

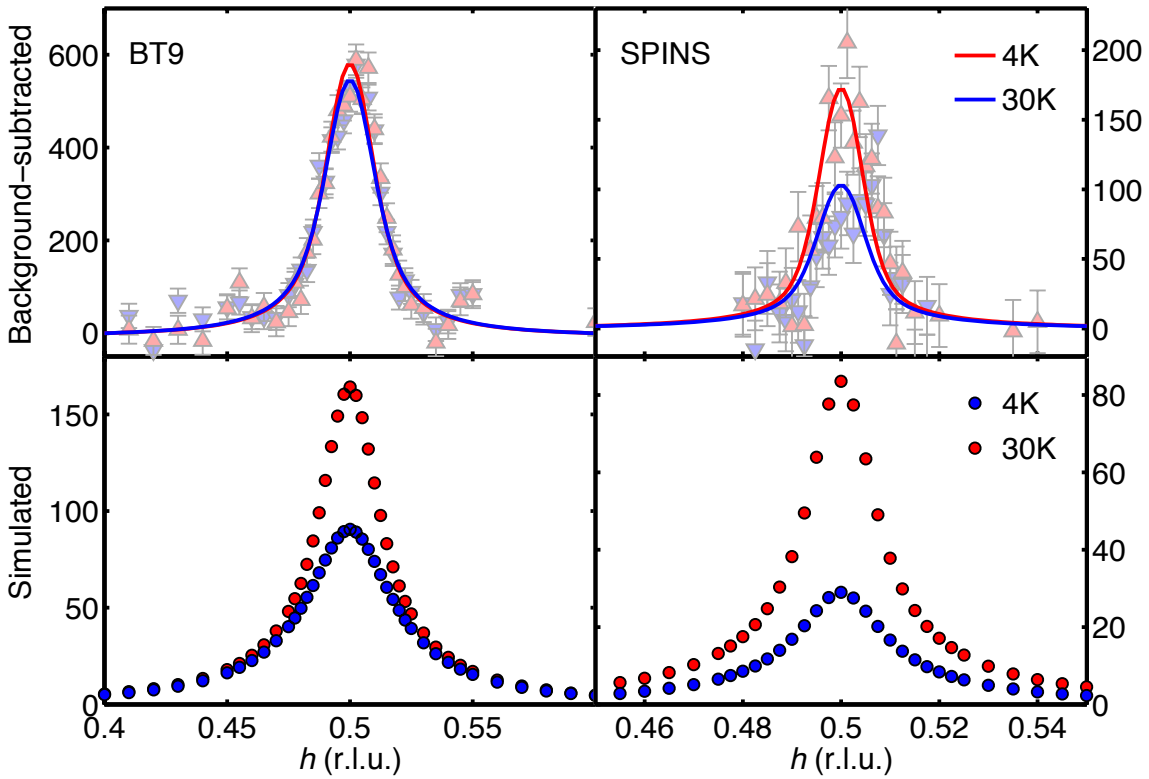

Figure A.11: Background-subtracted data and fits to the data (top panels) and simulated two-axis scans (bottom panels) for the BT9 thermal triple-axis spectrometer (left panels) and the SPINS cold triple-axis spectrometer (right panels). The BT9 experiment and simulation were performed with $E_i = 14.7\,\text{meV}$, and the SPINS experiment and simulation were performed with $E_i = 5.0\,\text{meV}$. Note the different scales on the h axes.

momentum widths. The two-axis measurements, on the other hand, use fine collimations resulting in an order-of-magnitude better momentum resolution. In fact, precise measurements of the correlation lengths, even to the moderate precision shown in Chapter 3, are only possible with the higher signal rates that are afforded by two-axis measurements.

Appendix B

Neutron scattering cross section

The goal of this Appendix is to derive formulae for the neutron scattering cross section. This Appendix largely follows the discussion in [159], with additional material and definitions from other sources [47, 160, 161]. In Section B.1 we derive the formulae for the nuclear scattering of neutrons. The general principles for this simpler case will then be applied in Section B.2 to derive formulae for magnetic neutron scattering. We first define some terms which we use throughout this Appendix.

A beam of neutrons with well-defined energy E_i is incident on a sample. The neutrons are scattered into various directions (θ, ϕ) with various energies E_f. If the incident flux (number of neutrons per second per unit area) is Φ, then the **partial differential cross section** is defined as

$$\frac{d^2\sigma}{d\Omega\, dE_f} = \frac{\begin{array}{c}\text{number of neutrons per second into } d\Omega \\ \text{with energy between } E_f \text{ and } dE_f\end{array}}{\Phi\, d\Omega\, dE_f}. \tag{B.1}$$

In general, the partial differential cross section depends on the direction (θ, ϕ) of the scattering as well as on E_f. Expressions for the partial differential cross section are what we wish to ultimately derive, both for nuclear and magnetic processes. In most contexts it is simply called the "cross section". We can also define the energy-integrated **differential cross section** as

$$\frac{d\sigma}{d\Omega} = \int_0^\infty \frac{d^2\sigma}{d\Omega\, dE_f}\, dE_f = \frac{\text{number of neutrons per second into } d\Omega}{\Phi\, d\Omega}. \tag{B.2}$$

This cross section is convenient in discussions of elastic scattering ($E_i = E_f$). Finally,

the **total scattering cross section** is defined as

$$\sigma_{\text{tot}} = \int \frac{d\sigma}{d\Omega}\, d\Omega = \frac{\text{total number of neutrons scattered per second}}{\Phi}. \tag{B.3}$$

B.1 Nuclear scattering

The derivation of formulae for nuclear scattering is simpler than that of magnetic scattering for two reasons: the spin degree of freedom of the neutron can be ignored, and the interaction potential between neutrons and nuclei is short-ranged enough to be approximated as a delta function. We thus begin the discussion with nuclear scattering, and the general principles learned in this section are applied later to the slightly more complicated case of magnetic scattering.

We begin in Section B.1.1 by finding an expression for a particular transition between two quantum states of the system using Fermi's golden rule, including deriving V, the interaction potential for nuclear scattering. Then in Section B.1.2 we find an expression for the measured cross section by summing over all final quantum states and taking the thermal average of the initial quantum states of the system. The expression is simplified by using the Heisenberg picture and also distinguishing between the coherent and incoherent parts of the cross section. Section B.1.3 defines the scattering function and discusses its properties. Finally, in Section B.1.4 we consider the case of a crystal lattice, ending with expressions for nuclear elastic scattering from the lattice and inelastic scattering from the phonon spectrum.

B.1.1 Transition between quantum states

If we ignore the spin of the neutron, the quantum state of the neutron is defined by its momentum[1] $\mathbf{k}$. In this section we consider a very specific interaction in which the quantum state of the neutron changes from $\mathbf{k}_i$ to $\mathbf{k}_f$, and the quantum state of the scattering system changes from λ_i to λ_f.

The differential cross section for this particular process can be written as

$$\left.\frac{d\sigma}{d\Omega}\right|_{\lambda_i \to \lambda_f} = \frac{1}{\Phi}\frac{1}{d\Omega} \sum_{\mathbf{k}_f \text{ in } d\Omega} W_{(\mathbf{k}_i,\lambda_i)\to(\mathbf{k}_f,\lambda_f)}\,, \tag{B.4}$$

where $W_{(\mathbf{k}_i,\lambda_i)\to(\mathbf{k}_f,\lambda_f)}$ is the number of transitions per second from $(\mathbf{k}_i, \lambda_i)$ to $(\mathbf{k}_f, \lambda_f)$.

[1] The momentum is technically $\mathbf{p} = \hbar\mathbf{k}$.

This transition rate can be calculated using Fermi's golden rule:

$$\sum_{\mathbf{k}_f \text{ in } d\Omega} W_{(\mathbf{k}_i,\lambda_i)\to(\mathbf{k}_f,\lambda_f)} = \frac{2\pi}{\hbar}\rho_{\mathbf{k}_f}|\langle \mathbf{k}_f\lambda_f|V|\mathbf{k}_i\lambda_i\rangle|^2\,, \tag{B.5}$$

where $\mathbf{k}_i$ is taken as a given value, $\mathbf{k}_f$ is the particular final neutron momentum that satisfies momentum and energy conservation for the total system, $\rho_{\mathbf{k}_f}$ is the number of quantum states in $d\Omega$ per unit energy at $\mathbf{k}_f$, and V is the scattering potential that defines the interaction of the neutron with the scattering system. The matrix element, if evaluated in real space, looks like

$$\langle \mathbf{k}_f\lambda_f|V|\mathbf{k}_i\lambda_i\rangle = \int \psi^*_{\mathbf{k}_f}\chi^*_{\lambda_f} V\psi_{\mathbf{k}_i}\chi_{\lambda_i}\, d\mathbf{r}_1\cdots d\mathbf{r}_N\, d\mathbf{r}\,, \tag{B.6}$$

where $\psi_{\mathbf{k}}$ is the wavefunction of a neutron in state $\mathbf{k}$, χ_λ is the wavefunction of the scattering system in state λ, $\mathbf{r}$ is the position of the neutron, and $\mathbf{r}_1, \mathbf{r}_2, \ldots, \mathbf{r}_N$ are the positions of the nuclei in the scattering system, with N being the number of nuclei.

The value $\rho_{\mathbf{k}_f}$ is proportional to the density of quantum states in $\mathbf{k}$-space, which depends on the neutron density. If the neutron density is n, then the volume associated with one neutron is $1/n$. The volume occupied by one quantum state in $\mathbf{k}$-space is then $n(2\pi)^3$.

The number of states in $d\Omega$ with energy between E_f and $E_f + dE_f$ is equal to the number of states in the volume element $k_f^2 dk_f d\Omega$:

$$\rho_{\mathbf{k}_f} dE_f = \frac{1}{n}\frac{1}{(2\pi)^3} k_f^2 dk_f d\Omega\,. \tag{B.7}$$

For neutrons, the relationship between E_f and k_f is

$$E_f = \frac{\hbar^2}{2m}k_f^2 \tag{B.8}$$

$$\frac{dE_f}{dk_f} = \frac{\hbar^2}{m}k_f \tag{B.9}$$

Thus we have

$$\rho_{\mathbf{k}_f} = \frac{1}{n}\frac{1}{(2\pi)^3} k_f \frac{m}{\hbar^2} d\Omega\,. \tag{B.10}$$

There are two other quantities in the cross section formula that depend on the

neutron density n. One is the incident flux Φ:

$$\Phi = n\frac{\hbar k_i}{m}\,. \tag{B.11}$$

The other is the neutron wavefunction $\psi_{\mathbf{k}}$:

$$\psi_{\mathbf{k}}(\mathbf{r}) = \sqrt{n}e^{i\mathbf{k}\cdot\mathbf{r}}\,. \tag{B.12}$$

We then see that the matrix element is

$$\langle \mathbf{k}_f\lambda_f|V|\mathbf{k}_i\lambda_i\rangle = n\int e^{-i\mathbf{k}_f\cdot\mathbf{r}}\chi^*_{\lambda_f}Ve^{i\mathbf{k}_i\cdot\mathbf{r}}\chi_{\lambda_i}\,d\mathbf{r}_1\cdots d\mathbf{r}_N\,d\mathbf{r}\,. \tag{B.13}$$

In the equation for the differential cross section, the factors of n all cancel, as they should:

$$\left.\frac{d\sigma}{d\Omega}\right|_{\lambda_i\to\lambda_f} = \frac{k_f}{k_i}\left(\frac{m}{2\pi\hbar^2}\right)^2|\langle \mathbf{k}_f\lambda_f|V|\mathbf{k}_i\lambda_i\rangle|^2\,, \tag{B.14}$$

where we have redefined the matrix element to be the right-hand side of (B.13) without the factor of n (i.e., redefine $\psi_{\mathbf{k}} \equiv e^{i\mathbf{k}\cdot\mathbf{r}}$).

We remind ourselves that, in general, the differential cross section is a function of the scattering angles θ and ϕ. However, the restriction to the transition $\lambda_i \to \lambda_f$ constrains the function to the scattering angle corresponding to outgoing neutron momentum $\mathbf{k}_f$, determined by conservation of momentum. In a similar fashion, the outgoing neutron energy E_f is constrained by conservation of energy. In particular, if E_{λ_i} and E_{λ_f} are the energies of the initial and final states of the scattering system, then

$$E_i + E_{\lambda_i} = E_f + E_{\lambda_f}\,. \tag{B.15}$$

The partial differential cross section, then, has a delta-function dependence on the outgoing energy E_f:

$$\left.\frac{d^2\sigma}{d\Omega dE_f}\right|_{\lambda_i\to\lambda_f} = \frac{k_f}{k_i}\left(\frac{m}{2\pi\hbar^2}\right)^2|\langle \mathbf{k}_f\lambda_f|V|\mathbf{k}_i\lambda_i\rangle|^2\delta(E_{\lambda_i} - E_{\lambda_f} + E_i - E_f)\,. \tag{B.16}$$

Interaction potential V

The potential V is the sum of all interactions V_j of the neutron with the j-th nucleus:

$$V = \sum_j V_j(\mathbf{R}_j)\,, \tag{B.17}$$

where V_j only depends on $\mathbf{R}_j \equiv \mathbf{r} - \mathbf{r}_j$, the position of the neutron with respect to the j-th nucleus. To calculate the matrix element, we first integrate over $\mathbf{r}$, the space coordinates of the neutron:

$$\begin{aligned}\langle \mathbf{k}_f | V | \mathbf{k}_i \rangle &= \sum_j \int e^{-i\mathbf{k}_f \cdot \mathbf{r}} V_j(\mathbf{R}_j) e^{i\mathbf{k}_i \cdot \mathbf{r}} d\mathbf{r} \\ &= \sum_j \int V_j(\mathbf{R}_j) e^{i\mathbf{Q}\cdot(\mathbf{r}_j + \mathbf{R}_j)} d\mathbf{R}_j \\ &= \sum_j V_j(\mathbf{Q}) e^{i\mathbf{Q}\cdot\mathbf{r}_j} ,\end{aligned} \tag{B.18}$$

where the Fourier transform is defined as

$$V_j(\mathbf{Q}) = \int V_j(\mathbf{R}_j) e^{i\mathbf{Q}\cdot\mathbf{R}_j} d\mathbf{R}_j , \tag{B.19}$$

and where

$$\mathbf{Q} = \mathbf{k}_i - \mathbf{k}_f \tag{B.20}$$

is the momentum transfer.[2] The whole matrix element thus becomes

$$\begin{aligned}\langle \mathbf{k}_f \lambda_f | V | \mathbf{k}_i \lambda_i \rangle &= \langle \lambda_f | \sum_j V_j(\mathbf{Q}) e^{i\mathbf{Q}\cdot\mathbf{r}_j} | \lambda_i \rangle \\ &= \sum_j V_j(\mathbf{Q}) \langle \lambda_f | e^{i\mathbf{Q}\cdot\mathbf{r}_j} | \lambda_i \rangle .\end{aligned} \tag{B.21}$$

What is the form of $V_j(\mathbf{R}_j)$? We know that the interaction of a neutron and a nucleus is mediated by the nuclear strong force, which is extremely short-ranged (on the order of 10^{-15} m) compared to the wavelength of the neutron (on the order of 10^{-10} m). Thus a good approximation to use a delta function, for which the Fourier transform is a constant:

$$V_j(\mathbf{R}_j) = a\delta(\mathbf{R}_j) , \tag{B.22}$$

$$V_j(\mathbf{Q}) = a . \tag{B.23}$$

It can be shown, using a classical partial-wave analysis of scattering from a single

[2] This convention (used in [159]) is opposite to that used in the main text (and used in [47]). Thus, strictly-speaking, the formulas derived in this Appendix only hold for this definition. However, we are justified in using the formulas in the main text in the (common) case of inversion symmetry ($\mathbf{Q} \leftrightarrow -\mathbf{Q}$).

fixed nucleus [159], that

$$a = \frac{2\pi\hbar^2}{m} b\,, \tag{B.24}$$

where b is called the scattering length. In general b is complex and energy-dependent; the imaginary part indicates the possibility of neutron capture (absorption), and only a few nuclides behave in this fashion. For most elements (i.e., all elements for which neutron scattering is feasible), b is real and energy-independent. Typically, the scattering length is on the order of a few fm (10^{-15} m). The cross section formula becomes

$$\left.\frac{d^2\sigma}{d\Omega dE_f}\right|_{\lambda_i\to\lambda_f} = \frac{k_f}{k_i}\left|\sum_j b_j \langle\lambda_f|e^{i\mathbf{Q}\cdot\mathbf{r}_j}|\lambda_i\rangle\right|^2 \delta(E_{\lambda_i} - E_{\lambda_f} + E_i - E_f)\,, \tag{B.25}$$

where b_j indicates the scattering length of the j-th nucleus.[3]

B.1.2 Sum over final states and average over initial states

The measured cross section does not discriminate against the quantum states λ_i and λ_f of the scattering system. In order to get the actual measured cross section, we need to first sum over all final states λ_f and then take the thermal average over all initial states λ_i. If the system is in thermal equilibrium at temperature T, the probability for the system to be in state λ is

$$p_\lambda = \frac{1}{Z} e^{-E_\lambda/k_\mathrm{B}T}\,, \tag{B.26}$$

where Z is the partition function

$$Z = \sum_\lambda e^{-E_\lambda/k_\mathrm{B}T}\,. \tag{B.27}$$

The measured cross section is then

$$\begin{aligned}\frac{d^2\sigma}{d\Omega dE_f} &= \sum_{\lambda_i\lambda_f} p_{\lambda_i} \left.\frac{d^2\sigma}{d\Omega dE_f}\right|_{\lambda_i\to\lambda_f} \\ &= \frac{k_f}{k_i}\sum_{\lambda_i\lambda_f} p_{\lambda_i}\left|\sum_j b_j\langle\lambda_f|e^{i\mathbf{Q}\cdot\mathbf{r}_j}|\lambda_i\rangle\right|^2 \delta(E_{\lambda_i} - E_{\lambda_f} + \hbar\omega)\,,\end{aligned} \tag{B.28}$$

[3] The scattering length b varies with the nuclide, but because the neutron has spin, it also depends on the combined spin ($I \pm \frac{1}{2}$) of the nucleus-neutron system. Although we ignore this detail here, all of the variations of b are taken into account in the incoherent cross section introduced later.

where we have defined the energy transfer

$$\hbar\omega = E_i - E_f \,. \tag{B.29}$$

We now simplify this expression by rewriting the delta function in energy as an integral and using the Heisenberg picture. The delta function becomes

$$\begin{aligned}
\delta(E_{\lambda_i} - E_{\lambda_f} + \hbar\omega) &= \frac{1}{\hbar}\delta(\omega - \frac{E_{\lambda_f} - E_{\lambda_i}}{\hbar}) \\
&= \frac{1}{2\pi\hbar}\int_{-\infty}^{\infty} e^{-i(\omega-(E_{\lambda_f}-E_{\lambda_i})/\hbar)t}\,dt \\
&= \frac{1}{2\pi\hbar}\int_{-\infty}^{\infty} e^{i(E_{\lambda_f}-E_{\lambda_i})t/\hbar}e^{-i\omega t}\,dt\,.
\end{aligned} \tag{B.30}$$

Expanding the square in (B.28) and using the new form for the delta function yields

$$\begin{aligned}
\frac{d^2\sigma}{d\Omega dE_f} &= \frac{k_f}{k_i}\frac{1}{2\pi\hbar}\sum_{\lambda_i\lambda_f} p_{\lambda_i}\sum_{jj'} b_j b_{j'}\langle\lambda_i|e^{-i\mathbf{Q}\cdot\mathbf{r}_{j'}}|\lambda_f\rangle\langle\lambda_f|e^{i\mathbf{Q}\cdot\mathbf{r}_j}|\lambda_i\rangle\int e^{i(E_{\lambda_f}-E_{\lambda_i})t/\hbar}e^{-i\omega t}\,dt \\
&= \frac{k_f}{k_i}\frac{1}{2\pi\hbar}\sum_{\lambda_i\lambda_f} p_{\lambda_i}\sum_{jj'} b_j b_{j'}\int\langle\lambda_i|e^{-i\mathbf{Q}\cdot\mathbf{r}_{j'}}|\lambda_f\rangle\langle\lambda_f|e^{iHt/\hbar}e^{i\mathbf{Q}\cdot\mathbf{r}_j}e^{-iHt/\hbar}|\lambda_i\rangle e^{-i\omega t}\,dt \\
&= \frac{k_f}{k_i}\frac{1}{2\pi\hbar}\sum_{\lambda_i\lambda_f} p_{\lambda_i}\sum_{jj'} b_j b_{j'}\int\langle\lambda_i|e^{-i\mathbf{Q}\cdot\mathbf{r}_{j'}(0)}|\lambda_f\rangle\langle\lambda_f|e^{i\mathbf{Q}\cdot\mathbf{r}_j(t)}|\lambda_i\rangle e^{-i\omega t}\,dt\,,
\end{aligned} \tag{B.31}$$

where H is the Hamiltonian for the scattering system, and in the last line we have changed to the Heisenberg picture with Heisenberg operator $\mathbf{r}_j(t)$ describing the time-dependent motion of nuclei. Applying the sum over λ_i and λ_f inside the integral, we have

$$\begin{aligned}
\frac{d^2\sigma}{d\Omega dE_f} &= \frac{k_f}{k_i}\frac{1}{2\pi\hbar}\sum_{jj'} b_j b_{j'}\int\sum_{\lambda_i\lambda_f} p_{\lambda_i}\langle\lambda_i|e^{-i\mathbf{Q}\cdot\mathbf{r}_{j'}(0)}|\lambda_f\rangle\langle\lambda_f|e^{i\mathbf{Q}\cdot\mathbf{r}_j(t)}|\lambda_i\rangle e^{-i\omega t}\,dt \\
&= \frac{k_f}{k_i}\frac{1}{2\pi\hbar}\sum_{jj'} b_j b_{j'}\int\sum_{\lambda_i} p_{\lambda_i}\langle\lambda_i|e^{-i\mathbf{Q}\cdot\mathbf{r}_{j'}(0)}e^{i\mathbf{Q}\cdot\mathbf{r}_j(t)}|\lambda_i\rangle e^{-i\omega t}\,dt \\
&= \frac{k_f}{k_i}\frac{1}{2\pi\hbar}\sum_{jj'} b_j b_{j'}\int\langle e^{-i\mathbf{Q}\cdot\mathbf{r}_{j'}(0)}e^{i\mathbf{Q}\cdot\mathbf{r}_j(t)}\rangle e^{-i\omega t}\,dt\,,
\end{aligned} \tag{B.32}$$

where we have used the closure relation $\sum_{\lambda_f}|\lambda_f\rangle\langle\lambda_f| = 1$, and $\langle\cdots\rangle$ denotes the thermal average $\sum_\lambda p_\lambda\langle\lambda|\cdots|\lambda\rangle$.

Now that we have summed and averaged over the quantum states of the system, the partial differential cross section is an unconstrained function of scattering angle and final neutron energy. We have found an expression in terms of the more physical variables $\mathbf{Q}$ and ω, which can be easily calculated from θ, ϕ, and E_f.

Coherent and incoherent scattering

As previously mentioned, the scattering length b differs among the nuclei in a general system. If we suppose that a certain value b_i occurs with frequency f_i, then the average value of b is

$$\overline{b} = \sum_i f_i b_i \,, \tag{B.33}$$

and the average value of b^2 is

$$\overline{b^2} = \sum_i f_i b_i^2 \,. \tag{B.34}$$

We first assume that there is no correlation between the value of b at one site to that of another; in particular, the treatment of multiple elements in a crystal lattice is different and is discussed later.

The cross section measured for a very large number of nuclei is very close to the average cross section for all distributions of b_i's. Thus

$$\frac{d^2\sigma}{d\Omega dE_f} = \frac{k_f}{k_i}\frac{1}{2\pi\hbar}\sum_{jj'}\overline{b_j b_{j'}}\int \langle e^{-i\mathbf{Q}\cdot\mathbf{r}_{j'}(0)} e^{i\mathbf{Q}\cdot\mathbf{r}_j(t)}\rangle e^{-i\omega t}\,dt \,. \tag{B.35}$$

Note that if $j' \neq j$, then $\overline{b_j b_{j'}} = \overline{b}_j \overline{b}_{j'} = \overline{b}^2$, and if $j' = j$, then $\overline{b_j b_{j'}} = \overline{b^2}$. So we can split the cross section into two terms:

$$\begin{aligned}\frac{d^2\sigma}{d\Omega dE_f} = \frac{k_f}{k_i}\frac{1}{2\pi\hbar}\overline{b}^2\sum_{j\neq j'}\int \langle e^{-i\mathbf{Q}\cdot\mathbf{r}_{j'}(0)} e^{i\mathbf{Q}\cdot\mathbf{r}_j(t)}\rangle e^{-i\omega t}\,dt \\ + \frac{k_f}{k_i}\frac{1}{2\pi\hbar}\overline{b^2}\sum_j\int \langle e^{-i\mathbf{Q}\cdot\mathbf{r}_j(0)} e^{i\mathbf{Q}\cdot\mathbf{r}_j(t)}\rangle e^{-i\omega t}\,dt \,.\end{aligned} \tag{B.36}$$

By allowing the first sum to be over all j, j' and subtracting the additional $j = j'$

term, we have

$$\frac{d^2\sigma}{d\Omega dE_f} = \frac{k_f}{k_i}\frac{1}{2\pi\hbar}\bar{b}^2 \sum_{jj'} \int \langle e^{-i\mathbf{Q}\cdot\mathbf{r}_{j'}(0)} e^{i\mathbf{Q}\cdot\mathbf{r}_j(t)}\rangle e^{-i\omega t}\, dt + \frac{k_f}{k_i}\frac{1}{2\pi\hbar}(\overline{b^2} - \bar{b}^2) \sum_{j} \int \langle e^{-i\mathbf{Q}\cdot\mathbf{r}_j(0)} e^{i\mathbf{Q}\cdot\mathbf{r}_j(t)}\rangle e^{-i\omega t}\, dt\,. \quad \text{(B.37)}$$

The first term is called the **coherent** cross section, and the second term is called the **incoherent** cross section. We can write

$$\left.\frac{d^2\sigma}{d\Omega dE_f}\right|_{\text{coh}} = \frac{\sigma_{\text{coh}}}{4\pi}\frac{k_f}{k_i}\frac{1}{2\pi\hbar}\sum_{jj'}\int \langle e^{-i\mathbf{Q}\cdot\mathbf{r}_{j'}(0)} e^{i\mathbf{Q}\cdot\mathbf{r}_j(t)}\rangle e^{-i\omega t}\, dt \quad \text{(B.38)}$$

$$\left.\frac{d^2\sigma}{d\Omega dE_f}\right|_{\text{inc}} = \frac{\sigma_{\text{inc}}}{4\pi}\frac{k_f}{k_i}\frac{1}{2\pi\hbar}\sum_{j}\int \langle e^{-i\mathbf{Q}\cdot\mathbf{r}_j(0)} e^{i\mathbf{Q}\cdot\mathbf{r}_j(t)}\rangle e^{-i\omega t}\, dt\,, \quad \text{(B.39)}$$

where $\sigma_{\text{coh}} = 4\pi\bar{b}^2$ and $\sigma_{\text{inc}} = 4\pi(\overline{b^2} - \bar{b}^2)$ are the coherent and incoherent cross section, which are specific to a nuclide or element and can be found listed in tables such as those in [47].

The coherent cross section is due to interference effects of different nuclei at different times, and is the measured cross section if all nuclei have the same scattering length $b = \bar{b}$. The incoherent cross section is due to the random distributions of the deviations of the scattering length from the average value $\bar{b}$. The coherent part is usually the more physically interesting and is the focus of the remainder of this Appendix.

B.1.3 Scattering function

The **scattering function** is a quantity dependent only on the parameters of the scattering system. It is defined as

$$S(\mathbf{Q},\omega) = \frac{1}{2\pi\hbar N}\sum_{jj'}\int \langle e^{-i\mathbf{Q}\cdot\mathbf{r}_{j'}(0)} e^{i\mathbf{Q}\cdot\mathbf{r}_j(t)}\rangle e^{-i\omega t}\, dt\,, \quad \text{(B.40)}$$

so that the coherent cross section can be written as

$$\left.\frac{d^2\sigma}{d\Omega dE_f}\right|_{\text{coh}} = \frac{k_f}{k_i}\bar{b}^2 NS(\mathbf{Q},\omega)\,. \quad \text{(B.41)}$$

where N is the number of nuclei.

The physical significance of the scattering function is that it is, up to a constant factor, the Fourier transform (in time and space) of the density-density correlation function $C_{\rho\rho}(\mathbf{r}, \mathbf{r}', t - t')$:[4]

$$S(\mathbf{Q}, \omega) = \frac{1}{2\pi\hbar N} \int C_{\rho\rho}(\mathbf{r}, \mathbf{r}', t) e^{-i(\mathbf{Q}\cdot(\mathbf{r}-\mathbf{r}')-\omega t)} \, d\mathbf{r} d\mathbf{r}' dt \,, \tag{B.42}$$

where

$$C_{\rho\rho}(\mathbf{r}, \mathbf{r}', t - t') = \langle \rho(\mathbf{r}, t) \rho(\mathbf{r}', t') \rangle \tag{B.43}$$

depends only on the time difference $t - t'$, as long as the Hamiltonian of the system is time-independent. The particle density $\rho(\mathbf{r}, t)$ of nuclei is given by

$$\rho(\mathbf{r}, t) = \sum_j \delta(\mathbf{r} - \mathbf{r}_j(t)) \,, \tag{B.44}$$

and so we have

$$C_{\rho\rho}(\mathbf{r}, \mathbf{r}', -t) = \sum_{jj'} \left\langle \delta(\mathbf{r} - \mathbf{r}_{j'}(0)) \delta(\mathbf{r}' - \mathbf{r}_j(t)) \right\rangle \,. \tag{B.45}$$

The spatial Fourier transform is then

$$\int C_{\rho\rho}(\mathbf{r}, \mathbf{r}', -t) e^{-i\mathbf{Q}\cdot(\mathbf{r}-\mathbf{r}')} \, d\mathbf{r} d\mathbf{r}' = \sum_{jj'} \langle e^{-i\mathbf{Q}\cdot\mathbf{r}_{j'}(0)} e^{i\mathbf{Q}\cdot\mathbf{r}_j(t)} \rangle \,, \tag{B.46}$$

and (B.42) follows upon changing the variable of integration $t \to -t$.

Principle of detailed balance

One of the general properties of the scattering function is that of detailed balance:

$$S(-\mathbf{Q}, -\omega) = e^{-\hbar\omega/k_B T} S(\mathbf{Q}, \omega) \,. \tag{B.47}$$

We can prove this relation by returning to the expression (B.28) for the cross section:

$$\frac{d^2\sigma}{d\Omega dE_f} = \frac{k_f}{k_i} \sum_{\lambda_i \lambda_f} p_{\lambda_i} \left| \sum_j b_j \langle \lambda_f | e^{i\mathbf{Q}\cdot\mathbf{r}_j} | \lambda_i \rangle \right|^2 \delta(E_{\lambda_i} - E_{\lambda_f} + \hbar\omega) \,. \tag{B.48}$$

[4]Correlation functions are also discussed later in the context of the fluctuation dissipation theorem in Section B.2.5

The coherent part of this is

$$\left.\frac{d^2\sigma}{d\Omega dE_f}\right|_{\text{coh}} = \frac{k_f}{k_i}\bar{b}^2\frac{1}{Z}\sum_{\lambda_i\lambda_f} e^{-E_{\lambda_i}/k_{\text{B}}T}\left|\sum_j \langle\lambda_f|e^{i\mathbf{Q}\cdot\mathbf{r}_j}|\lambda_i\rangle\right|^2 \delta(E_{\lambda_i} - E_{\lambda_f} + \hbar\omega)\,, \tag{B.49}$$

where we have written the explicit expression for p_{λ_i}. The scattering function is then

$$S(\mathbf{Q},\omega) = \frac{1}{NZ}\sum_{\lambda_i\lambda_f} e^{-E_{\lambda_i}/k_{\text{B}}T}\left|\sum_j \langle\lambda_f|e^{i\mathbf{Q}\cdot\mathbf{r}_j}|\lambda_i\rangle\right|^2 \delta(E_{\lambda_i} - E_{\lambda_f} + \hbar\omega)\,. \tag{B.50}$$

For $S(-\mathbf{Q},-\omega)$ we relabel λ_i as λ_f and vice-versa:

$$\begin{aligned} S(-\mathbf{Q},-\omega) &= \frac{1}{NZ}\sum_{\lambda_i\lambda_f} e^{-E_{\lambda_f}/k_{\text{B}}T}\left|\sum_j \langle\lambda_i|e^{-i\mathbf{Q}\cdot\mathbf{r}_j}|\lambda_f\rangle\right|^2 \delta(E_{\lambda_f} - E_{\lambda_i} - \hbar\omega) \\ &= \frac{1}{NZ}\sum_{\lambda_i\lambda_f} e^{-(E_{\lambda_f}-E_{\lambda_i})/k_{\text{B}}T} e^{-E_{\lambda_i}/k_{\text{B}}T}\left|\sum_j \langle\lambda_f|e^{i\mathbf{Q}\cdot\mathbf{r}_j}|\lambda_i\rangle\right|^2 \delta(E_{\lambda_i} - E_{\lambda_f} + \hbar\omega) \\ &= e^{-\hbar\omega/k_{\text{B}}T} S(\mathbf{Q},\omega)\,, \end{aligned} \tag{B.51}$$

which is the result we set out to prove.

The physical interpretation is that, *a priori*, the probabilities are the same that a neutron will bring about a transition from λ_i to λ_f or from λ_f to λ_i, but the probability of the system initially being in the higher energy state is lower by $e^{-|E_{\lambda_f}-E_{\lambda_i}|/k_{\text{B}}T}$ than the probability of being in the lower energy state. One implication of this result is that neutron scattering experiments are almost always performed with positive energy transfer ω (i.e., energy transferred from the neutron to the system).

B.1.4 Scattering from a crystal lattice

We now move our discussion from a general scattering system of nuclei to a scattering system in which the nuclei are arranged in a crystal lattice.

We first consider only Bravais lattices, in which there is one atom per unit cell. We use $\mathbf{R}$ to indicate the lattice positions

$$\mathbf{R} = n_1\mathbf{a}_1 + n_2\mathbf{a}_2 + n_3\mathbf{a}_3\,, \tag{B.52}$$

where $\mathbf{a}_1$, $\mathbf{a}_2$, and $\mathbf{a}_3$ are the vectors that define the primitive unit cell, and n_1, n_2 and n_3 are integers. The reciprocal lattice is defined as all vectors $\mathbf{G}$ such that $e^{i\mathbf{G}\cdot\mathbf{R}} = 1$.

This condition is satisfied by

$$\mathbf{G} = m_1\mathbf{b}_1 + m_2\mathbf{b}_2 + m_3\mathbf{b}_3\,, \tag{B.53}$$

where m_1, m_2 and m_3 are integers, and the primitive vectors $\mathbf{b}_i$ of the reciprocal lattice are defined in terms of the primitive vectors $\mathbf{a}_i$ of the real-space lattice:

$$\mathbf{b}_1 = \frac{2\pi}{v_0}\mathbf{a}_2 \times \mathbf{a}_3\,, \qquad \mathbf{b}_2 = \frac{2\pi}{v_0}\mathbf{a}_3 \times \mathbf{a}_1\,, \qquad \mathbf{b}_3 = \frac{2\pi}{v_0}\mathbf{a}_1 \times \mathbf{a}_2\,, \tag{B.54}$$

where $v_0 = \mathbf{a}_1 \cdot (\mathbf{a}_2 \times \mathbf{a}_3)$ is the volume of the real-space unit cell.

The lattice vectors $\mathbf{R}$ are the equilibrium positions of the nuclei in the crystal lattice. The motion of the ℓ-th nucleus is described by

$$\mathbf{r}_\ell(t) = \mathbf{R}_\ell + \mathbf{u}_\ell(t)\,, \tag{B.55}$$

where $\mathbf{u}_\ell(t)$ is the motion of the nucleus away from equilibrium. The scattering function (B.40) is now

$$\begin{aligned} S(\mathbf{Q},\omega) &= \frac{1}{2\pi\hbar N}\sum_{\ell\ell'}\int \langle e^{-i\mathbf{Q}\cdot\mathbf{r}_{\ell'}(0)} e^{i\mathbf{Q}\cdot\mathbf{r}_\ell(t)}\rangle e^{-i\omega t}\,dt \\ &= \frac{1}{2\pi\hbar N}\sum_{\ell\ell'}\int \langle e^{-i\mathbf{Q}\cdot\mathbf{R}_{\ell'}} e^{-i\mathbf{Q}\cdot\mathbf{u}_{\ell'}(0)} e^{i\mathbf{Q}\cdot\mathbf{R}_\ell} e^{i\mathbf{Q}\cdot\mathbf{u}_\ell(t)}\rangle e^{-i\omega t}\,dt \\ &= \frac{1}{2\pi\hbar N}\sum_{\ell\ell'} e^{i\mathbf{Q}\cdot(\mathbf{R}_\ell - \mathbf{R}_{\ell'})}\int \langle e^{-i\mathbf{Q}\cdot\mathbf{u}_{\ell'}(0)} e^{i\mathbf{Q}\cdot\mathbf{u}_\ell(t)}\rangle e^{-i\omega t}\,dt\,. \end{aligned} \tag{B.56}$$

If $\mathbf{R}_\ell$ and $\mathbf{R}_{\ell'}$ are lattice vectors, then $\mathbf{R}_{\ell''} = \mathbf{R}_\ell - \mathbf{R}_{\ell'}$ is also a lattice vector. Furthermore, we make the physical argument that the thermally averaged quantity cannot depend explicitly on the sites ℓ and ℓ', so that

$$\langle e^{-i\mathbf{Q}\cdot\mathbf{u}_{\ell'}(0)} e^{i\mathbf{Q}\cdot\mathbf{u}_\ell(t)}\rangle = \langle e^{-i\mathbf{Q}\cdot\mathbf{u}_0(0)} e^{i\mathbf{Q}\cdot\mathbf{u}_{\ell''}(t)}\rangle\,, \tag{B.57}$$

where the index 0 means $\mathbf{R}_0 = 0$, and the index ℓ'' is the same as defined above. In a sum over ℓ and ℓ', the value ℓ'' occurs N times. Thus we have

$$S(\mathbf{Q},\omega) = \frac{1}{2\pi\hbar}\sum_{\ell} e^{i\mathbf{Q}\cdot\mathbf{R}_\ell}\int \langle e^{-i\mathbf{Q}\cdot\mathbf{u}_0(0)} e^{i\mathbf{Q}\cdot\mathbf{u}_\ell(t)}\rangle e^{-i\omega t}\,dt\,. \tag{B.58}$$

We make the assumption that small deviations $\mathbf{u}_\ell$ from the equilibrium positions behave harmonically, and that they can be written in terms of the normal modes of the crystal. The standard method is to write the quantity in terms of creation and

annihilation operators:

$$\mathbf{u}_\ell = \sqrt{\frac{\hbar}{2MN}} \sum_s \frac{\mathbf{e}_s}{\sqrt{\omega_s}} \left(a_s e^{i\mathbf{q}_s \cdot \mathbf{R}_\ell} + a_s^\dagger e^{-i\mathbf{q}_s \cdot \mathbf{R}_\ell} \right) , \tag{B.59}$$

where M is the mass of an atom, s denotes one of the $3N$ phonon modes, $\mathbf{e}_s$ is the polarization vector, ω_s is the phonon frequency, $\mathbf{q}_s$ is the phonon wavevector, and $a_s^\dagger$ and a_s are the creation and annihilation operators, respectively. The time dependence is introduced by noting that

$$a_s(t) = a_s e^{-i\omega_s t} , \qquad a_s^\dagger(t) = a_s^\dagger e^{i\omega_s t} , \tag{B.60}$$

so that we have

$$\mathbf{u}_\ell(t) = \sqrt{\frac{\hbar}{2MN}} \sum_s \frac{\mathbf{e}_s}{\sqrt{\omega_s}} \left(a_s e^{i(\mathbf{q}_s \cdot \mathbf{R}_\ell - \omega_s t)} + a_s^\dagger e^{-i(\mathbf{q}_s \cdot \mathbf{R}_\ell - \omega_s t)} \right) . \tag{B.61}$$

Now we define

$$U \equiv -i\mathbf{Q} \cdot \mathbf{u}_0(0) = -i \sqrt{\frac{\hbar}{2MN}} \sum_s \frac{\mathbf{Q} \cdot \mathbf{e}_s}{\sqrt{\omega_s}} \left(a_s + a_s^\dagger \right) \tag{B.62}$$

$$V \equiv i\mathbf{Q} \cdot \mathbf{u}_\ell(t) = i \sqrt{\frac{\hbar}{2MN}} \sum_s \frac{\mathbf{Q} \cdot \mathbf{e}_s}{\sqrt{\omega_s}} \left(a_s e^{i(\mathbf{q}_s \cdot \mathbf{R}_\ell - \omega_s t)} + a_s^\dagger e^{-i(\mathbf{q}_s \cdot \mathbf{R}_\ell - \omega_s t)} \right) , \tag{B.63}$$

so that the thermal-averaged expression in (B.58) is $\langle e^U e^V \rangle$. We outline a proof that shows that

$$\langle e^U e^V \rangle = e^{\langle U^2 \rangle} e^{\langle UV \rangle} . \tag{B.64}$$

We use two results: one is that

$$e^A e^B = e^{A+B} e^{\frac{1}{2}[A,B]} \quad \text{if } [A, B] \text{ is a } c\text{-number.} \tag{B.65}$$

The other is that

$$\langle e^A \rangle = e^{\frac{1}{2}\langle A^2 \rangle} \quad \text{if } A \text{ has a Gaussian probability function.} \tag{B.66}$$

Both conditions are satisfied in our case. U and V are sums of a_s and $a_s^\dagger$, the commutators of which are all c-numbers. And it can be shown that the probability

function of a harmonic oscillator is Gaussian. Thus

$$\begin{aligned}\langle e^U e^V\rangle &= \langle e^{U+V}\rangle e^{\frac{1}{2}[U,V]} \\ &= e^{\frac{1}{2}\langle (U+V)^2\rangle} e^{\frac{1}{2}(UV-VU)} \\ &= e^{\frac{1}{2}\langle U^2+V^2\rangle} e^{\langle UV\rangle} \\ &= e^{\langle U^2\rangle} e^{\langle UV\rangle}\,,\end{aligned} \tag{B.67}$$

where in the last line we used the fact that $\langle U^2\rangle = \langle V^2\rangle$, since U and V are the same physical quantity.

Debye-Waller factor

The quantity $e^{\langle U^2\rangle}$ is called the **Debye-Waller factor**. It describes the decrease in overall scattering intensity due to thermal fluctuations of the nuclei. We use the definition of U to see that

$$\begin{aligned}\langle\lambda|U^2|\lambda\rangle &= -\frac{\hbar}{2MN}\sum_{ss'}\frac{(\mathbf{Q}\cdot\mathbf{e}_s)(\mathbf{Q}\cdot\mathbf{e}_{s'})}{\sqrt{\omega_s\omega_{s'}}}\langle\lambda|(a_s+a_s^\dagger)(a_{s'}+a_{s'}^\dagger)|\lambda\rangle \\ &= -\frac{\hbar}{2MN}\sum_{s}\frac{(\mathbf{Q}\cdot\mathbf{e}_s)^2}{\omega_s}\langle\lambda|a_s a_s^\dagger + a_s^\dagger a_s|\lambda\rangle \\ &= -\frac{\hbar}{2MN}\sum_{s}\frac{(\mathbf{Q}\cdot\mathbf{e}_s)^2}{\omega_s}\langle\lambda|2n_s+1|\lambda\rangle\,,\end{aligned} \tag{B.68}$$

so that

$$2W = -\langle U^2\rangle = \frac{\hbar}{2MN}\sum_{s}\frac{(\mathbf{Q}\cdot\mathbf{e}_s)^2}{\omega_s}\langle 2n_s+1\rangle\,, \tag{B.69}$$

where writing the Debye-Waller factor as e^{-2W} is standard notation. It can be shown that

$$\langle 2n_s+1\rangle \;= \frac{e^{\hbar\omega_s/k_\mathrm{B}T}+1}{e^{\hbar\omega_s/k_\mathrm{B}T}-1}\,. \tag{B.70}$$

Phonon expansion

The scattering function (B.58) now reads

$$S(\mathbf{Q},\omega) = \frac{1}{2\pi\hbar}e^{-2W}\sum_{\ell}e^{i\mathbf{Q}\cdot\mathbf{R}_\ell}\int e^{\langle UV\rangle}e^{-i\omega t}\,dt\,. \tag{B.71}$$

The quantity $\langle UV \rangle$ can be expanded in a similar fashion to $\langle U^2 \rangle$:

$$\langle \lambda | UV | \lambda \rangle = \frac{\hbar}{2MN} \sum_s \frac{(\mathbf{Q} \cdot \mathbf{e}_s)^2}{\omega_s} \left\langle \lambda \left| a_s a_s^\dagger e^{-i(\mathbf{q}_s \cdot \mathbf{R}_\ell - \omega_s t)} + a_s^\dagger a_s e^{i(\mathbf{q}_s \cdot \mathbf{R}_\ell - \omega_s t)} \right| \lambda \right\rangle , \tag{B.72}$$

giving

$$\langle UV \rangle = \frac{\hbar}{2MN} \sum_s \frac{(\mathbf{Q} \cdot \mathbf{e}_s)^2}{\omega_s} \left(\langle n_s + 1 \rangle e^{-i(\mathbf{q}_s \cdot \mathbf{R}_\ell - \omega_s t)} + \langle n_s \rangle e^{i(\mathbf{q}_s \cdot \mathbf{R}_\ell - \omega_s t)} \right) . \tag{B.73}$$

The process of Taylor-expanding the exponential is called the **phonon expansion**:

$$e^{\langle UV \rangle} = 1 + \langle UV \rangle + \frac{1}{2} \langle UV \rangle^2 + \cdots . \tag{B.74}$$

The first term corresponds to elastic scattering, the second term corresponds to one-phonon scattering processes, the third term to two-phonon scattering process, and so on. The reason for this is the phase factors in (B.73). This becomes clearer in the discussions below.

Elastic nuclear scattering

The elastic component of the scattering function is

$$S(\mathbf{Q}, \omega)_{\text{el}} = \frac{1}{2\pi\hbar} e^{-2W} \sum_\ell e^{i\mathbf{Q} \cdot \mathbf{R}_\ell} \int e^{-i\omega t} \, dt . \tag{B.75}$$

The sum over ℓ and the integral over time are independent, and both describe delta functions. It can be shown that

$$\sum_\ell e^{i\mathbf{Q} \cdot \mathbf{R}_\ell} = \frac{(2\pi)^3}{v_0} \sum_i \delta(\mathbf{Q} - \mathbf{G}_i) , \tag{B.76}$$

where the $\mathbf{G}_i$ are the reciprocal lattice vectors and v_0 is the volume of the unit cell. Furthermore, we know that

$$\int e^{i\omega t} dt = 2\pi\delta(\omega) = 2\pi\hbar\delta(\hbar\omega) . \tag{B.77}$$

Thus we have

$$S(\mathbf{Q}, \omega)_{\text{el}} = \frac{(2\pi)^3}{v_0} e^{-2W} \sum_i \delta(\mathbf{Q} - \mathbf{G}_i) \delta(\hbar\omega) . \tag{B.78}$$

The elastic component of the (coherent) cross section is usually expressed in its energy-integrated form as

$$\left.\frac{d\sigma}{d\Omega}\right|_{\text{coh,el}} = \bar{b}^2 N \frac{(2\pi)^3}{v_0} e^{-2W} \sum_i \delta(\mathbf{Q} - \mathbf{G}_i) \tag{B.79}$$

This simply states that elastic Bragg scattering occurs at reciprocal lattice vectors.

In the case of non-Bravais crystals, there are multiple atoms per unit cell. The nuclei are positioned at

$$\mathbf{r}_{\ell j} = \mathbf{R}_\ell + \mathbf{d}_j + \mathbf{u}_{\ell j}\,, \tag{B.80}$$

where $\mathbf{d}_j$ is the position of the j-th atom in a unit cell. If $\bar{b}_j$ is the mean scattering length for the nucleus at $\mathbf{d}_j$, then it can be shown that

$$\left.\frac{d\sigma}{d\Omega}\right|_{\text{coh,el}} = N \frac{(2\pi)^3}{v_0} |F_{\text{N}}(\mathbf{Q})|^2 \sum_i \delta(\mathbf{Q} - \mathbf{G}_i)\,, \tag{B.81}$$

where N is now the number of unit cells and the **static nuclear structure factor** is

$$F_{\text{N}}(\mathbf{Q}) = \sum_j \bar{b}_j e^{i\mathbf{Q}\cdot\mathbf{d}_j} e^{-W_j}\,, \tag{B.82}$$

in which

$$W_j = \frac{1}{2}\langle(\mathbf{Q}\cdot\mathbf{u}_{\ell j})^2\rangle = \frac{\hbar}{4M_j N} \sum_s \frac{(\mathbf{Q}\cdot\mathbf{e}_{sj})^2}{\omega_s} \langle 2n_s + 1\rangle\,. \tag{B.83}$$

The relative intensities of the Bragg peaks can thus be used to determine the structure of the unit cell.

One-phonon scattering

The second term in the phonon expansion gives us the one-phonon scattering function

$$S(\mathbf{Q},\omega)_{\text{1ph}} = \frac{1}{2\pi\hbar} e^{-2W} \sum_\ell e^{i\mathbf{Q}\cdot\mathbf{R}_\ell} \int \langle UV\rangle e^{-i\omega t}\, dt\,. \tag{B.84}$$

Using (B.73), we have

$$S(\mathbf{Q},\omega)_{1\text{ph}} = \frac{1}{4\pi MN} e^{-2W} \sum_s \frac{(\mathbf{Q}\cdot\mathbf{e}_s)^2}{\omega_s} \times \sum_\ell e^{i\mathbf{Q}\cdot\mathbf{R}_\ell} \int \left(\langle n_s+1\rangle e^{-i(\mathbf{q}_s\cdot\mathbf{R}_\ell - \omega_s t)} + \langle n_s\rangle e^{i(\mathbf{q}_s\cdot\mathbf{R}_\ell-\omega_s t)} \right) e^{-i\omega t}\, dt\,. \quad \text{(B.85)}$$

The first term becomes:

$$\begin{aligned} S(\mathbf{Q},\omega)_{+1} &= \frac{1}{4\pi MN} e^{-2W} \sum_s \frac{(\mathbf{Q}\cdot\mathbf{e}_s)^2}{\omega_s} \langle n_s+1\rangle \sum_\ell e^{i(\mathbf{Q}-\mathbf{q}_s)\cdot\mathbf{R}_\ell} \int e^{i(\omega_s-\omega)t}\, dt \\ &= \frac{1}{2MN} \frac{(2\pi)^3}{v_0} e^{-2W} \sum_{s,i} \frac{(\mathbf{Q}\cdot\mathbf{e}_s)^2}{\omega_s} \langle n_s+1\rangle \delta(\mathbf{Q}-\mathbf{q}_s-\mathbf{G}_i)\delta(\omega-\omega_s)\,, \end{aligned} \quad \text{(B.86)}$$

where

$$\langle n_s+1\rangle = \frac{1}{1-e^{-\hbar\omega_s/k_\text{B}T}} \quad \text{(B.87)}$$

is called the **Bose factor**. Similarly, the second term becomes

$$S(\mathbf{Q},\omega)_{-1} = \frac{1}{2MN} \frac{(2\pi)^3}{v_0} e^{-2W} \sum_{s,i} \frac{(\mathbf{Q}\cdot\mathbf{e}_s)^2}{\omega_s} \langle n_s\rangle \delta(\mathbf{Q}-\mathbf{q}_s-\mathbf{G}_i)\delta(\omega+\omega_s)\,, \quad \text{(B.88)}$$

where

$$\langle n_s\rangle = \frac{1}{1+e^{\hbar\omega_s/k_\text{B}T}}\,. \quad \text{(B.89)}$$

The first term describes a process in which the energy $\hbar\omega$ transferred to the system is positive and equal to the phonon frequency ω_s, and in which the momentum transferred to the system $\mathbf{Q}$ is equal to a reciprocal lattice vector $\mathbf{G}$ plus the phonon momentum $\mathbf{q}_s$. Thus it describes the emission of a phonon. Similarly, the second term describes the absorption of a phonon by the scattering process. The usual neutron scattering measurement is at positive ω and thus corresponds to the first term $S(\mathbf{Q},\omega)_{+1}$.

Recall that s indexes the $3N$ modes; the four-dimensional delta function in (B.86) indicates that one mode contributes to the cross section at a single point $(\mathbf{q}_s+\mathbf{G}_i,\omega_s)$ in $(\mathbf{Q},\omega)$-space (modulo the reciprocal lattice). We know, however, that these $3N$ modes form branches, and that within each branch the N values of $\mathbf{q}_s$ are evenly spaced in the Brillouin zone. Since N is so large, we can rewrite the expression in terms of continuous branches (rather than discrete modes). We effectively spread $\delta(\mathbf{Q}-\mathbf{q}_s-\mathbf{G}_i)$ evenly across the three-dimensional volume $(2\pi)^3/v_0N$. Since an

integral over this volume must be 1, the transformation is

$$\delta(\mathbf{Q} - \mathbf{q}_s - \mathbf{G}_i) \to N\frac{v_0}{(2\pi)^3}\,. \tag{B.90}$$

We replace ω_s by the continuous function $\omega_m(\mathbf{Q})$, where m indexes the branches. This function is periodic in the reciprocal lattice, i.e., $\omega_m(\mathbf{Q} + \mathbf{G}_i) = \omega_m(\mathbf{Q})$, and we can remove the sum over i. Finally, we have

$$S(\mathbf{Q},\omega)_{+1} = \sum_m \frac{n(\omega_m)+1}{2M\omega_m}(\mathbf{Q}\cdot\mathbf{e}_m)^2 e^{-2W}\delta(\omega - \omega_m(\mathbf{Q}))\,, \tag{B.91}$$

where we have expressed the Bose factor as a function $n(\omega) + 1$.

In the case of a non-Bravais lattice, it can be shown that the one-phonon scattering function[5] is

$$S(\mathbf{Q},\omega)_{+1} = \frac{1}{2N}\frac{(2\pi)^3}{v_0}\sum_{s,i}\frac{1}{\omega_s}|\mathcal{F}_{\mathrm{N}}(\mathbf{Q})|^2\langle n_s+1\rangle\delta(\mathbf{Q}-\mathbf{q}_s-\mathbf{G}_i)\delta(\omega-\omega_s)\,, \tag{B.92}$$

where N is now the number of unit cells, and where the **dynamic nuclear structure factor** is

$$\mathcal{F}_{\mathrm{N}}(\mathbf{Q}) = \sum_j \frac{\bar{b}_j}{\sqrt{M_j}}(\mathbf{Q}\cdot\mathbf{e}_{sj})e^{i\mathbf{Q}\cdot\mathbf{d}_j}e^{-W_j}\,. \tag{B.93}$$

In terms of continuous phonon branches, the expression becomes

$$S(\mathbf{Q},\omega)_{+1} = \sum_m \frac{n(\omega_m)+1}{2\omega_m}|\mathcal{F}_{\mathrm{N}}(\mathbf{Q})|^2\delta(\omega-\omega_m(\mathbf{Q}))\,. \tag{B.94}$$

B.2 Magnetic Scattering

We now discuss the scattering of neutrons that can occur due to its magnetic moment. The derivation of the formulae proceeds in a similar fashion to that of nuclear scattering. In Section B.2.1 the goal is to find an expression for the cross section for the transition between two quantum states. The bulk of this first section is spent

[5]Note that for a non-Bravais crystal the scattering function is defined differently. In particular, it includes the scattering lengths $\bar{b}_j$, whereas the previous definition (B.41) did not include $\bar{b}$. So we have

$$\left.\frac{d^2\sigma}{d\Omega dE_f}\right|_{\mathrm{coh}} = \frac{k_f}{k_i}NS(\mathbf{Q},\omega)\,.$$

finding an efficient way of expressing the magnetic interaction, which is considerably more complicated than the delta-function nuclear potential. Then in Section B.2.2 we derive an expression for the measured cross section by summing over final states and averaging over initial states. This section includes the discussion of the magnetization density. In Section B.2.3 we focus on the specific considerations of magnetic neutron scattering from a crystal lattice. Section B.2.4 discusses some aspects of elastic magnetic scattering, and section B.2.5 deals with inelastic magnetic scattering, including a brief discussion of the fluctuation-dissipation theorem.

B.2.1 Transition between quantum states

We write the partial differential cross section for magnetic scattering the same way as for nuclear scattering (B.16), except now we must keep track of the spin state σ of the neutron.

$$\left.\frac{d^2\sigma}{d\Omega dE_f}\right|_{\sigma_i\lambda_i\to\sigma_f\lambda_f} = \frac{k_f}{k_i}\left(\frac{m}{2\pi\hbar^2}\right)^2 |\langle \mathbf{k}_f\sigma_f\lambda_f|V|\mathbf{k}_i\sigma_i\lambda_i\rangle|^2\delta(E_{\lambda_i} - E_{\lambda_f} + \hbar\omega)\,. \tag{B.95}$$

Magnetic interaction potential

We must find an expression for the magnetic interaction V between the neutrons and the scattering system. A neutron has a magnetic dipole moment of

$$\boldsymbol{\mu}_n = -\gamma\mu_{\mathrm{N}}\boldsymbol{\sigma}\,, \tag{B.96}$$

where $\mu_{\mathrm{N}} = \frac{e\hbar}{2m_p}$ is the nuclear magneton, $\boldsymbol{\sigma}$ is the Pauli spin operator (with eigenvalues ±1), and the experimentally measured coefficient is $\gamma \approx 1.913$. This magnetic moment interacts with the magnetic field within the scattering system. Typically, the magnetic field of interest is that created by (unpaired) electrons in the scattering system. In general, of course, one may consider other effects, such as the nuclear spins or large-scale current loops, but here we restrict the discussion to electrons on atoms.

We can divide the effects of unpaired electrons into two components: that of the electron spin (i.e., the magnetic dipole moment of the electron), and that of electron motion (i.e., the orbital moment). The magnetic dipole moment of the electron is

$$\boldsymbol{\mu}_e = -2\mu_{\mathrm{B}}\mathbf{s}\,, \tag{B.97}$$

where $\mu_{\mathrm{B}} = \frac{e\hbar}{2m_e}$ is the Bohr magneton, $\mathbf{s}$ is the electron spin operator (with eigenvalues $\pm\frac{1}{2}$), and the coefficient 2 is for our purposes a good approximation to the

electron g-factor. The magnetic field due to the electron spin is then given by

$$\mathbf{B}_{\mathrm{S}} = \boldsymbol{\nabla} \times \mathbf{A}\,, \qquad \mathbf{A} = \frac{\mu_0}{4\pi} \frac{\boldsymbol{\mu}_e \times \hat{\mathbf{R}}}{R^2}\,, \tag{B.98}$$

where $\mathbf{R}$ is the position of the neutron with respect to the electron. The magnetic field due to electron motion is given by the Biot-Savart law:

$$\begin{aligned} \mathbf{B}_{\mathrm{L}} &= \frac{\mu_0}{4\pi} \frac{I d\boldsymbol{\ell} \times \hat{\mathbf{R}}}{R^2} \\ &= -\frac{\mu_0}{4\pi} \frac{e}{m_e} \frac{\mathbf{p} \times \hat{\mathbf{R}}}{R^2}\,, \end{aligned} \tag{B.99}$$

where the current element is $I d\boldsymbol{\ell} = -e\mathbf{p}/m_e$, and $\mathbf{p}$ is the electron momentum. The total magnetic field is thus

$$\begin{aligned} \mathbf{B} &= \frac{\mu_0}{4\pi} \left(\boldsymbol{\nabla} \times \frac{\boldsymbol{\mu}_e \times \hat{\mathbf{R}}}{R^2} - \frac{e}{m_e} \frac{\mathbf{p} \times \hat{\mathbf{R}}}{R^2} \right) \\ &= \frac{\mu_0}{4\pi} \left(-\boldsymbol{\nabla} \times \frac{2\mu_{\mathrm{B}} \mathbf{s} \times \hat{\mathbf{R}}}{R^2} - \frac{2\mu_{\mathrm{B}}}{\hbar} \frac{\mathbf{p} \times \hat{\mathbf{R}}}{R^2} \right) \\ &= -\frac{\mu_0}{4\pi} 2\mu_{\mathrm{B}} \left(\boldsymbol{\nabla} \times \frac{\mathbf{s} \times \hat{\mathbf{R}}}{R^2} + \frac{1}{\hbar} \frac{\mathbf{p} \times \hat{\mathbf{R}}}{R^2} \right). \end{aligned} \tag{B.100}$$

The magnetic potential of the neutron in this magnetic field is then

$$-\boldsymbol{\mu}_n \cdot \mathbf{B}_j = -\frac{\mu_0}{4\pi} 2\mu_{\mathrm{B}} \gamma \mu_{\mathrm{N}} \boldsymbol{\sigma} \cdot \left(\boldsymbol{\nabla} \times \frac{\mathbf{s}_j \times \hat{\mathbf{R}}}{R^2} + \frac{1}{\hbar} \frac{\mathbf{p}_j \times \hat{\mathbf{R}}}{R^2} \right), \tag{B.101}$$

where $\mathbf{B}_j$ is the magnetic field due to the j-th electron, and $\mathbf{s}_j$ and $\mathbf{p}_j$ are the spin and momentum of the j-th electron, respectively. Each electron in the scattering system contributes to the magnetic potential of the neutron, so that the total interaction is

$$V = \sum_j (-\boldsymbol{\mu}_n \cdot \mathbf{B}_j)\,. \tag{B.102}$$

Integration over spatial coordinates

In order to calculate the matrix element $\langle \mathbf{k}_f \sigma_f \lambda_f | V | \mathbf{k}_i \sigma_i \lambda_i \rangle$, we first integrate over the space coordinates $\mathbf{r}$ of the neutron, i.e., calculate $\langle \mathbf{k}_f | V | \mathbf{k}_i \rangle$. We use, but do not

prove, the following two identities:

$$\boldsymbol{\nabla} \times \frac{\mathbf{s} \times \hat{\mathbf{R}}}{R^2} = \frac{1}{2\pi^2} \int \hat{\mathbf{q}} \times (\mathbf{s} \times \hat{\mathbf{q}})\, e^{i\mathbf{q}\cdot\mathbf{R}}\, d\mathbf{q}\,, \tag{B.103}$$

$$\int \frac{\hat{\mathbf{R}}}{R^2} e^{i\mathbf{Q}\cdot\mathbf{R}}\, d\mathbf{R} = 4\pi i \frac{\hat{\mathbf{Q}}}{Q}\,. \tag{B.104}$$

We will also be substituting $\mathbf{r} = \mathbf{r}_j + \mathbf{R}$, where $\mathbf{r}_j$ is the position of the j-th electron. We consider the first term in the parenthesis of (B.101):

$$\begin{aligned}
\langle \mathbf{k}_f | \left(\boldsymbol{\nabla} \times \frac{\mathbf{s}_j \times \hat{\mathbf{R}}}{R^2} \right) | \mathbf{k}_i \rangle &= \int e^{-i\mathbf{k}_f\cdot\mathbf{r}} \left(\boldsymbol{\nabla} \times \frac{\mathbf{s}_j \times \hat{\mathbf{R}}}{R^2} \right) e^{i\mathbf{k}_i\cdot\mathbf{r}}\, d\mathbf{r} \\
&= \frac{1}{2\pi^2} \int e^{i\mathbf{Q}\cdot\mathbf{r}} \int \hat{\mathbf{q}} \times (\mathbf{s}_j \times \hat{\mathbf{q}})\, e^{i\mathbf{q}\cdot\mathbf{R}}\, d\mathbf{q}\, d\mathbf{r} \\
&= \frac{1}{2\pi^2} \int e^{i\mathbf{Q}\cdot\mathbf{r}_j}\, \hat{\mathbf{q}} \times (\mathbf{s}_j \times \hat{\mathbf{q}})\, d\mathbf{q} \int e^{i(\mathbf{Q}+\mathbf{q})\cdot\mathbf{R}}\, d\mathbf{R} \\
&= \frac{1}{2\pi^2} \int e^{i\mathbf{Q}\cdot\mathbf{r}_j}\, \hat{\mathbf{q}} \times (\mathbf{s}_j \times \hat{\mathbf{q}})\, d\mathbf{q}\, (2\pi)^3 \delta(\mathbf{Q} + \mathbf{q}) \\
&= 4\pi e^{i\mathbf{Q}\cdot\mathbf{r}_j}\, \hat{\mathbf{Q}} \times (\mathbf{s}_j \times \hat{\mathbf{Q}})\,.
\end{aligned} \tag{B.105}$$

The second term becomes:

$$\begin{aligned}
\langle \mathbf{k}_f | \left(\frac{1}{\hbar} \frac{\mathbf{p}_j \times \hat{\mathbf{R}}}{R^2} \right) | \mathbf{k}_i \rangle &= \frac{1}{\hbar} \int e^{i\mathbf{Q}\cdot\mathbf{r}} \frac{\mathbf{p}_j \times \hat{\mathbf{R}}}{R^2}\, d\mathbf{r} \\
&= \frac{1}{\hbar} e^{i\mathbf{Q}\cdot\mathbf{r}_j} \int e^{i\mathbf{Q}\cdot\mathbf{R}} \frac{\mathbf{p}_j \times \hat{\mathbf{R}}}{R^2}\, d\mathbf{R} \\
&= \frac{4\pi i}{\hbar Q} e^{i\mathbf{Q}\cdot\mathbf{r}_j} (\mathbf{p}_j \times \hat{\mathbf{Q}})\,.
\end{aligned} \tag{B.106}$$

Note that while some components of $\mathbf{r}_j$ and $\mathbf{p}_j$ do not commute, $\mathbf{Q} \cdot \mathbf{r}_j$ and $\mathbf{p}_j \times \hat{\mathbf{Q}}$ do commute. We now define

$$\mathbf{M}_\perp = -2\mu_\mathrm{B} \sum_j e^{i\mathbf{Q}\cdot\mathbf{r}_j} \left(\hat{\mathbf{Q}} \times (\mathbf{s}_j \times \hat{\mathbf{Q}}) + \frac{i}{\hbar Q} (\mathbf{p}_j \times \hat{\mathbf{Q}}) \right), \tag{B.107}$$

such that

$$\sum_j \langle \mathbf{k}_f | \left(\boldsymbol{\nabla} \times \frac{\mathbf{s}_j \times \hat{\mathbf{R}}}{R^2} + \frac{1}{\hbar} \frac{\mathbf{p}_j \times \hat{\mathbf{R}}}{R^2} \right) | \mathbf{k}_i \rangle = -\frac{4\pi}{2\mu_\mathrm{B}} \mathbf{M}_\perp\,. \tag{B.108}$$

We can now put everything together, combining the coefficients:

$$\begin{aligned}\frac{m_n}{2\pi\hbar^2}\langle \mathbf{k}_f|V|\mathbf{k}_i\rangle &= \frac{m_n}{2\pi\hbar^2}\frac{\mu_0}{4\pi}2\mu_\mathrm{B}\gamma\mu_\mathrm{N}\boldsymbol{\sigma}\cdot\left(\frac{4\pi}{2\mu_\mathrm{B}}\mathbf{M}_\perp\right)\\ &= \frac{\gamma}{2\mu_\mathrm{B}}\frac{\mu_0}{4\pi}\frac{m_n}{\pi\hbar^2}\frac{e\hbar}{2m_p}\frac{e\hbar}{2m_e}4\pi(\boldsymbol{\sigma}\cdot\mathbf{M}_\perp)\\ &= \frac{\gamma r_0}{2\mu_\mathrm{B}}(\boldsymbol{\sigma}\cdot\mathbf{M}_\perp)\,,\end{aligned} \tag{B.109}$$

where we have made the approximation $m_n \approx m_p$, and $r_0 = \frac{\mu_0}{4\pi}\frac{e^2}{m_e} \approx 2.82\times10^{-15}$ m is the classical electron radius.[6] The expression for the cross section becomes

$$\left.\frac{d^2\sigma}{d\Omega dE_f}\right|_{\sigma_i\lambda_i\to\sigma_f\lambda_f} = \left(\frac{\gamma r_0}{2\mu_\mathrm{B}}\right)^2\frac{k_f}{k_i}\left|\langle\sigma_f\lambda_f|\boldsymbol{\sigma}\cdot\mathbf{M}_\perp|\sigma_i\lambda_i\rangle\right|^2\delta(E_{\lambda_i}-E_{\lambda_f}+\hbar\omega)\,. \tag{B.110}$$

We see that the relevant length scale is $\gamma r_0 \approx 5.39$ fm, which is comparable to the typical nuclear scattering length. As a consequence, nuclear and magnetic neutron scattering have similar intensities. In principle, neutrons can also scatter magnetically from nuclei, but the scattering length is on the order of $r_0 m_e/m$ and thus negligible.

Magnetization density

We now discuss the physical significance of $\mathbf{M}_\perp$, namely its relation with the magnetization density of the scattering system. We first discuss the spin component

$$\mathbf{M}_{\perp\mathrm{S}} = -2\mu_\mathrm{B}\sum_j e^{i\mathbf{Q}\cdot\mathbf{r}_j}(\hat{\mathbf{Q}}\times(\mathbf{s}_j\times\hat{\mathbf{Q}}))\,. \tag{B.111}$$

If we write

$$\mathbf{M}_{\perp\mathrm{S}} = \hat{\mathbf{Q}}\times(\mathbf{M}_\mathrm{S}\times\hat{\mathbf{Q}})\,, \tag{B.112}$$

[6] Note that some texts [160] and articles [162] use the definition $r_0 = \gamma\frac{\mu_0}{4\pi}\frac{e^2}{m_e}$ and thus their equations contain r_0 instead of γr_0.

then we can see that $\mathbf{M}_S(\mathbf{Q})$ is

$$\begin{aligned}\mathbf{M}_S(\mathbf{Q}) &= -2\mu_B \sum_j e^{i\mathbf{Q}\cdot\mathbf{r}_j}\mathbf{s}_j \\ &= -2\mu_B \int \boldsymbol{\rho}_S(\mathbf{r}) e^{i\mathbf{Q}\cdot\mathbf{r}}\, d\mathbf{r} \\ &= \int \mathbf{M}_S(\mathbf{r}) e^{i\mathbf{Q}\cdot\mathbf{r}}\, d\mathbf{r}\,,\end{aligned} \tag{B.113}$$

where $\boldsymbol{\rho}_S$ is the electron spin density

$$\boldsymbol{\rho}_S(\mathbf{r}) = \sum_j \mathbf{s}_j \delta(\mathbf{r} - \mathbf{r}_j)\,, \tag{B.114}$$

and $\mathbf{M}_S(\mathbf{r})$ is the **spin magnetization density**

$$\mathbf{M}_S(\mathbf{r}) = -2\mu_B \boldsymbol{\rho}_S(\mathbf{r})\,. \tag{B.115}$$

It can be shown that similar relations hold for the orbital component of $\mathbf{M}_\perp$:

$$\mathbf{M}_{\perp L} = -2\mu_B \frac{i}{\hbar Q} \sum_j e^{i\mathbf{Q}\cdot\mathbf{r}_j}(\mathbf{p}_j \times \hat{\mathbf{Q}}) \tag{B.116}$$

$$\mathbf{M}_{\perp L} = \hat{\mathbf{Q}} \times (\mathbf{M}_L(\mathbf{Q}) \times \hat{\mathbf{Q}}) \tag{B.117}$$

$$\mathbf{M}_L(\mathbf{Q}) = \int \mathbf{M}_L(\mathbf{r}) e^{i\mathbf{Q}\cdot\mathbf{r}}\, d\mathbf{r}\,, \tag{B.118}$$

where $\mathbf{M}_L(\mathbf{Q})$ is the Fourier transform of the **orbital magnetization density** $\mathbf{M}_L(\mathbf{r})$, which is a function of the electron current density. Thus we can combine the spin and orbital components to write

$$\mathbf{M}_\perp = \hat{\mathbf{Q}} \times (\mathbf{M} \times \hat{\mathbf{Q}}) \tag{B.119}$$

where $\mathbf{M}(\mathbf{Q})$ is the Fourier transform of the total **magnetization density** $\mathbf{M}(\mathbf{r})$.

Geometrically, $\mathbf{M}_\perp = \hat{\mathbf{Q}} \times (\mathbf{M} \times \hat{\mathbf{Q}})$ is the vector projection of $\mathbf{M}$ onto the plane perpendicular to $\mathbf{Q}$. In other words, $\mathbf{M}_\perp$ is what remains when the component of $\mathbf{M}$ parallel to $\mathbf{Q}$ is subtracted:

$$\mathbf{M}_\perp = \mathbf{M} - (\mathbf{M} \cdot \hat{\mathbf{Q}})\hat{\mathbf{Q}}\,. \tag{B.120}$$

We use this property to derive the following useful result:

$$\begin{aligned}\mathbf{M}_\perp^\dagger \cdot \mathbf{M}_\perp &= (\mathbf{M}^\dagger - (\mathbf{M}^\dagger \cdot \hat{\mathbf{Q}})\hat{\mathbf{Q}}) \cdot (\mathbf{M} - (\mathbf{M} \cdot \hat{\mathbf{Q}})\hat{\mathbf{Q}}) \\ &= \mathbf{M}^\dagger \cdot \mathbf{M} - (\mathbf{M}^\dagger \cdot \hat{\mathbf{Q}})(\mathbf{M} \cdot \hat{\mathbf{Q}}) \\ &= \sum_{\alpha\beta} (\delta_{\alpha\beta} - \hat{Q}_\alpha \hat{Q}_\beta) M_\alpha^\dagger M_\beta \,,\end{aligned} \tag{B.121}$$

where $\alpha, \beta = x, y, z$ denote the cartesian components of the vectors.

B.2.2 Sum over final states and average over initial states

The measured cross section is found by summing over the final states σ_f, λ_f and taking the average over the initial states σ_i, λ_i.

Sum over σ_f and average over σ_i

We begin with σ_i and σ_f:

$$\begin{aligned}\sum_{\sigma_i\sigma_f} p_{\sigma_i} \left|\langle \sigma_f \lambda_f | \boldsymbol{\sigma} \cdot \mathbf{M}_\perp | \sigma_i \lambda_i \rangle\right|^2 &= \sum_{\sigma_i\sigma_f} p_{\sigma_i} |\, \langle \sigma_f | \boldsymbol{\sigma} | \sigma_i \rangle \cdot \langle \lambda_f | \mathbf{M}_\perp | \lambda_i \rangle \,|^2 \\ &= \sum_{\alpha\beta} \sum_{\sigma_i\sigma_f} p_{\sigma_i} \langle \sigma_i | \sigma_\alpha | \sigma_f \rangle \langle \sigma_f | \sigma_\beta | \sigma_i \rangle \langle \lambda_i | M_{\perp\alpha}^\dagger | \lambda_f \rangle \langle \lambda_f | M_{\perp\beta} | \lambda_i \rangle \\ &= \sum_{\alpha\beta} \sum_{\sigma_i} p_{\sigma_i} \langle \sigma_i | \sigma_\alpha \sigma_\beta | \sigma_i \rangle \langle \lambda_i | M_{\perp\alpha}^\dagger | \lambda_f \rangle \langle \lambda_f | M_{\perp\beta} | \lambda_i \rangle \,.\end{aligned} \tag{B.122}$$

We focus now on the matrix element $\langle \sigma_i | \sigma_\alpha \sigma_\beta | \sigma_i \rangle$. Note that $|\sigma_i\rangle$ refers to a particular spin state of the neutron (i.e., $|\uparrow\rangle$ or $|\downarrow\rangle$), whereas σ_α refers to the α-component of the Pauli spin operator. In the case that $\alpha = \beta$, we can use the properties of the Pauli matrices[7] to show that the diagonal matrix elements are equal to 1:

$$\langle \uparrow | \sigma_\alpha^2 | \uparrow \rangle = \langle \downarrow | \sigma_\alpha^2 | \downarrow \rangle = 1 \qquad \text{for all } \alpha \,. \tag{B.123}$$

[7] Recall that the Pauli matrices are:

$$\sigma_x = \begin{pmatrix} 0 & 1 \\ 1 & 0 \end{pmatrix} \qquad \sigma_y = \begin{pmatrix} 0 & -i \\ i & 0 \end{pmatrix} \qquad \sigma_z = \begin{pmatrix} 1 & 0 \\ 0 & -1 \end{pmatrix}.$$

Thus, averaged over σ_i we have

$$\sum_{\sigma_i} p_{\sigma_i} \langle \sigma_i | \sigma_\alpha \sigma_\beta | \sigma_i \rangle = 1 \qquad \text{for } \alpha = \beta \,. \tag{B.124}$$

For the case $\alpha \neq \beta$, it turns out that $\sigma_\alpha \sigma_\beta$ is traceless. For example,

$$\langle \uparrow | \sigma_x \sigma_y | \uparrow \rangle + \langle \downarrow | \sigma_x \sigma_y | \downarrow \rangle = i - i = 0 \,. \tag{B.125}$$

We consider only the case of unpolarized neutrons,[8] for which the probabilities p_{σ_i} are equal (i.e., $p_\uparrow = p_\downarrow = \frac{1}{2}$). Thus the average is

$$\sum_{\sigma_i} p_{\sigma_i} \langle \sigma_i | \sigma_\alpha \sigma_\beta | \sigma_i \rangle = 0 \qquad \text{for } \alpha \neq \beta \,. \tag{B.126}$$

Because only the $\alpha = \beta$ terms survive, we are left with

$$\begin{aligned} \sum_{\sigma_i \sigma_f} p_{\sigma_i} |\langle \sigma_f \lambda_f | \boldsymbol{\sigma} \cdot \mathbf{M}_\perp | \sigma_i \lambda_i \rangle|^2 &= \sum_\alpha \langle \lambda_i | M_{\perp\alpha}^\dagger | \lambda_f \rangle \langle \lambda_f | M_{\perp\alpha} | \lambda_i \rangle \\ &= \langle \lambda_i | \mathbf{M}_\perp^\dagger | \lambda_f \rangle \cdot \langle \lambda_f | \mathbf{M}_\perp | \lambda_i \rangle \\ &= \sum_{\alpha\beta} (\delta_{\alpha\beta} - \hat{Q}_\alpha \hat{Q}_\beta) \langle \lambda_i | M_\alpha^\dagger | \lambda_f \rangle \langle \lambda_f | M_\beta | \lambda_i \rangle \,. \end{aligned} \tag{B.127}$$

Sum over λ_f and average over λ_i

Finally, we sum over λ_f and average over λ_i to obtain the measured cross section for magnetic scattering:

$$\frac{d^2\sigma}{d\Omega dE_f} = \left(\frac{\gamma r_0}{2\mu_B} \right)^2 \frac{k_f}{k_i} \sum_{\alpha\beta} (\delta_{\alpha\beta} - \hat{Q}_\alpha \hat{Q}_\beta) \sum_{\lambda_i \lambda_f} p_{\lambda_i} \langle \lambda_i | M_\alpha^\dagger | \lambda_f \rangle \langle \lambda_f | M_\beta | \lambda_i \rangle \delta(E_{\lambda_i} - E_{\lambda_f} + \hbar\omega) \,. \tag{B.128}$$

[8] Polarized neutron scattering is, of course, a very interesting and useful technique. The measurements discussed in this Thesis used only unpolarized neutrons.

As before in the case of nuclear scattering, we replace the delta function in energies with a time integral to introduce time-dependent operators:

$$\begin{aligned}
&\sum_{\lambda_i\lambda_f} p_{\lambda_i}\langle\lambda_i|M_\alpha^\dagger|\lambda_f\rangle\langle\lambda_f|M_\beta|\lambda_i\rangle\delta(E_{\lambda_i}-E_{\lambda_f}+\hbar\omega) \\
&\qquad = \frac{1}{2\pi\hbar}\int\sum_{\lambda_i\lambda_f} p_{\lambda_i}\langle\lambda_i|M_\alpha^\dagger(0)|\lambda_f\rangle\langle\lambda_f|M_\beta(t)|\lambda_i\rangle e^{-i\omega t}\,dt \\
&\qquad = \frac{1}{2\pi\hbar}\int\left\langle M_\alpha^\dagger(0)M_\beta(t)\right\rangle e^{-i\omega t}\,dt\,.
\end{aligned} \tag{B.129}$$

The expression for the cross section becomes

$$\frac{d^2\sigma}{d\Omega dE_f} = \frac{1}{2\pi\hbar}\left(\frac{\gamma r_0}{2\mu_\mathrm{B}}\right)^2\frac{k_f}{k_i}\sum_{\alpha\beta}(\delta_{\alpha\beta}-\hat{Q}_\alpha\hat{Q}_\beta)\int\left\langle M_\alpha^\dagger(0)M_\beta(t)\right\rangle e^{-i\omega t}\,dt\,. \tag{B.130}$$

B.2.3 Magnetic scattering from a crystal lattice

We now impose a crystal structure on the positions $\mathbf{r}_j$ of the electrons. We make the following restrictions:

- The unpaired electrons contributing to the magnetization density are localized in atoms.
- We assume LS coupling, which means that
  - The individual orbital moments in an atom combine to form an orbital angular momentum characterized by a quantum number L.
  - The individual spins in an atom combine to form a spin angular momentum for the atom characterized by a quantum number S.
  - The spin and orbital angular momenta of an atom combine to form a total angular momentum $\mathbf{J} = \mathbf{L} + \mathbf{S}$.

  We begin by considering scattering due to spin only. This is the case when $L = 0$, or when the orbital momentum is quenched, such as in the transition metals.
- Two states λ_i and λ_f differ only in the orientation of the angular momentum (i.e., the direction of $\mathbf{S}$) and the positions of the nuclei. In general, the states λ also depend on the quantum number S and the spatial states of the electrons (i.e., the shape of the orbitals), but the typical neutron energies are too low to affect these properties.

For simplicity, we begin with a Bravais crystal. In a such a system, the nuclei have positions

$$\mathbf{r}_\ell = \mathbf{R}_\ell + \mathbf{u}_\ell \,. \tag{B.131}$$

Let $\mathbf{r}_i$ be the position of the i-th electron in an atom with respect to its nucleus, such that the positions of the electrons are now written as

$$\mathbf{r}_j \to \mathbf{r}_\ell + \mathbf{r}_i \,. \tag{B.132}$$

Recall that the magnetization density for spin scattering is

$$\mathbf{M} = \mathbf{M}_\mathrm{S} = -2\mu_\mathrm{B} \sum_j e^{i\mathbf{Q}\cdot\mathbf{r}_j} \mathbf{s}_j \,. \tag{B.133}$$

In a crystal lattice, we write this as

$$\mathbf{M} = -2\mu_\mathrm{B} \sum_\ell e^{i\mathbf{Q}\cdot\mathbf{r}_\ell} \sum_i e^{i\mathbf{Q}\cdot\mathbf{r}_i} \mathbf{s}_i \,. \tag{B.134}$$

We proceed by evaluating the matrix elements of $\mathbf{M}$:

$$\begin{aligned} -\frac{1}{2\mu_\mathrm{B}} \langle \lambda_f | \mathbf{M} | \lambda_i \rangle &= \langle \lambda_f | \sum_\ell e^{i\mathbf{Q}\cdot\mathbf{r}_\ell} \sum_i e^{i\mathbf{Q}\cdot\mathbf{r}_i} \mathbf{s}_i | \lambda_i \rangle \\ &= \sum_{\lambda'} \sum_{\ell i} \langle \lambda_f | e^{i\mathbf{Q}\cdot\mathbf{r}_i} | \lambda' \rangle \langle \lambda' | e^{i\mathbf{Q}\cdot\mathbf{r}_\ell} \mathbf{s}_i | \lambda_i \rangle \,. \end{aligned} \tag{B.135}$$

Note that in the first factor, $e^{i\mathbf{Q}\cdot\mathbf{r}_i}$ depends only on the space coordinates of the electrons. Because, according to our third assumption above, $|\lambda_f\rangle$ and $|\lambda'\rangle$ do not differ in the spatial state of the electrons, yet are otherwise orthogonal, we see that

$$\langle \lambda_f | e^{i\mathbf{Q}\cdot\mathbf{r}_i} | \lambda' \rangle = 0 \qquad \text{unless } \lambda' = \lambda_f \,. \tag{B.136}$$

Furthermore, if the spatial wavefunction shared by the λ states is

$$\phi(\mathbf{r}_1, \ldots, \mathbf{r}_i, \ldots, \mathbf{r}_n) = A\, \psi_1(\mathbf{r}_1) \cdots \psi_i(\mathbf{r}_i) \cdots \psi_n(\mathbf{r}_n) \,, \tag{B.137}$$

where n is the number of electrons in the atom and A is the antisymmetrization operator (Slater determinant), then it can be shown that for any function $g(\mathbf{r})$,

$$\langle \phi | g(\mathbf{r}_i) | \phi \rangle = \frac{1}{n} \int (|\psi_1(\mathbf{r})|^2 + \cdots + |\psi_n(\mathbf{r})|^2) g(\mathbf{r})\, d\mathbf{r} \,, \tag{B.138}$$

which is independent of i. Thus for $g(\mathbf{r}) = e^{i\mathbf{Q}\cdot\mathbf{r}}$, we have

$$\langle\lambda|e^{i\mathbf{Q}\cdot\mathbf{r}_i}|\lambda\rangle = \langle\phi|e^{i\mathbf{Q}\cdot\mathbf{r}_i}|\phi\rangle = \frac{1}{n}\int \rho_S(\mathbf{r})e^{i\mathbf{Q}\cdot\mathbf{r}} \equiv f(\mathbf{Q})\,, \tag{B.139}$$

where the spin density $\rho_S(\mathbf{r})$ here is limited to the scope of an atom, and $f(\mathbf{Q})$ is called the **magnetic form factor**. We see that the matrix element of $\mathbf{M}$ has become

$$\begin{aligned} -\frac{1}{2\mu_B}\langle\lambda_f|\mathbf{M}|\lambda_i\rangle &= \sum_{\ell i}\langle\lambda_f|e^{i\mathbf{Q}\cdot\mathbf{r}_i}|\lambda_f\rangle\langle\lambda_f|e^{i\mathbf{Q}\cdot\mathbf{r}_\ell}\mathbf{s}_i|\lambda_i\rangle \\ &= \sum_{\ell} f(\mathbf{Q})\langle\lambda_f|e^{i\mathbf{Q}\cdot\mathbf{r}_\ell}\sum_i \mathbf{s}_i|\lambda_i\rangle \\ &= f(\mathbf{Q})\sum_\ell \langle\lambda_f|e^{i\mathbf{Q}\cdot\mathbf{r}_\ell}\mathbf{S}_\ell|\lambda_i\rangle\,, \end{aligned} \tag{B.140}$$

where $\mathbf{S}_\ell$ is the total spin operator for the atom ℓ.

In the case of unquenched orbital angular momentum ($L \neq 0$), such as in the rare earth elements, there is only a minor change to the notation. First, the magnetic form factor $f(\mathbf{Q})$ is replaced with $\frac{1}{2}gf(\mathbf{Q})$, with g the Landé factor and $f(\mathbf{Q})$ a more complicated function of the spin density. The second change is that $\mathbf{S}$, although not explicitly rewritten, is considered to be the total angular momentum $\mathbf{J}$.

Now we can write

$$\begin{aligned} \frac{1}{(2\mu_B)^2}\left\langle M^\dagger_\alpha(0)M_\beta(t)\right\rangle &= |\tfrac{1}{2}gf(\mathbf{Q})|^2\sum_{\ell\ell'}\left\langle e^{-i\mathbf{Q}\cdot\mathbf{r}_{\ell'}(0)}S^\alpha_{\ell'}(0)e^{i\mathbf{Q}\cdot\mathbf{r}_\ell(t)}S^\beta_\ell(t)\right\rangle \\ &= |\tfrac{1}{2}gf(\mathbf{Q})|^2\sum_{\ell\ell'}\left\langle e^{-i\mathbf{Q}\cdot\mathbf{r}_{\ell'}(0)}e^{i\mathbf{Q}\cdot\mathbf{r}_\ell(t)}\right\rangle\left\langle S^\alpha_{\ell'}(0)S^\beta_\ell(t)\right\rangle\,. \end{aligned} \tag{B.141}$$

The second line is justified by noting that the orientation of the atomic spins have a minimal effect on the motions of the nuclei. The cross section becomes

$$\begin{aligned} \frac{d^2\sigma}{d\Omega dE_f} = \frac{(\gamma r_0)^2}{2\pi\hbar}\frac{k_f}{k_i}|\tfrac{1}{2}gf(\mathbf{Q})|^2\sum_{\alpha\beta}(\delta_{\alpha\beta}-\hat{Q}_\alpha\hat{Q}_\beta) \\ \times\sum_{\ell\ell'}\int\left\langle e^{-i\mathbf{Q}\cdot\mathbf{r}_{\ell'}(0)}e^{i\mathbf{Q}\cdot\mathbf{r}_\ell(t)}\right\rangle\left\langle S^\alpha_{\ell'}(0)S^\beta_\ell(t)\right\rangle e^{-i\omega t}\,dt\,. \end{aligned} \tag{B.142}$$

The expression on the second line above can be evaluated using the same technique as in the earlier discussion of nuclear scattering:

$$\begin{aligned}
&\sum_{\ell\ell'} \int \left\langle e^{-i\mathbf{Q}\cdot\mathbf{r}_{\ell'}(0)} e^{i\mathbf{Q}\cdot\mathbf{r}_{\ell}(t)} \right\rangle \left\langle S^{\alpha}_{\ell'}(0) S^{\beta}_{\ell}(t) \right\rangle e^{-i\omega t}\, dt \\
&\quad = \sum_{\ell\ell'} e^{i\mathbf{Q}\cdot(\mathbf{R}_{\ell}-\mathbf{R}_{\ell'})} \int \left\langle e^{-i\mathbf{Q}\cdot\mathbf{u}_{\ell'}(0)} e^{i\mathbf{Q}\cdot\mathbf{u}_{\ell}(t)} \right\rangle \left\langle S^{\alpha}_{\ell'}(0) S^{\beta}_{\ell}(t) \right\rangle e^{-i\omega t}\, dt \\
&\quad = N \sum_{\ell} e^{i\mathbf{Q}\cdot\mathbf{R}_{\ell}} \int \left\langle e^{-i\mathbf{Q}\cdot\mathbf{u}_{0}(0)} e^{i\mathbf{Q}\cdot\mathbf{u}_{\ell}(t)} \right\rangle \left\langle S^{\alpha}_{0}(0) S^{\beta}_{\ell}(t) \right\rangle e^{-i\omega t}\, dt
\end{aligned} \tag{B.143}$$

The first thermally averaged factor describes both elastic and inelastic scattering in the phonon system. The second factor describes both elastic and inelastic scattering in the spin system (i.e., due to changes in the orientation of electronic spins). We are primarily interested in the cases in which the scattering is elastic in the phonon system. (A process that does not fall into this category is **magnetovibrational scattering**, in which phonons are created or absorbed by scattering elastically from the electron spins.) Restricting ourselves to processes that are elastic in the phonon system is done by equating the first thermal factor to:

$$\langle e^{U} e^{V} \rangle_{\text{el}} = e^{\langle U^2 \rangle} e^{\langle UV \rangle}\Big|_{\text{el}} = e^{\langle U^2 \rangle} = e^{-2W}\,. \tag{B.144}$$

The cross section becomes

$$\begin{aligned}
\frac{d^2\sigma}{d\Omega dE_f} = \frac{N}{2\pi\hbar}(\gamma r_0)^2 \frac{k_f}{k_i} |\tfrac{1}{2} g f(\mathbf{Q})|^2 e^{-2W} \sum_{\alpha\beta} (\delta_{\alpha\beta} - \hat{Q}_{\alpha}\hat{Q}_{\beta}) \\
\times \sum_{\ell} e^{i\mathbf{Q}\cdot\mathbf{R}_{\ell}} \int \left\langle S^{\alpha}_{0}(0) S^{\beta}_{\ell}(t) \right\rangle e^{-i\omega t}\, dt\,.
\end{aligned} \tag{B.145}$$

The second half of this expression can be defined as the scattering function for magnetic scattering:

$$S_{\alpha\beta}(\mathbf{Q},\omega) = \frac{1}{2\pi\hbar} \sum_{\ell} e^{i\mathbf{Q}\cdot\mathbf{R}_{\ell}} \int \left\langle S^{\alpha}_{0}(0) S^{\beta}_{\ell}(t) \right\rangle e^{-i\omega t}\, dt\,. \tag{B.146}$$

B.2.4 Elastic magnetic scattering

When we consider the elastic component, we take the matrix element in the limit of $t \to \infty$:

$$\lim_{t\to\infty} \left\langle S^{\alpha}_{0}(0) S^{\beta}_{\ell}(t) \right\rangle = \langle S^{\alpha}_{0} \rangle \langle S^{\beta}_{\ell} \rangle\,. \tag{B.147}$$

The elastic cross section is thus

$$\left.\frac{d\sigma}{d\Omega}\right|_{\rm el} = (\gamma r_0)^2 N |\tfrac{1}{2} g f(\mathbf{Q})|^2 e^{-2W} \sum_{\alpha\beta} (\delta_{\alpha\beta} - \hat{Q}_\alpha \hat{Q}_\beta) \sum_\ell e^{i\mathbf{Q}\cdot\mathbf{R}_\ell} \langle S_0^\alpha \rangle \langle S_\ell^\beta \rangle \,. \tag{B.148}$$

Ferromagnet

It is easiest to start with a ferromagnet. In a typical ferromagnet, there are multiple domains in which the spins line up along some direction $\hat{\boldsymbol{\eta}}$. We start with a single domain of a Bravais ferromagnet. Only one component $\langle S_\ell^\eta \rangle$ of the spin is nonzero, and furthermore, $\langle S_\ell^\eta \rangle = \langle S^\eta \rangle$ is independent of the site position ℓ. Thus we have

$$\left.\frac{d\sigma}{d\Omega}\right|_{\rm el} = (\gamma r_0)^2 N |\tfrac{1}{2} g f(\mathbf{Q})|^2 e^{-2W} (1 - (\hat{\mathbf{Q}} \cdot \hat{\boldsymbol{\eta}})^2) \langle S^\eta \rangle^2 \sum_\ell e^{i\mathbf{Q}\cdot\mathbf{R}_\ell} \,. \tag{B.149}$$

Using (B.76), and generalizing to multiple domains, we have

$$\left.\frac{d\sigma}{d\Omega}\right|_{\rm el} = (\gamma r_0)^2 N \frac{(2\pi)^3}{v_0} \langle S^\eta \rangle^2 \sum_i \delta(\mathbf{Q} - \mathbf{G}_i) |\tfrac{1}{2} g f(\mathbf{Q})|^2 (1 - (\hat{\mathbf{Q}} \cdot \hat{\boldsymbol{\eta}})^2_{\rm av}) e^{-2W} \,, \tag{B.150}$$

where $(1 - (\hat{\mathbf{Q}} \cdot \hat{\boldsymbol{\eta}})^2_{\rm av})$ is the average over all domains. If $\hat{\boldsymbol{\eta}}$ is equally likely to be in any direction, or if it has cubic symmetry, then

$$(1 - (\hat{\mathbf{Q}} \cdot \hat{\boldsymbol{\eta}})^2_{\rm av}) = \frac{2}{3} \,. \tag{B.151}$$

For a non-Bravais ferromagnet, in analogy with (B.81) we can generalize to

$$\left.\frac{d\sigma}{d\Omega}\right|_{\rm el} = N \frac{(2\pi)^3}{v_0} \sum_i \delta(\mathbf{Q} - \mathbf{G}_i) |\mathbf{F}_{\rm M}(\mathbf{Q})|^2 \,, \tag{B.152}$$

where the **static magnetic structure factor** is defined as

$$\mathbf{F}_{\rm M}(\mathbf{Q}) = \sum_j \gamma r_0 (\tfrac{1}{2} g_j f_j(\mathbf{Q})) \langle \mathbf{S}^\eta_{\perp j} \rangle e^{\mathbf{Q}\cdot\mathbf{d}_j} e^{-W_j} \,. \tag{B.153}$$

The ferromagnetic Bragg peaks occur at the same locations as the nuclear Bragg peaks, namely at the reciprocal lattice vectors $\mathbf{G}_i$. However, there are some principal differences in the behavior of the magnetic peaks:

- The temperature-dependence of $\langle S^\eta \rangle^2$, which decreases down to zero at the ferromagnetic critical temperature $T_{\rm C}$.

- The $\mathbf{Q}$-dependence of $f(\mathbf{Q})$. Because the magnetic potential is larger than the delta-function nuclear potential, the magnetic response drops off at large $\mathbf{Q}$.
- The magnetic-field-dependence of $(1-(\hat{\mathbf{Q}}\cdot\hat{\boldsymbol{\eta}})^2_{\rm av})$. For instance, if the spins are polarized along a certain $\mathbf{G}_i$, the magnetic scattering there vanishes.

Antiferromagnet

Now consider the case of an antiferromagnet. The usual picture is to divide the lattice into two interpenetrating sublattices which have opposite directions for their spins. We can use the formula above for a non-Bravais ferromagnet with some changes. The magnetic sublattices define a new **magnetic unit cell** with volume $v_{0\rm M} = 2v_0$. A sublattice has $N_{\rm M} = N/2$ sites and has a different set of reciprocal lattice vectors $\mathbf{G}_{\rm M}$. The formula becomes

$$\left.\frac{d\sigma}{d\Omega}\right|_{\rm el} = N_{\rm M}\frac{(2\pi)^3}{v_{0\rm M}}\sum_i \delta(\mathbf{Q}-\mathbf{G}_{{\rm M}i})|\mathbf{F}_{\rm M}(\mathbf{Q})|^2\,, \tag{B.154}$$

where the magnetic structure factor is

$$\mathbf{F}_{\rm M}(\mathbf{Q}) = \sum_j \gamma r_0(\tfrac{1}{2}g_j f_j(\mathbf{Q}))\langle \mathbf{S}^\eta_{\perp j}\rangle e^{\mathbf{Q}\cdot\mathbf{d}_j}e^{-W}\,, \tag{B.155}$$

where in this case the j label the spins in the magnetic unit cell. In the case of an overall Bravais arrangement of magnetic atoms, there are two spins in a unit cell that are oppositely aligned. The magnetic structure factor becomes

$$\mathbf{F}_{\rm M}(\mathbf{Q}) = \gamma r_0(\tfrac{1}{2}gf(\mathbf{Q}))\langle \mathbf{S}^\eta_\perp\rangle\left(1-e^{\mathbf{Q}\cdot\mathbf{R}_0}\right)e^{-W}\,, \tag{B.156}$$

where $\mathbf{R}_0$ is the distance between the two sublattices, namely a vector connecting nearest neighbors in the nuclear lattice. We can see that for $\mathbf{Q} = \mathbf{G}_{\rm M}$ such that $e^{\mathbf{G}_{\rm M}\cdot\mathbf{R}_0} = 1$, namely a nuclear reciprocal lattice vector, the magnetic structure factor is zero. The magnetic structure factor is nonzero at magnetic reciprocal lattice vectors which are not also nuclear reciprocal lattice vectors. In the square-lattice antiferromagnet, $\mathbf{Q} = (\frac{1}{2},\frac{1}{2})$ is one of these vectors, and is often called the antiferromagnetic zone center.

B.2.5 Inelastic magnetic scattering

Recall the equation for the total magnetic scattering cross section (B.145):

$$\frac{d^2\sigma}{d\Omega dE_f} = (\gamma r_0)^2 \frac{k_f}{k_i} N |\tfrac{1}{2} g f(\mathbf{Q})|^2 e^{-2W} \sum_{\alpha\beta} (\delta_{\alpha\beta} - \hat{Q}_\alpha \hat{Q}_\beta) S_{\alpha\beta}(\mathbf{Q}, \omega)\,, \tag{B.157}$$

where the scattering function is

$$S_{\alpha\beta}(\mathbf{Q}, \omega) = \frac{1}{2\pi\hbar} \sum_\ell e^{i\mathbf{Q}\cdot\mathbf{R}_\ell} \int \left\langle S_0^\alpha(0) S_\ell^\beta(t) \right\rangle e^{-i\omega t}\, dt\,. \tag{B.158}$$

Notice that, just as in the definition for nuclear scattering, the scattering function is a Fourier transform of a correlation function. This time, instead of the density-density correlation function $C_{\rho\rho}$, it is the spin-spin correlation function

$$C_{SS}^{\alpha\beta}(\ell, \ell', t - t') = \left\langle S_\ell^\alpha(t) S_{\ell'}^\beta(t') \right\rangle\,. \tag{B.159}$$

The goal of this section is to rewrite the magnetic cross section in terms of a generalized susceptibility that is more physically meaningful and which is more amenable to calculations. To do this, we will be using the **fluctuation-dissipation theorem**, which relates the time-dependent correlation function C_{AB} of a system in thermal equilibrium to the linear response χ_{AB} of a system perturbed by a generalized external field.

Fluctuation-dissipation theorem

As implied above, a correlation function has the general form

$$C_{AB}(t - t') = \langle A(t) B(t') \rangle\,, \tag{B.160}$$

where we have suppressed the dependence on spatial coordinates. In order to define the susceptibility we need a few more definitions. When an external field h_B conjugate to a variable B is applied to the system, the Hamiltonian changes as

$$H(t) = H_0 + H_1 = H_0 - B h_B(t)\,, \tag{B.161}$$

and in the linear approximation, the change in a quantity A is given as

$$A(\mathbf{r}, t) = \langle A \rangle + \int_{-\infty}^{t} dt' \widetilde{\chi}_{AB}(t - t') h_B(t')\,, \tag{B.162}$$

where $\widetilde{\chi}_{AB}(t)$ is called the **response function**, defined only for $t \geq 0$. The response function can shown to be equal to

$$\widetilde{\chi}_{AB}(t) = \frac{i}{\hbar}\langle [A(t), B(0)] \rangle \,, \tag{B.163}$$

where the pair of brackets indicates the commutator. Note that if $h_B(t) = h_B e^{i\omega t}$, then

$$\begin{aligned} \delta A(t) &= \int_{-\infty}^{t} \widetilde{\chi}_{AB}(t-t') h_B e^{i\omega t'} \, dt' \\ &= h_B e^{i\omega t} \int_{-\infty}^{t} \widetilde{\chi}_{AB}(t-t') e^{-i\omega(t-t')} \, dt' \\ &= -h_B e^{i\omega t} \int_{0}^{\infty} \widetilde{\chi}_{AB}(t') e^{-i\omega t'} \, dt' \,, \end{aligned} \tag{B.164}$$

which means that in general the Fourier transforms of $\delta A(t)$ and $h_B(t)$ are related by

$$\delta A(\omega) = \chi_{AB}(\omega) h_B(\omega) \,, \tag{B.165}$$

where the one-sided Fourier transform

$$\chi_{AB}(\omega) = -\int_{0}^{\infty} \widetilde{\chi}_{AB}(t) e^{-i\omega t} \, dt \tag{B.166}$$

is the **generalized susceptibility**. The statement of the fluctuation-dissipation theorem is then that

$$\chi''_{AB}(\omega) = \frac{1}{2\hbar}\left(1 - e^{\hbar\omega/k_{\mathrm{B}}T}\right) C_{AB}(\omega) \,, \tag{B.167}$$

namely that the imaginary (dissipative) part of the susceptibility is equal to a simple prefactor times the Fourier transform of the correlation function. Note that since the prefactor is zero at $\omega = 0$, it is only the fluctuating part ($\omega \neq 0$) of the correlation function which is related to the dissipation. We now prove this relationship for our particular situation.

Magnetic susceptibility

In the case of the magnetic neutron scattering cross section, the variables A and B in the correlation function are most easily seen to be the spin $\mathbf{S}_\ell$. However, we will instead use the magnetization $\mathbf{M}_\ell = -g\mu_{\mathrm{B}}\mathbf{S}_\ell$, because its conjugate field is

the (external) magnetic field $\mathbf{B}_\ell(t)$. The magnetization due to a space- and time-dependent magnetic field is then

$$M_\ell^\alpha(t) = -g\mu_B\langle S_\ell^\alpha\rangle + \sum_{\ell'}\int_{-\infty}^{t}\sum_\beta \widetilde{\chi}_{\alpha\beta}(\ell-\ell', t-t')B_{\ell'}^\beta(t')\,dt'\,, \tag{B.168}$$

where $\widetilde{\chi}_{\alpha\beta} \equiv \widetilde{\chi}_{MM}^{\alpha\beta}$ is the response function, and where $\ell-\ell'$ is shorthand for $\mathbf{R}_\ell - \mathbf{R}_{\ell'}$. The response function is, according to (B.163),

$$\widetilde{\chi}_{\alpha\beta}(\ell, t) = (g\mu_B)^2\frac{i}{\hbar}\left\langle\left[S_\ell^\alpha(t), S_0^\beta\right]\right\rangle\,, \tag{B.169}$$

and the generalized magnetic susceptibility is defined as

$$\chi_{\alpha\beta}(\ell,\omega) = \int_0^\infty \widetilde{\chi}_{\alpha\beta}(\ell,t)e^{-i\omega t}\,dt\,. \tag{B.170}$$

It is convenient to use the real-space transform of the scattering function given by

$$S_{\alpha\beta}(\ell,\omega) = \frac{1}{2\pi\hbar}\int\left\langle S_0^\alpha(0)S_\ell^\beta(t)\right\rangle e^{-i\omega t}\,dt\,. \tag{B.171}$$

We also need the following identity:

$$\begin{aligned}
\langle A(t)B(0)\rangle &= \sum_\lambda \frac{1}{Z}e^{-E_\lambda/k_BT}\langle\lambda|A(t)B(0)|\lambda\rangle \\
&= \sum_{\lambda\lambda'}\frac{1}{Z}\langle\lambda|e^{-H/k_BT}A(t)e^{H/k_BT}|\lambda'\rangle\langle\lambda'|e^{-H/k_BT}B(0)|\lambda\rangle \\
&= \sum_{\lambda\lambda'}\frac{1}{Z}\langle\lambda'|e^{-H/k_BT}B(0)|\lambda\rangle\langle\lambda|A(t+\tfrac{i\hbar}{k_BT})|\lambda'\rangle \\
&= \sum_{\lambda'}\frac{1}{Z}e^{-E_{\lambda'}/k_BT}\langle\lambda'|B(0)A(t+\tfrac{i\hbar}{k_BT})|\lambda'\rangle \\
&= \langle B(0)A(t+\tfrac{i\hbar}{k_BT})\rangle
\end{aligned} \tag{B.172}$$

Now consider the (full) Fourier transform of the response function, allowing t to take on negative values. Using the identity above and a change of variables in the

integration, we find

$$\begin{aligned}
&\frac{1}{2\pi}\int \widetilde{\chi}_{\alpha\beta}(\ell,t)e^{-i\omega t}\,dt \\
&\qquad = (g\mu_{\mathrm{B}})^2\frac{i}{2\pi\hbar}\int \left\langle S^{\alpha}_{\ell}(t)S^{\beta}_{0}(0) - S^{\beta}_{0}(0)S^{\alpha}_{\ell}(t)\right\rangle e^{-i\omega t}\,dt \\
&\qquad = (g\mu_{\mathrm{B}})^2\frac{i}{2\pi\hbar}\int \left\langle S^{\beta}_{0}(0)S^{\alpha}_{\ell}(t+\tfrac{i\hbar}{k_{\mathrm{B}}T})\right\rangle - \left\langle S^{\beta}_{0}(0)S^{\alpha}_{\ell}(t)\right\rangle e^{-i\omega t}\,dt \\
&\qquad = i(g\mu_{\mathrm{B}})^2\left(e^{-\hbar\omega/k_{\mathrm{B}}T}-1\right)S_{\beta\alpha}(\ell,\omega)_{\mathrm{inel}}\,,
\end{aligned} \tag{B.173}$$

where, as discussed before, the inelastic ($\omega \neq 0$) part is now the only relevant component. Note that because of the sum over the factor $(\delta_{\alpha\beta} - \hat{Q}_\alpha\hat{Q}_\beta)$ in the cross section, the scattering factor $S_{\alpha\beta}$ must be symmetric with respect to α and β, namely $S_{\beta\alpha}(\ell,\omega) = S_{\alpha\beta}(\ell,\omega)$. Thus we have

$$S_{\alpha\beta}(\ell,\omega)_{\mathrm{inel}} = \frac{i}{2\pi(g\mu_{\mathrm{B}})^2}(n(\omega)+1)\int \widetilde{\chi}_{\alpha\beta}(\ell,t)e^{-i\omega t}\,dt\,, \tag{B.174}$$

where, as before, the Bose factor is

$$n(\omega)+1 = \frac{1}{1-e^{-\hbar\omega/k_{\mathrm{B}}T}}\,. \tag{B.175}$$

It can be shown that, in the case of inversion symmetry, the response function given by (B.169) is odd in t. In this case,

$$\begin{aligned}
\int \widetilde{\chi}_{\alpha\beta}(\ell,t)e^{-i\omega t}\,dt &= \int_{-\infty}^{0}\widetilde{\chi}_{\alpha\beta}(\ell,t)e^{-i\omega t}\,dt + \int_{0}^{\infty}\widetilde{\chi}_{\alpha\beta}(\ell,t)e^{-i\omega t}\,dt \\
&= -\int_{0}^{\infty}\widetilde{\chi}_{\alpha\beta}(\ell,t)e^{i\omega t}\,dt + \int_{0}^{\infty}\widetilde{\chi}_{\alpha\beta}(\ell,t)e^{-i\omega t}\,dt \\
&= \chi^{*}_{\alpha\beta}(\ell,\omega) - \chi_{\alpha\beta}(\ell,\omega) \\
&= -2i\chi''_{\alpha\beta}(\ell,\omega)\,,
\end{aligned} \tag{B.176}$$

and so we have

$$S_{\alpha\beta}(\ell,\omega)_{\mathrm{inel}} = \frac{1}{\pi(g\mu_{\mathrm{B}})^2}(n(\omega)+1)\chi''_{\alpha\beta}(\ell,\omega)\,. \tag{B.177}$$

If we define the Fourier transform

$$\chi''_{\alpha\beta}(\mathbf{Q},\omega) = \sum_{\ell} e^{i\mathbf{Q}\cdot\mathbf{R}_\ell}\chi''_{\alpha\beta}(\ell,\omega)\,, \tag{B.178}$$

then

$$S_{\alpha\beta}(\mathbf{Q},\omega)_{\text{inel}} = \frac{1}{\pi(g\mu_{\text{B}})^2}(n(\omega)+1)\chi''_{\alpha\beta}(\mathbf{Q},\omega)\,, \tag{B.179}$$

and thus the inelastic magnetic scattering cross section is

$$\left.\frac{d^2\sigma}{d\Omega dE_f}\right|_{\text{inel}} = (\gamma r_0)^2\frac{k_f}{k_i}N|\tfrac{1}{2}gf(\mathbf{Q})|^2e^{-2W}\frac{n(\omega)+1}{\pi(g\mu_{\text{B}})^2}\sum_{\alpha\beta}(\delta_{\alpha\beta}-\hat{Q}_\alpha\hat{Q}_\beta)\chi''_{\alpha\beta}(\mathbf{Q},\omega)\,, \tag{B.180}$$

In the absence of long-range order, and in particular, when there is no preferred orientation of the spins, $\chi''_{\alpha\beta}$ is isotropic. If we define $\chi''_{xx} = \chi''_{yy} = \chi''_{zz} \equiv \chi''$, then the equation simplifies to

$$\left.\frac{d^2\sigma}{d\Omega dE_f}\right|_{\text{inel}} = 2(\gamma r_0)^2\frac{k_f}{k_i}N|\tfrac{1}{2}gf(\mathbf{Q})|^2e^{-2W}\frac{n(\omega)+1}{\pi(g\mu_{\text{B}})^2}\chi''(\mathbf{Q},\omega)\,. \tag{B.181}$$

Even in cases of spin anisotropy, it is often desirable to make this approximation and quote a scalar value. In most neutron-scattering publications, the susceptibility $\chi''(\mathbf{Q},\omega)$ is given in "arbitrary units" simply by dividing the count rate by the Bose factor. Conversion to absolute units can be performed by phonon normalization, discussed in Section 2.4.1 of the main text.

Appendix C

Calculation of the resolution function

In this Appendix, I calculate the resolution function used for neutron scattering measurements. The calculation for the triple-axis spectrometer in Section C.1 follows the work of Cooper and Nathans [163] and Chesser and Axe [164]. In Section C.2, I describe the calculation for the two-axis method according to Cooper and Nathans' second article [165]. However, they do not consider the effect of inelastic scattering, and so I also describe the calculation required for a complete treatment of the two-axis energy-integrating method, as well as how we handle the vertical resolution using a trapezoid approximation.

C.1 Resolution function for triple-axis spectrometer

C.1.1 Definition of variables

In the discussion that follows, it is necessary to distinguish values that define the configuration of the spectrometer (e.g., k_I or ω_0) from those that describe a neutron traveling a slightly different path through the spectrometer (e.g., k_i or ω). The notation and variable names used here are largely unchanged from [163].

Suppose a triple-axis spectrometer is configured to measure a certain scattering process with energy transfer $\hbar\omega_0$ and momentum transfer $\mathbf{Q}_0$. Due to the finite mosaic spread of the monochromator and analyzer crystals and the finite collimations, less-probable neutrons corresponding to slightly different scattering processes are also counted in the detector. The **resolution function** of the spectrometer is the probability of detection of neutrons as a function of $\Delta\omega$ and $\Delta\mathbf{Q}$.

We assume that the four segments of the neutron path through the spectrometer are collimated: before the monochromator, between the monochromator and sample, between the sample and analyzer, and between the analyzer and detector. To make the calculation tractable, we assume that the transmission functions

are Gaussian, in both horizontal and vertical directions. We label the Gaussian widths of the horizontal collimations as $\alpha_0, \alpha_1, \alpha_2, \alpha_3$, while we label the vertical collimations $\beta_0, \beta_1, \beta_2, \beta_3$.

We also assume that the mosaic spread of the monochromator and analyzer are Gaussian. In other words, there is a Gaussian distribution of the orientation of crystal grains.[1] We label the horizontal mosaicities η_M and η_A, and the vertical mosaicities η'_M and η'_A.

The position of the arms of the spectrometer define the three scattering angles $2\theta_M$, $2\theta_S$, and $2\theta_A$. The angles at the monochromator and analyzer determine the (most probable) incident momentum k_I and scattered momentum k_F respectively:

$$k_I = \frac{\pi}{d_M \sin\theta_M} \qquad k_F = \frac{\pi}{d_A \sin\theta_A} \,. \tag{C.1}$$

These relations come directly from Bragg's law. The momentum transfer is then[2]

$$\mathbf{Q}_0 = \mathbf{k}_F - \mathbf{k}_I \,, \tag{C.2}$$

and the energy transfer is

$$\hbar\omega_0 = \frac{\hbar^2}{2m}(k_I^2 - k_F^2) \tag{C.3}$$

If the actual incident and scattered momenta of a particular neutron are $\mathbf{k}_i$ and $\mathbf{k}_f$, then we define

$$\Delta\mathbf{k}_i \equiv \mathbf{k}_i - \mathbf{k}_I$$
$$\Delta\mathbf{k}_f \equiv \mathbf{k}_f - \mathbf{k}_F \,.$$

The difference in momentum transfer is then

$$\Delta\mathbf{Q} \equiv \mathbf{Q} - \mathbf{Q}_0 = \Delta\mathbf{k}_f - \Delta\mathbf{k}_i \,. \tag{C.4}$$

It is also useful to have separate names for the angles at which the neutron differs from the most probable directions in the four segments of the scattering path. The horizontal divergence angles we label $\gamma_0, \gamma_1, \gamma_2, \gamma_3$ and the vertical divergence angles we label $\delta_0, \delta_1, \delta_2, \delta_3$. The energy transfer corresponding to this particular

[1] Monochromator and analyzer crystals, typically made of pyrolytic graphite, are purposefully deformed to have a larger mosaic, allowing a larger number of neutrons to be reflected [47].

[2] As with [163], we follow here the convention in which the momentum and energy transfers have opposite signs. See Footnote 2 on page 146.

neutron path is

$$\hbar\omega = \frac{\hbar^2 k_i^2}{2m} - \frac{\hbar^2 k_f^2}{2m} \tag{C.5}$$

$$\omega = \frac{\hbar}{2m}(k_i^2 - k_f^2)\,, \tag{C.6}$$

which means that the energy transfer differs from the most probable value by (to first order)

$$\Delta\omega = \frac{\hbar}{m}(k_I \Delta k_i - k_F \Delta k_f)\,, \tag{C.7}$$

where $\Delta k_i = k_i - k_I$ and $\Delta k_f = k_f - k_F$ are the differences in the magnitudes of the wavevectors.

The ultimate goal of the calculation is to write the resolution function in terms of $\Delta\mathbf{Q}$ and $\Delta\omega$. The first step is to write the resolution function as a product of probabilities from the various components of the spectrometer. It is a simple matter to then translate the expression to use the components of $\Delta\mathbf{k}_i$ and $\Delta\mathbf{k}_f$. These are then written in terms of $\Delta\mathbf{Q}$ and $\Delta\omega$ with the help of the expressions above, and extraneous degrees of freedom are integrated out.

C.1.2 Product of probabilities

Probability of transmission through a collimator

The simplest probabilities to write down are those of the transmission through a collimator. For example, the probability of transmission through the in-pile collimator is

$$P(\gamma_0, \delta_0) = \exp\left[-\frac{1}{2}\left[\left(\frac{\gamma_0}{\alpha_0}\right)^2 + \left(\frac{\delta_0}{\beta_0}\right)^2\right]\right], \tag{C.8}$$

where the normalization constant is left out by convention. The transmission functions for the other collimators are, of course, the same but with different subscripts.

Notice that the horizontal and vertical probabilities are independent of each other, and can be written as, for example, $P = P_H P_V$. This turns out to be true for the more complicated situation of reflection as well, so we calculate them separately.

Probability of reflection from a monochromator: horizontal component

Consider a monochromator with horizontal mosaicity η_M. Figure C.1 illustrates the following angles: $2\theta_M$ and $2\theta'_M$ are the reflection angle for the most probable neutron path and a less probable neutron path, respectively. $\phi_M = \theta_M$ is the angular

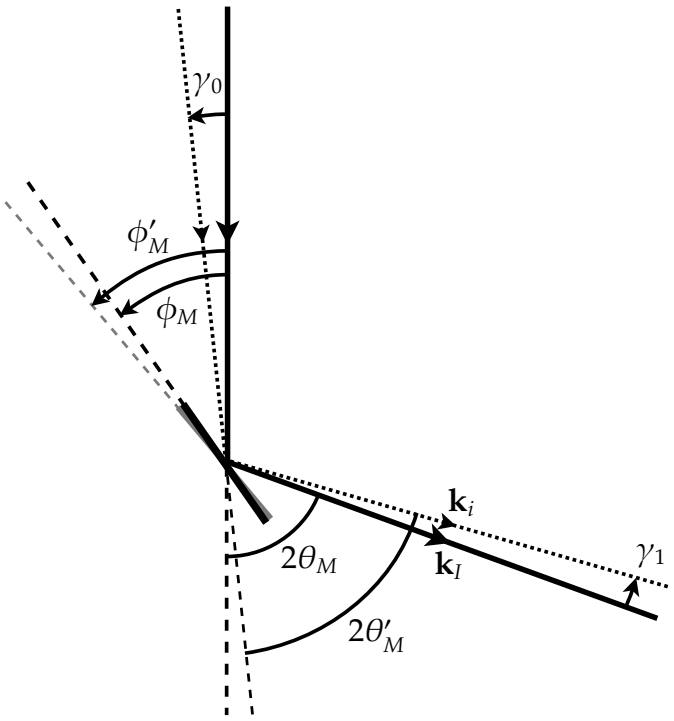

Figure C.1: Reflection from a monochromator with finite mosaicity. The solid arrows indicate the most probable neutron path, reflecting off of a crystal grain oriented at an angle ϕ_M and reflecting with angle $2\theta_M = 2\phi_M$. The dotted arrows indicate a less probable neutron path, which reflects with angle $2\theta'_M$ off of a crystal grain oriented at an angle ϕ'_M.

orientation of the crystal grain reflecting the most probable neutron, and ϕ'_M is the angular orientation of the crystal grain reflecting the less probable neutron. We wish to find an expression for $\Delta\phi_M = \phi'_M - \phi_M$.

From the figure we can see that

$$\phi'_M = \phi_M + \tfrac{1}{2}(\gamma_0 + \gamma_1) \tag{C.9}$$

$$\Delta\phi_M = \tfrac{1}{2}(\gamma_0 + \gamma_1)\,, \tag{C.10}$$

and also that

$$2\theta'_M = 2\theta_M + (\gamma_1 - \gamma_0) \tag{C.11}$$

$$\Delta\theta_M = \tfrac{1}{2}(\gamma_1 - \gamma_0)\,. \tag{C.12}$$

Thus we can write

$$\Delta\phi_M = -\Delta\theta_M + \gamma_1\,, \tag{C.13}$$

and now the objective is to find $\Delta\theta$. We know that

$$k_I = \frac{\pi}{d_M \sin\theta_M}\,, \qquad k_i = \frac{\pi}{d_M \sin\theta'_M}\,, \tag{C.14}$$

and so to first order,

$$\Delta k_i = -\frac{\pi}{d_M \sin\theta_M \tan\theta_M}\Delta\theta_M\,, \tag{C.15}$$

which can be written

$$\frac{\Delta k_i}{k_I} = -\frac{\Delta\theta_M}{\tan\theta_M}\,, \tag{C.16}$$

and thus we have

$$\Delta\theta_M = -\frac{\Delta k_i}{k_I}\tan\theta_M\,. \tag{C.17}$$

Using (C.13), then, we arrive at

$$\Delta\phi_M = \frac{\Delta k_i}{k_I}\tan\theta_M + \gamma_1\,. \tag{C.18}$$

The horizontal component of the probability of reflection is thus

$$P(\Delta k_i, \gamma_1) = \exp\left[-\frac{1}{2}\left(\frac{(\Delta k_i/k_I)\tan\theta_M + \gamma_1}{\eta_M}\right)^2\right], \tag{C.19}$$

where the normalization constant is left out by convention.

The situation with the analyzer is similar, but a sign difference arises from keeping γ_2:

$$\Delta\phi_A = \tfrac{1}{2}(\gamma_2 + \gamma_3) \tag{C.20}$$

$$\Delta\theta_A = \tfrac{1}{2}(\gamma_3 - \gamma_2)\,, \tag{C.21}$$

and thus,

$$\Delta\phi_A = \Delta\theta_A + \gamma_2 \tag{C.22}$$

$$= -\frac{\Delta k_f}{k_F}\tan\theta_A + \gamma_2\,. \tag{C.23}$$

The probability of reflection is then

$$P(\Delta k_f, \gamma_2) = \exp\left[-\frac{1}{2}\left(\frac{(\Delta k_f/k_F)\tan\theta_A - \gamma_2}{\eta_A}\right)^2\right]. \tag{C.24}$$

Total horizontal component

The total horizontal component of probability is simply the product of probabilities from the monochromator, analyzer, and collimators. However, from the discussion above we can write γ_0 and γ_3 in the collimator expressions in terms of the other variables:

$$\gamma_0 = \Delta\phi_M - \Delta\theta_M = \frac{2\Delta k_i}{k_I}\tan\theta_M + \gamma_1$$
$$\gamma_3 = \Delta\phi_A + \Delta\theta_A = -\frac{2\Delta k_f}{k_F}\tan\theta_A - \gamma_2\,.$$

Thus the total horizontal component is a function of Δk_i, Δk_f, γ_1, and γ_2:

$$P_H = \exp\left[-\frac{1}{2}\left[\left(\frac{(\Delta k_i/k_I)\tan\theta_M + \gamma_1}{\eta_M}\right)^2 + \left(\frac{(\Delta k_f/k_F)\tan\theta_A - \gamma_2}{\eta_A}\right)^2 + \left(\frac{2(\Delta k_i/k_I)\tan\theta_M + \gamma_1}{\alpha_0}\right)^2 + \left(\frac{\gamma_1}{\alpha_1}\right)^2 + \left(\frac{\gamma_2}{\alpha_2}\right)^2 + \left(\frac{2(\Delta k_f/k_F)\tan\theta_A - \gamma_2}{\alpha_3}\right)^2\right]\right]. \tag{C.25}$$

Probability of reflection from a monochromator: vertical component

Now consider the vertical mosaicity η'_M of a monochromator. A neutron incident on the monochromator travels at an angle δ_0 from the horizontal plane. In order to compare this angle to the mosaicity, we must project this angle onto the vertical plane containing the normal vector to the monochromator surface. At a distance L from the point of reflection, the neutron is at a vertical position of $L\delta_0$ (using the small angle approximation). The horizontal distance along the normal vector to this point is $L\sin\theta_M$, which means the projected vertical angle is $\delta_0/\sin\theta_M$.

A reflection of the neutron into the horizontal plane would need a crystal grain oriented at half of that angle: $\delta_0/2\sin\theta_M$. And if we also take into account the vertical divergence δ_1 of the reflected neutron, it is the difference $\delta_0 - \delta_1$ that matters. Thus the vertical component of the probability of reflection is

$$P(\delta_1 - \delta_0) = \exp\left[-\frac{1}{2}\left(\frac{\delta_1 - \delta_0}{2\eta'_M\sin\theta_M}\right)^2\right]. \tag{C.26}$$

Total vertical component

While the probability of reflection or transmission can depend on a great many variables, we are only ultimately concerned on the probability as a function of $\Delta\mathbf{Q}$ and $\Delta\omega$. Once we rewrite the expressions in terms of these physical variables, we must integrate out all other degrees of freedom. One set of integrations we can perform already are over δ_0 and δ_3. Essentially, we do not need to keep track of how much vertical divergence a neutron has before the first collimator because the white beam contains neutrons of all divergences, and we do not need to keep track of how much vertical divergence a neutron has after the last collimator because all such neutrons are counted in the detector.

The expression for the first collimator and the monochromator are integrated together over δ_0:

$$P(\delta_1) = \int d\delta_0 \, \exp\left[-\frac{1}{2}\left[\left(\frac{\delta_0}{\beta_0}\right)^2 + \left(\frac{\delta_1 - \delta_0}{2\eta'_M \sin\theta_M}\right)^2\right]\right] \tag{C.27}$$

$$= P_{0M} \exp\left[-\frac{1}{2}\left(\frac{\delta_1^2}{(2\eta'_M \sin\theta_M)^2 + \beta_0^2}\right)\right], \tag{C.28}$$

where

$$P_{0M} = \sqrt{2\pi}\left(\frac{1}{\beta_0^2} + \frac{1}{(2\eta'_M \sin\theta_M)^2}\right)^{-\frac{1}{2}}. \tag{C.29}$$

Thus the total vertical component is a function of δ_1 and δ_2:

$$P_V = P_{0M} P_{0A} \exp\left[-\frac{1}{2}\left(\frac{\delta_1^2}{(2\eta'_M \sin\theta_M)^2 + \beta_0^2} + \frac{\delta_1^2}{\beta_1^2} + \frac{\delta_2^2}{\beta_2^2} + \frac{\delta_2^2}{(2\eta'_A \sin\theta_A)^2 + \beta_3^2}\right)\right]. \tag{C.30}$$

C.1.3 The resolution function in terms of $\Delta\mathbf{Q}$ and $\Delta\omega$

We now proceed with writing the resolution function in terms of $\Delta\mathbf{Q}$ and $\Delta\omega$. The first step is to explicitly write the components of $\Delta\mathbf{k}_i$ and $\Delta\mathbf{k}_f$:

$$\Delta\mathbf{k}_i = x_1\mathbf{i}_1 + y_1\mathbf{j}_1 + z_1\mathbf{l}_1 \tag{C.31}$$

$$\Delta\mathbf{k}_f = x_2\mathbf{i}_2 + y_2\mathbf{j}_2 + z_2\mathbf{l}_2\,, \tag{C.32}$$

where the basis vectors $\mathbf{i}_1, \mathbf{j}_1$ and $\mathbf{i}_2, \mathbf{j}_2$ are illustrated in Figure C.2, and $\mathbf{l}_1 = \mathbf{l}_2$ is along the vertical direction. Notice that these six components correspond to the six

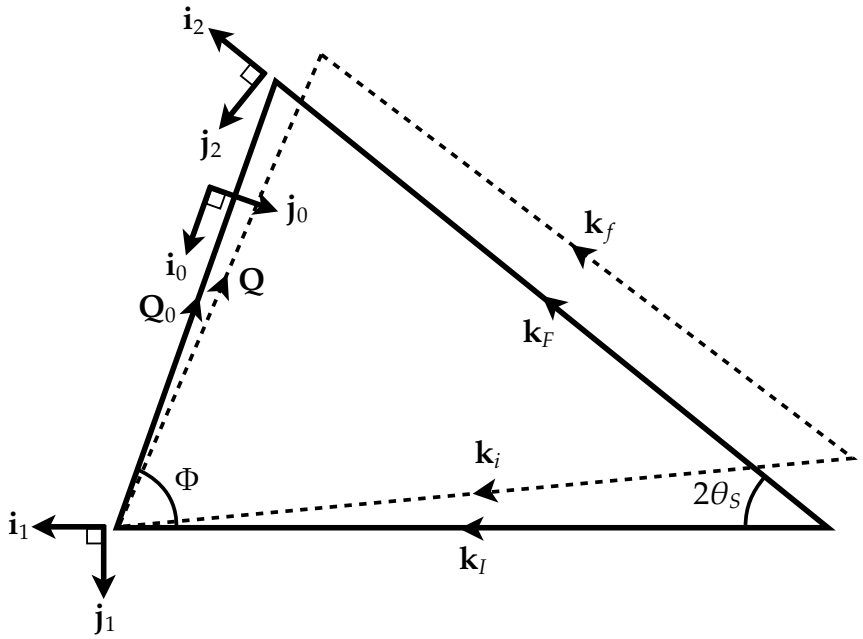

Figure C.2: Reciprocal-space diagram of scattering process, illustrating the angles and basis vectors used in the text.

variables used in the product of probabilities (C.25) and (C.30):

$$\begin{aligned} \Delta k_i &= x_1\,, \qquad \gamma_1 = y_1/k_I\,, \qquad \delta_1 = z_1/k_I\,, \\ \Delta k_f &= x_2\,, \qquad \gamma_2 = y_2/k_F\,, \qquad \delta_2 = z_2/k_F\,, \end{aligned} \tag{C.33}$$

so we rewrite them as

$$\begin{aligned} P_H = \exp\Bigg[-\frac{1}{2}\Bigg[&\left(\frac{\tan\theta_M}{\eta_M k_I}x_1 + \frac{1}{\eta_M k_I}y_1\right)^2 + \left(\frac{\tan\theta_A}{\eta_A k_F}x_2 - \frac{1}{\eta_A k_F}y_2\right)^2 \\ &+ \left(\frac{2\tan\theta_M}{\alpha_0 k_I}x_1 + \frac{1}{\alpha_0 k_I}y_1\right)^2 + \left(\frac{1}{\alpha_1 k_I}y_1\right)^2 \\ &+ \left(\frac{1}{\alpha_2 k_F}y_2\right)^2 + \left(\frac{2\tan\theta_A}{\alpha_3 k_F}x_2 - \frac{1}{\alpha_3 k_F}y_2\right)^2\Bigg]\Bigg] \end{aligned} \tag{C.34}$$

and

$$P_V = P_{0M}P_{0A}\exp\left[-\frac{1}{2}\left(\frac{z_1^2}{(4\eta_M'^2\sin^2\theta_M + \beta_0^2)k_I^2} + \frac{z_1^2}{\beta_1^2 k_I^2} + \frac{z_2^2}{\beta_2^2 k_F^2} + \frac{z_2^2}{(4\eta_A'^2\sin^2\theta_A + \beta_3^2)k_F^2}\right)\right]. \tag{C.35}$$

Next we must write out the components of $\Delta\mathbf{Q}$ in the coordinate system $(\mathbf{i}_0, \mathbf{j}_0, \mathbf{l}_0)$ as indicated in Figure C.2. Note that the components of $\Delta\mathbf{Q}$ are defined with respect to $\mathbf{Q}_0$, and not with respect to the crystal axes. The calculated resolution function must be rotated into the crystal axes coordinate system for comparisons with data.

In the $\mathbf{Q}_0$-based coordinate system, the components of $\Delta\mathbf{k}_i$ and $\Delta\mathbf{k}_f$ become

$$\Delta\mathbf{k}_i = (x_1 b + y_1 a)\mathbf{i}_0 + (-x_1 a + y_1 b)\mathbf{j}_0 + z_1\mathbf{l}_0\,, \tag{C.36}$$

$$\Delta\mathbf{k}_f = (x_2 B + y_2 A)\mathbf{i}_0 + (-x_2 A + y_2 B)\mathbf{j}_0 + z_2\mathbf{l}_0\,, \tag{C.37}$$

where we define

$$\begin{aligned} a &\equiv \sin\Phi\,, & A &\equiv \sin(2\theta_S + \Phi)\,, \\ b &\equiv \cos\Phi\,, & B &\equiv \cos(2\theta_S + \Phi)\,. \end{aligned} \tag{C.38}$$

The components of $\Delta\mathbf{Q}$ are then

$$\Delta Q_x = x_2 B + y_2 A - x_1 b - y_1 a\,, \tag{C.39}$$

$$\Delta Q_y = -x_2 A + y_2 B + x_1 a - y_1 b\,, \tag{C.40}$$

$$\Delta Q_z = z_2 - z_1\,. \tag{C.41}$$

And from (C.7) we can write down $\Delta\omega$ in terms of these same components:

$$\Delta\omega = \frac{\hbar}{m}(x_1 k_I - x_2 k_F)\,. \tag{C.42}$$

At this point it is easy to see that the horizontal component of the resolution function depends only on ΔQ_x, ΔQ_y, and $\Delta\omega$, whereas the vertical component depends only on ΔQ_z. We will thus treat them separately.

Horizontal component of the resolution function

So far, the expression in (C.34) depends on x_1, y_1, x_2, and y_2. With the three equations (C.39), (C.40), and (C.42) for ΔQ_x, ΔQ_y, and $\Delta\omega$, we have one extra degree of freedom. We arbitrarily choose to write y_1, y_2 and x_2 in terms of x_1. After some algebra we find that

$$y_1 = -\frac{\lambda - \beta}{\alpha}x_1 + \frac{B}{\alpha}\Delta Q_x - \frac{A}{\alpha}\Delta Q_y + \frac{m}{\alpha\hbar k_F}\Delta\omega\,, \tag{C.43}$$

$$y_2 = -\frac{\beta\lambda - 1}{\alpha}x_1 + \frac{b}{\alpha}\Delta Q_x - \frac{a}{\alpha}\Delta Q_y + \frac{\beta m}{\alpha\hbar k_F}\Delta\omega\,, \tag{C.44}$$

$$x_2 = \lambda x_1 - \frac{m}{\hbar k_F}\Delta\omega\,, \tag{C.45}$$

where we define

$$\alpha \equiv \sin 2\theta_S\,, \qquad \beta \equiv \cos 2\theta_S\,, \qquad \lambda \equiv \frac{k_I}{k_F}\,. \tag{C.46}$$

The horizontal component of the resolution function is then (C.34) integrated over x_1, which can be written

$$R_H = \int_{-\infty}^{\infty} \exp(-\tfrac{1}{2}[A'x_1^2 + B'x_1 + C'])\,dx_1\,, \tag{C.47}$$

where A', B', and C' are functions of ΔQ_x, ΔQ_y and $\Delta\omega$ involving the coefficients found in (C.34), (C.43), (C.44), and (C.45). The integration yields

$$R_H = R_0^H \exp\left(-\frac{1}{2}\left(C' - \frac{B'^2}{4A'}\right)\right). \tag{C.48}$$

All terms in $(C' - B'^2/4A')$ are second-order in ΔQ_x, ΔQ_y and $\Delta\omega$. We define

$$X_1 \equiv \Delta Q_x\,, \qquad X_2 \equiv \Delta Q_y\,, \qquad X_4 \equiv \Delta\omega\,, \tag{C.49}$$

so that we can write

$$R_H = R_0^H \exp(-\tfrac{1}{2}M_{k\ell}X_kX_\ell)\,, \tag{C.50}$$

where k and ℓ are summed over $1, 2, 4$. The details of how to calculate the matrix elements $M_{k\ell}$ are given in a later section.

Vertical component of the resolution function

The expression so far (C.35) depends on z_1 and z_2. Because, $\Delta Q_z = z_2 - z_1$, we substitute

$$z_2 = z_1 + \Delta Q_z \tag{C.51}$$

into the expression and integrate over z_1. Letting

$$X_3 \equiv \Delta Q_z\,, \tag{C.52}$$

we have

$$R_V = R_0^V \exp(-\tfrac{1}{2}M_{33}X_3^2)\,. \tag{C.53}$$

Horizontal and vertical components combined

Thus if we let $M_{k3} = M_{3\ell} = 0$ for all k and ℓ, we can write down the horizontal and vertical components together as

$$R = R_0 \exp(-\tfrac{1}{2} M_{k\ell} X_k X_\ell)\,, \tag{C.54}$$

where k and ℓ are now summed over $1, 2, 3, 4$. Visualizing the resolution function is done by plotting the contour $R = R_0/2$, which is an ellipsoid in four-dimensional energy-momentum space. Projecting this ellipsoid onto any of the axes then yields the FWHM resolution for that direction. There is a freely-available Matlab package called ResLib [49] that calculates and plots resolution ellipsoids.

C.1.4 Algorithm for calculating the resolution function

Here we describe the algorithm used for calculating the $M_{k\ell}$. The notation used is from Cooper and Nathans [163].

We begin with the horizontal component. Defining $X_1 \equiv \Delta Q_x$, $X_2 \equiv \Delta Q_y$, and $X_4 \equiv \Delta\omega$ as above, we write

$$\begin{aligned} y_1 &= Cx_1 + D\,, & D &= d_1 X_1 + d_2 X_2 + d_4 X_4\,, \\ y_2 &= Ex_1 + F\,, & F &= f_1 X_1 + f_2 X_2 + f_4 X_4\,, \\ x_2 &= \lambda x_1 + H\,, & H &= h_1 X_1 + h_2 X_2 + h_4 X_4\,, \end{aligned} \tag{C.55}$$

where we define

$$\begin{aligned} C &= -\frac{\lambda - \beta}{\alpha}\,, & d_1 &= \frac{B}{\alpha}\,, & d_2 &= -\frac{A}{\alpha}\,, & d_4 &= \frac{m}{\alpha \hbar k_F}\,, \\ E &= -\frac{\beta\lambda - 1}{\alpha}\,, & f_1 &= \frac{b}{\alpha}\,, & f_2 &= -\frac{a}{\alpha}\,, & f_4 &= \frac{\beta m}{\alpha \hbar k_F}\,, \\ & & h_1 &= 0\,, & h_2 &= 0\,, & h_4 &= -\frac{m}{\hbar k_F}\,. \end{aligned} \tag{C.56}$$

Now we write the horizontal component of the resolution function (C.34) as

$$P_H = \exp[-\tfrac{1}{2}(a_1 x_1 + a_2 y_1)^2 + a_3^2 y_1^2 + a_4^2 y_2^2 + (a_5 x_2 + a_6 y_2)^2 + (a_7 x_1 + a_8 y_1)^2 + (a_9 x_2 + a_{10} y_2)^2)]\,, \tag{C.57}$$

where

$$a_1 = \frac{\tan\theta_M}{\eta_M k_I}, \quad a_2 = \frac{1}{\eta_M k_I}, \quad a_3 = \frac{1}{\alpha_1 k_I}, \quad a_4 = \frac{1}{\alpha_2 k_F}, \quad a_5 = \frac{\tan\theta_A}{\eta_A k_F},$$
$$a_6 = -\frac{1}{\eta_A k_F}, \quad a_7 = \frac{2\tan\theta_M}{\alpha_0 k_I}, \quad a_8 = \frac{1}{\alpha_0 k_I}, \quad a_9 = \frac{2\tan\theta_A}{\alpha_3 k_F}, \quad a_{10} = -\frac{1}{\alpha_3 k_F}. \tag{C.58}$$

To write the resolution function in the form of (C.47), we first define

$$\begin{aligned} b_0 &= a_1a_2 + a_7a_8, & b_1 &= a_2^2 + a_3^2 + a_8^2, & b_2 &= a_4^2 + a_6^2 + a_{10}^2, \\ b_3 &= a_5^2 + a_9^2, & b_4 &= a_5a_6 + a_9a_{10}, & b_5 &= a_1^2 + a_7^2, \end{aligned} \tag{C.59}$$

which lets us write

$$A' = 2b_0C + b_1C^2 + b_2E^2 + b_3\lambda^2 + 2b_4\lambda E + b_5, \tag{C.60}$$
$$B' = 2[(b_0 + b_1C)D + (b_2E + b_4\lambda)F + (b_3\lambda + b_4E)H], \tag{C.61}$$
$$C' = b_1D^2 + b_2F^2 + b_3H^2 + 2b_4FH, \tag{C.62}$$

where it becomes clear that A' is constant in the X's, B' is linear in the X's, and C' is quadratic in the X's, from the definitions of D, F, and H. When the integral is solved as (C.48), the final value in the exponent is $C' - B'^2/4A'$, which is quadratic in the X's. If we define

$$\begin{aligned} g_0 &= b_1 - (b_0 + b_1C)^2/A', & g_3 &= 2b_4 - 2(b_2E + b_4\lambda)(b_3\lambda + b_4E)/A', \\ g_1 &= b_2 - (b_2E + b_4\lambda)^2/A', & g_4 &= -2(b_0 + b_1C)(b_2E + b_4\lambda)/A', \\ g_2 &= b_3 - (b_3\lambda + b_4E)^2/A', & g_5 &= -2(b_0 + b_1C)(b_3\lambda + b_4E)/A', \end{aligned} \tag{C.63}$$

then we can write

$$C' - \frac{B'^2}{4A'} = g_0D^2 + g_1F^2 + g_2H^2 + g_3FH + g_4DF + g_5DH. \tag{C.64}$$

Finally, we can use this to write a formula for the matrix elements:

$$M_{k\ell} = g_0d_kd_\ell + g_1f_kf_\ell + g_2h_kh_\ell + \tfrac{1}{2}g_3(f_kh_\ell + f_\ell h_k) + \tfrac{1}{2}g_4(d_kf_\ell + d_\ell f_k) + \tfrac{1}{2}g_5(d_kh_\ell + d_\ell h_k), \tag{C.65}$$

for $k, \ell = 1, 2, 4$.

For the vertical component, we write (C.35) as

$$P_V \propto \exp[-\tfrac{1}{2}(a_{11}^2z_1^2 + a_{12}^2z_2^2)], \tag{C.66}$$

where

$$a_{11}^2 = \frac{1}{(4\sin^2\theta_M\eta_M'^2 + \beta_0^2)k_I^2} + \frac{1}{\beta_1^2 k_I^2}\,, \qquad a_{12}^2 = \frac{1}{\beta_2^2 k_F^2} + \frac{1}{(4\sin^2\theta_A\eta_A'^2 + \beta_3^2)k_F^2}\,. \quad \text{(C.67)}$$

Integration over z_1 yields the final matrix element

$$M_{33} = \frac{a_{11}^2 a_{12}^2}{a_{11}^2 + a_{12}^2}\,. \quad \text{(C.68)}$$

C.1.5 Normalization

In the above discussion the normalization factor has not been explicitly calculated. A few years after the article by Cooper and Nathans [163], an article by Chesser and Axe [164] was published on how to calculate the normalization factor. Their results are discussed here.

The normalization factor is not just calculated for completeness. Even though it is a constant with respect to the important variables $\Delta\mathbf{Q}$ and $\Delta\omega$, it is still a complicated function of the angles of the spectrometer. Thus to properly normalize data across a large range of spectrometer configurations, one must take into account the effects of this normalization factor.

The prefactor R_0 in (C.54) is composed of a number of factors, some of which we have already encountered:

$$R_0 = \phi \cdot \epsilon_D \cdot P_{0M} \cdot P_{0A} \cdot N_M \cdot N_A \cdot J \cdot R_{0x} \cdot R_{0z}\,. \quad \text{(C.69)}$$

The reactor flux ϕ and the detector efficiency ϵ_D are true constants for data from the same spectrometer and are therefore not included in our calculations. P_{0M} and P_{0A} are factors that arise when performing an integration over δ_0 and δ_3, respectively (see the earlier discussion at (C.29)), and are given by

$$P_{0M} = \sqrt{2\pi}\left(\frac{1}{\beta_0^2} + \frac{1}{(2\eta_M'\sin\theta_M)^2}\right)^{-\frac{1}{2}}\,, \quad \text{(C.70)}$$

$$P_{0A} = \sqrt{2\pi}\left(\frac{1}{\beta_3^2} + \frac{1}{(2\eta_A'\sin\theta_A)^2}\right)^{-\frac{1}{2}}\,. \quad \text{(C.71)}$$

The factors N_M and N_A are prefactors that should have been included[3] in (C.26) and the corresponding equation for the analyzer. If we equate the integral over all

[3] All of the other Gaussian probabilities can have prefactors as well, but N_M and N_A are the only ones which involve changing variables of the spectrometer.

$\delta_1 - \delta_0$ in (C.26) to a total reflectivity constant P_M, then

$$N_M = \frac{1}{\sqrt{2\pi}} \frac{P_M}{2\eta'_M \sin\theta_M}, \tag{C.72}$$

and the corresponding prefactor for the analyzer is

$$N_A = \frac{1}{\sqrt{2\pi}} \frac{P_A}{2\eta'_A \sin\theta_A}, \tag{C.73}$$

where the reflectivity constants P_M and P_A are not included in our calculations. N_M and N_A can be combined with P_{0M} and P_{0A}, respectively, to give

$$P_{0M} N_M = \frac{P_M \beta_0}{\sqrt{\beta_0^2 + (2\eta'_M \sin\theta_M)^2}}, \tag{C.74}$$

$$P_{0A} N_A = \frac{P_A \beta_3}{\sqrt{\beta_3^2 + (2\eta'_A \sin\theta_A)^2}}. \tag{C.75}$$

J is the Jacobian after change of variables, given by

$$J = \frac{m}{\hbar} \frac{1}{k_I^2 k_F^3 \sin 2\theta_S}, \tag{C.76}$$

where the constant $m/\hbar$ is not included during calculations. Finally, R_0^H is the constant that comes out of integrating over x_1, and R_0^V is the constant that comes out of integrating over z_1. They are given by

$$R_{0x} = \sqrt{2\pi} \frac{1}{\sqrt{A'}}, \qquad R_{0z} = \sqrt{2\pi} \frac{1}{\sqrt{a_{11}^2 + a_{12}^2}}. \tag{C.77}$$

The total normalization factor, then, excluding the true constants, is

$$R_0 = 2\pi \frac{1}{k_I^2 k_F^3 \sin 2\theta_S} \frac{1}{\sqrt{A'(a_{11}^2 + a_{12}^2)}} \frac{\beta_0}{\sqrt{\beta_0^2 + (2\eta'_M \sin\theta_M)^2}} \frac{\beta_3}{\sqrt{\beta_3^2 + (2\eta'_A \sin\theta_A)^2}}. \tag{C.78}$$

C.1.6 Sample mosaic correction

One component of the system we have so far completely neglected is the sample itself. The mosaicity of the sample itself will effectively broaden the resolution of the spectrometer. This correction to the resolution function was first detailed by Werner and Pynn [166].

Consider a sample with a horizontal mosaic with Gaussian width η_{SH} and vertical mosaic with Gaussian width η_{SV}. Then the matrix elements $M_{k\ell}$ is replaced with

$$M'_{k\ell} = M_{k\ell} - M_{k2}M_{\ell 2}\left(\frac{1}{\eta_{SH}^2 Q_0^2} + M_{22}\right)^{-1} \tag{C.79}$$

for the horizontal components, where $k, \ell = 1, 2, 4$ as before, and

$$M'_{33} = M_{33} - M_{33}^2\left(\frac{1}{\eta_{SV}^2 Q_0^2} + M_{33}\right)^{-1} \tag{C.80}$$

for the vertical term. In addition, the normalization factor is replaced with

$$R'_0 = R_0 \frac{1}{\eta_{SH}\eta_{SV}}\left(\frac{1}{\eta_{SV}^2} + Q_0^2 M_{33}\right)^{-\frac{1}{2}}\left(\frac{1}{\eta_{SH}^2} + Q_0^2 M_{22}\right)^{-\frac{1}{2}}. \tag{C.81}$$

The complete resolution function corrected for the sample mosaic is thus

$$R' = R'_0 \exp(-\tfrac{1}{2}M'_{k\ell}X_k X_\ell), \tag{C.82}$$

for $k, \ell = 1, 2, 3, 4$.

C.2 Resolution function for two-axis method

A two-axis spectrometer is one in which there is no analyzer, and the detector captures all neutrons scattered into it, regardless of their energies. A triple-axis spectrometer can be put into two-axis mode by removing the analyzer,[4] moving the detector arm to $\theta_A = 0$, and removing the collimator right before the detector (i.e., collimator 3). Thus in calculating the resolution function for a two-axis spectrometer, the probability of detection can be written from the triple-axis formulae (C.25) and (C.30) by setting $\tan\theta_A = 0$ and $\eta_A = \eta'_A = \alpha_3 = \beta_3 = \infty$. The horizontal

[4] If removing the analyzer is not possible, it can be rotated to be perpendicular to the beam; if it is a simple (non-focusing) crystal, the vast majority of neutrons pass through.

component is

$$P_H = \exp\left[-\frac{1}{2}\left(\frac{(\Delta k_i/k_I)\tan\theta_M + \gamma_1}{\eta_M}\right)^2 + \left(\frac{2(\Delta k_i/k_I)\tan\theta_M + \gamma_1}{\alpha_0}\right)^2 + \left(\frac{\gamma_1}{\alpha_1}\right)^2 + \left(\frac{\gamma_2}{\alpha_2}\right)^2\right], \quad \text{(C.83)}$$

and the vertical component is

$$P_V = P_{0M}\exp\left[-\frac{1}{2}\left(\frac{\delta_1^2}{(2\eta'_M\sin\theta_M)^2 + \beta_0^2} + \frac{\delta_1^2}{\beta_1^2} + \frac{\delta_2^2}{\beta_2^2}\right)\right]. \quad \text{(C.84)}$$

How to proceed from here depends on what type of measurement is being performed. Historically, two-axis spectrometers were used for measuring elastic scattering. The resolution function for this case was calculated by Cooper and Nathans in a second article [165]. I describe their algorithm in Section C.2.1. However, the two-axis scattering measurements performed on NCCO and described in this Thesis use a method of integrating over inelastically scattered neutrons. I describe how to calculate the resolution function for this case in Section C.2.2. Our group has traditionally used the two-axis method of Cooper and Nathans [165] to analyze our data. Fortunately, this does not significantly affect the results; the reasons are discussed in Section A.3.

C.2.1 Elastic scattering

In the case of elastic scattering, we set $\omega_0 = 0$, but since we consider only elastically scattered neutrons, we also set $\Delta\omega = 0$. Because $k_F = k_I$, the angles of the scattering triangle (Figure C.2) simplify as well:

$$\Phi = \frac{\pi}{2} - \theta_S\,, \qquad 2\theta_S + \Phi = \frac{\pi}{2} + \theta_S\,, \quad \text{(C.85)}$$

so that

$$\begin{aligned} \mathbf{i}_1 &= \mathbf{i}_0\sin\theta_S - \mathbf{j}_0\cos\theta_S\,, & \mathbf{i}_2 &= -\mathbf{i}_0\sin\theta_S - \mathbf{j}_0\cos\theta_S\,, \\ \mathbf{j}_1 &= \mathbf{i}_0\cos\theta_S + \mathbf{j}_0\sin\theta_S\,, & \mathbf{j}_2 &= \mathbf{i}_0\cos\theta_S - \mathbf{j}_0\sin\theta_S\,. \end{aligned} \quad \text{(C.86)}$$

The components of $\Delta\mathbf{k}_i$ and $\Delta\mathbf{k}_f$ are then

$$\Delta\mathbf{k}_i = (x_1 b + y_1 a)\mathbf{i}_0 + (-x_1 a + y_1 b)\mathbf{j}_0 + z_1\mathbf{l}_0\,, \quad \text{(C.87)}$$

$$\Delta\mathbf{k}_f = (-x_1 b + y_2 a)\mathbf{i}_0 + (-x_1 a - y_2 b)\mathbf{j}_0 + z_2\mathbf{l}_0\,, \quad \text{(C.88)}$$

where $a = \sin\Phi = \cos\theta_S$, $b = \cos\Phi = \sin\theta_S$, and where we have also set $x_2 = x_1$ because $\Delta\omega = 0$. The components of $\Delta\mathbf{Q}$ become

$$\Delta Q_x = -2x_1 b + y_2 a - y_1 a\,, \tag{C.89}$$
$$\Delta Q_y = -y_2 b - y_1 b\,, \tag{C.90}$$
$$\Delta Q_z = z_2 - z_1\,. \tag{C.91}$$

Defining $X_1 \equiv \Delta Q_x$, $X_2 \equiv \Delta Q_y$ and $X_3 \equiv \Delta Q_z$ as before, we write

$$\begin{aligned} y_1 &= Cx_1 + D\,, \qquad D = d_1 X_1 + d_2 X_2\,, \\ y_2 &= Ex_1 + F\,, \qquad F = f_1 X_1 + f_2 X_2\,, \end{aligned} \tag{C.92}$$

where

$$\begin{aligned} C &= -\frac{b}{a} = -\tan\theta_S\,, \qquad d_1 = -\frac{1}{2a}\,, \qquad d_2 = -\frac{1}{2b}\,, \\ E &= \frac{b}{a} = \tan\theta_S\,, \qquad f_1 = \frac{1}{2a}\,, \qquad f_2 = -\frac{1}{2b}\,. \end{aligned} \tag{C.93}$$

Following (C.57), the horizontal component (C.83) is written as

$$P_H = \exp[-\tfrac{1}{2}(a_1 x_1 + a_2 y_1)^2 + a_3^2 y_1^2 + a_4^2 y_2^2 + (a_7 x_1 + a_8 y_1)^2]\,, \tag{C.94}$$

where

$$\begin{aligned} a_1 &= \frac{\tan\theta_M}{\eta_M k_I}\,, \qquad a_2 = \frac{1}{\eta_M k_I}\,, \qquad a_3 = \frac{1}{\alpha_1 k_I}\,, \\ a_4 &= \frac{1}{\alpha_2 k_I}\,, \qquad a_7 = \frac{2\tan\theta_M}{\alpha_0 k_I}\,, \qquad a_8 = \frac{1}{\alpha_0 k_I}\,. \end{aligned} \tag{C.95}$$

We write the integral in the same form as (C.47):

$$R_H = \int \exp(-\tfrac{1}{2}[A' x_1^2 + B' x_1 + C'])\, dx_1\,, \tag{C.96}$$

where if we define

$$b_0 = a_1 a_2 + a_7 a_8\,, \qquad b_1 = a_2^2 + a_3^2 + a_8^2\,, \qquad b_2 = a_4^2\,, \qquad b_5 = a_1^2 + a_7^2\,, \tag{C.97}$$

then

$$A' = 2b_0 C + b_1 C^2 + b_2 E^2 + b_5\,, \tag{C.98}$$
$$B' = 2[(b_0 + b_1 C)D + b_2 EF]\,, \tag{C.99}$$
$$C' = b_1 D^2 + b_2 F^2\,, \tag{C.100}$$

Solving the integral gives the same form as (C.48) with an exponent of $C' - B'^2/4A'$, given as

$$C' - \frac{B'^2}{4A'} = g_0 D^2 + g_1 F^2 + g_4 DF\,, \tag{C.101}$$

where

$$g_0 = b_1 - (b_0 + b_1 C)^2/A'\,, \qquad g_1 = b_2 - (b_2 E)^2/A'\,, \qquad g_4 = -2(b_0 + b_1 C) b_2 E/A'\,. \tag{C.102}$$

The matrix elements $M_{k\ell}$ are then

$$M_{k\ell} = g_0 d_k d_\ell + g_1 f_k f_\ell + \tfrac{1}{2} g_4 (d_k f_\ell + d_\ell f_k)\,, \tag{C.103}$$

for $k, \ell = 1, 2$. The vertical component of the resolution function is written the same as before:

$$P_V \propto \exp[-\tfrac{1}{2}(a_{11}^2 z_1^2 + a_{12}^2 z_2^2)]\,, \tag{C.104}$$

except this time

$$a_{11}^2 = \frac{1}{(4\sin^2\theta_M \eta_M'^2 + \beta_0^2) k_I^2} + \frac{1}{\beta_1^2 k_I^2}\,, \qquad a_{12}^2 = \frac{1}{\beta_2^2 k_F^2}\,. \tag{C.105}$$

Integration over z_1 yields, as before,

$$M_{33} = \frac{a_{11}^2 a_{12}^2}{a_{11}^2 + a_{12}^2}\,, \tag{C.106}$$

and this allows us to write the complete resolution function as

$$R_H = R_0 \exp(-\tfrac{1}{2} M_{k\ell} X_k X_\ell)\,, \tag{C.107}$$

for $k, \ell = 1, 2, 3$, and where the normalization factor R_0 is

$$R_0 = \phi \cdot \epsilon_D \cdot P_{0M} \cdot N_M \cdot J \cdot R_{0x} \cdot R_{0z}\,, \tag{C.108}$$

which, when the excluding the true constants, is

$$R_0 = 2\pi \frac{1}{k_I^5 \sin 2\theta_S} \frac{1}{\sqrt{A'(a_{11}^2 + a_{12}^2)}} \frac{\beta_0}{\sqrt{\beta_0^2 + (2\eta_M' \sin\theta_M)^2}}\,. \tag{C.109}$$

C.2.2 Inelastic scattering

In a two-axis measurement, because the detector counts neutrons regardless of their energy, the energy resolution is infinitely broad. The four-dimensional energy-momentum resolution function cannot be described by an ellipsoid because the most probable momentum transfer $\mathbf{Q}_0$ depends non-trivially on the energy transfer ω_0 considered.

However, given an energy transfer ω_0, and given the proper $\mathbf{Q}_0$ which corresponds to ω_0, the resolution function about $(\mathbf{Q}_0, \omega_0)$ is an ellipsoid in the momentum directions. It is this resolution function I calculate here. To fully simulate a two-axis measurement (see Section A.3), this momentum-space resolution function is calculated for many energies ω_0, convoluted with the intrinsic signal, and integrated over all of the energies that are physically allowed.

The overall procedure is very similar to the situation two-axis elastic scattering, so I refer often to those equations. In fact, the vertical component of the resolution function is identical to the elastic case, as one may expect. We thus discuss only the horizontal component.

The key differences with the elastic case are that $k_F \neq k_I$ (so that λ is again relevant), and that the angles in the scattering triangle no longer simplify. We write

$$\begin{aligned} y_1 &= Cx_1 + D\,, & D &= d_1X_1 + d_2X_2\,, \\ y_2 &= Ex_1 + F\,, & F &= f_1X_1 + f_2X_2\,, \\ x_2 &= \lambda x_1\,, \end{aligned} \tag{C.110}$$

where

$$\begin{aligned} C &= -\frac{\lambda-\beta}{\alpha}\,, & d_1 &= \frac{B}{\alpha}\,, & d_2 &= -\frac{A}{\alpha}\,, \\ E &= -\frac{\beta\lambda-1}{\alpha}\,, & f_1 &= \frac{b}{\alpha}\,, & f_2 &= -\frac{a}{\alpha}\,, \end{aligned} \tag{C.111}$$

and where

$$\begin{aligned} a &= \sin\Phi\,, & A &= \sin(2\theta_S+\Phi)\,, & \alpha &= \sin 2\theta_S\,, & \lambda &= \frac{k_I}{k_F}\,. \\ b &= \cos\Phi\,, & B &= \cos(2\theta_S+\Phi)\,, & \beta &= \cos 2\theta_S\,, \end{aligned} \tag{C.112}$$

The horizontal component of the resolution function is then written in the form (C.94) where

$$\begin{aligned} a_1 &= \frac{\tan\theta_M}{\eta_M k_I}\,, & a_2 &= \frac{1}{\eta_M k_I}\,, & a_3 &= \frac{1}{\alpha_1 k_I}\,, \\ a_4 &= \frac{1}{\alpha_2 k_F}\,, & a_7 &= \frac{2\tan\theta_M}{\alpha_0 k_I}\,, & a_8 &= \frac{1}{\alpha_0 k_I}\,. \end{aligned} \tag{C.113}$$

Now that these variables have been defined, the remainder of the procedure is the same as with the elastic case, from (C.96) to (C.108). The resolution function is given by

$$R_H = R_0 \exp(-\tfrac{1}{2} M_{k\ell} X_k X_\ell)\,, \tag{C.114}$$

where

$$R_0 = 2\pi \frac{1}{k_I^2 k_F^3 \sin 2\theta_S} \frac{1}{\sqrt{A'(a_{11}^2 + a_{12}^2)}} \frac{\beta_0}{\sqrt{\beta_0^2 + (2\eta'_M \sin\theta_M)^2}}\,. \tag{C.115}$$

Bibliography

[1] J. G. Bednorz and K. A. Müller. Possible high T_c superconductivity in the Ba-La-Cu-O system. *Z. Phys. B.* **64**, 189–193 (1986).

[2] American Superconductor. World's first transmission voltage superconductor cable energized in LIPA's power grid. http://www.amsc.com/newsroom/documents/LIPA%20Energized%200408%20-%20Final.pdf (2008).

[3] H. Kamerlingh Onnes. The superconductivity of mercury. *Comm. Phys. Lab. Univ. Leiden* **122b** (1911).

[4] J. Bardeen, L. N. Cooper, and J. R. Schrieffer. Microscopic theory of superconductivity. *Phys. Rev.* **106**, 162–164 (1957).

[5] M. A. Kastner, R. J. Birgeneau, G. Shirane, and Y. Endoh. Magnetic, transport, and optical properties of monolayer copper oxides. *Rev. Mod. Phys.* **70**, 897–928 (1998).

[6] A. Schilling, M. Cantoni, J. D. Guo, and H. R. Ott. Superconductivity above 130 K in the Hg-Ba-Ca-Cu-O system. *Nature* **363**, 56–58 (1993).

[7] P. G. Radaelli, J. D. Jorgensen, A. J. Schultz, J. L. Peng, and R. L. Greene. Evidence of apical oxygen in Nd_2CuO_y determined by single-crystal neutron diffraction. *Phys. Rev. B* **49**, 15322–15326 (1994).

[8] N. F. Mott. Metal-insulator transition. *Rev. Mod. Phys.* **40**, 677–683 (1968).

[9] L. F. Mattheiss. Electronic band properties and superconductivity in $La_{2-y}X_yCuO_4$. *Phys. Rev. Lett.* **58**, 1028–1030 (1987).

[10] E. Dagotto. Correlated electrons in high-temperature superconductors. *Rev. Mod. Phys.* **66**, 763–840 (1994).

[11] P. W. Anderson. Antiferromagnetism. Theory of superexchange interaction. *Phys. Rev.* **79**, 350–356 (1950).

[12] B. Keimer, N. Belk, R. J. Birgeneau, A. Cassanho, *et al.* Magnetic excitations in pure, lightly doped, and weakly metallic La_2CuO_4. *Phys. Rev. B* **46**, 14034–14053 (1992).

[13] G. M. Luke, L. P. Le, B. J. Sternlieb, Y. J. Uemura, *et al.* Magnetic order and electronic phase diagrams of electron-doped copper oxide materials. *Phys. Rev. B* **42**, 7981–7988 (1990).

[14] P. K. Mang, O. P. Vajk, A. Arvanitaki, J. W. Lynn, and M. Greven. Spin correlations and magnetic order in nonsuperconducting $Nd_{2-x}Ce_xCuO_{4\pm\delta}$. *Phys. Rev. Lett.* **93**, 027002 (2004).

[15] M. Matsuda, Y. Endoh, K. Yamada, H. Kojima, *et al.* Magnetic order, spin correlations, and superconductivity in single crystal $Nd_{1.85}Ce_{0.15}CuO_{4+\delta}$. *Phys. Rev. B* **45**, 12548–12555 (1992).

[16] T. Uefuji, T. Kubo, K. Yamada, M. Fujita, *et al.* Coexistence of antiferromagnetic ordering and high-T_c superconductivity in electron-doped superconductor $Nd_{2-x}Ce_xCuO_4$. *Physica C* **357**, 208–211 (2001).

[17] Y. Tokura, H. Takagi, and S. Uchida. A superconducting copper oxide compound with electrons as the charge carriers. *Nature* **337**, 345–347 (1989).

[18] T. Uefuji, S. Kuroshima, M. Fujita, and K. Yamada. Superconducting phase diagram of electron-doped cuprates $Nd_{2-x}Ce_xCuO_4$. *Physica C* **392/396**, 189–193 (2003).

[19] E. M. Motoyama, G. Yu, I. M. Vishik, O. P. Vajk, *et al.* Spin correlations in the electron-doped high-transition-temperature superconductor $Nd_{2-x}Ce_xCuO_{4\pm\delta}$. *Nature* **445**, 186–189 (2007).

[20] T. Uefuji, K. Kurahashi, M. Fujita, M. Matsuda, and K. Yamada. Electron-doping effect on magnetic order and superconductivity in $Nd_{2-x}Ce_xCuO_4$ single crystals. *Physica C* **378-381**, 273–277 (2002).

[21] I. Tanaka, N. Komai, and H. Kojima. Phase equilibrium in the Nd-Ce-Cu-O system. *Physica C* **190**, 112–113 (1991).

[22] O. P. Vajk. *Quantum impurities in a two-dimensional Heisenberg antiferromagnet*. Ph.D. thesis, Stanford University (2003).

[23] P. K. Mang, S. Larochelle, A. Mehta, O. P. Vajk, *et al.* Phase decomposition and chemical inhomogeneity in $Nd_{2-x}Ce_xCuO_{4\pm\delta}$. *Phys. Rev. B* **70**, 094507 (2004).

[24] M. Lambacher. *Crystal growth and normal state transport of electron doped high temperature superconductors*. Ph.D. thesis, Technische Universität München (2008).

[25] H. Eisaki, N. Kaneko, D. L. Feng, A. Damascelli, *et al.* Effect of chemical inhomogeneity in bismuth-based copper oxide superconductors. *Phys. Rev. B* **69**, 064512 (2004).

[26] W. Jiang, J. L. Peng, Z. Y. Li, and R. L. Greene. Transport properties of $Nd_{1.85}Ce_{0.15}CuO_{4+\delta}$ crystals before and after reduction. *Phys. Rev. B* **47**, 8151–8155 (1993).

[27] X. Q. Xu, S. N. Mao, W. Jiang, J. L. Peng, and R. L. Greene. Oxygen dependence of the transport properties of $Nd_{1.78}Ce_{0.22}CuO_{4\pm\delta}$. *Phys. Rev. B* **53**, 871–875 (1996).

[28] A. J. Schultz, J. D. Jorgensen, J. L. Peng, and R. L. Greene. Single-crystal neutron-diffraction structures of reduced and oxygenated $Nd_{2-x}Ce_xCuO_y$. *Phys. Rev. B* **53**, 5157–5159 (1996).

[29] J. S. Higgins, Y. Dagan, M. C. Barr, B. D. Weaver, and R. L. Greene. Role of oxygen in the electron-doped superconducting cuprates. *Phys. Rev. B* **73**, 104510 (2006).

[30] P. Richard, G. Riou, I. Hetel, S. Jandl, *et al.* Role of oxygen nonstoichiometry and the reduction process on the local structure of $Nd_{2-x}Ce_xCuO_{4\pm\delta}$. *Phys. Rev. B* **70**, 064513 (2004).

[31] G. Riou, P. Richard, S. Jandl, M. Poirier, *et al.* Pr^{3+} crystal-field excitation study of apical oxygen and reduction processes in $Pr_{2-x}Ce_xCuO_{4\pm\delta}$. *Phys. Rev. B* **69**, 024511 (2004).

[32] H. J. Kang, P. Dai, B. J. Campbell, P. J. Chupas, *et al.* Microscopic annealing process and its impact on superconductivity in *T'*-structure electron-doped copper oxides. *Nat. Mater.* **6**, 224–229 (2007).

[33] X. Xu, H. Yang, S. Ke, and C. Sun. Analysis of the effects of annealing on the electron-doped cuprate superconductor $Nd_{1.85}Ce_{0.15}CuO_{4-\delta}$ using x-ray photoemission spectroscopy. *Supercond. Sci. Technol.* **22**, 075013 (2009).

[34] P. Richard, M. Neupane, Y.-M. Xu, P. Fournier, *et al.* Competition between antiferromagnetism and superconductivity in the electron-doped cuprates triggered by oxygen reduction. *Phys. Rev. Lett.* **99**, 157002 (2007).

[35] J. Gauthier, S. Gagne, J. Renaud, M.-E. Gosselin, *et al.* Different roles of cerium substitution and oxygen reduction in transport in $Pr_{2-x}Ce_xCuO_4$ thin films. *Phys. Rev. B* **75**, 024424 (2007).

[36] J. S. Kim and D. R. Gaskell. The phase stability diagrams for the systems $Nd_2CuO_{4-\delta}$ and $Nd_{1.85}Ce_{0.15}CuO_{4-\delta}$. *Physica C* **209**, 381–388 (1993).

[37] P. K. Mang. *Magnetic, phonon, and structural scattering studies of the electron-doped high-temperature superconductor neodymium cerium copper oxide*. Ph.D. thesis, Stanford University (2004).

[38] J. Clarke. SQUIDs. *Sci. Am.* **271**, 36–43 (1994).

[39] Quantum Design, San Diego, CA. *MPMS Hardware Manual* (1996).

[40] J. R. Thompson, D. K. Christen, H. R. Kerchner, L. A. Boatner, *et al.* Studies of 'non-ideal' superconductors using DC magnetic methods. In R. A. Hein, T. L. Francavilla, and D. H. Liebenberg, editors, *Magnetic Susceptibility of Superconductors and Other Spin Systems*, pp. 157–176 (Plenum, New York, 1991).

[41] N. Barišić, Y. Li, X. Zhao, Y.-C. Cho, *et al.* Demonstrating the model nature of the high-temperature superconductor $HgBa_2CuO_{4+\delta}$. *Phys. Rev. B* **78**, 054518 (2008).

[42] M. D. Lan, J. Z. Liu, and R. N. Shelton. Effects of Cu substitution by Fe on the magnetic properties of $YBa_2Cu_3O_{7-y}$ single crystals. *Phys. Rev. B* **43**, 12989–12993 (1991).

[43] Stanford University Environmental Measurement I: Gas-Solution Analytical Center. About ICP. http://em-1.stanford.edu/Schedule/ICP/abouticp.htm.

[44] J. M. Mermet. Is it still possible, necessary and beneficial to perform research in ICP-atomic emission spectrometry? *J. Anal. At. Spectrom.* **20**, 11–16 (2005).

[45] K. Gamayunov, I. Tanaka, and H. Kojima. TSFZ growth of $Nd_{2-x}Ce_xCuO_4$ single crystals at low oxygen pressure. *Physica C* **235-240**, 557 – 558 (1994).

[46] W. Friedrich, P. Knipping, and M. von Laue. Interferenz-Ercheinungen bei Röntgenstrahlen. *Sitzungsberichte der Kgl. Bayer. Akad. der Wiss.* pp. 303–322 (1912).

[47] G. Shirane, S. M. Shapiro, and J. M. Tranquada. *Neutron scattering with a triple-axis spectrometer* (Cambridge University Press, 2002).

[48] L. Pintschovius and W. Reichardt. Neutron scattering in layered copper-oxide superconductors. In A. Furrer, editor, *Physics and Chemistry of Materials with Low-Dimensional Structures*, vol. 20, p. 165 (Kluwer Academic, Dordrecht, 1998).

[49] A. Zheludev. Reslib. http://neutron.ornl.gov/~zhelud/reslib/index.html.

[50] M. Matsuda, K. Yamada, K. Kakurai, H. Kadowaki, *et al.* Three-dimensional magnetic structures and rare-earth magnetic ordering in Nd_2CuO_4 and Pr_2CuO_4. *Phys. Rev. B* **42**, 10098–10107 (1990).

[51] S. Skanthakumar, J. W. Lynn, J. L. Peng, and Z. Y. Li. Observation of non-collinear magnetic structure for the Cu spins in Nd_2CuO_4-type systems. *Phys. Rev. B* **47**, 6173–6176 (1993).

[52] S. Shamoto, M. Sato, J. M. Tranquada, B. J. Sternlieb, and G. Shirane. Neutron-scattering study of antiferromagnetism in $YBa_2Cu_3O_{6.15}$. *Phys. Rev. B* **48**, 13817–13825 (1993).

[53] E. Prince, editor. *International Tables for Crystallography*, vol. C, chap. 4.4, pp. 430–487 (International Union of Crystallography, 2006), 1st online ed.

[54] R. J. Birgeneau, J. Skalyo, J., and G. Shirane. Critical magnetic scattering in K_2NiF_4. *Phys. Rev. B* **3**, 1736–1749 (1971).

[55] R. J. Birgeneau, M. Greven, M. A. Kastner, Y. S. Lee, *et al.* Instantaneous spin correlations in La_2CuO_4. *Phys. Rev. B* **59**, 13788–13794 (1999).

[56] O. P. Vajk, M. Greven, P. K. Mang, and J. W. Lynn. Neutron scattering, magnetometry, and quantum Monte Carlo study of the randomly diluted spin-1/2 square-lattice Heisenberg antiferromagnet. *Solid State Commun.* **126**, 93–101 (2003).

[57] J. E. Sonier. Muon spin rotation/relaxation/resonance (μSR). http://musr.ca/intro/musr/muSRBrochure.pdf.

[58] S. Chakravarty, B. I. Halperin, and D. R. Nelson. Two-dimensional quantum Heisenberg antiferromagnet at low temperatures. *Phys. Rev. B* **39**, 2344–2371 (1989).

[59] Y. Endoh, K. Yamada, R. J. Birgeneau, D. R. Gabbe, *et al.* Static and dynamic spin correlations in pure and doped La_2CuO_4. *Phys. Rev. B* **37**, 7443–7453 (1988).

[60] E. Manousakis. The spin-$\frac{1}{2}$ Heisenberg antiferromagnet on a square lattice and its application to the cuprous oxides. *Rev. Mod. Phys.* **63**, 1–62 (1991).

[61] F. D. M. Haldane. Nonlinear field theory of large-spin heisenberg antiferromagnets: Semiclassically quantized solitons of the one-dimensional easy-axis Néel state. *Phys. Rev. Lett.* **50**, 1153–1156 (1983).

[62] T. Einarsson and H. J. Schulz. Direct calculation of the spin stiffness in the J_1-J_2 heisenberg antiferromagnet. *Phys. Rev. B* **51**, 6151–6154 (1995).

[63] B. B. Beard, R. J. Birgeneau, M. Greven, and U.-J. Wiese. Square-lattice Heisenberg antiferromagnet at very large correlation lengths. *Phys. Rev. Lett.* **80**, 1742–1745 (1998).

[64] S. Chakravarty, B. I. Halperin, and D. R. Nelson. Low-temperature behavior of two-dimensional quantum antiferromagnets. *Phys. Rev. Lett.* **60**, 1057–1060 (1988).

[65] P. Hasenfratz and F. Niedermayer. The exact correlation length of the antiferromagnetic $d = 2 + 1$ Heisenberg model at low temperatures. *Phys. Lett. B* **268**, 231–235 (1991).

[66] P. Hasenfratz. The correlation length of the heisenberg antiferromagnet with arbitrary spin s. *Eur. Phys. J. B* **13**, 11–14 (2000).

[67] N. D. Mermin and H. Wagner. Absence of ferromagnetism or antiferromagnetism in one- or two-dimensional isotropic heisenberg models. *Phys. Rev. Lett.* **17**, 1133–1136 (1966).

[68] J. M. Kosterlitz and D. J. Thouless. Ordering, metastability and phase transitions in two-dimensional systems. *J. Phys. C* **6**, 1181–1203 (1973).

[69] H.-Q. Ding. Could in-plane exchange anisotropy induce the observed antiferromagnetic transitions in the undoped high-T_c materials? *Phys. Rev. Lett.* **68**, 1927–1930 (1992).

[70] M. Greven, R. J. Birgeneau, Y. Endoh, M. A. Kastner, *et al.* Spin correlations in the 2D Heisenberg antiferromagnet $Sr_2CuO_2Cl_2$: neutron scattering, Monte Carlo simulation, and theory. *Phys. Rev. Lett.* **72**, 1096–1099 (1994).

[71] Y. S. Lee, M. Greven, B. O. Wells, R. J. Birgeneau, and G. Shirane. Spin correlations in the two-dimensional spin-5/2 Heisenberg antiferromagnet. *Eur. Phys. J. B* **5**, 15–22 (1998).

[72] O. P. Vajk, P. K. Mang, M. Greven, P. M. Gehring, and J. W. Lynn. Quantum impurities in the two-dimensional spin one-half Heisenberg antiferromagnet. *Science* **295**, 1691–1695 (2002).

[73] T. R. Thurston, M. Matsuda, K. Kakurai, K. Yamada, *et al.* Antiferromagnetic spin correlations in $(Nd,Pr)_{2-x}Ce_xCuO_4$. *Phys. Rev. Lett.* **65**, 263–266 (1990).

[74] S. T. Bramwell and P. C. W. Holdsworth. Universality in two-dimensional magnetic systems. *J. App. Phys.* **73**, 6096–6098 (1993).

[75] S. T. Bramwell and P. C. W. Holdsworth. Magnetization and universal sub-critical behaviour in two-dimensional *XY* magnets. *J. Phys. Condens. Matter* **5**, L53–L59 (1993).

[76] M. J. Rosseinsky, K. Prassides, and P. Day. Magnetic order and crystal chemistry of neodymium cerium copper oxide, $Nd_{2-x}Ce_xCuO_{4-\delta}$. *Inorg. Chem.* **30**, 2680–2687 (1991).

[77] C. Kusko, R. S. Markiewicz, M. Lindroos, and A. Bansil. Fermi surface evolution and collapse of the Mott pseudogap in $Nd_{2-x}Ce_xCuO_{4\pm\delta}$. *Phys. Rev. B* **66**, 140513 (2002).

[78] Q. S. Yuan, Y. Chen, T. K. Lee, and C. S. Ting. Fermi surface evolution in the antiferromagnetic state for the electron-doped *t*-*t*′-*t*′′-*J* model. *Phys. Rev. B* **69**, 214523 (2004).

[79] T. Xiang, H. G. Luo, D. H. Lu, K. M. Shen, and Z. X. Shen. Intrinsic electron and hole bands in electron-doped cuprate superconductors. *Phys. Rev. B* **79**, 014524 (2009).

[80] N. P. Armitage, F. Ronning, D. H. Lu, C. Kim, *et al.* Doping dependence of an *n*-type cuprate superconductor investigated by angle-resolved photoemission spectroscopy. *Phys. Rev. Lett.* **88**, 257001 (2002).

[81] G. Yu, Y. Li, E. M. Motoyama, K. Hradil, *et al.* Two characteristic energies in the low-energy antiferromagnetic response of the electron-doped high-temperature superconductor $Nd_{2-x}Ce_xCuO_{4+\delta}$. arXiv:0803.3250v2.

[82] R. S. Markiewicz. Mode-coupling model of Mott gap collapse in the cuprates: Natural phase boundary for quantum critical points. *Phys. Rev. B* **70**, 174518 (2004).

[83] T. Kubo, T. Uefuji, M. Fujita, K. Yamada, *et al.* Magnetic phase diagrams of electron-doped high-T_c cuprates $Pr_{1-x}LaCe_xCuO_{4-\delta}$ and $Nd_{2-x}Ce_xCuO_{4-\delta}$ studied by μSR measurements. *Physica C* **378**, 354–359 (2002).

[84] M. Fujita, T. Kubo, S. Kuroshima, T. Uefuji, *et al.* Magnetic and superconducting phase diagram of electron-doped $Pr_{1-x}LaCe_xCuO_4$. *Phys. Rev. B* **67**, 014514 (2003).

[85] B. Keimer, R. J. Birgeneau, A. Cassanho, Y. Endoh, *et al.* Soft phonon behavior and magnetism at the low temperature structural phase transition of $La_{1.65}Nd_{0.35}CuO_4$. *Z. Phys. B* **91**, 373–382 (1993).

[86] P. Bourges, A. S. Ivanov, D. Petitgrand, J. Rossat-Mignod, and L. Boudarene. Two-dimensional antiferromagnetic excitations in Nd_2CuO_4. *Physica B* **186-188**, 925–927 (1993).

[87] M. Greven, R. J. Birgeneau, Y. Endoh, M. A. Kastner, *et al.* Neutron-scattering study of the 2-dimensional spin $S = 1/2$ square-lattice Heisenberg-antiferromagnet $Sr_2CuO_2Cl_2$. *Z. Phys. B* **96**, 465–477 (1995).

[88] Y. Dagan, M. M. Qazilbash, C. P. Hill, V. N. Kulkarni, and R. L. Greene. Evidence for a quantum phase transition in $Pr_{2-x}Ce_xCuO_{4-\delta}$ from transport measurements. *Phys. Rev. Lett.* **92**, 167001 (2004).

[89] Y. Dagan, M. M. Qazilbash, and R. L. Greene. Tunneling into the normal state of $Pr_{2-x}Ce_xCuO_4$. *Phys. Rev. Lett.* **94**, 187003 (2005).

[90] Ch. Niedermayer, C. Bernhard, T. Blasius, A. Golnik, *et al.* Common phase diagram for antiferromagnetism in $La_{2-x}Sr_xCuO_4$ and $Y_{1-x}Ca_xBa_2Cu_3O_6$ as seen by muon spin rotation. *Phys. Rev. Lett.* **80**, 3843–3846 (1998).

[91] M. Matsuda, Y. S. Lee, M. Greven, M. A. Kastner, *et al.* Freezing of anisotropic spin clusters in $La_{1.98}Sr_{0.02}CuO_4$. *Phys. Rev. B* **61**, 4326–4333 (2000).

[92] S. Wakimoto, S. Ueki, Y. Endoh, and K. Yamada. Systematic study of short-range antiferromagnetic order and the spin-glass state in lightly doped $La_{2-x}Sr_xCuO_4$. *Phys. Rev. B* **62**, 3547–3553 (2000).

[93] S. Kuroshima, M. Fujita, T. Uefuji, M. Matsuda, and K. Yamada. Phase diagram of the electron-doped superconductor $Pr_{1-x}LaCe_xCuO_{4-\delta}$. *Physica C* **392/396**, 216–220 (2003).

[94] H. Luetkens, H. H. Klauss, M. Kraken, F. J. Litterst, *et al.* The electronic phase diagram of the $LaO_{1-x}F_xFeAs$ superconductor. *Nat. Mater.* **8**, 305–309 (2009).

[95] A. J. Drew, Ch. Niedermayer, P. J. Baker, F. L. Pratt, *et al.* Coexistence of static magnetism and superconductivity in $SmFeAsO_{1-x}F_x$ as revealed by muon spin rotation. *Nat. Mater.* **8**, 310–314 (2009).

[96] J. Zhao, Q. Huang, C. de la Cruz, S. Li, *et al.* Structural and magnetic phase diagram of $CeFeAsO_{1-x}F_x$ and its relation to high-temperature superconductivity. *Nat. Mater.* **7**, 953–959 (2008).

[97] H. Chen, Y. Ren, Y. Qiu, W. Bao, *et al.* Coexistence of the spin-density wave and superconductivity in $Ba_{1-x}K_xFe_2As_2$. *Europhys. Lett.* **85**, 17006 (2009).

[98] F. Kagawa, K. Miyagawa, and K. Kanoda. Unconventional critical behaviour in a quasi-two-dimensional organic conductor. *Nature* **436**, 534–537 (2005).

[99] T. Park, F. Ronning, H. Q. Yuan, M. B. Salamon, *et al.* Hidden magnetism and quantum criticality in the heavy fermion superconductor $CeRhIn_5$. *Nature* **440**, 65–68 (2006).

[100] Y. J. Uemura. Superconductivity: Commonalities in phase and mode. *Nat. Mater.* **8**, 253–255 (2009).

[101] E. M. Motoyama, P. K. Mang, D. Petitgrand, G. Yu, *et al.* Magnetic field effect on the superconducting magnetic gap of $Nd_{1.85}Ce_{0.15}CuO_4$. *Phys. Rev. Lett.* **96**, 137002 (2006).

[102] R. P. Feynman, R. B. Leighton, and M. L. Sands. *The Feynman Lectures on Physics*, vol. III (Addison-Wesley, Reading, Massachusetts, 1965).

[103] M. Tinkham. *Introduction to Superconductivity* (McGraw-Hill, New York, 1996), 2nd ed.

[104] A. Bianchi, R. Movshovich, N. Oeschler, P. Gegenwart, *et al.* First-order superconducting phase transition in $CeCoIn_5$. *Phys. Rev. Lett.* **89**, 137002 (2002).

[105] B. S. Chandrasekhar. A note on the maximum critical field of high-field superconductors. *Appl. Phys. Lett.* **1**, 7–8 (1962).

[106] A. M. Clogston. Upper limit for critical field in hard superconductors. *Phys. Rev. Lett.* **9**, 266–267 (1962).

[107] Y. Y. Wang, S. Ono, Y. Onose, G. Gu, *et al.* Dependence of upper critical field and pairing strength on doping in cuprates. *Science* **299**, 86–89 (2003).

[108] O. Cyr-Choiniere, R. Daou, F. Laliberte, D. LeBoeuf, *et al.* Enhancement of the Nernst effect by stripe order in a high-T_c superconductor. *Nature* **458**, 743–745 (2009).

[109] H. Matsui, K. Terashima, T. Sato, T. Takahashi, *et al.* Direct observation of a nonmonotonic $d_{x^2-y^2}$-wave superconducting gap in the electron-doped high-T_c superconductor $Pr_{0.89}LaCe_{0.11}CuO_4$. *Phys. Rev. Lett.* **95**, 017003 (2005).

[110] M. M. Qazilbash, A. Koitzsch, B. S. Dennis, A. Gozar, *et al.* Evolution of superconductivity in electron-doped cuprates: Magneto-Raman spectroscopy. *Phys. Rev. B* **72**, 214510 (2005).

[111] P. Li, F. F. Balakirev, and R. L. Greene. Upper critical field of electron-doped $Pr_{2-x}Ce_xCuO_{4-\delta}$ in parallel magnetic fields. *Phys. Rev. B* **75**, 172508 (2007).

[112] S. W. Cheong, G. Aeppli, T. E. Mason, H. Mook, *et al.* Incommensurate magnetic fluctuations in $La_{2-x}Sr_xCuO_4$. *Phys. Rev. Lett.* **67**, 1791–1794 (1991).

[113] K. Yamada, C. H. Lee, K. Kurahashi, J. Wada, *et al.* Doping dependence of the spatially modulated dynamical spin correlations and the superconducting-transition temperature in $La_{2-x}Sr_xCuO_4$. *Phys. Rev. B* **57**, 6165–6172 (1998).

[114] H. A. Mook, P. C. Dai, S. M. Hayden, G. Aeppli, *et al.* Spin fluctuations in $YBa_2Cu_3O_{6.6}$. *Nature* **395**, 580–582 (1998).

[115] B. Lake, H. M. Ronnow, N. B. Christensen, G. Aeppli, *et al.* Antiferromagnetic order induced by an applied magnetic field in a high-temperature superconductor. *Nature* **415**, 299–302 (2002).

[116] B. Khaykovich, Y. S. Lee, R. W. Erwin, S. H. Lee, *et al.* Enhancement of long-range magnetic order by magnetic field in superconducting La_2CuO_{4+y}. *Phys. Rev. B* **66**, 014528 (2002).

[117] J. M. Tranquada, H. Woo, T. G. Perring, H. Goka, *et al.* Quantum magnetic excitations from stripes in copper oxide superconductors. *Nature* **429**, 534–538 (2004).

[118] K. Yamada, S. Wakimoto, G. Shirane, C. H. Lee, *et al.* Direct observation of a magnetic gap in superconducting $La_{1.85}Sr_{0.15}CuO_4$ (T_c = 37.3 K). *Phys. Rev. Lett.* **75**, 1626–1629 (1995).

[119] B. Lake, G. Aeppli, K. N. Clausen, D. F. McMorrow, *et al.* Spins in the vortices of a high-temperature superconductor. *Science* **291**, 1759–1762 (2001).

[120] R. Gilardi, A. Hiess, N. Momono, M. Oda, *et al.* Unusual interplay between copper-spin and vortex dynamics in slightly overdoped $La_{1.83}Sr_{0.17}CuO_4$. *Europhys. Lett.* **66**, 840–846 (2004).

[121] J. M. Tranquada, C. H. Lee, K. Yamada, Y. S. Lee, *et al.* Evidence for an incommensurate magnetic resonance in $La_{2-x}Sr_xCuO_4$. *Phys. Rev. B* **69**, 174507 (2004).

[122] E. Demler, S. Sachdev, and Y. Zhang. Spin-ordering quantum transitions of superconductors in a magnetic field. *Phys. Rev. Lett.* **87**, 067202 (2001).

[123] Y. Zhang, E. Demler, and S. Sachdev. Competing orders in a magnetic field: Spin and charge order in the cuprate superconductors. *Phys. Rev. B* **66**, 094501 (2002).

[124] B. Khaykovich, S. Wakimoto, R. J. Birgeneau, M. A. Kastner, *et al.* Field-induced transition between magnetically disordered and ordered phases in underdoped $La_{2-x}Sr_xCuO_4$. *Phys. Rev. B* **71**, 220508 (2005).

[125] D. Haug, V. Hinkov, A. Suchaneck, D. S. Inosov, *et al.* Magnetic-field-enhanced incommensurate magnetic order in the underdoped high-temperature superconductor $YBa_2Cu_3O_{6.45}$. *Phys. Rev. Lett.* **103**, 017001 (2009).

[126] K. Yamada, K. Kurahashi, T. Uefuji, M. Fujita, *et al.* Commensurate spin dynamics in the superconducting state of an electron-doped cuprate superconductor. *Phys. Rev. Lett.* **90**, 137004 (2003).

[127] H. J. Kang, P. C. Dai, J. W. Lynn, M. Matsuura, *et al.* Antiferromagnetic order as the competing ground state in electron-doped $Nd_{1.85}Ce_{0.15}CuO_4$. *Nature* **423**, 522–525 (2003).

[128] P. K. Mang, S. Larochelle, and M. Greven. Spurious magnetism in high-T_c superconductor. *Nature* **426**, 139–140 (2003).

[129] M. Fujita, M. Matsuda, S. Katano, and K. Yamada. Magnetic field effect on the static antiferromagnetism of the electron-doped superconductor $Pr_{1-x}LaCe_xCuO_4$ (x = 0.11 and 0.15). *Phys. Rev. Lett.* **93**, 147003–147004 (2004).

[130] S. Li, S. Chi, J. Zhao, H.-H. Wen, *et al.* Impact of oxygen annealing on the heat capacity and magnetic resonance of superconducting $Pr_{0.88}LaCe_{0.12}CuO_{4-\delta}$. *Phys. Rev. B* **78**, 014520 (2008).

[131] H. J. Kang, P. Dai, H. A. Mook, D. N. Argyriou, *et al.* Electronically competing phases and their magnetic field dependence in electron-doped non-superconducting and superconducting $Pr_{0.88}LaCe_{0.12}CuO_{4\pm\delta}$. *Phys. Rev. B* **71**, 214512–214517 (2005).

[132] D. Petitgrand, K. Yamada, M. Fujita, and T. Uefuji. Superconductivity induced spin gap in $Nd_{1.85}Ce_{0.15}CuO_4$. *Physica C* **408-410**, 778–779 (2004).

[133] S. D. Wilson, P. Dai, S. Li, S. Chi, *et al.* Resonance in the electron-doped high-transition-temperature superconductor $Pr_{0.88}LaCe_{0.12}CuO_{4-\delta}$. *Nature* **442**, 59–62 (2006).

[134] J. M. Tarascon, E. Wang, S. Kivelson, B. G. Bagley, *et al.* Magnetic versus nonmagnetic ion substitution effects on T_c in the La-Sr-Cu-O and Nd-Ce-Cu-O systems. *Phys. Rev. B* **42**, 218–222 (1990).

[135] J. Sugiyama, S. Tokuono, S. Koriyama, H. Yamauchi, and S. Tanaka. Comparison of paramagnetic- and nonmagnetic-impurity effects on superconductivity in $Nd_{1.85}Ce_{0.15}CuO_4$. *Phys. Rev. B* **43**, 10489–10495 (1991).

[136] B. Jayaram, H. Chen, and J. Callaway. Magnetism of Fe, Ni, and Zn in $Nd_{1.85}Ce_{0.15}CuO_4$: comparison of experiment and theory. *Phys. Rev. B* **52**, 3742–3747 (1995).

[137] J. Rossat-Mignod, L. P. Regnault, C. Vettier, P. Bourges, *et al.* Neutron scattering study of the $YBa_2Cu_3O_{6+x}$ system. *Physica C* **185-189**, 86–92 (1991).

[138] H. A. Mook, M. Yethiraj, G. Aeppli, T. E. Mason, and T. Armstrong. Polarized neutron determination of the magnetic excitations in $YBa_2Cu_3O_7$. *Phys. Rev. Lett.* **70**, 3490–3493 (1993).

[139] H. F. Fong, B. Keimer, P. W. Anderson, D. Reznik, *et al.* Phonon and magnetic neutron scattering at 41 meV in $YBa_2Cu_3O_7$. *Phys. Rev. Lett.* **75**, 316–319 (1995).

[140] P. Bourges, L. P. Regnault, Y. Sidis, and C. Vettier. Inelastic-neutron-scattering study of antiferromagnetic fluctuations in $YBa_2Cu_3O_{6.97}$. *Phys. Rev. B* **53**, 876–885 (1996).

[141] H. F. Fong, P. Bourges, Y. Sidis, L. P. Regnault, *et al.* Neutron scattering from magnetic excitation in $Bi_2Sr_2CaCu_2O_{8+\delta}$. *Nature* **398**, 588–591 (1999).

[142] H. He, Y. Sidis, P. Bourges, G. D. Gu, *et al.* Resonant spin excitation in an overdoped high temperature superconductor. *Phys. Rev. Lett.* **86**, 1610–1613 (2001).

[143] H. He, P. Bourges, Y. Sidis, C. Ulrich, *et al.* Magnetic resonant mode in the single-layer high-temperature superconductor $Tl_2Ba_2CuO_{6+\delta}$. *Science* **295**, 1045–1047 (2002).

[144] G. Yu, Y. Li, E. M. Motoyama, X. Zhao, *et al.* Magnetic resonance in the model high-temperature superconductor $HgBa_2CuO_{4+\delta}$. arXiv:0810.5759v1.

[145] N. K. Sato, N. Aso, K. Miyake, R. Shiina, *et al.* Strong coupling between local moments and superconducting 'heavy' electrons in UPd_2Al_3. *Nature* **410**, 340–343 (2001).

[146] C. Stock, C. Broholm, J. Hudis, H. J. Kang, and C. Petrovic. Spin resonance in the *d*-wave superconductor $CeCoIn_5$. *Phys. Rev. Lett.* **100**, 087001 (2008).

[147] A. D. Christianson, E. A. Goremychkin, R. Osborn, S. Rosenkranz, *et al.* Unconventional superconductivity in $Ba_{0.6}K_{0.4}Fe_2As_2$ from inelastic neutron scattering. *Nature* **456**, 930–932 (2008).

[148] G. Yu, Y. Li, E. M. Motoyama, and M. Greven. A universal relationship between magnetic resonance and superconducting gap in unconventional superconductors. *Nat. Phys.* **5**, 873–875 (2009).

[149] J. Zhao, P. Dai, S. Li, P. G. Freeman, *et al.* Neutron-spin resonance in the optimally electron-doped superconductor $Nd_{1.85}Ce_{0.15}CuO_{4-\delta}$. *Phys. Rev. Lett.* **99**, 017001 (2007).

[150] Y. Gallais, A. Sacuto, P. Bourges, Y. Sidis, *et al.* Evidence for two distinct energy scales in the raman spectra of $YBa_2(Cu_{1-x}Ni_x)_3O_{6.95}$. *Phys. Rev. Lett.* **88**, 177401 (2002).

[151] B. Kyung, V. Hankevych, A. M. Dare, and A. M. Tremblay. Pseudogap and spin fluctuations in the normal state of the electron-doped cuprates. *Phys. Rev. Lett.* **93**, 147004 (2004).

[152] H. Matsui, K. Terashima, T. Sato, T. Takahashi, *et al.* Angle-resolved photoemission spectroscopy of the antiferromagnetic superconductor $Nd_{1.87}Ce_{0.13}CuO_4$: anisotropic spin-correlation gap, pseudogap, and the induced quasiparticle mass enhancement. *Phys. Rev. Lett.* **94**, 047005 (2005).

[153] T. Timusk and B. Statt. The pseudogap in high-temperature superconductors: an experimental survey. *Rep. Prog. Phys.* **62**, 61–122 (1999).

[154] Y. Onose, Y. Taguchi, K. Ishizaka, and Y. Tokura. Charge dynamics in underdoped $Nd_{2-x}Ce_xCuO_4$: Pseudogap and related phenomena. *Phys. Rev. B* **69**, 024504 (2004).

[155] A. Zimmers, J. M. Tomczak, R. P. M. Lobo, N. Bontemps, *et al.* Infrared properties of electron-doped cuprates: Tracking normal-state gaps and quantum critical behavior in $Pr_{2-x}Ce_xCuO_4$. *Europhys. Lett.* **70**, 225–231 (2005).

[156] B. Fauque, Y. Sidis, V. Hinkov, S. Pailhes, *et al.* Magnetic order in the pseudogap phase of high-T_c superconductors. *Phys. Rev. Lett.* **96**, 197001 (2006).

[157] H. A. Mook, Y. Sidis, B. Fauque, V. Baledent, and P. Bourges. Observation of magnetic order in a superconducting $YBa_2Cu_3O_{6.6}$ single crystal using polarized neutron scattering. *Phys. Rev. B* **78**, 020506 (2008).

[158] Y. Li, V. Baledent, N. Barisic, Y. Cho, *et al.* Unusual magnetic order in the pseudogap region of the superconductor $HgBa_2CuO_{4+\delta}$. *Nature* **455**, 372–375 (2008).

[159] G. L. Squires. *Introduction to the Theory of Thermal Neutron Scattering* (Cambridge University Press, London, 1978).

[160] S. W. Lovesey. *Theory of Neutron Scattering from Condensed Matter*, vol. 2 (Clarendon Press, Oxford, 1984).

[161] P. M. Chaikin and T. C. Lubensky. *Principles of condensed matter physics* (Cambridge University Press, Cambridge, 1995).

[162] H. F. Fong, P. Bourges, Y. Sidis, L. P. Regnault, *et al.* Spin susceptibility in underdoped $YBa_2Cu_3O_{6+x}$. *Phys. Rev. B* **61**, 14773–14786 (2000).

[163] M. J. Cooper and R. Nathans. The resolution function in neutron diffractometry. I. The resolution function of a neutron diffractometer and its application to phonon measurements. *Acta Cryst.* **23**, 357–367 (1967).

[164] N. J. Chesser and J. D. Axe. Derivation and experimental verification of the normalized resolution function for inelastic neutron scattering. *Acta Cryst. A* **29**, 160 (1973).

[165] M. J. Cooper and R. Nathans. The resolution function in neutron diffractometry. II. The resolution function of a conventional two-crystal diffractometer for elastic scattering. *Acta Cryst. A* **24**, 481–484 (1968).

[166] S. A. Werner and R. Pynn. Resolution effects in the measurement of phonons in sodium metal. *J. App. Phys.* **42**, 4736–4749 (1971).